

AD-A020 712

PASSIVE NOSETIP TECHNOLOGY (PANT) PROGRAM. VOLUME
XIV. AN EXPERIMENTAL STUDY TO EVALUATE THE IRREGULAR
NOSETIP SHAPE REGIME - DATA REPORT

E. V. Nelson, et al

Acurex Corporation

Prepared for:

Space and Missile Systems Organization

April 1974

DISTRIBUTED BY:

NTIS

National Technical Information Service
U. S. DEPARTMENT OF COMMERCE

055044

SAMSO-TR-74-36
Volume XIV

(1)

DA020712

INTERIM REPORT
PASSIVE NOSETIP TECHNOLOGY
(PANT) PROGRAM

Volume XIV. An Experimental Study to Evaluate the Irregular
Nosetip Shape Regime - Data Report

E. V. Nelson
T. C. Derbidge
D. Chan

Aerotherm Division/Acurex Corporation

SAMSO-TR-74-86

April 1974

AEROTHERM REPORT 74-100

3500
RECEIVED
APR 1974
1076

CL

This document may be distributed further by any holder
only with specific prior approval of Space and Missile
Systems Organization (SOS), Los Angeles, California.

Air Force Space and Missile
Systems Organization
Los Angeles, California

Contract F04701-71-C-0027

Reproduced by
NATIONAL TECHNICAL
INFORMATION SERVICE
U.S. Department of Commerce
Springfield, VA 22151

SAMSO-TR-74-86
Volume XIV

C/N 7045.427

INTERIM REPORT
PASSIVE NOSETIP TECHNOLOGY
(PANT) PROGRAM

Volume XIV. An Experimental Study to Evaluate the Irregular
Nosetip Shape Regime - Data Report

E. V. Nelson
T. C. Derbidge
D. Chan

This document may be distributed further by any holder
only with specific prior approval of Space and Missile
Systems Organization (SAMSO), Los Angeles, California.

1

ACKNOWLEDGEMENT

Special thanks go to Messrs. Frank Baltakis, Steve Pronchick, Bob Ball, Karl Hoffman, and the rest of the NOL test crew and photographers for their excellent technical support; and to Bertha Ward and the Aerotherm technical typists for their indispensable parts in the preparation of this report.

Preceding page blank

SEARCHED	INDEXED
SERIALIZED	FILED
JUN 19 1969	
FBI - NEW YORK	
<i>Letter on file</i>	
<i>SB</i>	
<i>A</i>	

FOREWORD

This document is Volume XIV of the Interim Report series for the Passive Noisetip Technology (PANT) program. A summary of the documents in this series prepared to date is as follows:

- Volume I - Program Overview (U)
- Volume II - Environment and Material Response Procedures for Noisetip Design (U)
- Volume III - Surface Roughness Data
 - Part I - Experimental Data
 - Part II - Roughness Augmented Heating Data Correlation and Analysis (U)
 - Part III - Boundary Layer Transition Data Correlation and Analysis (U)
- Volume IV - Heat Transfer and Pressure Distributions on Ablated Shapes
 - Part I - Experimental Data
 - Part II - Data Correlation
- Volume V - Definition of Shape Change Phenomenology from Low Temperature Ablator Experiments
 - Part I - Experimental Data, Series C (Preliminary Test Series)
 - Part II - Experimental Data, Series D (Final Test Series)
 - Part III - Shape Change Data Correlation and Analysis
- Volume VI - Graphite Ablation Data Correlation and Analysis (U)
- Volume VII - Computer User's Manual, Steady-State Analysis of Ablating Noisetips (SAANT) Program
- Volume VIII - Computer User's Manual, Passive Graphite Ablating Noisetip (PAGAN) Program
- Volume IX - Unsteady Flow on Ablated Noisetip Shapes - PANT Series G Test and Analysis Report

- Volume X - Summary of Experimental and Analytical Results
- Volume XI - Analysis and Review of the ABRES Combustion Test Facility for High Pressure Hyperthermal Reentry Nosetip Systems Tests
- Volume XII - Nosetip Transition and Shape Change Tests in the AFFDL 50 MW RENT Arc - Data Report
- Volume XIII - An Experimental Study to Evaluate Heat Transfer Rates to Scalloped Surfaces - Data Report
- Volume XIV - An Experimental Study to Evaluate the Irregular Nosetip Shape Regime - Data Report
- Volume XV - Roughness Induced Transition Experiments - Data Report

This report was prepared by Aerotherm Division/Acurex Corporation under Contract F04701-71-C-0027. Volumes I through IX covered PANT activities from April 1971 through April 1973. Volumes X through XV represent contract efforts from May 1973 to December 1974. Volume X summarizes the respective test programs and describes improvements in nosetip analysis capabilities. Volume XI presents an evaluation of the ABRES test facility in terms of performing thermostructural and reentry flight simulation testing. Volumes XII through XV are data reports which summarize the experiments performed for the purpose of defining the irregular flight regime. The analysis of these data are presented in Volume X.

This work was administered under the direction of the Space and Missile Systems Organization with Lieutenant A. T. Hopkins and Lieutenant E. G. Taylor as Project Officers with Mr. W. Portenier and Dr. R. L. Baker of the Aerospace Corporation serving as principal technical monitors. Mr. E. V. Nelson was test engineer and principal Aerotherm investigator for the work described in this volume.

This technical report has been reviewed and is approved.

E. G. Taylor

E. G. Taylor, Lt., USAF
 Project Officer
 Aero and Materials Division
 Directorate of Systems Engineering
 Deputy for Reentry Systems

ABSTRACT

Hypersonic wind tunnel tests conducted in the Naval Ordnance Laboratory Tunnel No. 8 are described. Thirty (30) low temperature ablator (LTA) models were tested at Mach 5, with total temperatures between 493°F and 1013°F and free stream unit Reynolds numbers from 0.77×10^6 to $15.70 \times 10^6/\text{ft}$. The Reynolds number regime for the formation of irregular shapes was found to be significantly influenced by nosetip size (nose radius) and wall temperature ratio (T_e/T_w).

TABLE OF CONTENTS

<u>Section</u>	<u>Page</u>
1 INTRODUCTION	1-1
2 PROCEDURE	2-1
2.1 Model Fabrication and Mounting	2-1
2.2 Test Conditions	2-13
2.3 Description of Recorded Data	2-22
2.3.1 Timing and Recording	2-22
2.3.2 Pulsed Photography	2-22
2.3.3 Motion Picture Photography	2-28
2.3.4 Additional Data	2-29
3 TEST RESULTS	3-1
3.1 General Shape Change	3-1
3.2 Transition and Sharpening Phenomena	3-2
3.3 Unsteady Flow Field Phenomena	3-5
4 SUMMARY AND DISCUSSION	4-1
4.1 Primary Test Objective	4-1
4.2 Secondary Test Objectives	4-8
REFERENCES	R-1
APPENDIX A - SELECTED SIDEVIEW SHADOWGRAPHS AND POST-TEST PHOTOGRAPHS, RUNS 801-831	A-1
APPENDIX B - SHAPE PROFILE HISTORIES, RUNS 801-831	B-1
APPENDIX C - STAGNATION POINT AXIAL RECESSION PLOTS, RUNS 801-831	C-1
APPENDIX D - SELECTED 70MM FRONT-VIEW PHOTOGRAPHS, RUNS 801-803, 805-807, 809, 810, 813-816, 818-828, 830, 831	D-1
APPENDIX E - SELECTED 70MM PROFILE-VIEW PHOTOGRAPHS, RUNS 802-816, 818-831	E-1
APPENDIX F - INITIAL TRANSITION LOCATION TRACINGS AND INITIAL TRANSITION LOCATION PLOTS, RUNS 802, 803, 805, 806, 809, 810, 813, 816, 818, 823, 824, 827, 828, 829	F-1

LIST OF FIGURES

Figure		Page
2-1	Geometry for 2.5-inch R_N Sphere-Cone Model	2-2
2-2	Geometry for 1.5-inch R_N Sphere-Cone Model	2-3
2-3	Geometry for 0.75-inch R_N Sphere-Cone Model	2-4
2-4	Geometry for 1.5-inch R_S Laminar-Blunt Model	2-5
2-5	Geometry for 3.5-inch R_S Laminar-Blunt Model	2-6
2-6	Geometry for 1.5-inch $R_S/60^\circ/8^\circ$ Biconic Model	2-7
2-7	Geometry for 1.5-inch $R_S/75^\circ/8^\circ$ Biconic Model	2-8
2-8	Geometry for 2.5-inch $R_S/55^\circ/6^\circ$ Biconic Model	2-9
2-9	Model Pretest Photographs	2-10
2-10	Boundary Layer Trip Groove Locations	2-14
2-11	Example of Mounting Hardware Arrangement (for 2.5-in. R_N LTA Model)	2-16
2-12	NOL Hypersonic Tunnel No. 8 Operating Envelope at $M_\infty = 5.0$	2-17
2-13	Reynolds Number History for Run 828	2-19
2-14	Reynolds Number History for Run 829	2-20
2-15	Test Cell Schematic, Model in Test Position	2-23
2-16	Test Cell Schematic, Model in Retracted Position	2-24
2-17	Test Setup Electrical Diagram	2-25
2-18	Instrumented Spacer Detail	2-30
3-1	Example of Transitional Gouge Development from 16mm Overhead Camera. (Run 805; 1.5-inch R_N Sphere-Cone; $Re_\infty = 6.56 \times 10^6/\text{ft}$, $T_0 = 987^\circ\text{F}$)	3-4
3-2	Examples of Unsteady Flow Phenomena During Run 805 (1.5-inch R_N Sphere-Cone; $Re_\infty = 6.56 \times 10^6/\text{ft}$, $T_0 = 987^\circ\text{F}$)	3-8
3-3	Example of Accelerometer Response for Run 805	3-9
4-1	Reynolds Number Effect on Model Final Shape (All 1.5-inch Sphere-Cones, Nominal $T_0 = 1010^\circ\text{F}$)	4-2
4-2	Effect of Model Size on Shape Development	4-4
4-3	Comparison of Post-Sharpening and Final Shapes for Different Initial Geometry Models	4-5
4-4	Effect of Supply Temperature (T_0) on Shape Development	4-9

LIST OF TABLES

Table		Page
2-1	Coordinates Defining Laminar Nose Profiles	2-15
2-2	Test Conditions for Pant Series I Test March/April 1974	2-18
2-3	Camera Framing: Rates and Photo Times	2-27
4-1	Summary of Different Initial Geometry Runs (Nominal $T_0 = 1000^\circ\text{R}$)	4-1

LIST OF SYMBOLS

B'	nondimensional blowing rate
M	Mach number
P	pressure
Re	unit Reynolds number
R_N	spherical nose radius
R_S	nonspherical nose shoulder radius
s	surface distance (streamlength) from stagnation point
T	temperature
θ	circumferential angle

Subscripts

∞	free-stream condition
o	wind tunnel supply condition
e	boundary layer edge condition
w	wall (surface) condition

SECTION 1

INTRODUCTION

The overall objective of the PANT program (Contract F04701-71-C-0027) is to improve and validate the accuracy of existing nosetip design analysis computer codes. Task 4.2.5 of the PANT program has the objective of defining the environmental regimes which produce irregular nosetip shapes and updating nosetip design analysis codes. In order to satisfy this objective a series of wind tunnel and high-pressure ablation tests was required. The tests were designed to obtain calorimeter and shape-change data for geometries and environments of interest. The objectives of the four test series are given below.

50 MW Arc Heater Tests - Test ATJ-S graphite, Mod-III carbon/carbon, and reverse chevron carbon phenolic nosetip models in the 50 MW arc using a $M_\infty = 3$ nozzle to assess the transition behavior and shape-change response of "real" materials in a hyperthermal environment.

Series H Wind Tunnel Tests - Generate heat transfer data for a calorimeter replica of an LTA scallop roughened surface for comparison with inferred heat transfer data and predictions.

Series I Wind Tunnel Tests - Generate low temperature ablator (LTA) shape change data to determine the effect of relevant nosetip parameters on the formation and extent of irregular shapes.

Series J Wind Tunnel Tests - Generate heat transfer data which show the effect of surface roughness and model size on boundary layer transition and augmentation of smooth wall heat flux.

The 50 MW tests were conducted in the RENT leg of the 50 MW arc facility at the Air Force Materials Flight Dynamics Laboratory. Test series H and J were conducted in Tunnel No. 8 at the Naval Ordnance Laboratory (NOL) from February 21 to February 26, 1974. Test Series I was conducted at NOL from March 27 to April 4, 1974.

These test series complement Series E and G which were directed at obtaining pressure data on nosetips of irregular shape. A brief description of these two test series is given below:

Series E (Task 4.2.3) - Generate high-frequency pressure, acceleration, and shock-shape stability data to establish the possibility of high-frequency flow field pulsations on ablated nosetip shapes.

Series G (Task 4.2.7) - Generate high-frequency pressure, acceleration, and shock-shape stability data to determine the envelope of realistic nosetip shapes which induce high-frequency flow field pulsations.

Test Series E and G were conducted in NOL Tunnel No. 8; Series E was conducted in October of 1972 and Series G was conducted from July 25 to August 1, 1973.

This data report describes the results of the Series I LTA tests. The objectives of this experimental program were as follows:

- Evaluate the effects of
 - Reynolds number
 - Transition control
 - Surface roughness
 - Model size
 - Initial geometry
 - Blowing rate and wall temperature ratioon nosetip sharpening and the formation and extent of irregular shapes.
- Generate accurate recession data to evaluate heat transfer rates to scalloped surfaces.
- Generate shape-change and shock-shape data to evaluate the phenomena associated with the growth and degradation of small nose protuberances.
- Generate high-frequency acceleration data to evaluate the effects of oscillating shocks.
- Simulate flight shape-change response in a wind tunnel.

The test objectives were satisfied by exposing 30 low temperature ablator (LTA) models of 8 initial geometries at several Reynolds number conditions in the NOL No. 8 hypersonic wind tunnel at a free stream Mach number of 5. The eight geometries were:

- 0.75-inch nose radius, 8-degree half angle sphere-cone
- 1.5-inch nose radius, 8-degree half angle sphere-cone
- 2.5-inch nose radius, 8-degree half angle sphere-cone
- 1.5-inch shoulder radius laminar-blunt nose with 8-degree half angle cone
- 3.5-inch shoulder radius laminar-blunt nose with cylindrical aft body
- 1.5-inch shoulder radius, 60-degree/8-degree biconic
- 1.5-inch shoulder radius, 75-degree/8-degree biconic
- 2.5-inch shoulder radius, 55-degree/6-degree biconic

The first objective was addressed by experimentally assessing each of the following:

- The Reynolds number regime for the formation of irregular shapes
- The effect of different nose radius sphere-cone models on transition, sharpening and the formation of irregular shapes
- The effect of laminar-shape blunted cones and biconic models on transition, sharpening and the formation of irregular shapes
- The effect of blowing rate and wall temperature ratio on transition, sharpening and the formation of irregular shapes.

During most of the tests photographs were taken of the nose region to evaluate the significance of asymmetric transition on nosetip sharpening and the formation of irregular shapes.

The second objective was accomplished by taking high-quality photographs of all models, which can be used to measure surface recession. The third objective was satisfied by taking close-up movies of the nose region of all models with back lighting to visualize the bow shock. High-frequency accelerometers were attached to the model sting support to generate the data for the fourth objective. To satisfy the fifth objective two models were tested in a variable Reynolds number environment, where the stream variation and model exposure time were calculated to simulate pertinent nosetip parameters for typical flights.

Details of model fabrication, test conditions, and data acquisition are given in Section 2. The overall shape-change response of the models, transition and sharpening data, and unsteady flow phenomena observations are presented in Section 3. Finally, preliminary data trends are summarized in Section 4.

SECTION 2

PROCEDURE

Details of the experimental program are presented here. Model fabrication is described in Section 2.1, actual test conditions are summarized in Section 2.2, and data acquisition is described in Section 2.3.

2.1 MODEL FABRICATION AND MOUNTING

Camphor and camphor with distributed glass particles were the materials for the low temperature ablator shape-change models tested in Series I. The models were fabricated by molding the camphor at room temperature and high pressure (20,000 psi) into cylindrical billets, 9 inches in diameter by 13 inches long. These billets were machined to the final configurations. The three billets with distributed glass particles were produced by thoroughly mixing glass beads, having diameters of 7.5 ± 1.5 mils, with the camphor granules prior to molding.

A particle loading fraction of 0.75 lb glass/lb camphor was selected to optimize particle distribution uniformity without compromising strength requirements, based on a comparison of sample specimens with various particle loading fractions.

Before machining, two sample specimens were taken from each camphor billet and subjected to a three-point flexural strength test. Previous experience (Reference 1) indicated that a 175-psi minimum flexural strength would insure good mechanical properties, and this condition was surpassed by all but two of the billets used for this program. The two billets which were below this specification had average flexural strengths of 124 psi and 109 psi, and were machined to the 3.5-inch laminar-blunt models tested in Runs 830 and 831. These models had a "cloudy" appearance, in contrast to the typical translucence of well-molded camphor, and are assumed to have had mechanical properties somewhat different from the remaining models.

The eight LTA model geometries tested in this series are shown in Figures 2-1 through 2-8, and pretest photographs of each geometry are shown in Figure 2-9. Two of the 1.5-inch sphere-cones had boundary layer trip grooves machined on the spherical nose. The criteria for determining groove locations

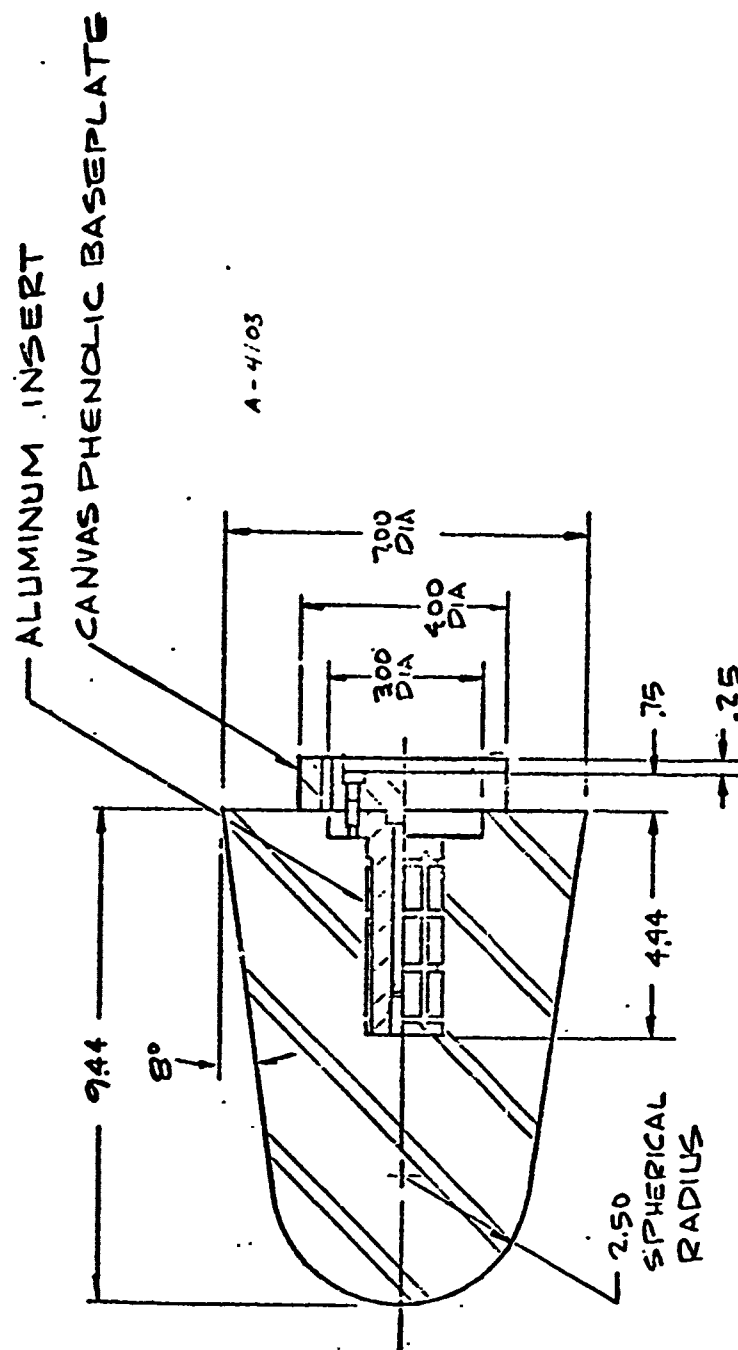
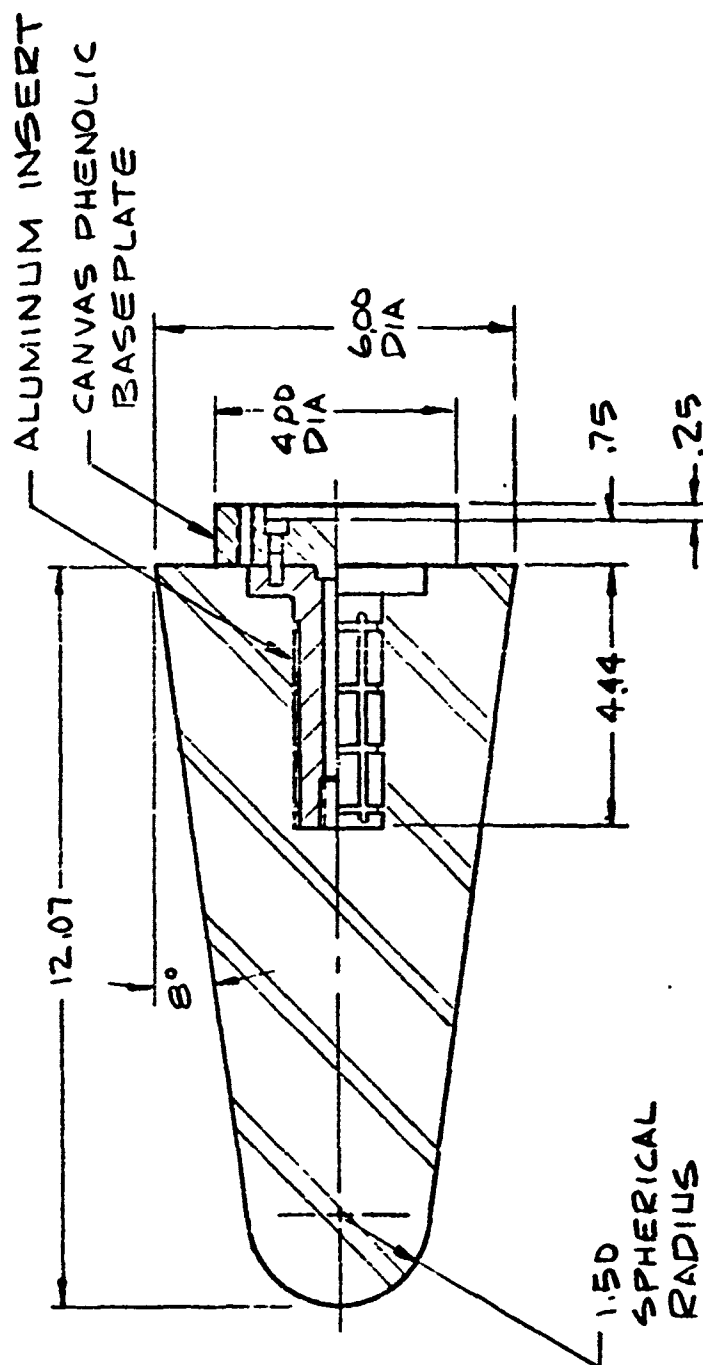


Figure 2-1. Geometry for 2.5-inch R_N Sphere-Cone Model



A-4101

Figure 2-2. Geometry for 1.5-inch R_N Sphere-Cone Model

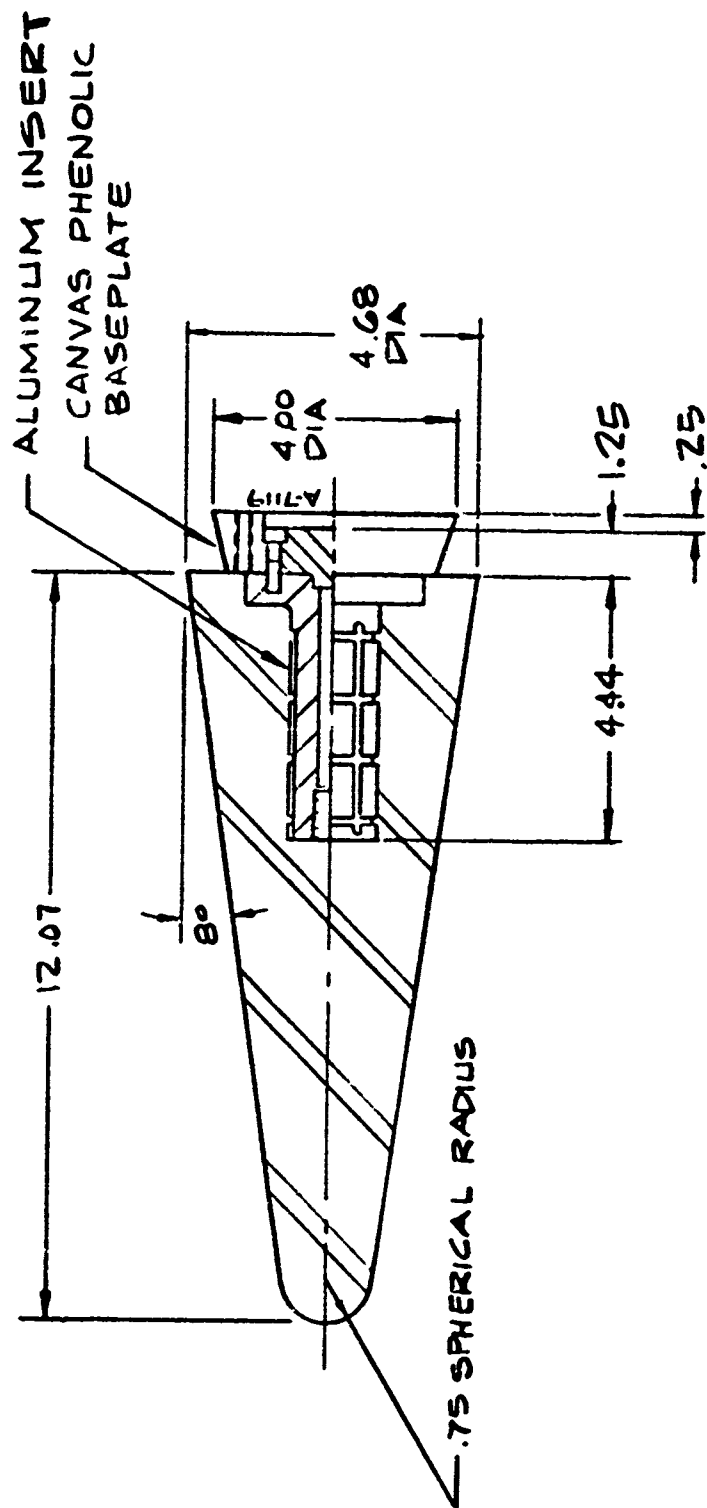


Figure 2-3. Geometry for 0.75-inch R_N Sphere-Cone Model

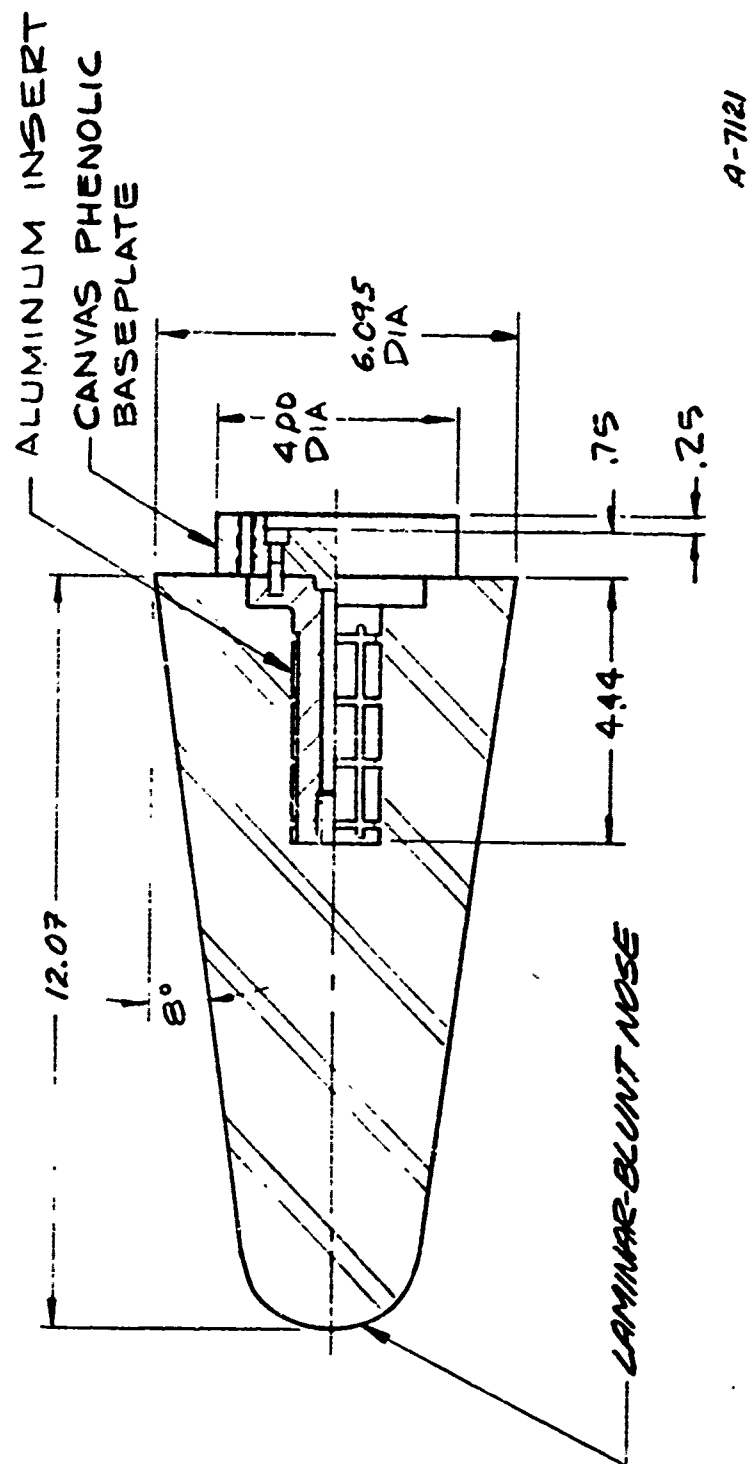


Figure 2-4. Geometry for 1.5-inch R_S Laminar-Blunt Model

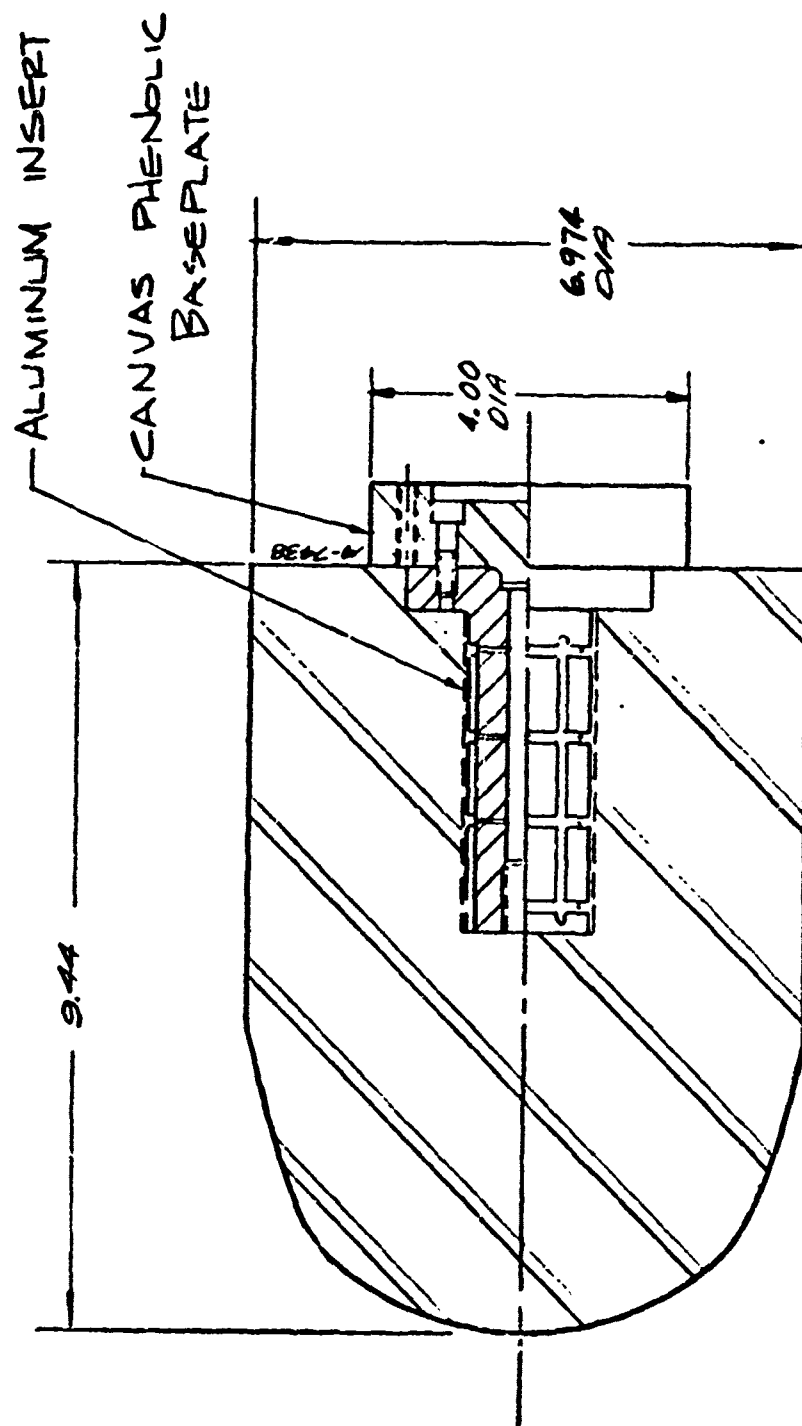


Figure 2-5. Geometry for 3.5-inch R_5 Laminar-Blunt Model

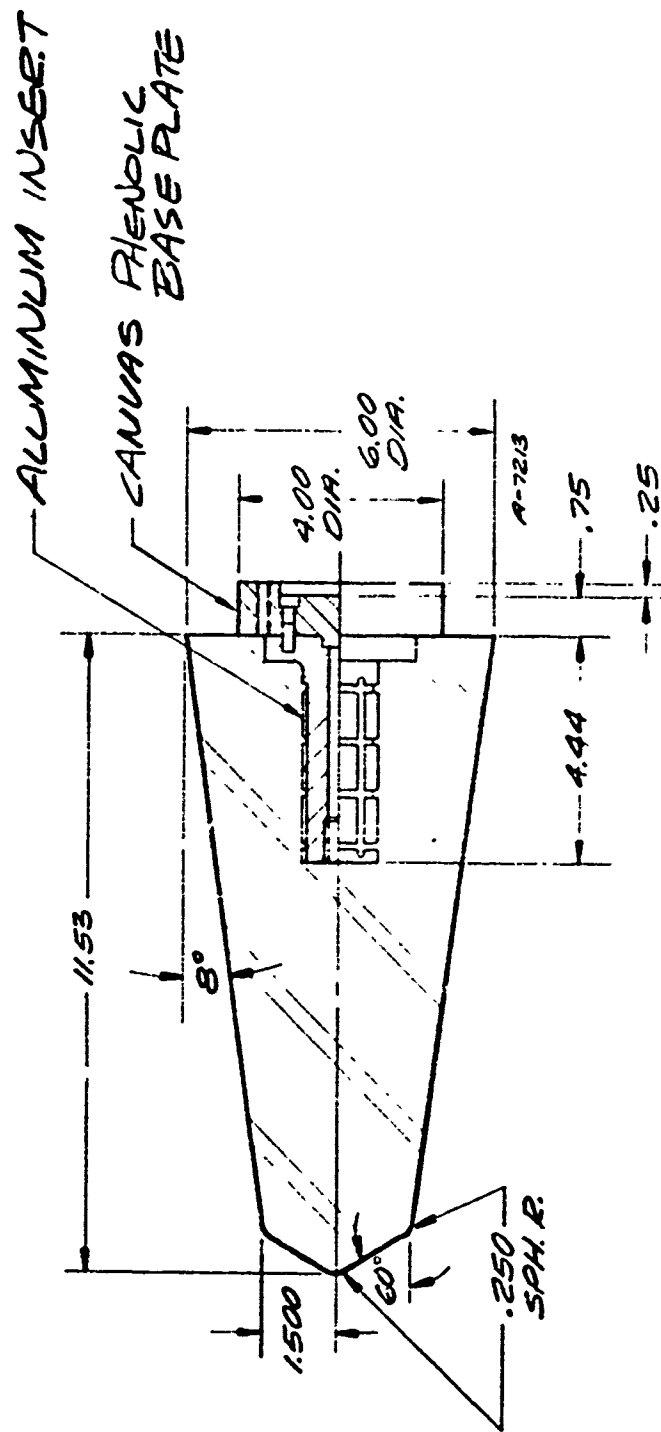


Figure 2-6. Geometry for 1.5-inch $R_S/60^\circ/8^\circ$ Biconic Model

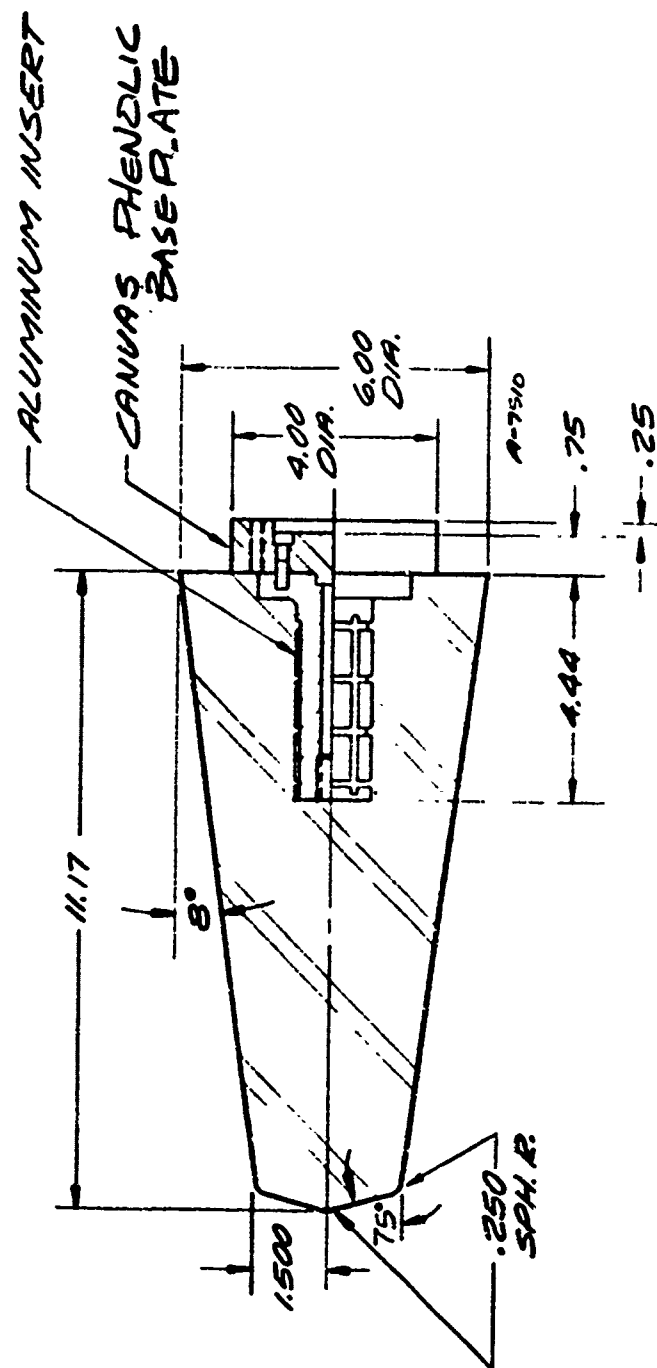


Figure 2-7. Geometry for 1.5-Inch $R_5/75^\circ/8^\circ$ Biconic Model

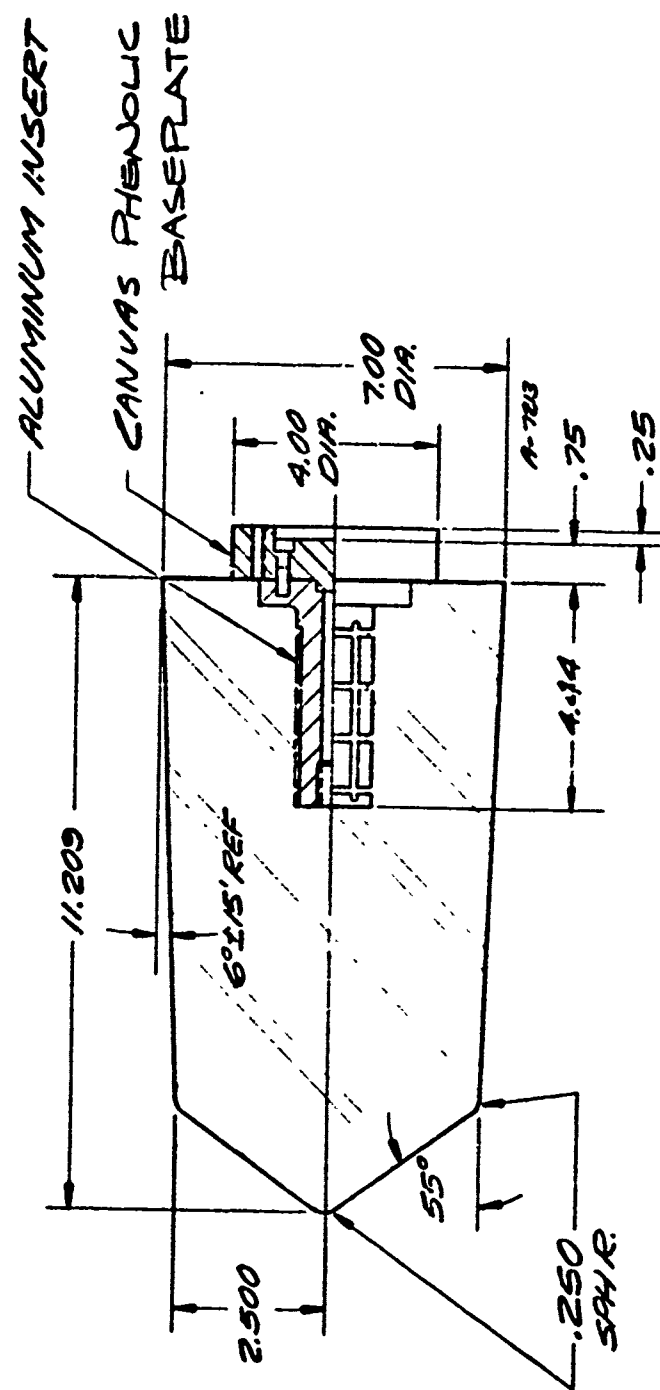
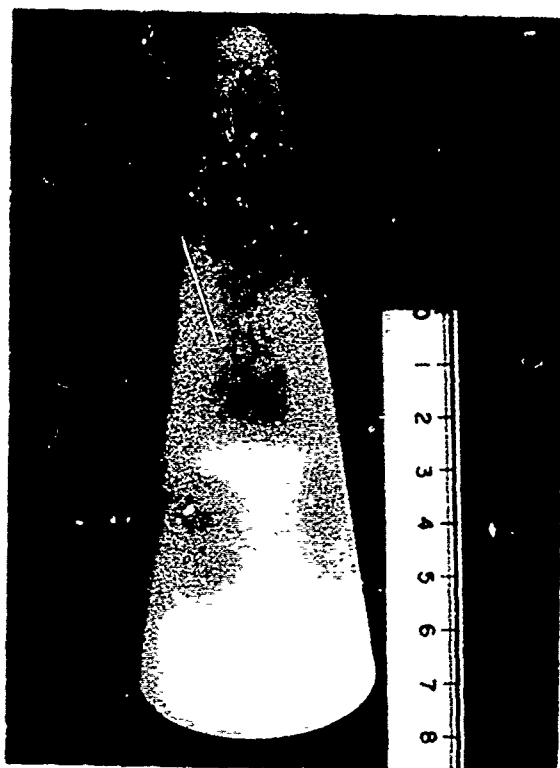
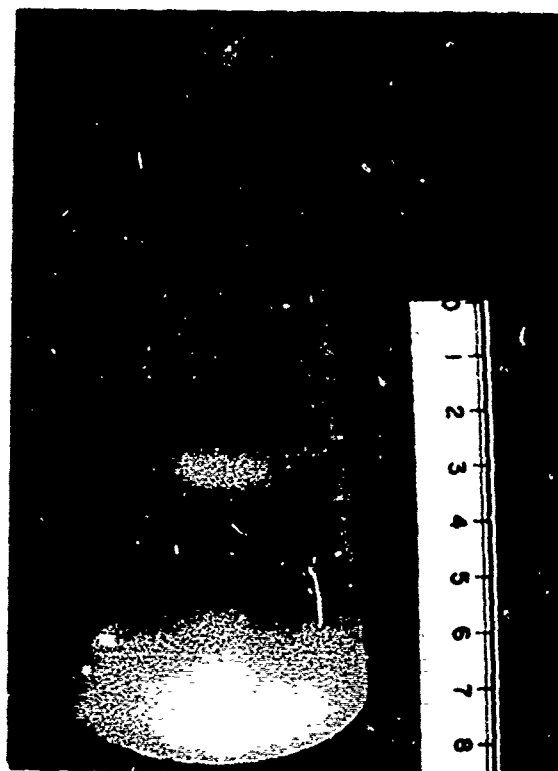


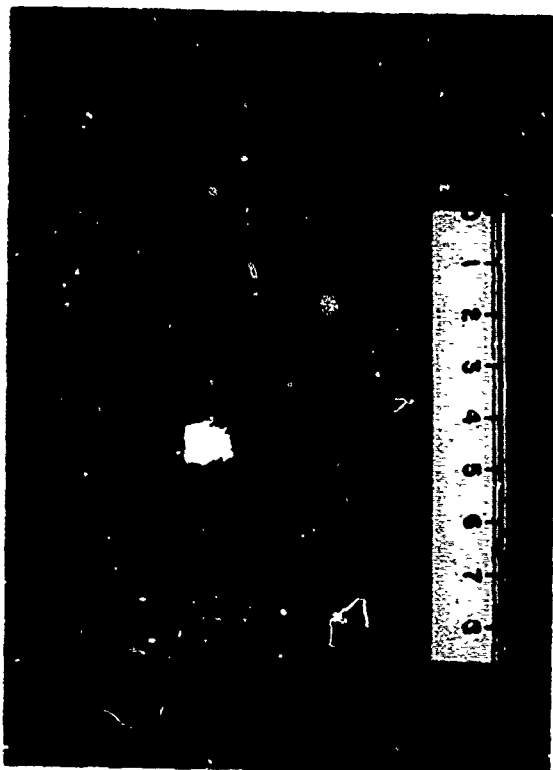
Figure 2-8. Geometry for 2.5-inch $R_5/55^\circ/6^\circ$ Biconic Model



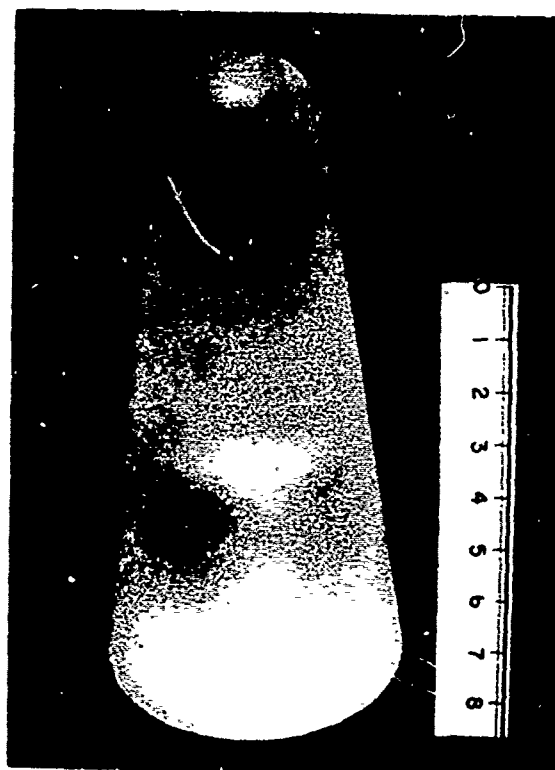
0.75-inch R_N Sphere-Cone



1.5-inch R_N Sphere-Cone

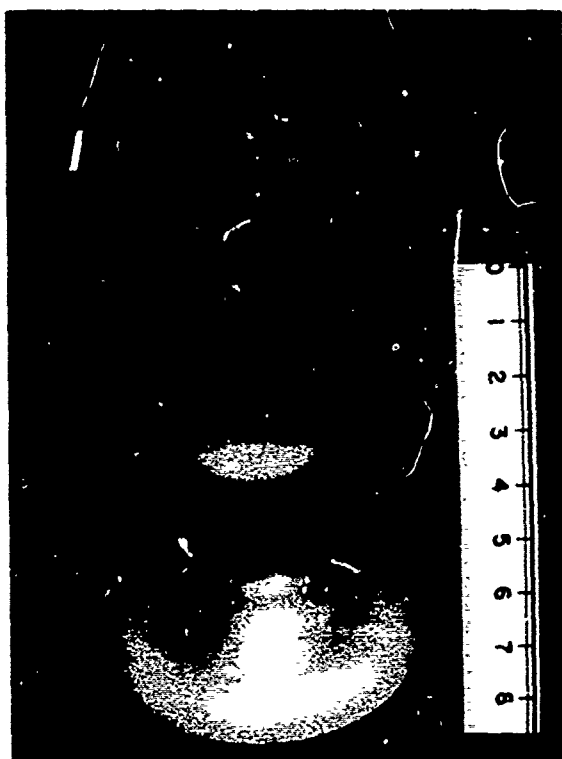


2.5-inch R_N Sphere-Cone

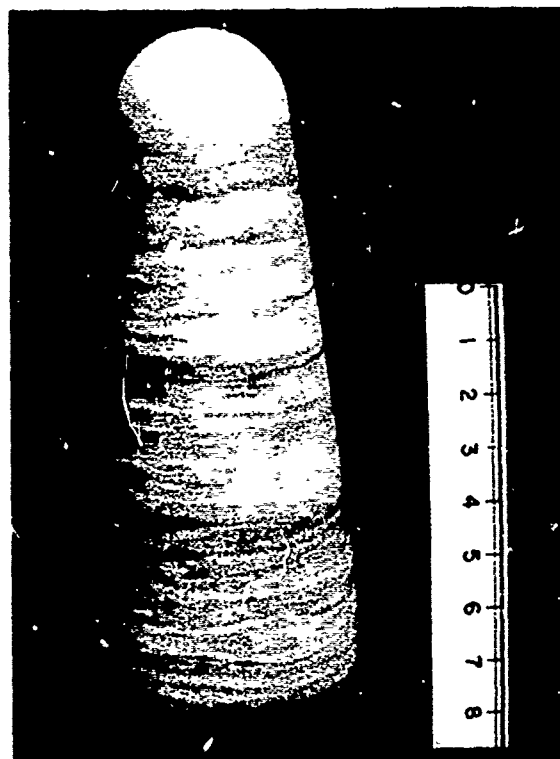


1.5-inch R_N Sphere-Cone with Groove

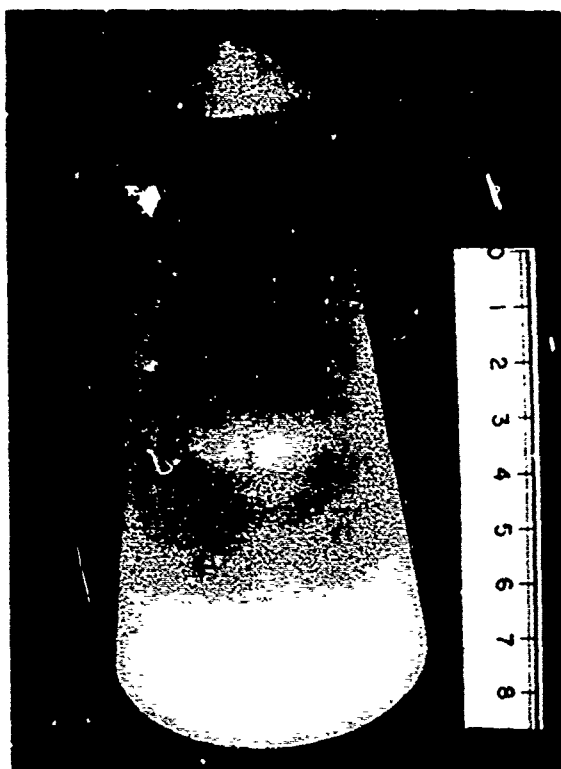
Figure 2-9. Model Pretest Photographs



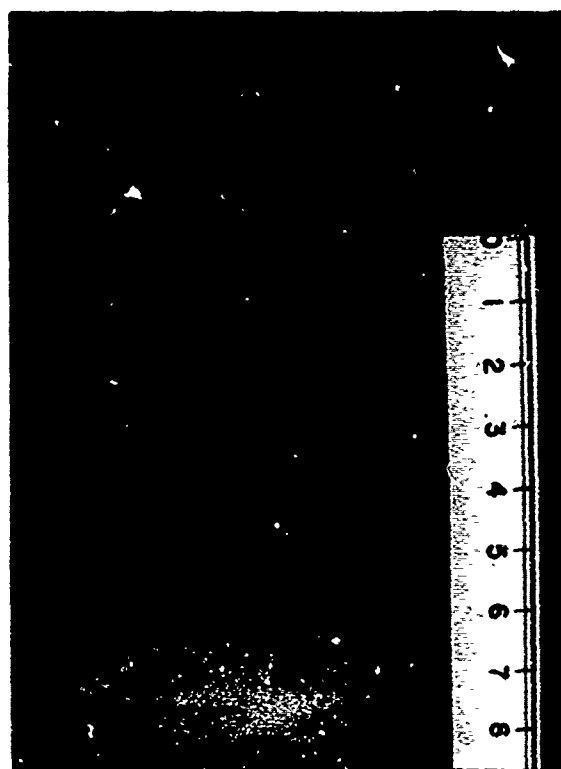
1.5-inch R_N Sphere-Cone with
3 Grooves



1.5-inch R_N Sphere-Cone,
Particle-Loaded

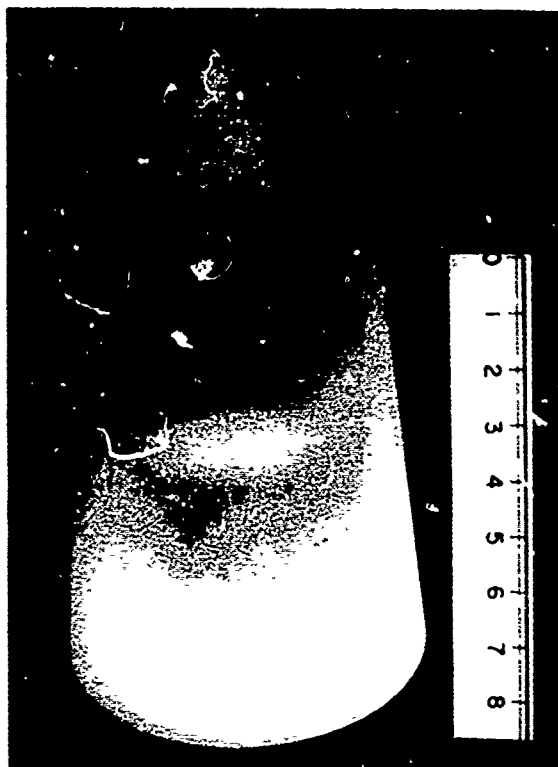


1.5 inch $R_S/60^\circ/8^\circ$ Biconic

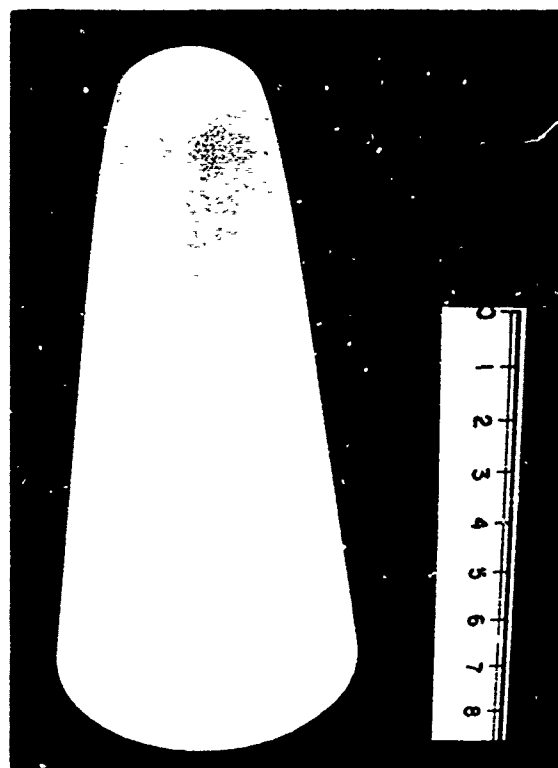


1.5-inch $R_S/75^\circ/8^\circ$ Biconic

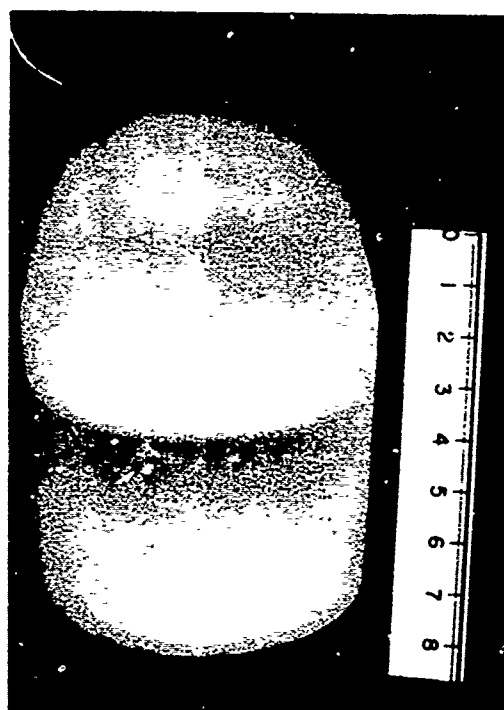
Figure 2-9. Continued



2.5-inch $R_s/55^\circ/6^\circ$ Biconic



1.5-inch R_s Laminar-Blunt



3.5 inch R_s Laminar-Blunt

Figure 2-9. Concluded

were given in Reference 2; Figure 2-10 shows the actual locations and geometries selected during testing. Reference 2 also discusses the analysis of Reference 4 which determined the shape for the laminar-blunt models, and Table 2-1 specifies the resultant axial and radial coordinate points. The 1.5-inch and 3.5-inch laminar-blunt models had geometrically similar shapes with a difference only in scale.

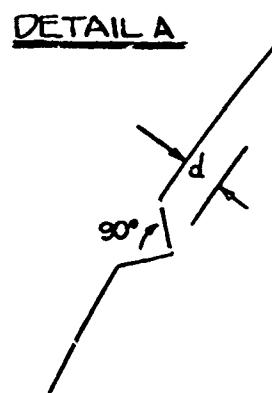
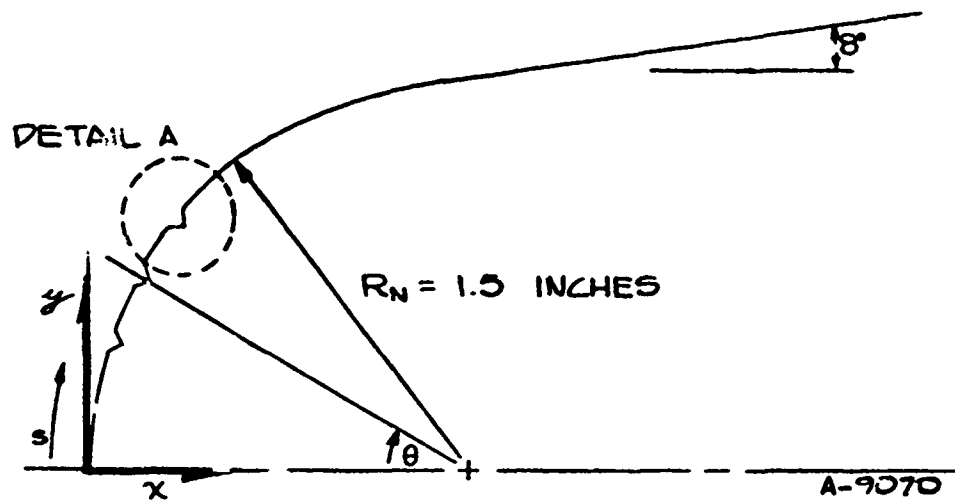
For model mounting, the camphor was molded onto an aluminum insert which was hollowed to allow venting of entrapped gas during molding. As shown in Figure 2-11, the model insert was bolted to an aluminum mounting plate, and the mounting plate was then bolted to the sting insert. An instrumented spacer with a three-axis high-frequency accelerometer system was located between the mounting plate and sting insert. Various aluminum spacers were used to compensate for the different model lengths and maintain the initial stagnation points at approximately the same axial location in the tunnel.

2.2 TEST CONDITIONS

The wind tunnel used in this test program was the Naval Ordnance Laboratory Tunnel No. 8, an intermittent blowdown hypersonic wind tunnel using air as the working gas. The air is compressed and stored in high pressure containers. In transit to the nozzle, the air is heated in a pebble bed heater which can be supplemented by an electric resistance heater when the required air temperature exceeds 1150°F. The tunnel has an open jet test section and a constant geometry diffuser. Nozzle selection is dependent on the required Mach number.

The selected Mach number for this test series was $M_\infty = 5$. The associated nozzle has a rectangular cross section with throat dimensions of 0.6398 in. x 16.00 in. and exit dimensions of 17.37 in. x 16.97 in. The resulting Reynolds number operating envelope at Mach 5 is presented in Figure 2-12 as a function of supply temperature and pressure. Figure 2-12 also indicates the various operating conditions run during the test series. A nominal supply temperature (T_0) of 1000°F was maintained for the majority of the runs. The remaining runs were performed at lower T_0 conditions to investigate transition onset and shape-change behavior at higher wall temperature ratios (T_w/T_e) and lower blowing rates (B'), or to avoid nozzle degradation at high Reynolds number conditions.

Table 2-2 presents the actual test conditions, time averaged for each run, and the total model exposure times, determined from film data. Also indicated are the test point numbers from the test plan (Reference 2). Runs 828 and 829 were the variable test condition runs designed to simulate flight



RUN	θ	x	y	s	d
807	30	.201	.750	.785	.025
814	20	.090	.513	.524	.050
	30	.201	.750	.785	.050
	40	.351	.964	1.047	.050

Figure 2-10. Boundary Layer Trip Groove Locations

TABLE 2-1
COORDINATES DEFINING LAMINAR
NOSE PROFILES

a). Coordinates* for nominal 1.5-inch
shoulder radius model (Figure 2-4)

AXIS (inches)	RADIUS (inches)
.000	.000
.002	.083
.008	.165
.019	.247
.033	.328
.052	.409
.074	.488
.101	.566
.132	.642
.167	.718
.206	.790
.249	.860
.322	.961
.348	.953
.404	1.054
.464	1.110
.530	1.158
.602	1.196
.678	1.229
.756	1.259
.833	1.285
.912	1.310
.990	1.335
1.069	1.358
1.148	1.379
1.229	1.401
1.308	1.422
1.389	1.442
1.470	1.460
1.549	1.480
1.630	1.498
1.792	1.533
2.114	1.600
2.439	1.662
2.764	1.719
3.089	1.774
3.415	1.827
3.741	1.876
4.067	1.924
4.191	1.940

b). Coordinates* for nominal 3.5-inch
shoulder radius model (Figure 2-5)

AXIS (inches)	RADIUS (inches)
.000	.000
.005	.192
.011	.288
.019	.384
.043	.576
.077	.764
.120	.952
.173	1.137
.235	1.317
.306	1.494
.388	1.670
.480	1.839
.580	2.001
.691	2.162
.810	2.312
.941	2.454
1.079	2.584
1.233	2.696
1.402	2.784
1.578	2.861
1.759	2.930
1.939	2.991
2.124	3.049
2.304	3.107
2.488	3.160
2.673	3.210
2.861	3.260
3.045	3.310
3.233	3.356
3.421	3.398
3.606	3.444
3.794	3.487

* Measured relative to stagnation point

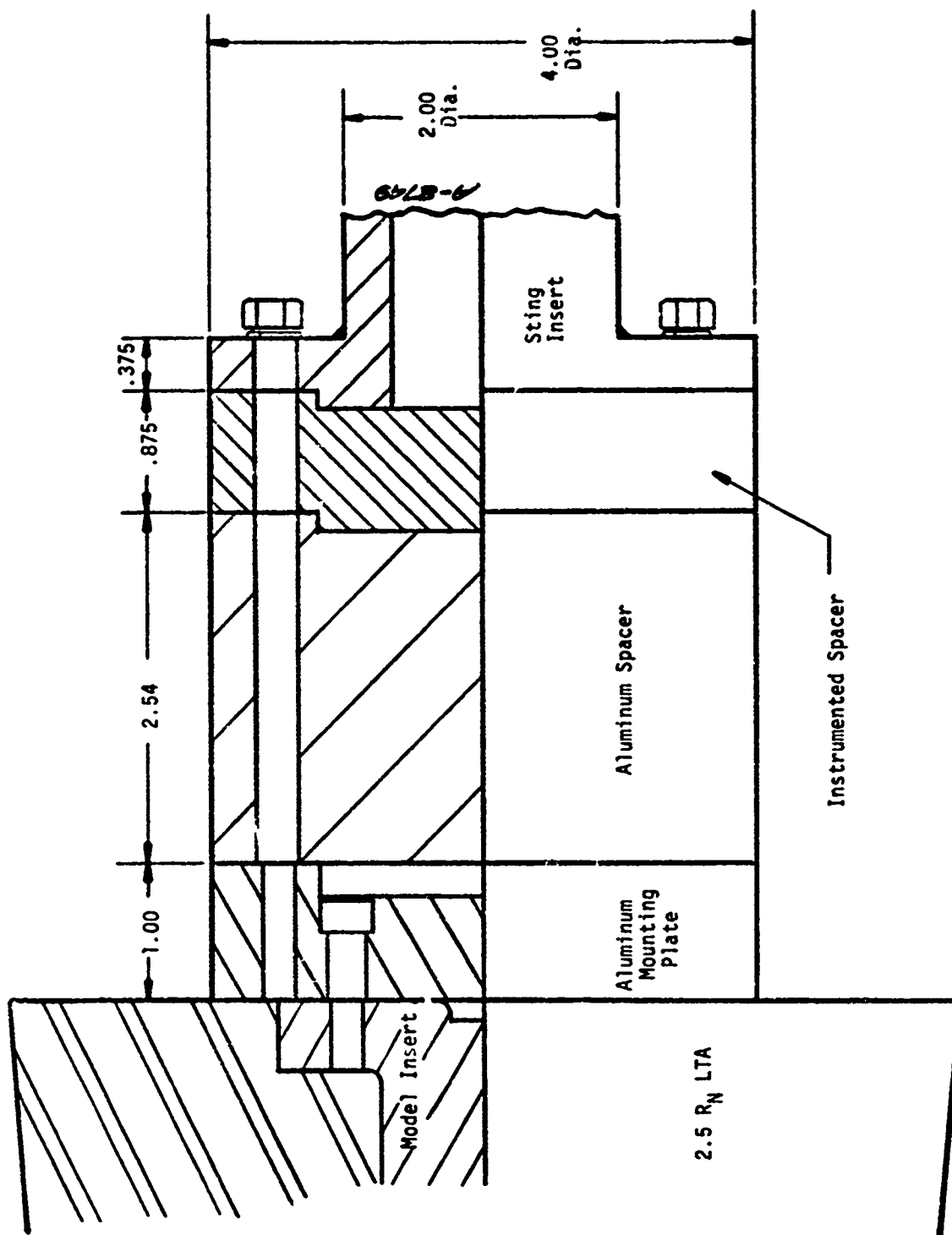


Figure 2-11. Example of Mounting Hardware Arrangement:
(for 2.5-in. R_N LTA Model)

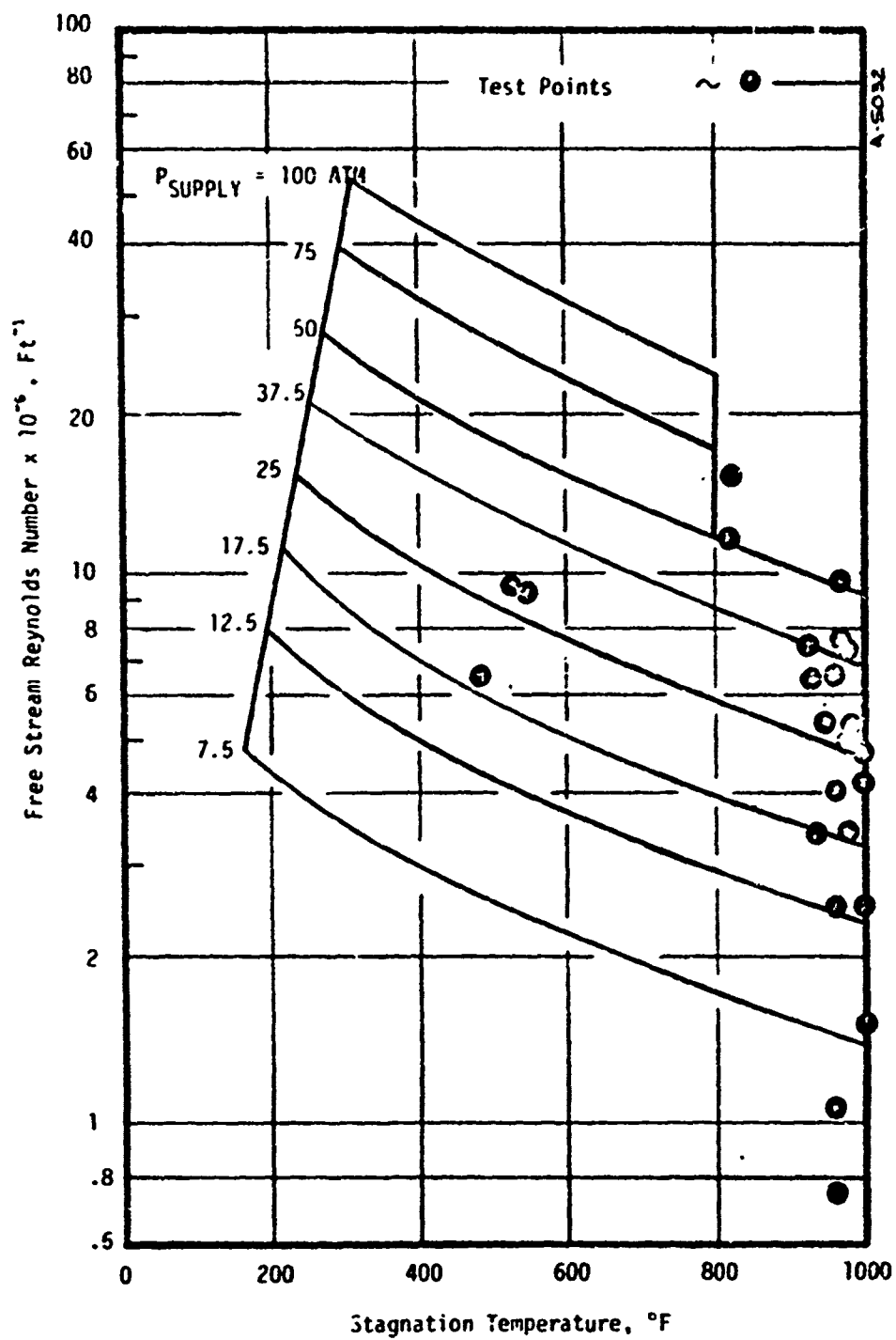


Figure 2-12. NOL Hypersonic Tunnel
No. 8 Operating Envelope at $M_{\infty} = 5.0$

TABLE 2-2

TEST CONDITIONS FOR PANT SERIES I TESTS
MARCH/APRIL 1974

Run No.	Test Plan Point No.	Test Conditions				Camphor Model Configuration	Exposure Time (sec)
		Air Supply		Free Stream			
		P ₀ (psia)	T ₀ (°F)	Re _∞ (10 ⁶ /ft)	M _∞		
801	1	256	953	3.44	4.98	1.5" R _N Sphere-cone	186.33
802	3	311	970	4.09	4.98	1.5" R _N Sphere-cone	157.89
803	2	475	927	6.54	4.99	1.5" R _N Sphere-cone	115.80
804	8	190	983	2.51	4.96	1.5" R _N Sphere-cone, particle-loaded	178.91
805	4	507	987	6.56	5.00	1.5" R _N Sphere-cone	99.60
806	12	531	921	7.36	5.00	0.75" R _N Sphere-cone	87.19
807	5	323	1013	4.08	4.98	1.5" R _N Sphere-cone with groove	156.24
808	9	117	996	1.50	4.96	1.5" R _N Sphere-cone, particle-loaded	288 ^b
809	13	713	971	9.38	5.00	0.75" R _N Sphere-cone	58.63
810	22	508	964	6.73	5.00	1.5" R _S /60°/8° Biconic	109.47
811 ^a	10	58.8/ 85.3	972/ 972	0.77/ 1.12	4.95/ 4.95	1.5" R _N Sphere-cone, particle-loaded	172.83/ 305.43
812	14	998	807	15.70	5.01	0.75" R _N Sphere-cone	63.49
813	24	509	970	6.70	5.00	1.5" R _S /75°/8° Biconic	115.74
814	6	324	998	4.15	4.98	1.5" R _N Sphere-cone with 3 grooves	172.91
815	19	497	944	6.72	5.00	1.5" R _S Laminar-blunt	123.15
816	23	388	954	5.20	4.98	.5" R _S /60°/8° Biconic	126.28
817	27	268	493	6.52	4.98	1.5" R _N Sphere-cone	325.48
818	28	403	508	9.56	4.99	1.5" R _N Sphere-cone	253.84
819 ^a	15	360/ 821	812/ 804	5.69/ 12.96	4.98/ 5.01	0.75" R _N Sphere-cone	20.84/ 69.04
820	16	378	986	4.90	4.99	3.5" R _S Laminar-blunt	122.83
821	11A	569	973	7.47	5.00	2.5" R _N Sphere-cone	13.47
822	20	302	960	4.02	4.98	1.5" R _S Laminar-blunt	224 ^b
823	25	400	986	5.18	4.99	1.5" R _S /75°/8° Biconic	130.48
824	7	416	535	9.44	4.99	1.5" R _N Sphere-cone	242.75
825	11B	558	990	7.20	5.00	2.5" R _N Sphere-cone	67.73
826	21	263	987	3.41	4.98	1.5" R _S Laminar-blunt	192.33
827	26	375	1008	4.76	4.99	2.5" R _S /55°/6° Biconic	139.04
828	30	v a r i a b l e			4.99	0.75" R _N Sphere-cone	91.11
829	29	v a r i a b l e			4.99	0.75" R _N Sphere-cone	116.03
830	17	268	985	3.47	4.98	3.5" R _S Laminar-blunt	153.52
831	18	197	998	2.52	4.97	3.5" R _S Laminar-blunt	231.08

^aDual Re_∞ test - values given are for first portion/second portion^bApproximate time only; film data incomplete

trajectories; their Reynolds number histories are shown in Figures 2-13 and 2-14, respectively. Run 828 was interrupted after about 30 seconds exposure time because of difficulties with the tunnel control system, but was restarted and completed. Run 829 proceeded smoothly and was successfully completed.

Two of the runs, 811 and 819, were conducted as dual Reynolds number tests, in order to maximize the number of test points. The objective of these tests was to determine the Reynolds numbers for the onset of boundary layer transition for particle-loaded and small nose radius ($R_N = 0.75$ inch) models. In these cases, the model was removed from the air stream while the tunnel was running at the lower Reynolds number, and the Reynolds number was increased before the model was reinserted. Because of mechanical problems the model on Run 819 was not fully injected into the test stream during the first exposure, but it appears likely that the nose region of the model was largely in the uniform portion of the test stream and transition was observed.

Runs 821 and 825 were a multiple exposure test, in which a 2.5-inch R_N sphere-cone was exposed to a nominal 7.5×10^6 /ft Reynolds number air stream, removed completely from the tunnel for photographs and elastomeric molds (see Section 2.3), and then reexposed to the same nominal conditions. This was done to produce a replica of an ablated model for possible later use in constructing a calorimeter replica for measurement of heat flux to an ablated surface.

Five of the models (Runs 810, 818, 823, 830, and 831) experienced loss of the sharpened nose during the tests due to fractures in the camphor. Only in the case of Run 818 was the loss of the nose significant, since it occurred at 100.8 seconds exposure time and the model assumed a blunt shape thereafter. The other four nose fractures occurred late in the tests, usually while the model was being extracted from the test stream. Three of these models had a "cloudy" appearance, and two of the three were the laminar-blunt models with low material flexural strengths. None of these failures, however, were significant in regard to the data acquired, and there were no other anomalies in model performance for the series.

The model exposure times given for Runs 808 and 822 are the nominal times taken from the wind tunnel recording facilities and are not as accurate as those taken from photographic data. For these two runs, both film and oscillogram coverage were incomplete at the end of the tests and thus could not be used for exposure time determination.

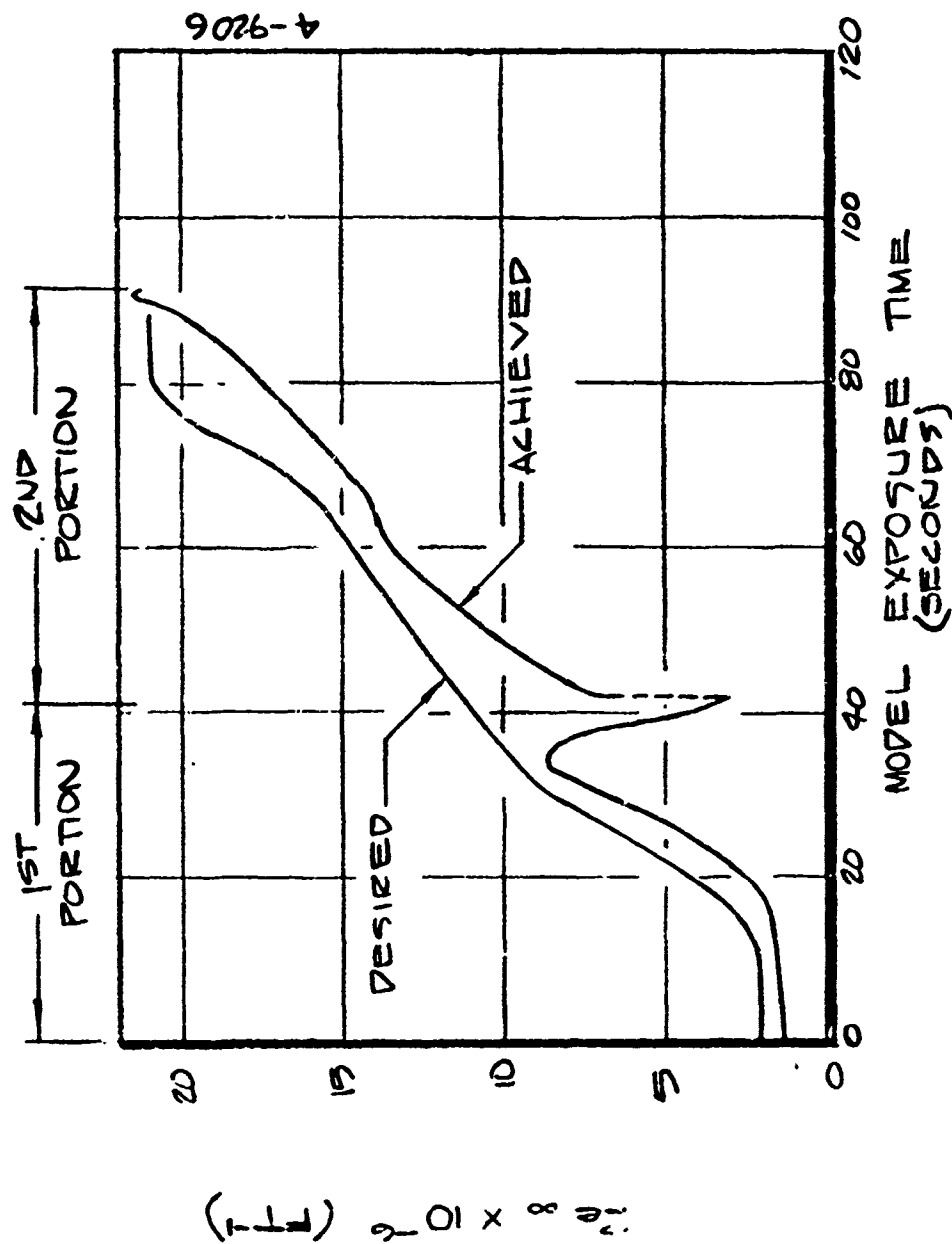


Figure 2-13. Reynolds Number History for Run 828

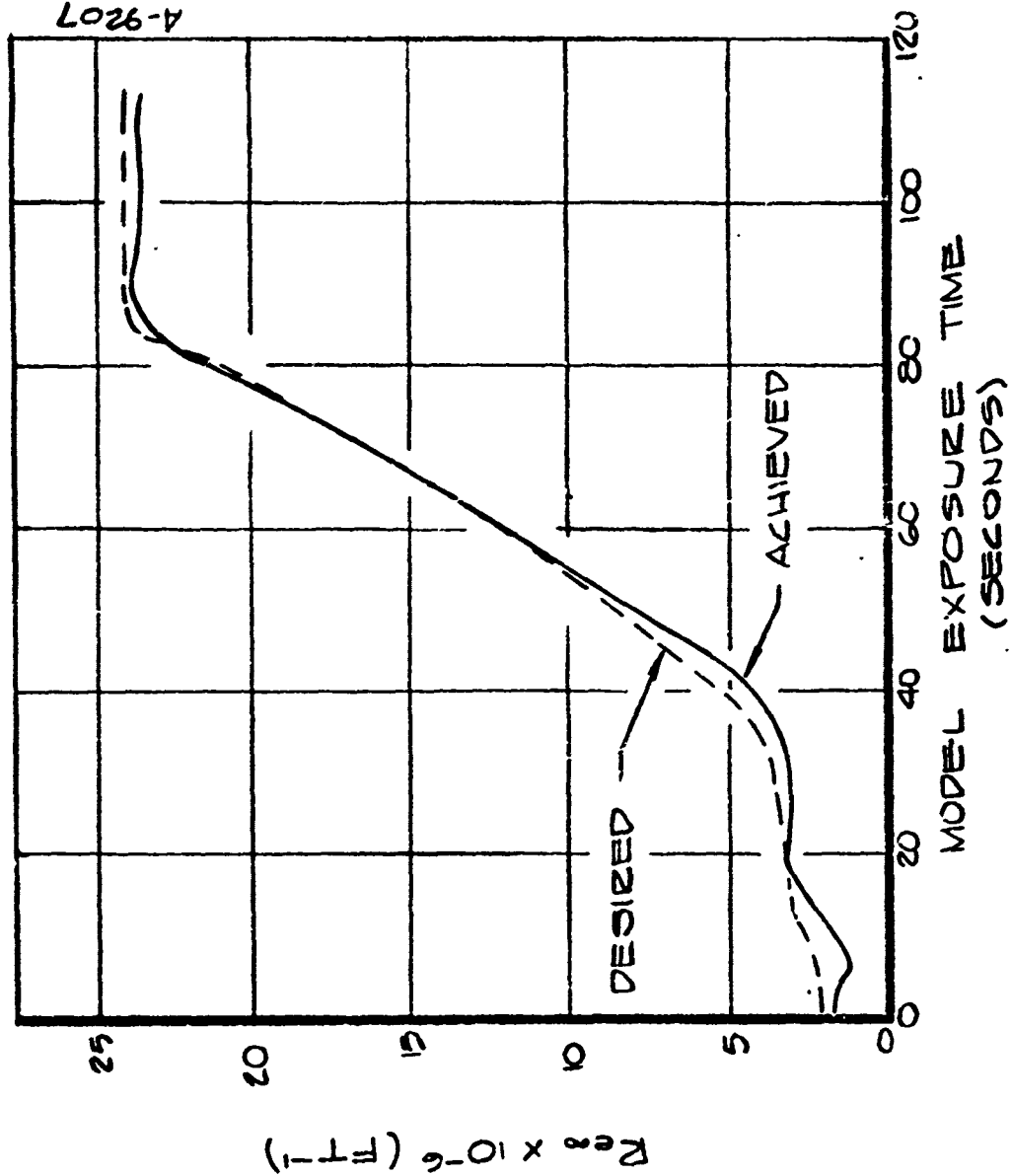


Figure 2-14. Reynolds Number History for Run 829

2.3 DESCRIPTION OF RECORDED DATA

The recorded data for this test series consisted of:

- 16mm sideview shadowgraph movies
- 16mm closeup high-speed overhead movies
- 16mm Hycam (20,000 frames/second) sideview shadowgraph movies (pitch plane)
- 35mm sideview shadowgraph pulsed photography (pitch plane)
- 35mm overhead pulsed photography (yaw plane)
- 70mm underside profile-view pulsed photography (yaw plane)
- 70mm front-view nose photographs
- Pre- and post-test photographs
- Three-axis acceleration measurements
- Post-test elastomeric molds
- Wind tunnel test conditions

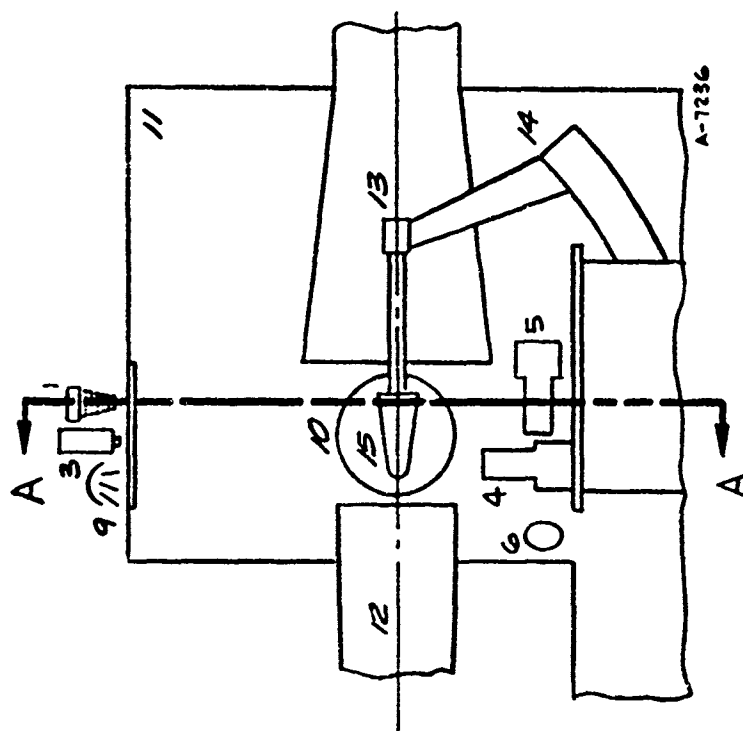
This data acquisition system provided coverage primarily of model shape-change histories, and additionally of model surface characteristics, boundary layer transition location, bow shock shape, and model accelerations. A schematic of the test setup is shown in Figures 2-15 and 2-16. A complete description of the timing and recording system is given in Section 2.3.1, the pulsed photography is covered in Section 2.3.2, motion picture photography in Section 2.3.3, and miscellaneous additional data in Section 2.3.4.

2.3.1 Timing and Recording

The timing and recording system is diagramed in Figure 2-17. Seven channels of a Honeywell 5600C FM tape recorder, run at 60 inches/second, were used to record accelerometer outputs, model entrances and exits, 70mm profile-view camera triggerings, 16mm Hycam triggerings, a 50 KHz reference signal, and an electronically generated time signal. The IRIG B time signal generator also powered the digital displays which were located within the fields of view of the 35 mm sideview and overhead cameras.

2.3.2 Pulsed Photography

For the descriptions to follow, the circumferential angle ray designation is as shown below. Thus the pitch plane contains the 0-degree and 180-degree rays, while the yaw plane includes the 90-degree and 270-degree rays.



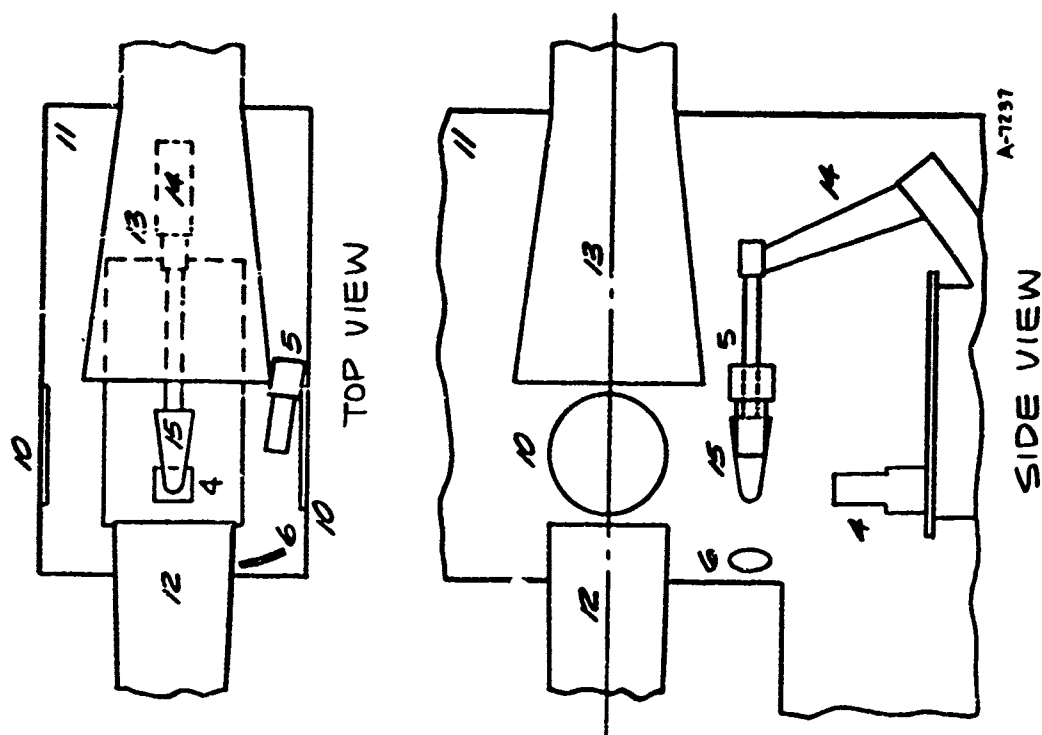
SECTION A-A

1. 35MM PULSED CAMERA
2. 16MM MOVIE CAMERA
3. 16MM CLOSEUP MOVIE CAMERA
4. 20MM PROFILE-VIEW CAMERA
5. 20MM FRONT-VIEW CAMERA (SIDEWALL MOUNTED)
6. MIRRORS FOR FRONT-VIEW 20MM CAMERA
7. MIRRORS FOR SHADOWGRAPH SYSTEM
8. LIGHT SOURCE FOR SHADOWGRAPH SYSTEM

SIDE VIEW

9. OVERHEAD LIGHTING
10. WINDOWS, 16" DIA.
11. TEST CELL - 90"x68"x130"
12. NOZZLE, 17"x17" EXIT
13. DIFFUSER, 28" DIA. INLET
14. STING
15. MODEL
16. 16MM HYDAM MOVIE CAMERA

Figure 2-15. Test Cell Schematic, Model in Test Position



4. 70 MM FRONT-VIEW CAMERA
5. 70 MM FRONT-VIEW CAMERA
6. MIRROR FOR 70 MM FRONT-VIEW CAMERA
10. WINDOWS, 16" DIA.
11. TEST CELL, 40"x68"x130"
12. NOZZLE, 17"x17" EXIT
13. DIFFUSER, 28" DIA. INLET
14. STING
15. MODEL

Figure 2-16. Test Cell Schematic, Model in Retracted Position

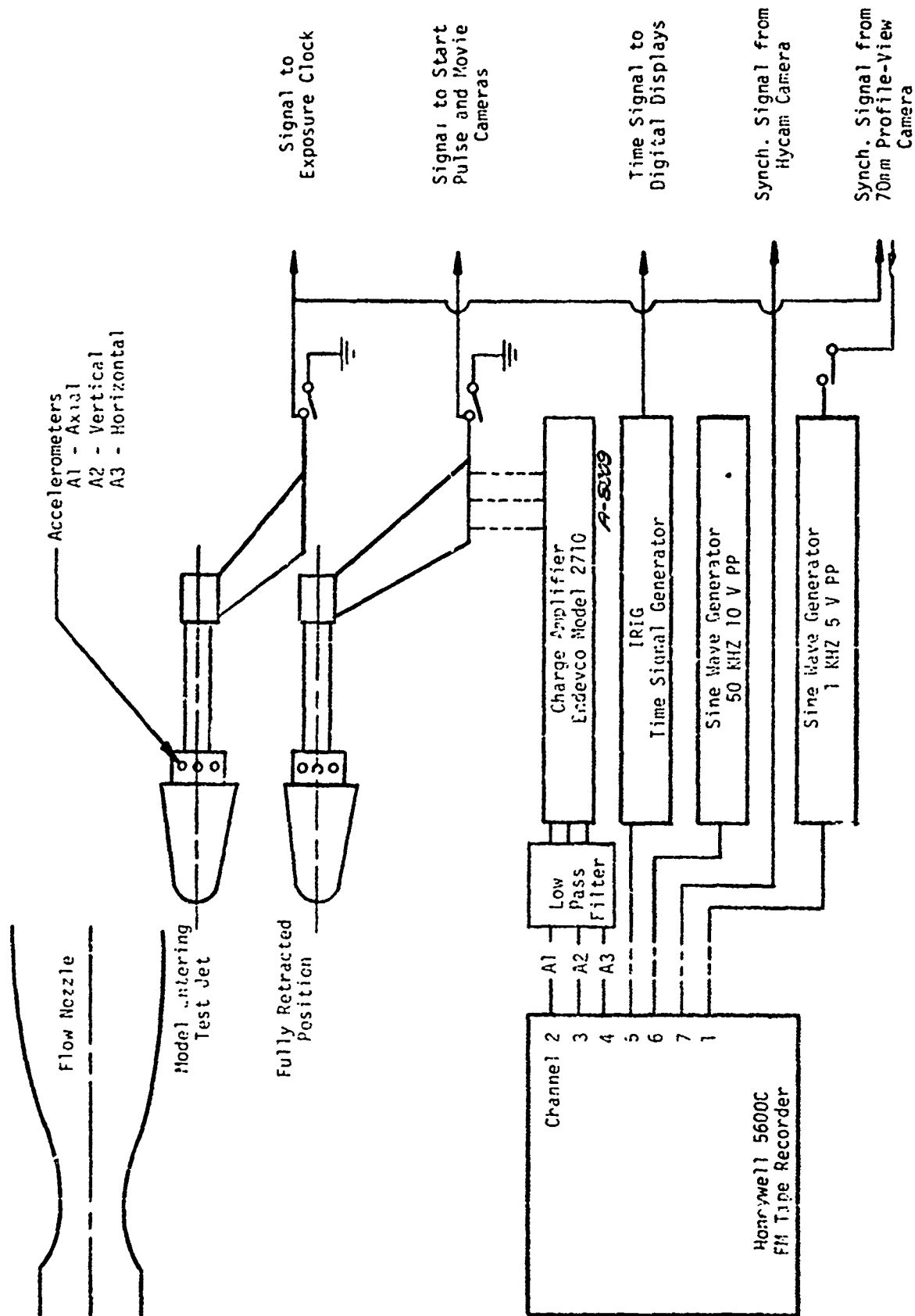
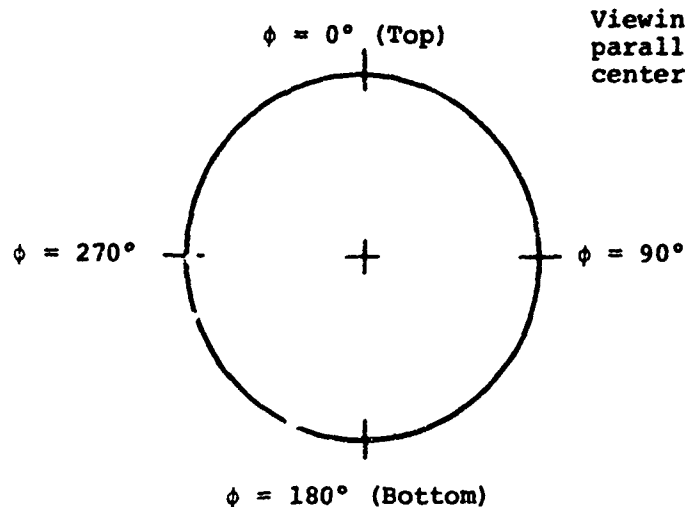


Figure 2-17. Test Setup Electrical Diagram



Viewing front of model,
parallel to tunnel
centerline

The primary quantitative data are derived from the two pulsed 35mm camers and the pulsed 70mm camera. The 35mm sideview shadowgraph camera was a Flight Research Model IV multidata camera operating with a 3-microsecond strobe. This camera had a full view of the model, the mounting hardware, and a digital clock. It recorded shock shape and model shape in the pitch plane. Framing rates of two to six frames/second were selected based on expected model exposure times and film capacity (about 80 feet of film per run). Framing rates for this and all other cameras are given in Table 2-3.

The overhead 35mm was also a Flight Research Model IV, but used reflected light from an overhead 3-microsecond strobe firing 20 milliseconds after the sideview 35mm. The field of view included the entire model, the mounting hardware, a digital clock, and a striped background reference board. This camera thus recorded model shape in the yaw plane and surface features on the model top, again at two to six frames/second with 80 feet of film per run.

The 70mm underside profile-view camera was a Hasselblad model 500 EL using a synchronized circular Honeywell strobe mounted around the lens. It had a field of view of about 4-1/2 x 4-1/2 inches, with the upstream edge about 1/4 inch ahead of the initial model stagnation point. A reference grid was located in the film focal plane to aid in data measurements. This camera recorded model shape and surface details of the model underside at a rate of one frame every 2 seconds, using about 16 feet of film per run. The bow shock shape was also visible in a large number of the 70mm film frames; this unexpected benefit was apparently due to backlighting from the overhead cameras. As indicated in Figure 2-17, firing times for the 70mm camera were recorded by interruptions in a sine wave (input to the tape recorder) which were correlated with the IRIG time signal during data reduction.

TABLE 2-3
CAMERA FRAMING RATES AND PHOTO TIMES

Run No.	Framing Rates (frames/seconds)				Hycam Firing Time ^a (seconds)	70mm Front-View Photo Times ^a (seconds)		
	35mm Cameras	70mm Profile	16mm Side	16mm Top		#1	#2	#3
801	6	1/2	16	30	167.79	15.82	-	-
802	6	1/2	24	40	89.54	10.35	21.52	43.19
803	6	1/2	24	40	54.40	10.53	30.60	58.89
804	6	1/2.5	16	30	-	9.37	18.91	28.11
805	6	1/2	24	40	- ^b	6.20	11.74	19.13
806	6	1/2	24	40	-	4.70	9.73	14.79
807	6	1/2	24	40	-	14.90	29.13	43.52
808	4	1/3	16	30	-	-	-	-
809	6	1/2	48	70	-	3.52	9.21	-
810	6	1/2	24	40	-	4.77	10.30	17.84
811	2	1/4	16	16	-	-	-	-
812	6	1/2	48	70	-	-	-	-
813	6	1/2	24	40	-	-	9.35	13.79
814	6	1/2	24	40	121.91	-	29.86	44.26
815	6	1/2	24	40	- ^b	4.11	8.71	13.14
816	6	1/2	24	40	80.63	10.34	20.05	30.41
817	3	1/2	16	30	-	-	-	-
818	4	1/2	16	30	-	11.50	22.75	47.02
819	6	1/2	24	40	-	29.55	-	-
820	6	1/2	24	40	104.56	9.48	-	-
821	6	1/2	48	70	-	-	-	-
822	6	1/2	24	40	-	14.29	29.24	43.85
823	6	1/2	24	40	114.75	11.81	22.94	-
824	3	1/3	16	30	106.94	15.13	29.58	44.03
825	6	1/2	24	40	-	6.53	-	-
826	6	1/2	16	30	-	19.72	-	-
827	6	1/2	24	40	- ^b	14.87	-	44.28
828	6	1/2	24	40	-	-	-	-
829	6	1/2	24	40	79.78	-	38.84	-
830	4	1/2	16	30	- ^b	19.42	38.84	58.75
831	4	1/2	16	20	213.96	19.42	38.10	58.01

^a Model exposure time at which photos were taken
^b Hycam signal not recorded

The 70mm front-view camera was also a Hasselblad 500 EL and used the same type of strobe as the profile-view camera. It had a field of view of about 5 x 5 inches, viewing the model nose in a mirror mounted beneath the nozzle, when the model was in the retracted position (Figure 2-16). The front-view nose photos were taken by manual triggering while the tunnel was running, with the model retracted. About 8 seconds were required to retract the model from the stream, manually trigger the camera and reinsert the model into the stream. This camera was primarily intended to record features associated with initial transition and sharpening. It also had a focal plane reference grid. A maximum of three in-test photos were taken for each run at the times indicated in Table 2-2.

2.3.3 Motion Picture Photography

The three 16mm movie cameras provided additional coverage of phenomena of interest to augment pulsed photography data. The 16mm sideview shadowgraph camera was a Milliken DBM-54 which used a continuous light source in the shadowgraph system. It had a full view of the model and mounting hardware, but not the digital clock. Its primary purpose was to record general shape-change response and shock shape over the entire length of the test. Framing rates on this camera were adjusted to provide maximum framing rates over the duration of the test. This was based on the film capacity, approximately 100 feet, and expected model exposure times.

The 16mm closeup high-speed overhead camera was a Milliken DBM-55 which used a synchronized overhead 3-microsecond strobe which was interrupted for 80 milliseconds when the 35mm overhead camera strobe was on. The field of view was about 2 x 3 inches and was centered on the nose of the model. This camera recorded local shock shape and body shape in the yaw plane and high-quality surface detail on the top of the model. About 100 feet of film were used per run. Framing rates of 16 to 70 frames/second were selected to insure maximum coverage prior to the model receding out of the field of view.

A high-speed 16mm Hycam movie camera was focused on the model through the shadowgraph system to record flow field oscillations. The view of field and illumination for this camera was the same as for the 16mm sideview Milliken; its film capacity is 400 feet. The camera accelerates to a framing rate of approximately 20,000 frames/second with coverage lasting approximately 2 seconds. The Hycam was to be triggered manually during periods of high model accelerations as determined from real time monitoring of the axial accelerometer. It was, however, quite difficult in general to assess increased model accelerations resulting from flow oscillations, and the phenomena of interest were not always

recorded. Triggering of the Hycam was recorded on Magnetic tape (see Figure 2-17) to allow determination of the exact time from the IRIG signal.

2.3.4 Additional Data

In addition to the pulsed and motion picture photography, pre- and post-test still photographs were taken of each model to fully document initial model condition and all important features of final model shape. For the pre-test photos, front views and isometric views were taken; the post-test photos include -- as a minimum -- front, isometric, pitch plane, topside and underside views.

Three Endevco 2220C high-frequency accelerometers were mounted aft of the model in the instrumented spacer, as illustrated in Figures 2-11 and 2-18. These accelerometers have a range of 0 to 5000 g and a natural frequency of 50 KHz. Accelerometers 1, 2, and 3 measured accelerations in the axial, vertical, and horizontal directions, respectively. As indicated in Figure 2-17, Endevco 2710 charge amplifiers were used to amplify the output of the piezo-electric accelerometers. The 2710 has a frequency range of 2 to 20,000 Hz, with a maximum gain of 10 volts per pico coulomb input.

In addition to recording the response of the accelerometers on magnetic tape, a Tektronix Type 454 oscilloscope was used to display the response of the axial accelerometer during a test, and the response of the other accelerometers after completing a test. A six-channel Midwestern Instruments oscillograph was also used to obtain paper tape oscillograms for each run. These oscillograms included accelerometer data, the IRIG time signal, 70mm profile-view time signal, and Hycam time signal. This data was used primarily to obtain the times at which 70mm profile-view pictures were taken.

Three-dimensional elastomeric molds were made of all post-test models to accurately record all features. The encapsulant used for molding was Dow Corning 3110 RTV. The RTV molds were subsequently used to cast plaster replicas.

All runs were accompanied by normal facility recording of wind tunnel operating parameters including total temperature, total pressure, and nozzle film cooling pressure difference. Time average values of temperature and pressure and computed values of free stream Reynolds number and Mach number were presented in Table 2-1.

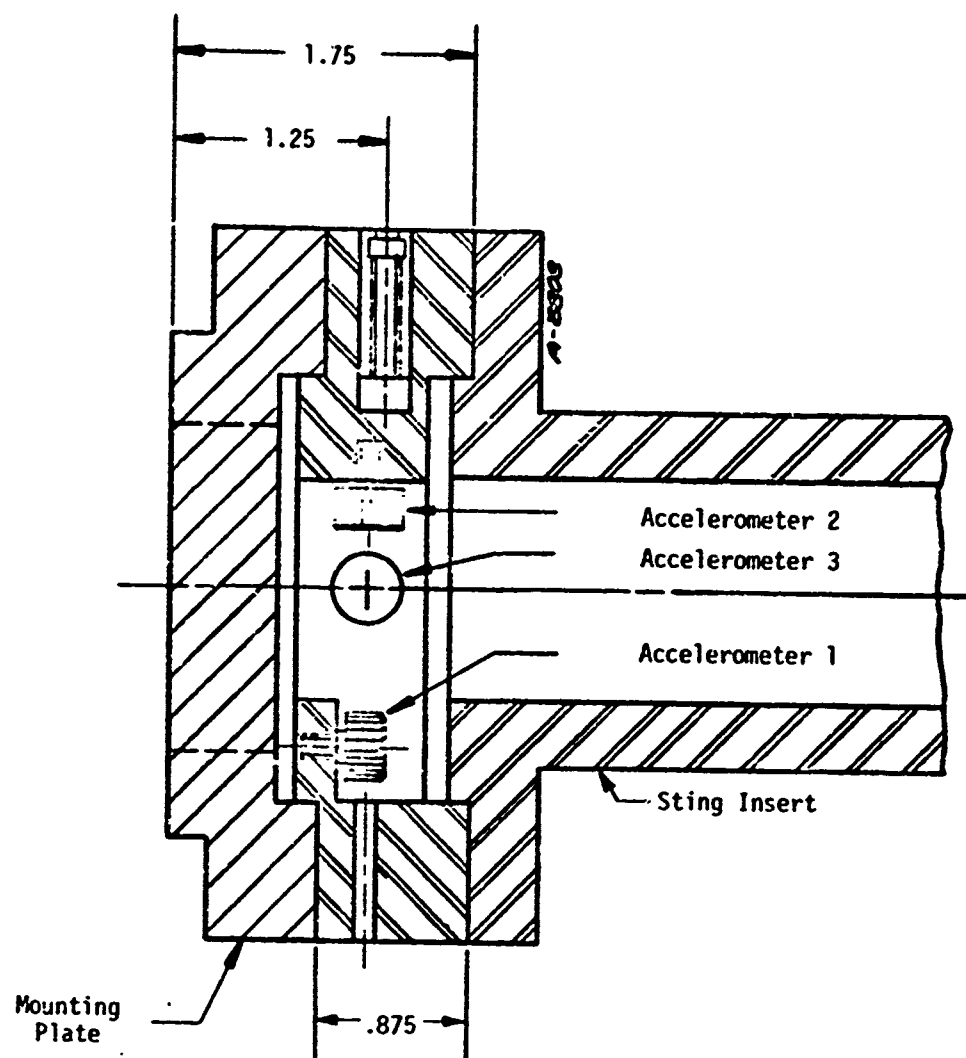


Figure 2-18. Instrumented Spacer Detail

SECTION 3

TEST RESULTS

In this section a compilation of the data acquired from the Series I tests is presented. The data of primary interest, namely the shape-change histories of the LTA models, are presented in Section 3.1. Data related to boundary layer transition location and subsequent sharpening phenomena are presented in Section 3.2. Finally, unsteady flow phenomena resulting from irregular shape development are discussed in Section 3.3.

3.1 GENERAL SHAPE CHANGE

The 35mm pulsed cameras provided the basic shape-change data which are required to investigate the irregular nosetip shape regime. These film data are useful in several ways, three of which are demonstrated here. First, Appendix A gives three typical 35mm sideview shadowgraphs and the corresponding pitch-plane post-test photograph for each run. These photographs represent the most significant shapes resulting from a particular run and their progression with time. Table A-1 gives the model exposure time for each photograph. It should be noted that although the shock shapes are not clearly visible in the photographs shown here because of loss in clarity during reproduction, they are more easily visible in the original film and do provide useful data. Secondly, model shape profiles were traced from 35mm film for several times during each run to give the shape profile histories shown in Appendix B. In the pitch (vertical) plane profiles, taken from the sideview shadowgraphs, initial and final shock shapes are also shown. In cases where the initial and/or final shock shapes were difficult to define, they were omitted or partially drawn in for the visible portions. The yaw (horizontal) plane profiles are taken from the overhead 35mm film at the same model exposure times as the pitch-plane profiles. Due to camera malfunctions, no photos were taken with the overhead 35mm camera for the first 27 seconds of Run 810, nor for the entirety of Run 817. Similarly, there is no shadowgraph film for Run 812. Finally, the first portion of Run 819

yielded no useful shape profile data because the model was not fully inserted into the test stream and could not be viewed properly by the cameras.

The third use demonstrated here for the 35mm film is measuring stagnation point surface recession for each run. This was done with a Telereadex film data processor which provided precise measurements and automatic punched card data recording. For the purpose of these measurements, the stagnation point was taken to be the forwardmost point on the model, not necessarily on the model centerline. All measurements were made relative to the initial stagnation point location in the first film frame after the model was completely inserted into the test stream. The reference point used for this was the vertical pin visible at the top of the model mounting plate. These measurements are of axial recession; that is, they are taken in the direction parallel to the tunnel (and model) centerline. The results are presented in Appendix C. About one-third of these plots were prepared from the overhead 35mm film, and the remainder from the 35mm sideview shadowgraph film. To insure consistency of the data, recession plots were prepared using both film sources on several of the runs; sample results for Run 802 are presented in Figures C-2 and C-3, and show excellent agreement.

For Run 811, the time of changeover from the first portion test conditions to the second is indicated on the plot. Only the second portion of Run 819 is represented because of the previously mentioned problem with incomplete model insertion. The recession data for the first 27 seconds of Run 810 came from 70mm profile-view film because of the lack of 35mm data during that time. Finally, the large jump in recession at about 100 seconds in the plot for Run 818 is due to a nose breakage when the stagnation point receded to the vicinity of a subsurface crack in the camphor model.

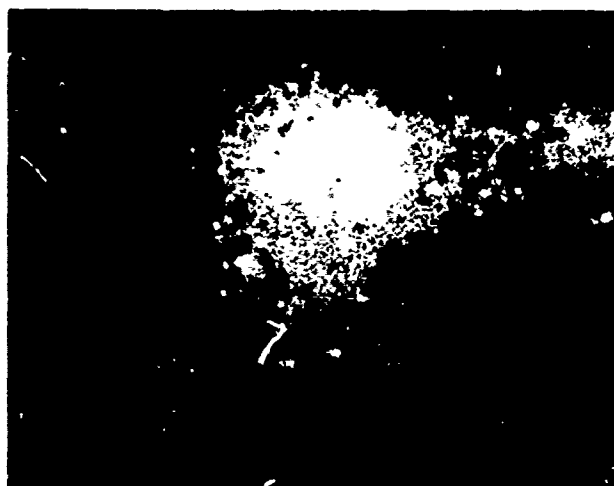
3.2 TRANSITION AND SHARPENING PHENOMENA

The sequence of events which leads to irregular shapes generally begins with boundary layer transition at discrete points on the model nose; that is followed by development of these initial "gouges" into a "transition line" which progresses forward during sharpening. The data presented in this section are primarily directed toward providing a record of these phenomena, although most of the raw data are also useful for other ablation information.

In general, transition is observable on camphor LTA models by virtue of gouges, scallops, and associated surface roughness features caused by the highly "disorganized" local turbulent flow patterns, higher heating, and resultant higher mass removal rates. This is in contrast to areas of laminar flow, which appear smooth and undisturbed in photographic data. The transitional gouges mentioned above generally occur first in a fairly random manner, appearing as relatively long, narrow furrows (Figure 3-1a). These furrows widen into shapes similar to semicircles or arcs (Figure 3-1b and c) at which time they can be distinguished from spurious, nontransitional gouges (e.g., those caused by particle impaction) which tend to disappear without widening. During the widening stage of development, the upstream edges of the gouges (which are the points used to define locations) tend to remain fixed, although some exceptions have been noted. It has also been observed that in many cases the development of a particular gouge may preclude the development of others nearby; this may be due to the tendency of the local flow to divert into the lower pressure region within the gouge, thus decreasing the boundary layer thickness. The widening of the gouges leads to their merging together to form the transition line (the downstream border of a laminar cap) which moves forward toward the stagnation point as sharpening progresses.

Examples of the phenomena discussed above can be seen in the selected 70mm front-view photographs presented in Appendix D. The photographs were taken during short preplanned interruptions in the tests. The times indicated are total model exposure times prior to the removal of the model from the test stream (Section 2.3.1). The orientation of the photographs is such that the titles are under the 180-degree ray; that is, the 0-degree ray is then at the top. The main purpose of taking the 70mm front-view photos was to study transition locations and the initial phases of sharpening, and the photos obviously provide a clear and unique record of those phenomena.

A different view of the same phenomena, plus later stages of sharpening and shape change, was provided by the 70mm profile-view camera. Three selected profile-view frames from most of the runs are presented in Appendix E. In this case, the three frames for each run generally show initial transition, the final stages of sharpening, and post-sharpening shapes of interest. The area covered is the lower surface of the model, with the 180-degree ray at the center of each photograph (see Section 2.3). Those runs for which no profile-view photographs are presented (e.g., Run 801) were in general omitted because the 70mm camera recorded relatively slight shape change.



(a)
Model exposure time
approximately 0.5 second



(b)
0.4 second after (a)



(c)
1.1 seconds after (a)

Figure 3-1. Example of Transitional Gouge Development from 16mm Overhead Camera. (Run 805; 1.5-inch R_N Sphere-Cone; $Re_\infty = 6.56 \times 10^6/\text{ft}$, $T_0 = 987^\circ\text{F}$)

The 70mm photographs discussed above represent raw transition and sharpening data; in addition to these raw data, reduced data showing initial transition locations were prepared. The approach taken here was to locate gouges using the 70mm profile-view film for the lower side and the 35mm overhead film for the upper side. Tracings were made of model outlines and gouge shapes using an enlarged projection of the film. Selection of a particular time was based primarily on the selection of a 70mm film frame which showed as many initial gouges as possible at a time prior to any significant movement of the gouges. The 35mm frame to be traced was then taken for the same time as the 70mm frame, if possible; this procedure was necessary because of the much lower framing rates for the 70mm camera (Table 2-3). Cartesian coordinate values for each gouge relative to the stagnation point were used to calculate the corresponding circumferential angle ϕ and streamlength S . This is based on the assumption that the model nose has not ablated sufficiently to change the initial shape. This assumption is valid for the early times involved here. Fourteen of the runs were used in this procedure, since the remainder either did not experience the sequence of events which typify the transitional regime (i.e., they evolved in the laminar, incipient transitional, or fully turbulent regimes) or did not lend themselves to accurate measurements because of their shapes (e.g., the laminar-blunt shapes).

The model exposure times for which the transition location measurements were taken are given in Table F-1. Appendix F gives the gouge location tracings for the measurements and the reduced results, plotted in the (ϕ, S) plane, for each run. As indicated in Section 2.3, data from the 70mm film covers the ϕ range from 90 degrees through 180 degrees to 270 degrees (wind side) while the 35mm film data is for ϕ from 270 degrees through 0 degrees to 90 degrees.

3.3 UNSTEADY FLOW FIELD PHENOMENA

The irregular shapes which can evolve during LTA shape change often cause flow field oscillations. This section briefly presents examples of data pertaining to such unsteady flow fields which resulted during the Series I tests. Having anticipated the probable existence of flow field oscillation in the present series of tests (Reference 2), special efforts were taken to accurately record this phenomenon. This included, as discussed in Section 2, a three-axis high-frequency accelerometer system, 35mm pulsed shadowgraph photography, and 16mm low- and high-speed photography. All data

sources except the low-speed 16mm camera were referenced to an IRIG time signal (see Section 2 for details). The accelerometers, the 16mm low-speed camera, and the 35mm pulsed camera were run continuously during a test. The high-speed 16mm Hycam camera was to be triggered manually when model accelerations increased significantly, indicating flow field oscillations. This technique was unsatisfactory for two reasons: 1) flow field oscillations, when they occurred, lasted for only brief periods, and 2) model accelerations were constantly changing character throughout a given test. Therefore, when flow oscillations did occur, it was very difficult to assess if model accelerations had changed due to flow oscillations or for some other reasons. In general, whether or not flow oscillations occurred, the model accelerations tended to increase throughout a test. This is probably a result of the increased surface roughness characteristic of ablating bodies in turbulent flow. In particular, the formation and growth of scallops, as illustrated by the 70mm photographs shown in Section 3.2, could very well result in the observed changes in model accelerations. Fortunately, however, the 35mm and 16mm low-speed cameras were sufficient to detect flow oscillations.

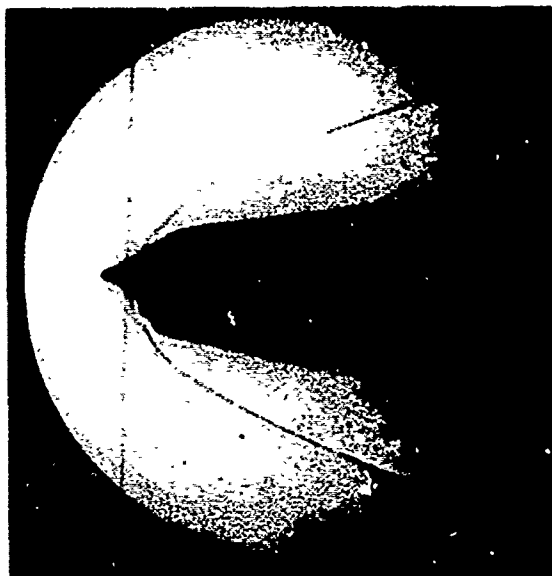
Preliminary observation of the data described above indicates that unsteady flow fields existed for portions of about two-thirds of the runs, and for portions of virtually all runs which developed irregular shapes. The nature and magnitude of the resultant oscillations varied greatly, depending on the model shape. For example, distinct model accelerations were recorded for Runs 803 and 805, which developed the cusped shapes that typified many of the other runs (and that were studied in detail in the PANT Series G tests; see Reference 3). In addition, though, the Run 826 model experienced substantial accelerations with an incipient transitional shape, and the models in Runs 814 and 822 showed periodic sustained high accelerations associated with the development of double stagnation points.

There obviously is a large amount of data available from this test series documenting unsteady flow fields, but the presentation of all such data is not within the scope of this report. Therefore, only sample data from a typical test, Run 805, is presented here. A 1.5-inch R_N sphere cone was tested in Run 805, at $Re_\infty = 6.56 \times 10^6/\text{ft}$ and $T_o = 987^\circ\text{F}$. The model went through the stages of transition and sharpening described in Section 3.2 and developed the expected slender shape, passing through at least two distinct periods of flow field oscillation. These oscillations are visible by virtue of the associated unsteady bow shock recorded by the cameras in the shadowgraph system. Figure

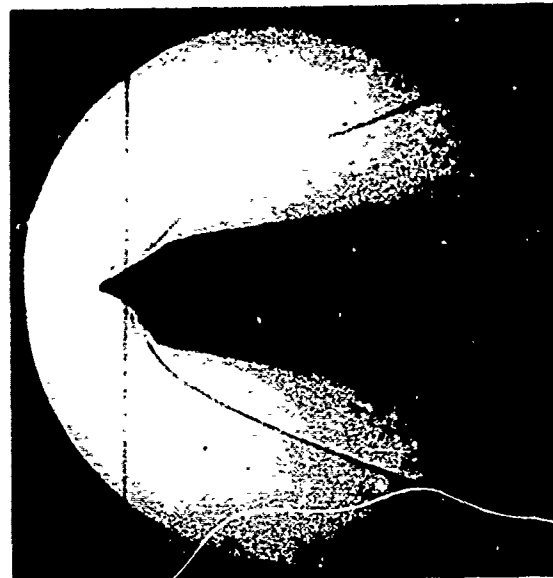
3-2 presents four sample 16mm shadowgraph frames in which the model shape and bow shock are visible. The 35mm shadowgraph film is not presented here because, as mentioned previously, the shock shape is difficult to discern in reproductions of the original film. As indicated by the model exposure time below each frame, the phenomena in frames (a) and (b) were part of a particular period of flow field oscillation, while frames (c) and (d) represent a later period. The indicated exposure times were calculated using the camera framing rate, since the 16mm cameras did not view a clock; thus the times are not necessarily precise and are given mainly for comparison among the given frames.

Although the frames in Figure 3-2 are not as clear as the original film because of reproduction losses in quality, the state of the flow field can still be discerned. In frames (a) and (c), the bow shock is attached to the conical nose and barely visible, whereas the strong secondary shock is fairly clear. In frames (b) and (d), the separation regions on the model nose have grown, and the secondary shocks have moved off the nose. This type of unsteady flow field is characterized as shock "buzzing", as contrasted to shock "jumping" (e.g., Run 826) and fully pulsating flow (not observed during this test series).

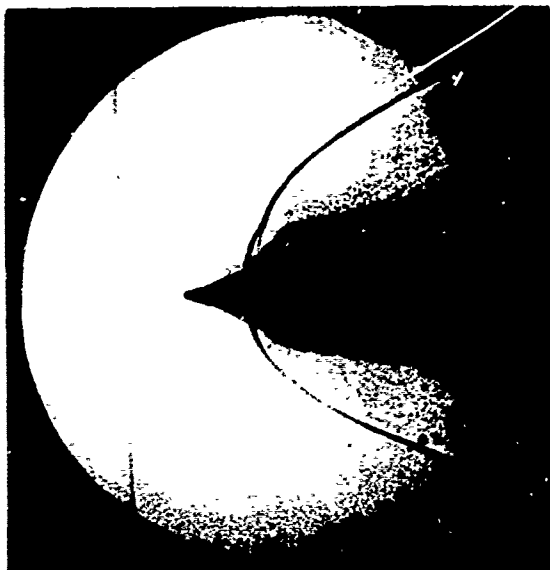
Corresponding examples of the accelerometer responses for the unsteady flow fields demonstrated in Figure 3-2 are shown in the oscillogram segments presented in Figure 3-3. As indicated on the figure, each segment covers about one second of exposure time. Segment (a) is at approximately 44 seconds exposure time, thus indicating the nature of the model accelerations corresponding to the configurations in Figure 3-2 (a) and (b); while segment (b) is at approximately 88 seconds exposure time and corresponds to Figure 3-2 (c) and (d). Although these samples of accelerometer response are intended to be only qualitative, it is clear that the forces on the model resulting from an unsteady flow field are significantly higher than the usual aerodynamic loadings.



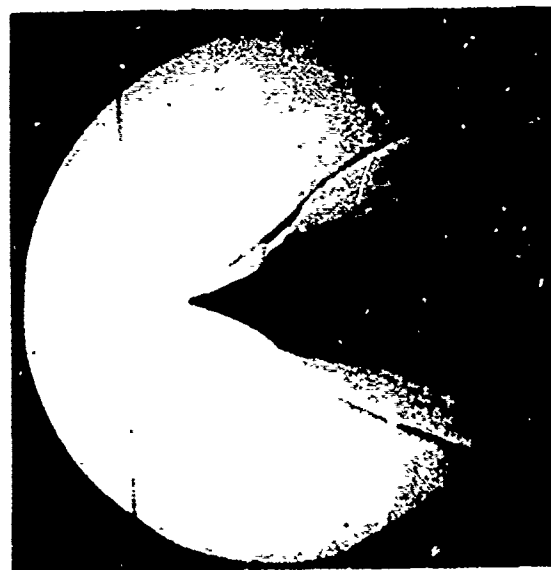
(a)
43.80 seconds



(b)
43.84 seconds



(c)
87.21 seconds



(d)
88.13 seconds

Figure 3-2. Examples of Unsteady Flow Phenomena During Run 205
(1.5-inch R_N Sphere-Cone; $Re_\infty = 6.56 \times 10^6/\text{ft}$,
 $T_0 = 987^\circ\text{F}$)



(a)

1 second



(b)

Figure 3-3. Example of Accelerometer Response for Run 805

SECTION 4

SUMMARY AND DISCUSSION

The experimental data recorded during the wind tunnel test series provides the basis for satisfying the test objectives. However, the determination of whether or not they have been satisfied can be made only after the experimental data have been reduced and analyzed. This section presents a brief discussion of data and data trends relative to the test objectives given in Section 1. Preliminary data trends relative to the primary test objective are given in Section 4.1. Secondary objectives and data which satisfy these objectives are discussed in Section 4.2.

4.1 PRIMARY TEST OBJECTIVE

The primary objective of this wind tunnel test series was to evaluate the effects of six significant parameters on the formation and extent of irregular shapes.

The effects of each parameter are discussed in the following paragraphs.

Reynolds Number

Reynolds number is a primary nosetip shape-change parameter. A summary of final shape trend with Reynolds number is shown in Figure 4-1 for the baseline geometry (1.5-inch R_N sphere-cone). The top profiles in Figure 4.1 are final shapes for models tested over a spectrum of Reynolds numbers and demonstrate the basic trend. The lower profiles are for two tests conducted at intermediate Reynolds numbers and shows that at certain test conditions the final model profile is not always indicative of shape-change regime.

Transition Control

Boundary layer trip grooves were used on Runs 807 and 814 in an attempt to produce symmetric transition at lower Reynolds numbers. These grooves did not produce symmetric transition but did demonstrate that indentations in the nose region tend to grow and deepen.

Surface Roughness

The particle-loaded models showed that surface roughness has a strong effect on sharpening and irregular shape development. These models (Run 804,

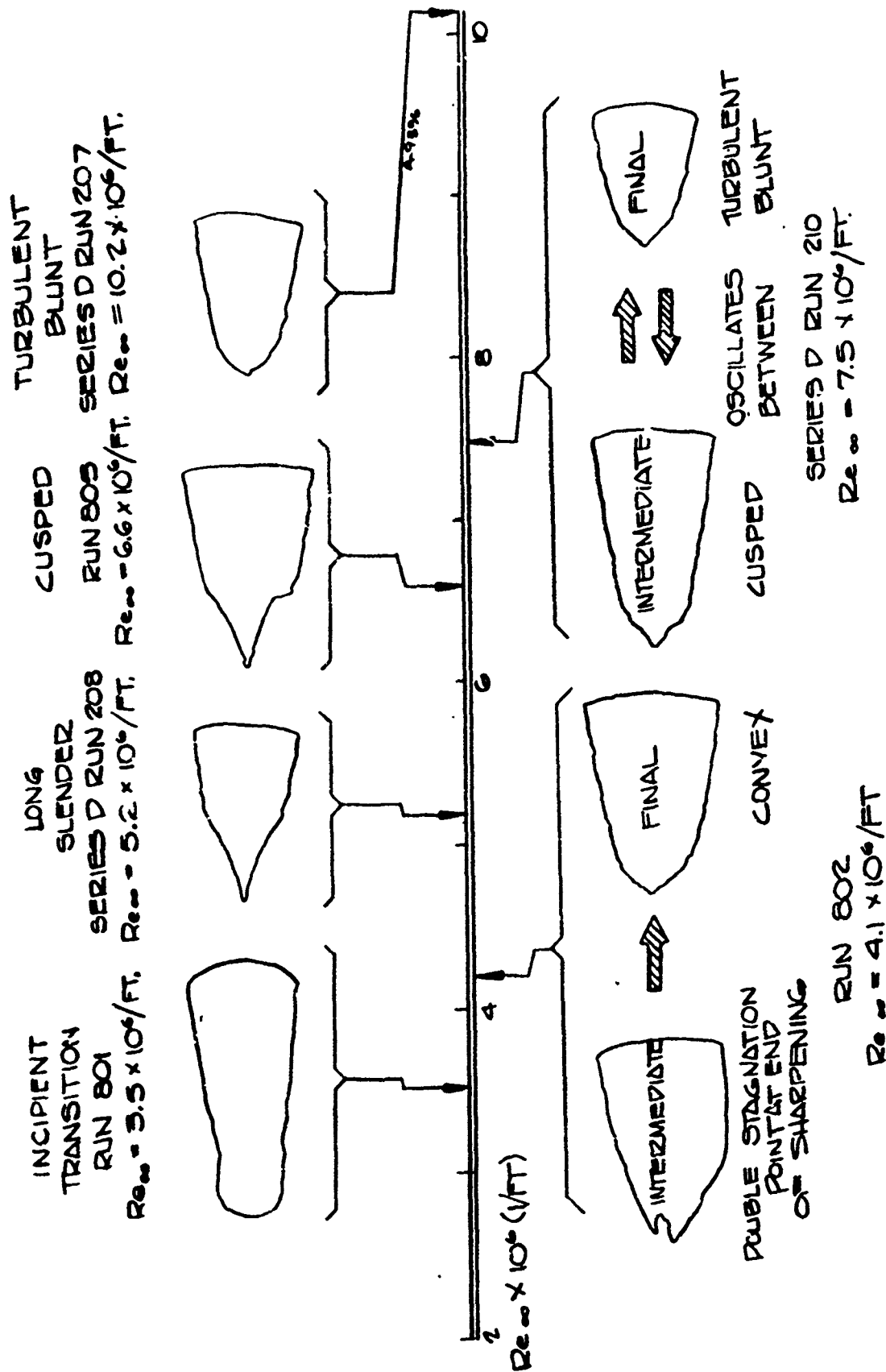


Figure 4-1. Reynolds Number Effect on Model Final Shape
(All 1.5-Inch Sphere-Cones, Nominal $T_o = 1000^\circ\text{F}$)

808, and 811) were tested over a range of Reynolds number and achieved final shapes which were either laminar (Run 811, first exposure) or generally convex. Although relatively few data points exist, the conclusion is that the particle presence impeded the formation of the irregular shape regime.

Model Size

The effect of model size was evaluated by testing sphere-cone models of three different nose radii. These tests are summarized in Figure 4-2, which presents final shapes from both this test series and Series D (Reference 1). This figure demonstrates that decreasing the model size causes an increase in the Reynolds number required to attain a given shape regime.

Initial Geometry

Models with six different types and sizes of initial geometry variation were tested. Table 4-1 gives a summary of those runs for which cross comparisons are available.

TABLE 4-1
SUMMARY OF DIFFERENT INITIAL GEOMETRY RUNS
(NOMINAL $T_o = 1000^\circ\text{F}$)

Initial Geometry	Nominal $Re_\infty \times 10^{-6}$ (1/ft)		
	4.0	5.0	6.7
1.5" R_N Sphere-Cone	802	208 (Series D)	805
1.5" $R_S/60^\circ/8^\circ$ Biconic		816	810
1.5" $R_S/75^\circ/8^\circ$ Biconic		823	813
1.5" R_S /Laminar-Blunt	822		815

Figure 4-3 shows comparisons, at each nominal Reynolds number, of the post-sharpening and final shapes for the runs indicated in Table 4-1. Overall there appears to be no significant differences in final shape between the sphere-cone and the various other initial geometry models. This trend is particularly apparent at the nominal $Re_\infty = 5 \times 10^6/\text{ft}$ condition which, as Figure 4-1 demonstrates, is definitely within the irregular Reynolds number regime. At the intermediate Reynolds number conditions of 4.0 and 6.5 $\times 10^6/\text{ft}$ the trend is not as clear, but as indicated in Figure 4-1, at these intermediate conditions the final profile is not always indicative of the shape-change regime.

- PROFILES SHOWN ARE FINAL SHAPES FROM SERIES D (200's) AND SERIES I (800's) TESTS
- NUMBERS INSIDE SHAPE PROFILES ARE VALUES OF $Re_{\infty} \times 10^6 (1/FT)$

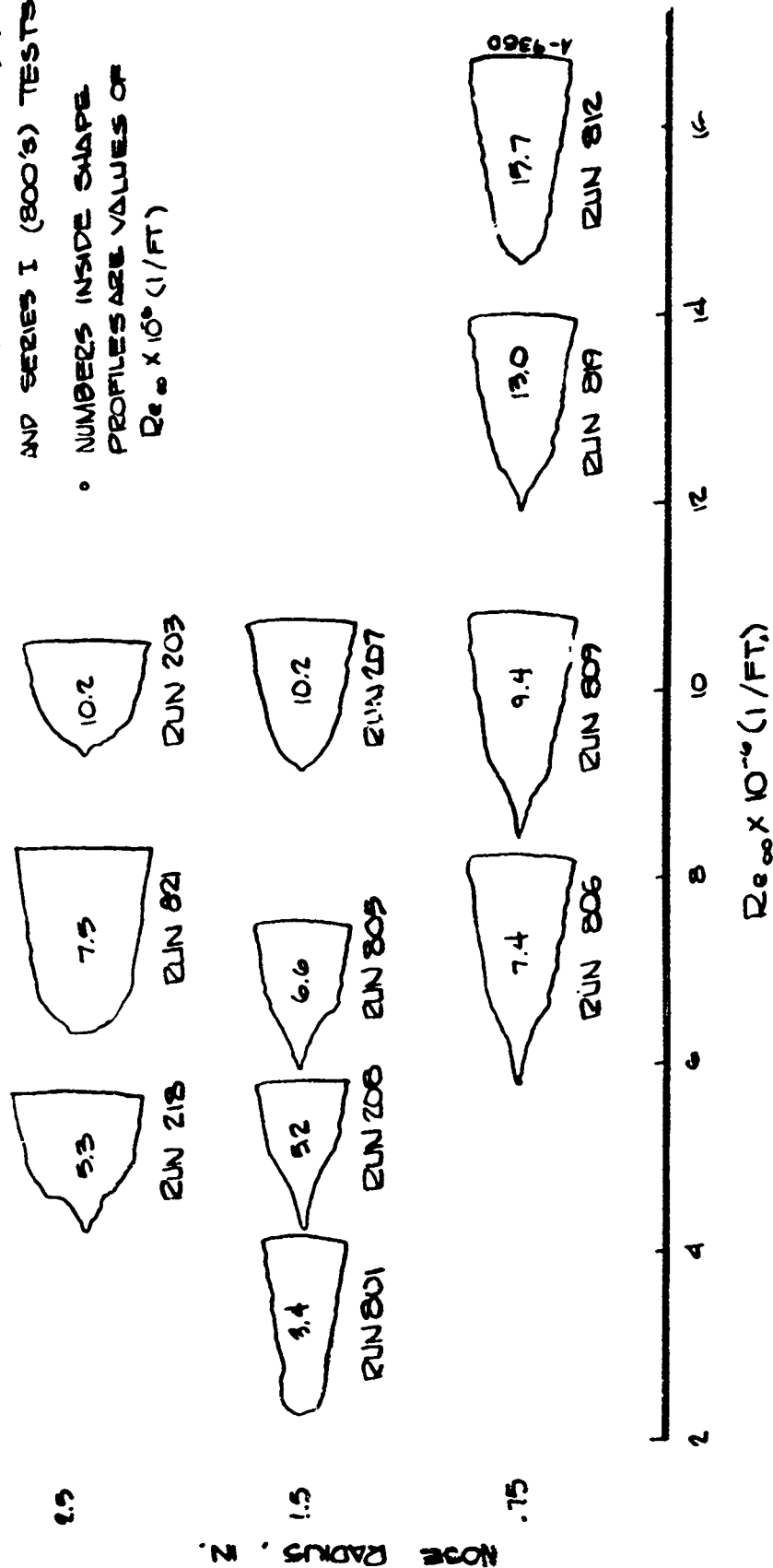


Figure 4-2. Effect of Model Size on Shape Development

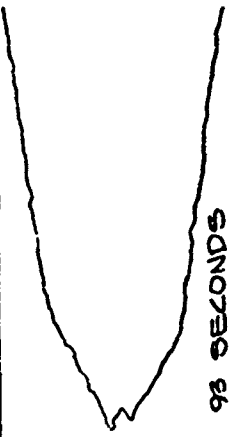
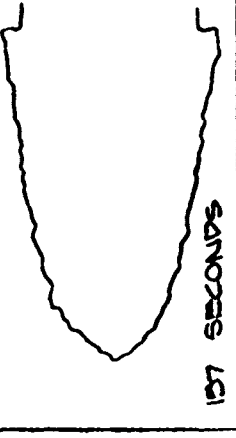
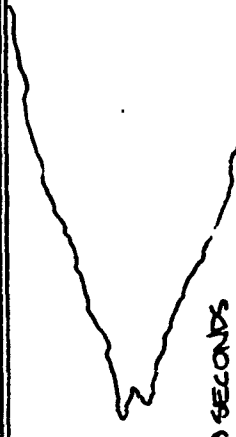

INITIAL MODEL GEOMETRY	RUN No.	Re (10 ⁶ /FT)	SHARPENING TIME (SEC)	POST- SHARPENING SHAPE	FINAL SHAPE
1.5" D _N SPHERE- CONE	802	4.09	60	 98 SECONDS	 137 SECONDS
1.5" D _s LAMINAR- BLUNT	822	4.02	140	THIS SHAPE, TAKEN DURING SHARPENING, IS SHOWN FOR COMPARISON TO RUN 802 AT SIMILAR TIME.	
1.5" D _s LAMINAR- BLUNT	822	4.02	140	 169 SECONDS	 198 SECONDS

Figure 4-3. Comparison of Post-Sharpening and Final Shapes for Different Initial Geometry Models

(a) Nominal $Re_{\infty} = 4 \times 10^6/\text{ft}$

A-0359

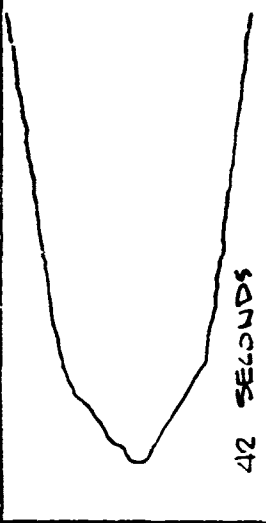
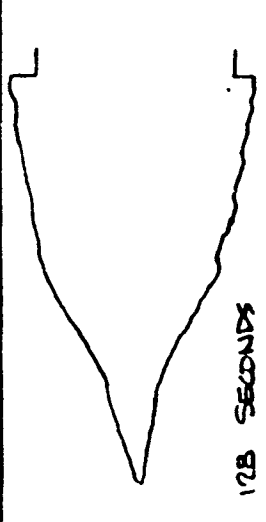
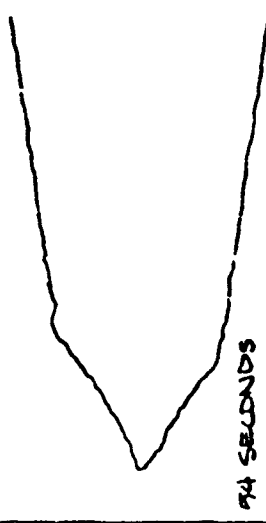
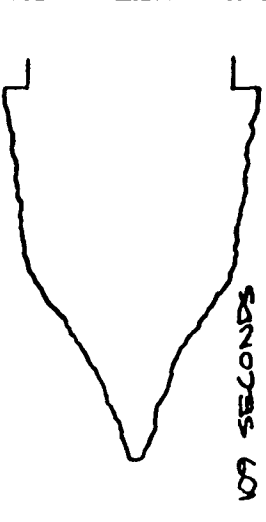
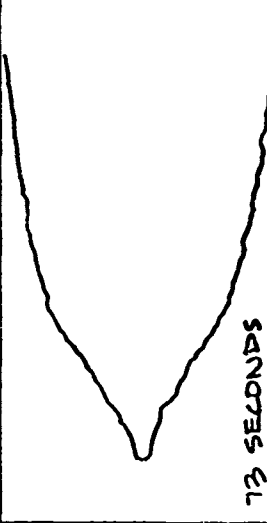
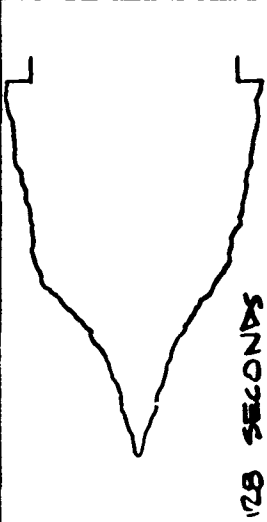
INITIAL MODEL GEOMETRY	RUN NO.	Re_{∞} (10 ⁶ /FT.)	SHARPENING TIME (SEC.)	POST- SHARPENING SHAPE	FINAL SHAPE
1.5" R_N SPHERE- CONE	208	5.23	40		
1.5" R_s 60°/8° BICONIC	816	5.20	50		
1.5" R_s 75°/8° BICONIC	828	5.18	60		
1.5" R_s LAMINAR- BLUNT					

Figure 4-3. Continued

(b) Nominal $Re_{\infty} = 5 \times 10^6/\text{ft}$

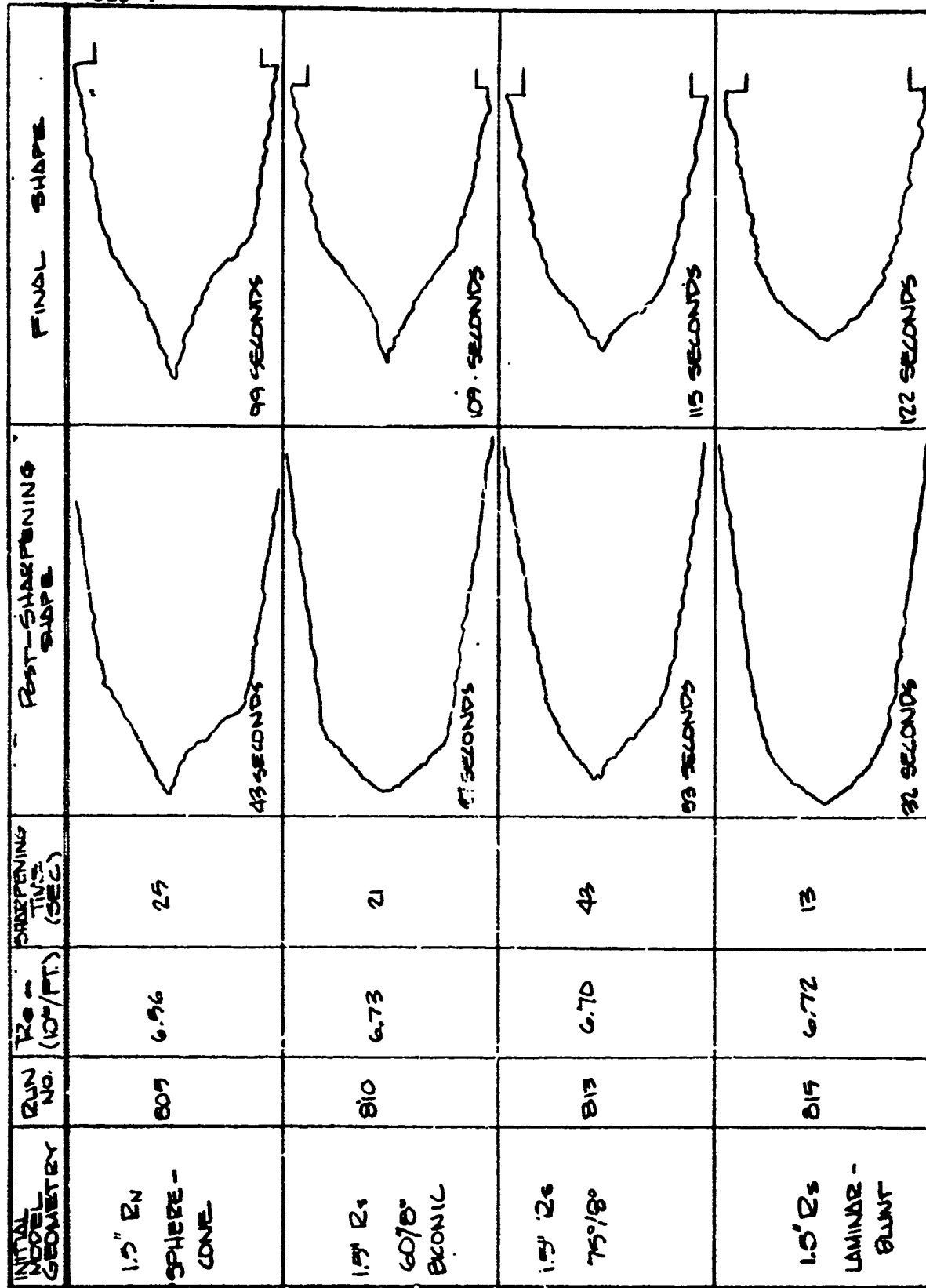


Figure 4-3. Concluded

(c) Nominal $Re_{\infty} = 6.7 \times 10^4$ /ft

Also shown on Figure 4-3 are the sharpening times and profiles for each run. These sharpening times show significant variation, particularly at the lower Reynolds number. The current data are not adequate to indicate whether these variations represent basic variability in the physical phenomena or a trend with initial model shape.

Blowing Rate and Wall Temperature Ratio

Finally, the effect of blowing rate (B') and wall temperature ratio (T_w/T_e) can be assessed by comparing the results of the low total temperature (T_o) tests (Runs 817, 818, and 824) to the baseline since both B' and T_w/T_e are functions of T_o . This combined effect is shown in Figure 4-4. For the lower (500°F) supply temperature (i.e., lower B' and higher T_w/T_e) a given shape regime exists at higher Reynolds numbers than it does for the nominal (1000°F) supply temperature. The stagnation point values of B' and T_w/T_e are about 0.3 and 0.7, respectively, for the lower supply temperature, compared to about 0.6 and 0.55, respectively, for the nominal supply temperature.

4.2 SECONDARY TEST OBJECTIVES

There were four secondary test objectives dealing with additional data and wind tunnel testing capability. These objectives and available data are reviewed below:

- Generate accurate recession data to evaluate heat transfer rates to scalloped surfaces – these data are available from the 70mm profile-view and 35mm sideview shadowgraph film
- Generate shape-change and shock-shape data to evaluate the phenomena associated with the growth and degradation of small nose protuberances – these data are available from the 70mm profile-view and 16mm overhead close-up film
- Generate high-frequency acceleration data to evaluate the effects of oscillating shocks – high-frequency acceleration data are recorded on magnetic tape for all runs.
- Simulate flight shape-change response in a wide tunnel – Run 829 indicates that NOL Tunnel No. 8 has the capability to produce prescribed time-dependent environments. Further analysis is required to assess flight response similitude.

- PROFILES SHOWN ARE FINAL SHAPES FROM SERIES D (200's) AND SERIES I (800's) TESTS.
- NUMBERS INSIDE SHAPE PROFILES ARE VALUES OF $Re \propto 10^{-6} (1/FT)$.

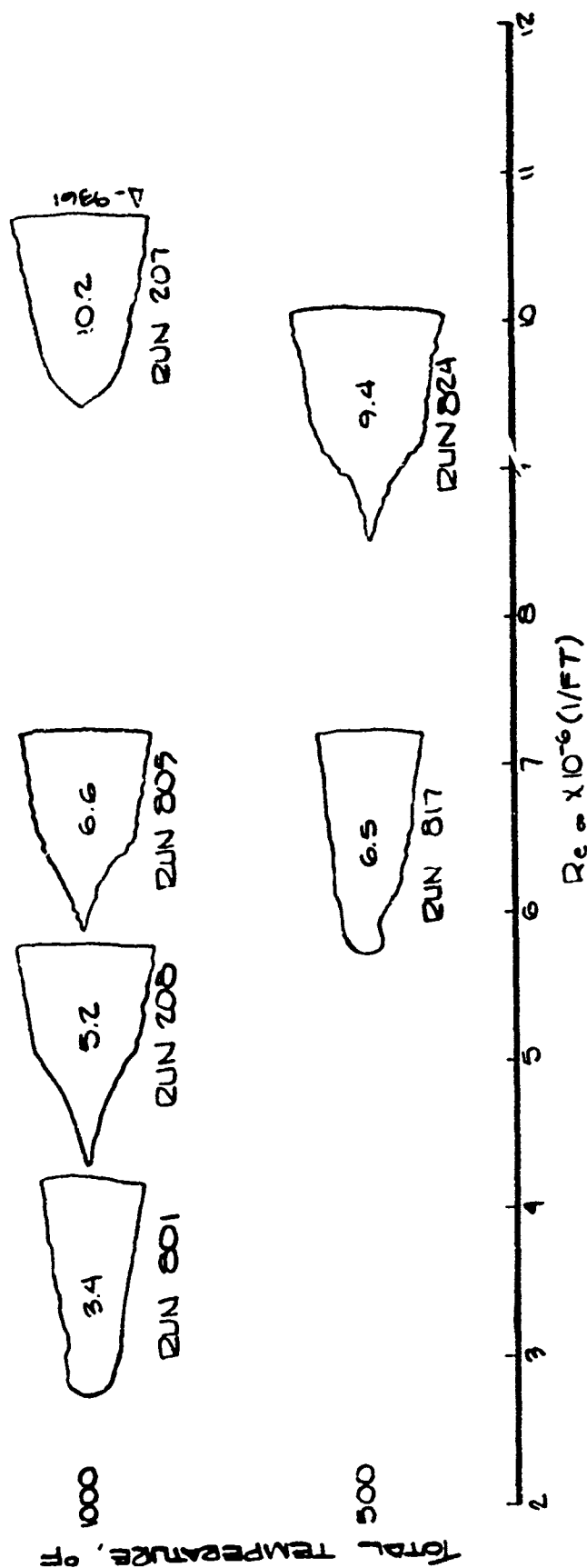


Figure 4-4. Effect of Supply Temperature (T_0) on Shape Development

REFERENCES

1. Derbidge, T. C., Wool, M. R., and Baker, D. L., "Interim Report, Passive Nosetip Technology (PANT) Program," Vol. V, "Definition of Shape Change Phenomenology from Low Temperature Ablator Experiments," Part II, "Experimental Data, Series D (Final Test Series)," Aerotherm Report 74-90, January 1974.
2. Derbidge, T. C., and Nelson, E. V., "An Experimental Study to Evaluate the Irregular Nosetip Shape Regime - PANT Environmental Test Plan, Series I," Aerotherm Report 74-93, C/N 7040.370, January 1974.
3. Abbett, M. J., Cooper, L., Jackson, M. D., and Dahm, T. J., "Unsteady Flow on Ablated Nosetip Shapes, PANT Series G Test and Analysis Report," Aerotherm Report 73-87, C/N 7040.353, December 1973.
4. Baker, R. L., "The Effect of Free Stream and Material Parameters on Stable Ablating Nosetip Shapes," Report No. TOR-0074(4450-76)-10, The Aerospace Corporation, El Segundo, California, April 1974.

APPENDIX A

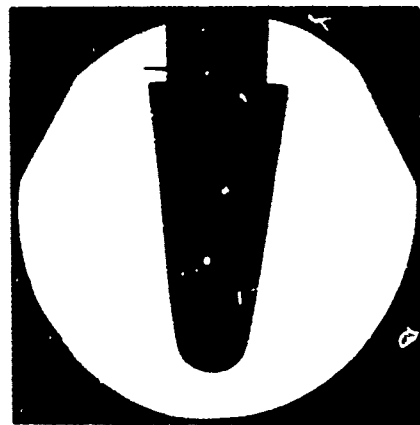
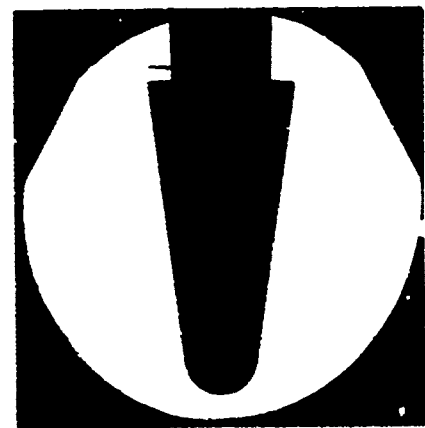
SELECTED SIDEVIEW SHADOWGRAPHS
AND POST-TEST PHOTOGRAPHS
RUNS 801-831

TABLE A-1
MODEL EXPOSURE TIMES CORRESPONDING TO SIDEVIEW SHADOWGRAPHS
AND POST-TEST PHOTOGRAPHS

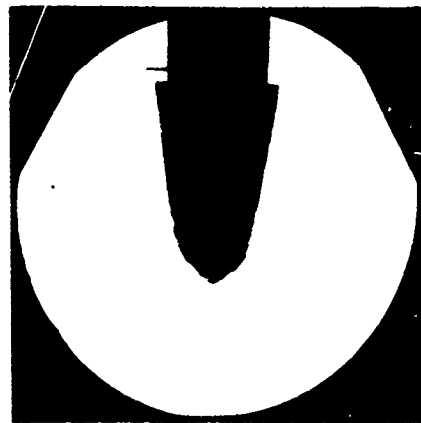
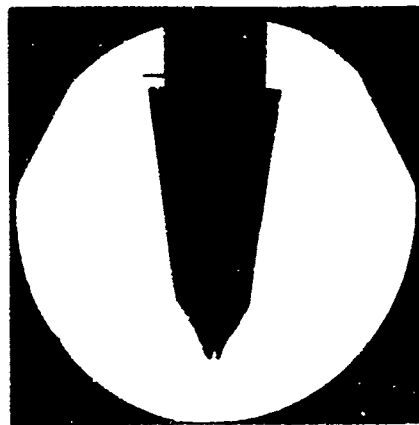
Run No.	Exposure Time (sec)			
	Sideview Shadowgraph			Post-Test ^a
	1	2	3	
801	0.54	91.60	151.40	186.33
802	49.93	87.07	139.16	157.89
803	22.54	52.49	97.87	115.80
804	10.03	102.87	140.64	178.91
805	18.45	38.15	71.56	99.60
806	.83	11.44	67.74	87.19
807	1.00	58.42	111.02	156.24
808	60.24	148.22	241.76	288 ^b
809	8.71	19.43	39.03	58.63
810	.67	20.62	76.17	109.47
811	104.79	251.79	437.04	478.26
813	.82	28.57	64.03	115.74
814	.66	50.15	134.39	172.91
815	1.15	12.65	86.52	123.15
816	49.50	74.31	115.42	126.28
817	122.01	180.83	257.21	325.48
818	48.27	100.79	210.07	253.84
819	25.72	47.54	63.21	89.88
820	1.00	38.17	97.57	122.83
821	1.00	12.97	--	13.47
822	1.49	99180	164.92	224 ^b
823	46.37	90.09	118.35	130.48
824	44.80	152.01	211.50	242.75
825	20.24	51.00	55.86	67.73
826	61.96	118.76	164.95	192.33
827	1.01	35.42	107.29	139.04
828	42.38	55.06	74.09	91.11
829	66.78	93.16	106.58	116.03
830	40.33	63.15	105.71	153.52
831	59.40	144.23	217.88	231.08

^aTotal model exposure time

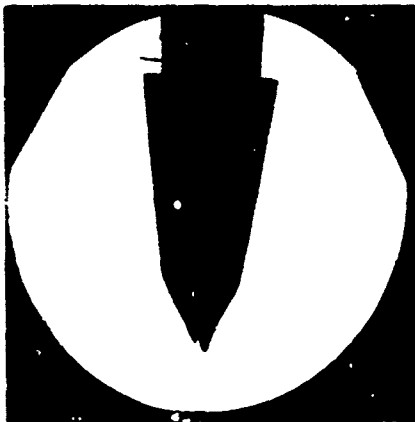
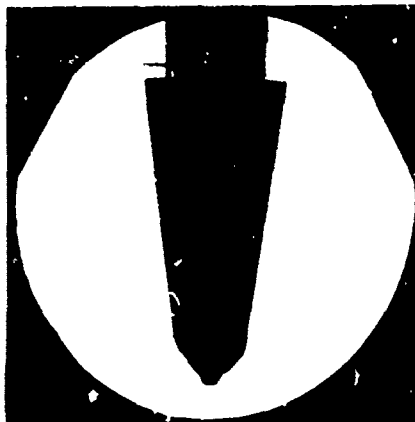
^bApproximate time only; film data incomplete



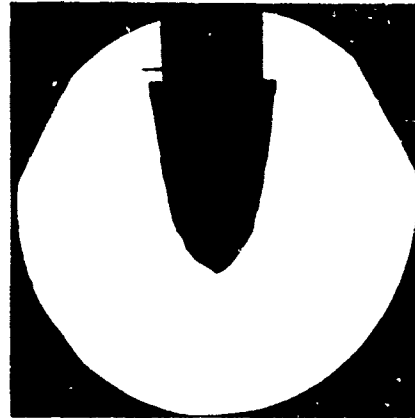
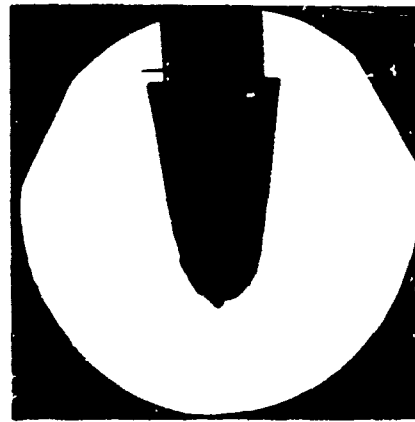
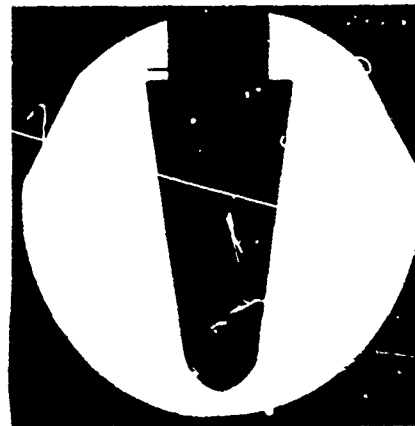
Run 801
1.5-inch R_N Sphere-Cone
 $Re_\infty = 3.44 \times 10^6$ /ft, $T_0 = 953^\circ\text{F}$



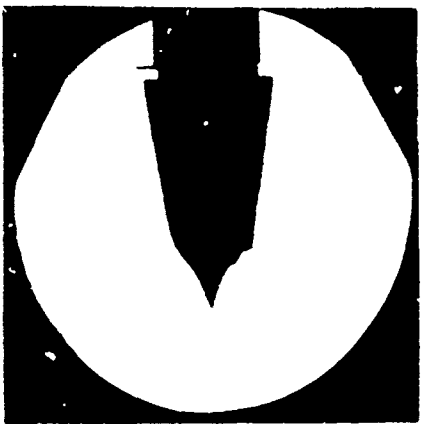
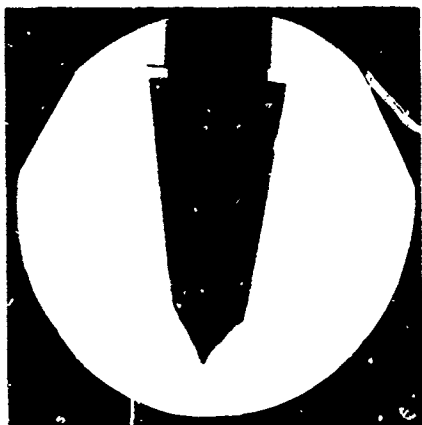
Run 802
1.5-inch R_N Sphere-Cone
 $Re_\infty = 4.09 \times 10^6$ /ft, $T_0 = 970^\circ\text{F}$



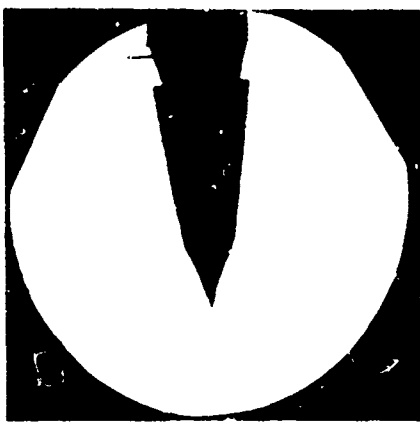
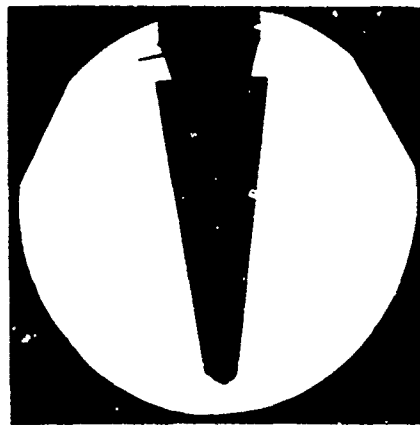
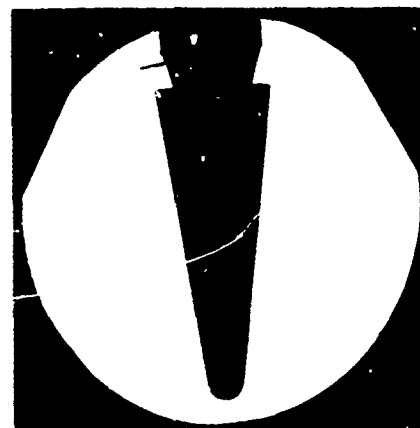
Run 803
1.5-inch RN Sphere-Cone
 $Re_{\infty} = 6.54 \times 10^6 / ft, T_0 = 927^{\circ}F$



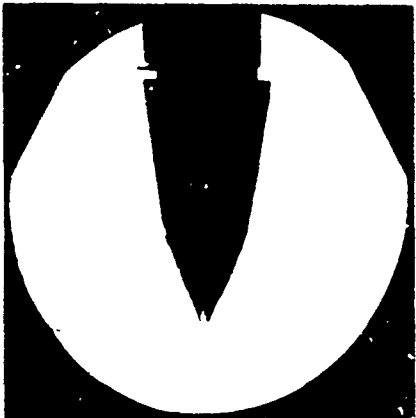
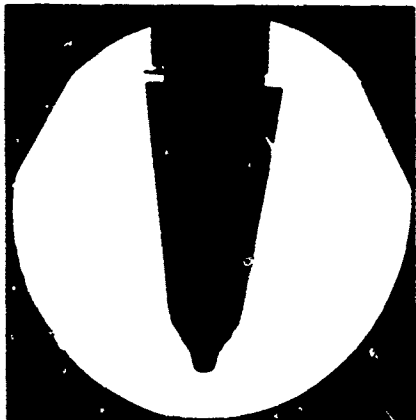
Run 804
1.5-inch RN Sphere-Cone, Particle-Loaded
 $Re_{\infty} = 2.51 \times 10^6 / ft, T_0 = 983^{\circ}F$



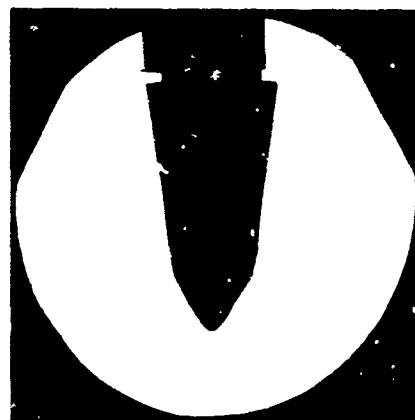
Run 805
1.5-inch R_N Sphere-Cone
 $Re_\infty = 6.56 \times 10^6/\text{ft}$, $T_0 = 987^\circ\text{F}$



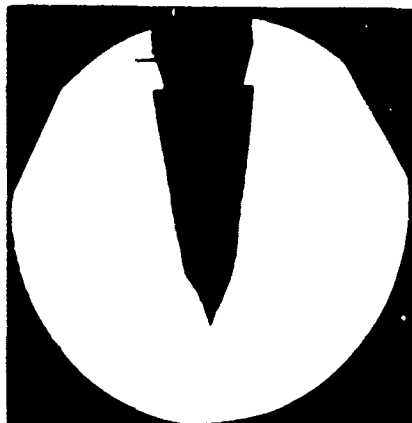
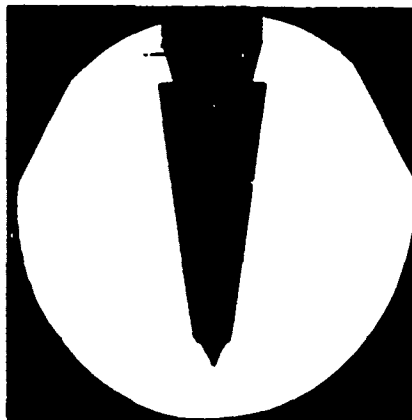
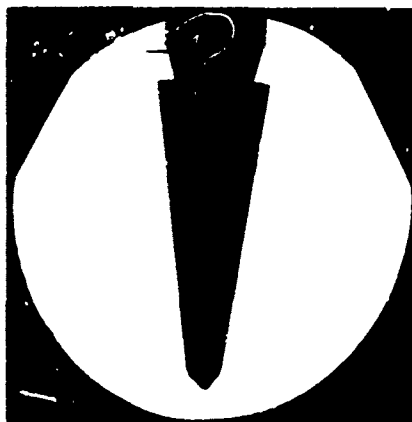
Run 806
0.75-inch R_N Sphere-Cone
 $Re_\infty = 7.36 \times 10^6/\text{ft}$, $T_0 = 921^\circ\text{F}$



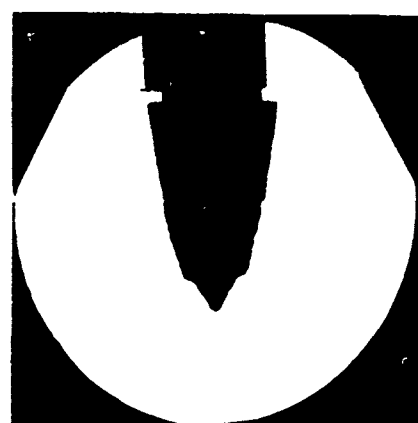
Run 807
1.5-inch R_N Sphere-Cone with Groove
 $Re_\infty = 4.08 \times 10^6/\text{ft}$, $T_o = 1013^\circ\text{F}$



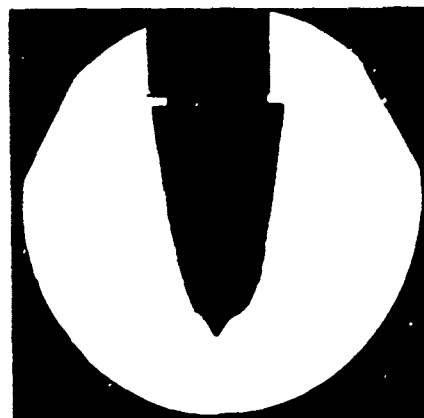
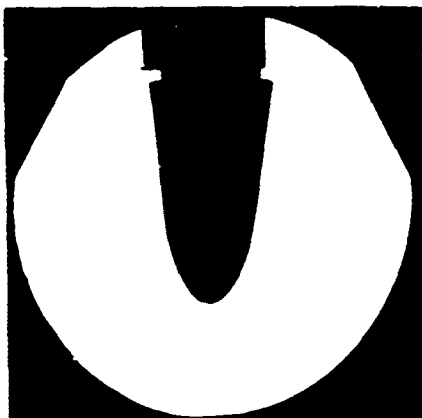
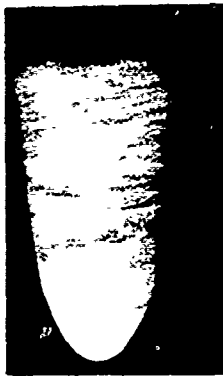
Run 808
1.5-inch R_N Sphere-Cone, Particle-Loaded
 $Re_\infty = 1.50 \times 10^6/\text{ft}$, $T_o = 996^\circ\text{F}$



Run 809
0.75-inch R_N Sphere-Cone
 $Re_\infty = 9.38 \times 10^6 / \text{ft}$, $T_0 = 971^\circ\text{F}$

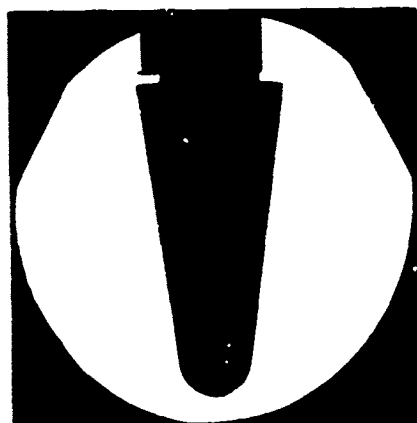
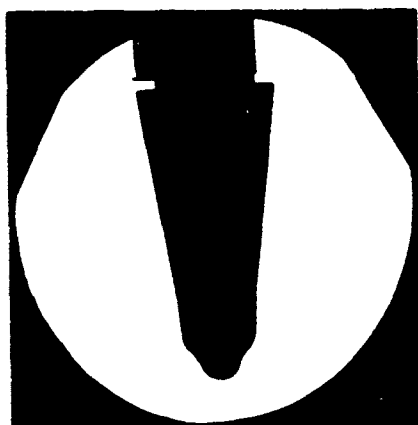
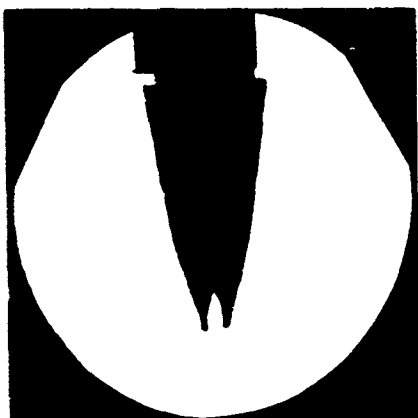


Run 810
1.5-inch $R_S / 60^\circ / 8^\circ$ Biconic
 $Re_\infty = 6.73 \times 10^6 / \text{ft}$, $T_0 = 964^\circ\text{F}$

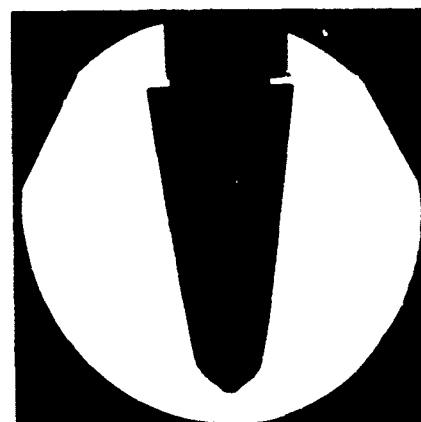


Run 811
1.5-inch Ry Sphere-Cone, Particle-Loaded
 $Re_{\infty} = 0.77/1.12 \times 10^6/\text{ft}$, $T_0 = 972^\circ\text{F}$

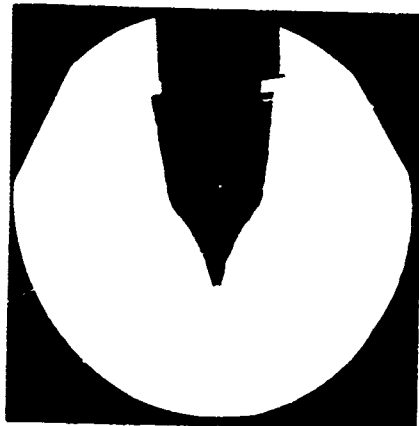
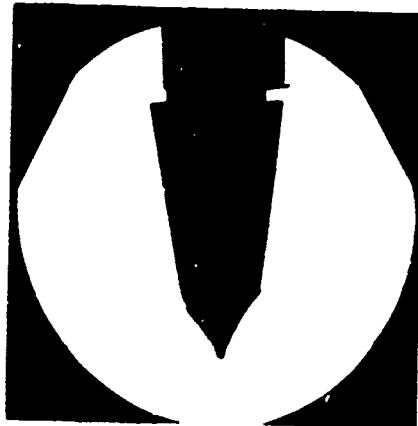
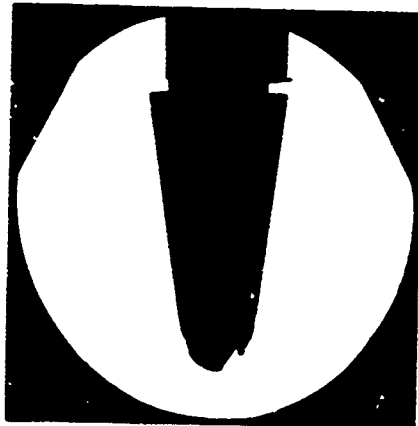
Run 813
1.5-inch $R_s/75^\circ/8^\circ$ Biconic
 $Re_{\infty} = 6.70 \times 10^6/\text{ft}$, $T_0 = 970^\circ\text{F}$



Run 814
1.5-inch R_N Sphere-Cone with Grooves
 $Re_\infty = 4.15 \times 10^5/\text{ft}$, $T_0 = 998^\circ\text{F}$



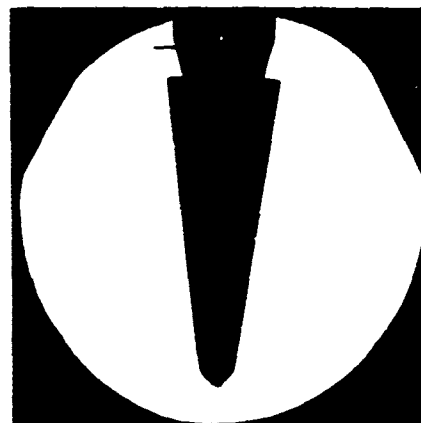
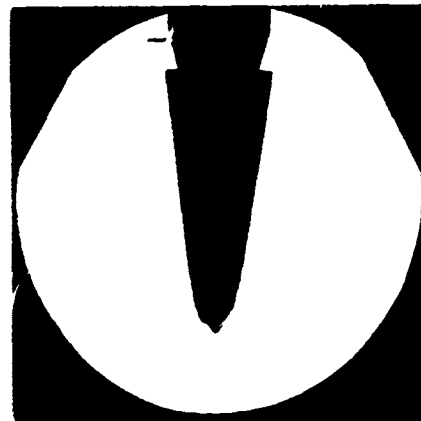
Run 815
1.5-inch R_S Laminar-Blunt
 $Re_\infty = 6.72 \times 10^6/\text{ft}$, $T_0 = 944^\circ\text{F}$



Run 816
1.5-inch $R_S/60^\circ/8^\circ$ Biconic
 $Re_\infty = 5.20 \times 10^6/\text{ft}$, $T_0 = 954^\circ\text{F}$

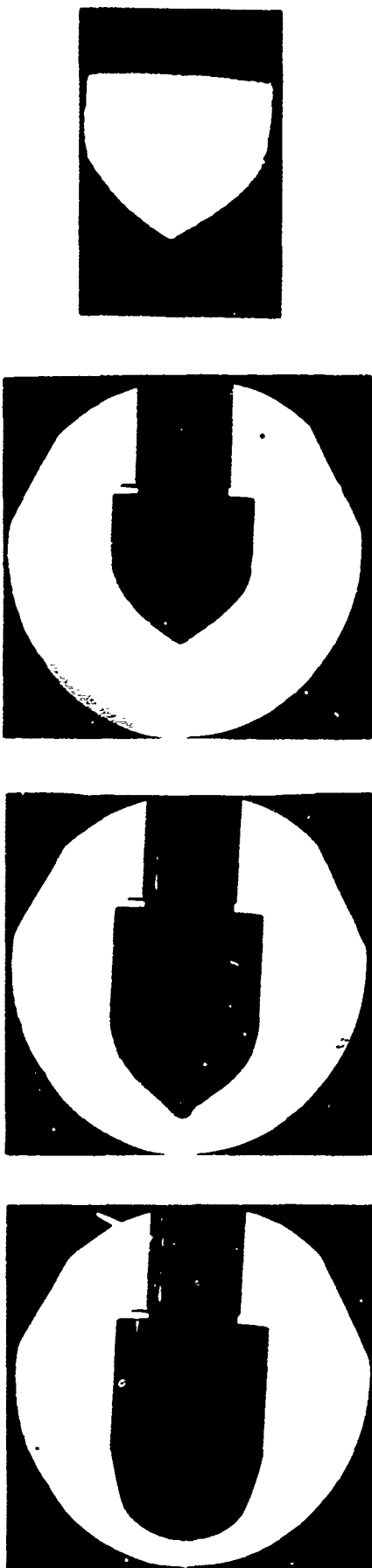


Run 817
1.5-inch R_N Sphere-Cone
 $Re_\infty = 6.52 \times 10^6/\text{ft}$, $T_0 = 493^\circ\text{F}$

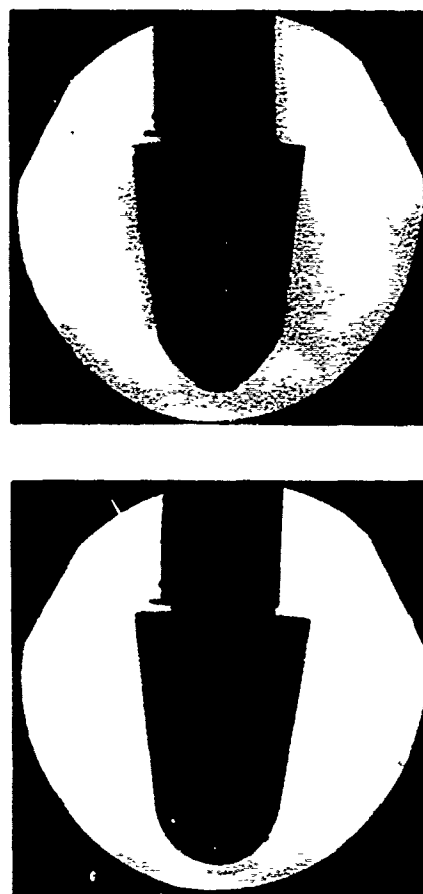


Run 818
1.5-inch R_N Sphere-Cone
 $Re_\infty = 9.56 \times 10^6/\text{ft}$, $T_0 = 508^\circ\text{F}$

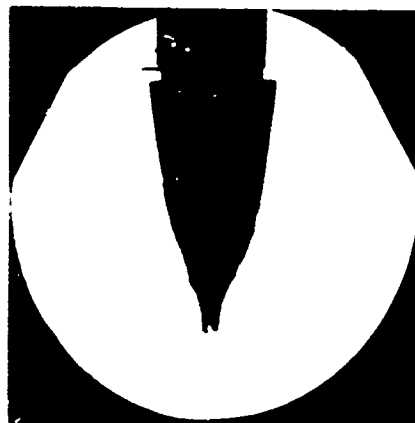
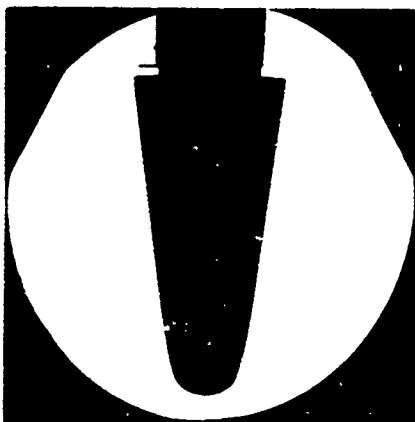
Run 819
0.75-inch R_N Sphere-Cone
 $Re_\infty = 5.69/12.96 \times 10^6/\text{ft}$, $T_0 = 812/804^\circ\text{F}$



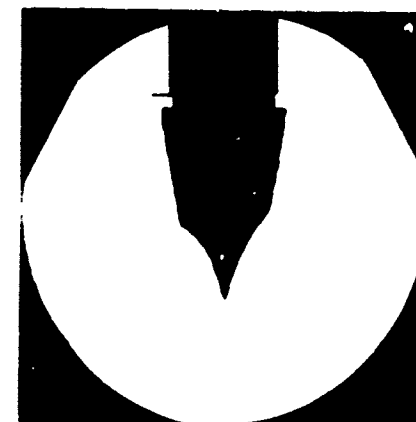
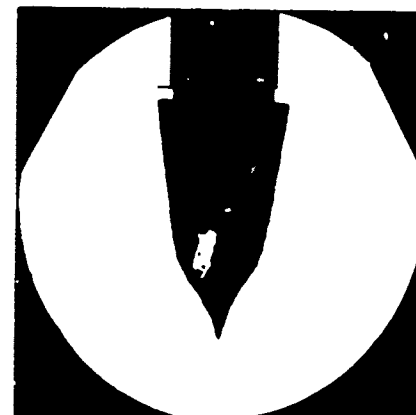
Run 820
3.5-inch R_5 Laminar-Blunt
 $Re_\infty = 4.90 \times 10^6/\text{ft}$, $T_0 = 986^\circ\text{F}$



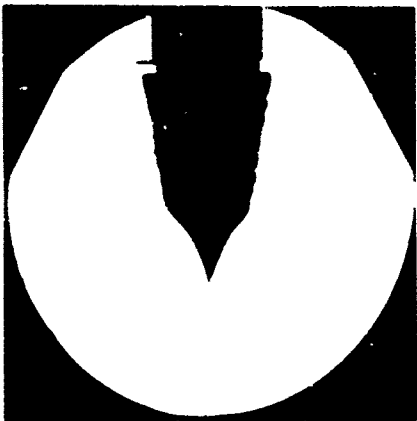
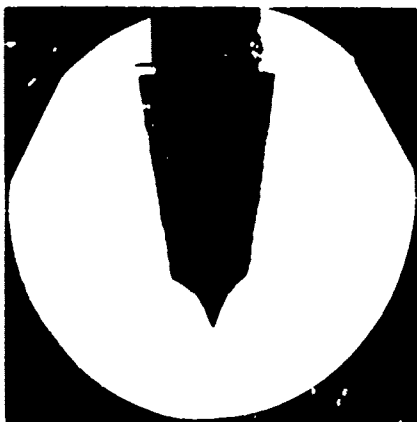
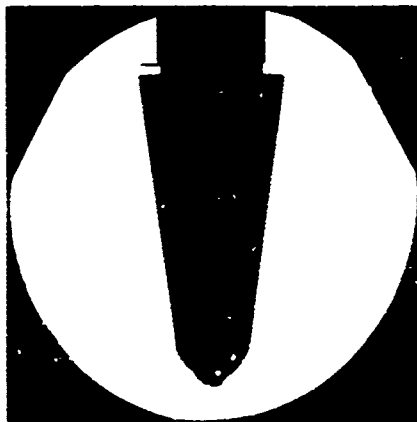
Run 821
2.5-inch R_N Sphere-Cone
 $Re_\infty = 7.47 \times 10^6/\text{ft}$, $T_0 = 973^\circ\text{F}$



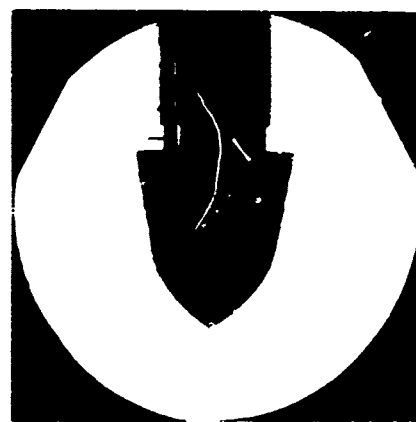
Run 822
1.5-inch, R_s Laminar-Blunt
 $Re_{\infty} = 4.02 \times 10^6/\text{ft}$, $T_o = 960^\circ\text{F}$



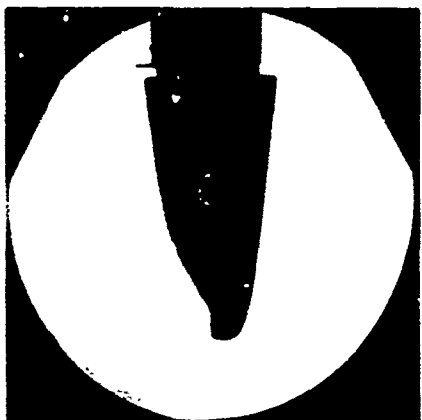
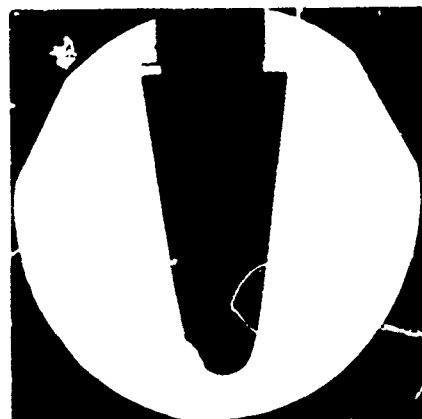
Run 823
1.5-inch $R_s/75^\circ/8^\circ$ Biconic
 $Re_{\infty} = 5.18 \times 10^6/\text{ft}$, $T_o = 986^\circ\text{F}$



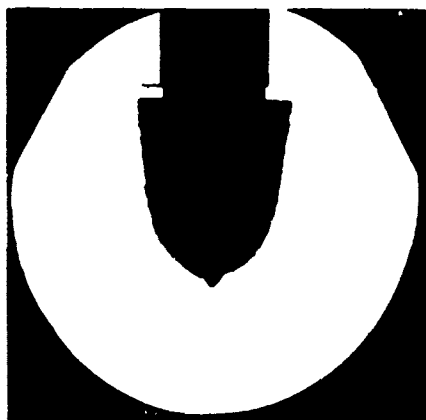
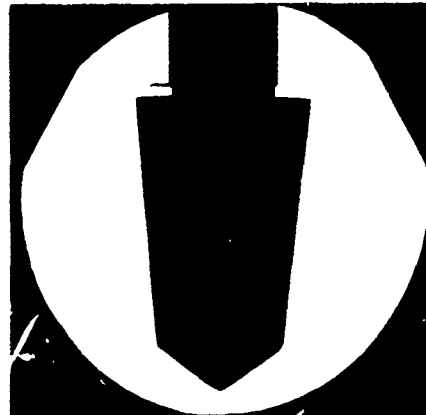
Run 824
1.5-inch RN Sphere-Cone
 $Re_m = 9.44 \times 10^6$ /ft, $T_o = 535^\circ\text{F}$



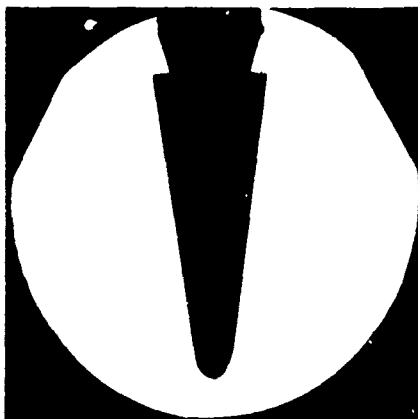
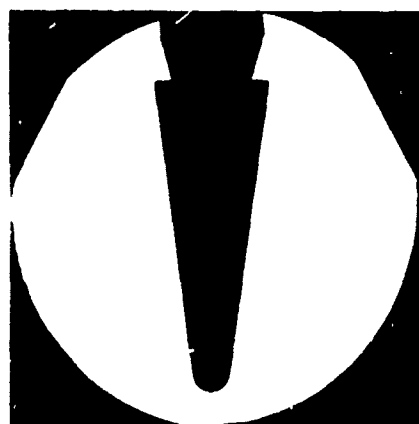
Run 825
2.5-inch RN Sphere-Cone
 $Re_\infty = 7.20 \times 10^6$ /ft, $T_o = 990^\circ\text{F}$



Run 826
1.5-inch R_s Laminar-Blunt
 $Re_\infty = 3.41 \times 10^6/\text{ft}$, $T_o = 987^\circ\text{F}$



Run 827
2.5-inch $R_s/55^\circ/6^\circ$ Biconic
 $Re_\infty = 4.76 \times 10^6/\text{ft}$, $T_o = 1008^\circ\text{F}$



Run 828
0.75-inch R_N Sphere-Cone
Variable Re_∞

Run 829
0.75-inch R_N Sphere-Cone
Variable Re_∞



Run 830
3.5-inch R_s Laminar-Blunt
 $Re_\infty = 3.47 \times 10^6/\text{ft}$, $T_0 = 985^\circ\text{F}$

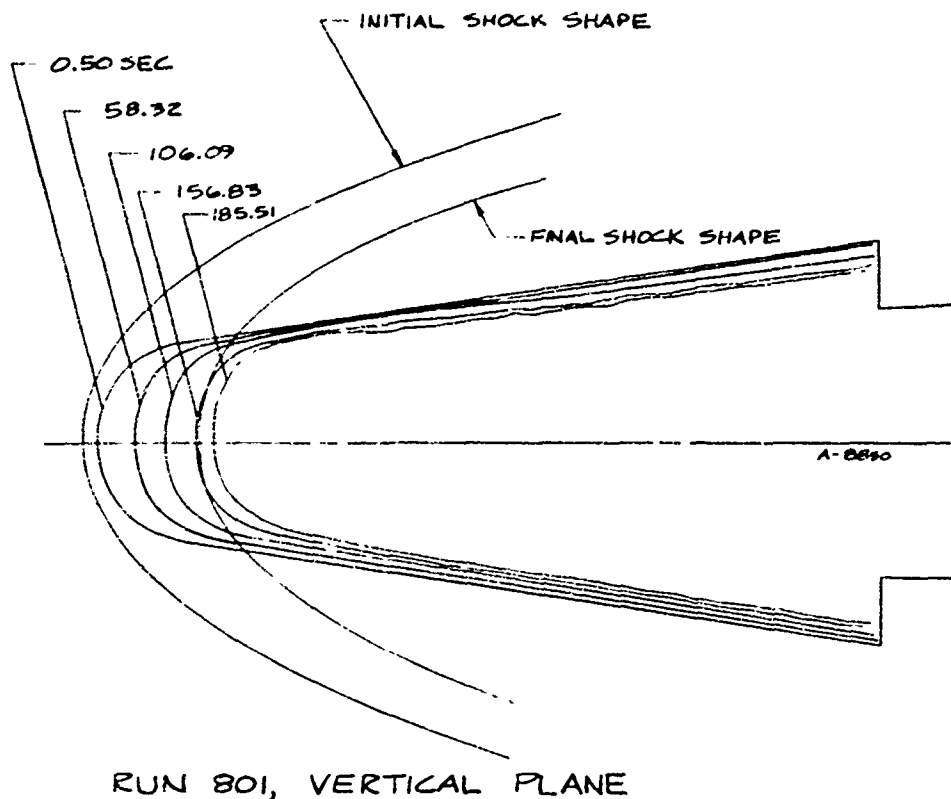


Run 831
3.5-inch R_s Laminar-Blunt
 $Re_\infty = 2.52 \times 10^6/\text{ft}$, $T_0 = 998^\circ\text{F}$

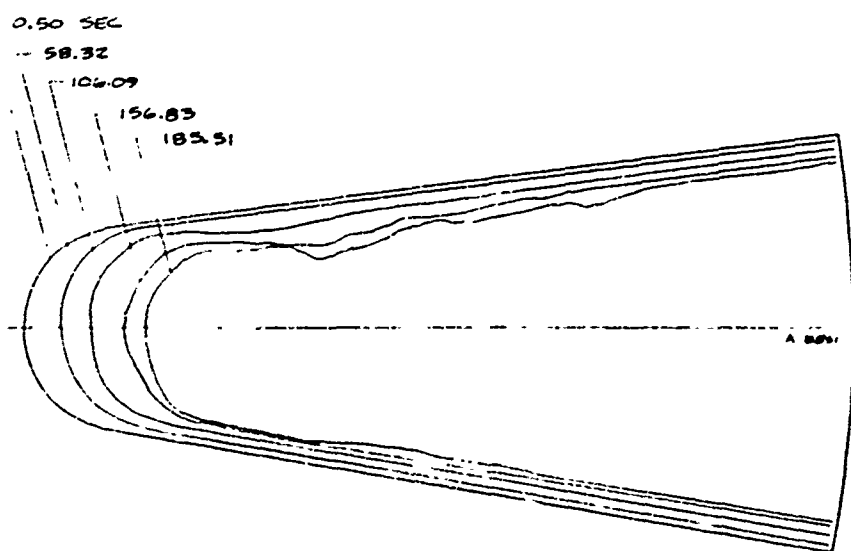
APPENDIX B

SHAPE PROFILE HISTORIES

RUNS 801-831

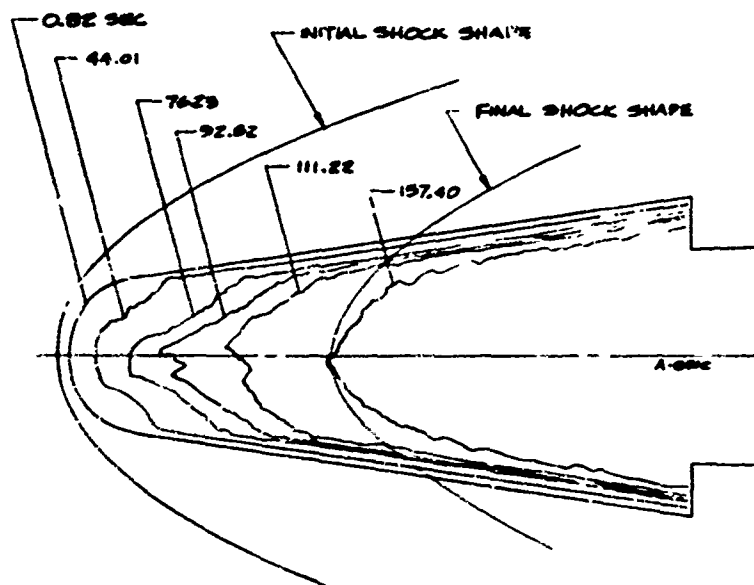


RUN 801, VERTICAL PLANE

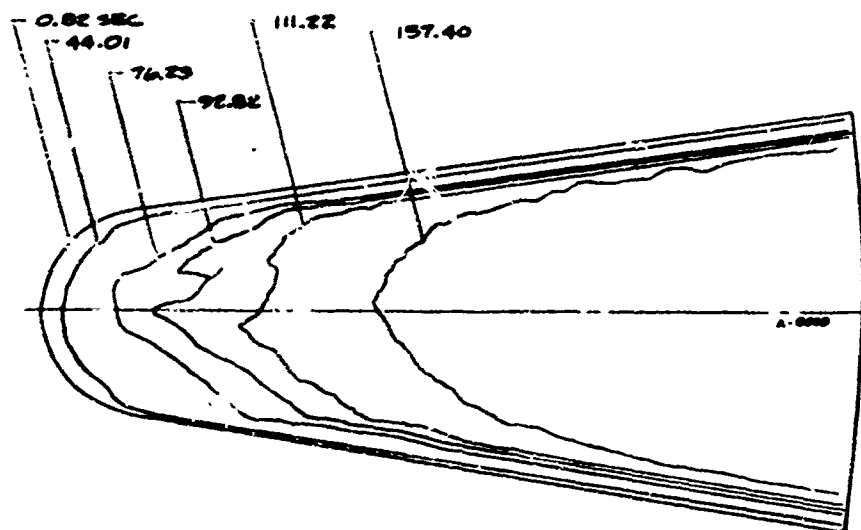


RUN 801, HORIZONTAL PLANE

Figure B-1. Shape Profile History for Run 801 (1.5-Inch R_N Sphere-Cone;
 $Re_\infty = 3.44 \times 10^6/\text{ft}$; $T_0 = 953^\circ\text{F}$)

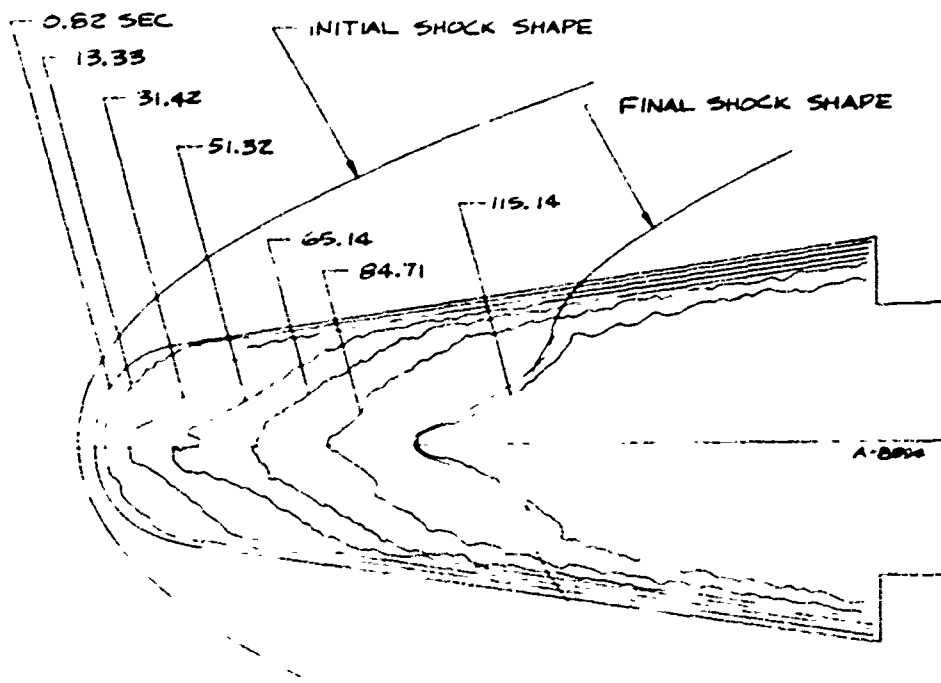


RUN 802, VERTICAL PLANE

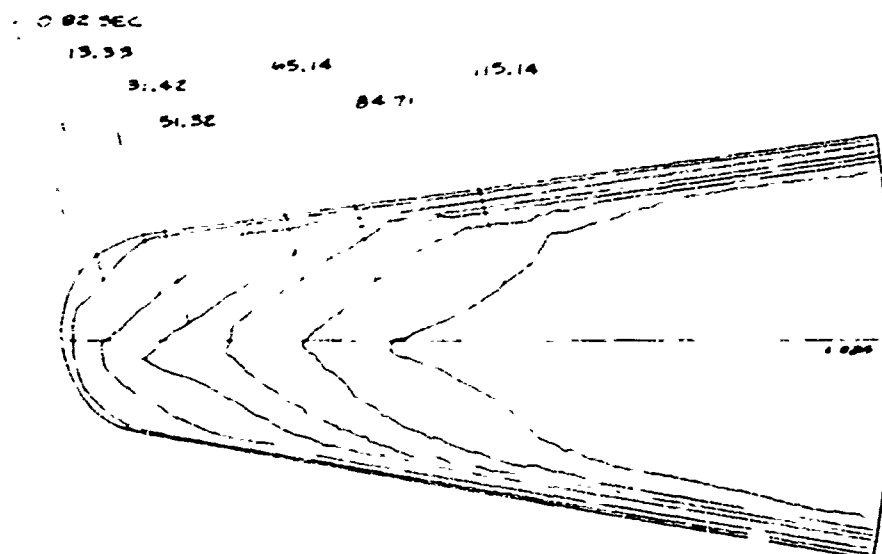


RUN 802, HORIZONTAL PLANE

Figure B-2. Shape Profile History for Run 802 (1.5-Inch R_1 Sphere-Cone; $Re_\infty = 4.09 \times 10^5/\text{ft}$; $T_0 = 970^\circ\text{F}$)

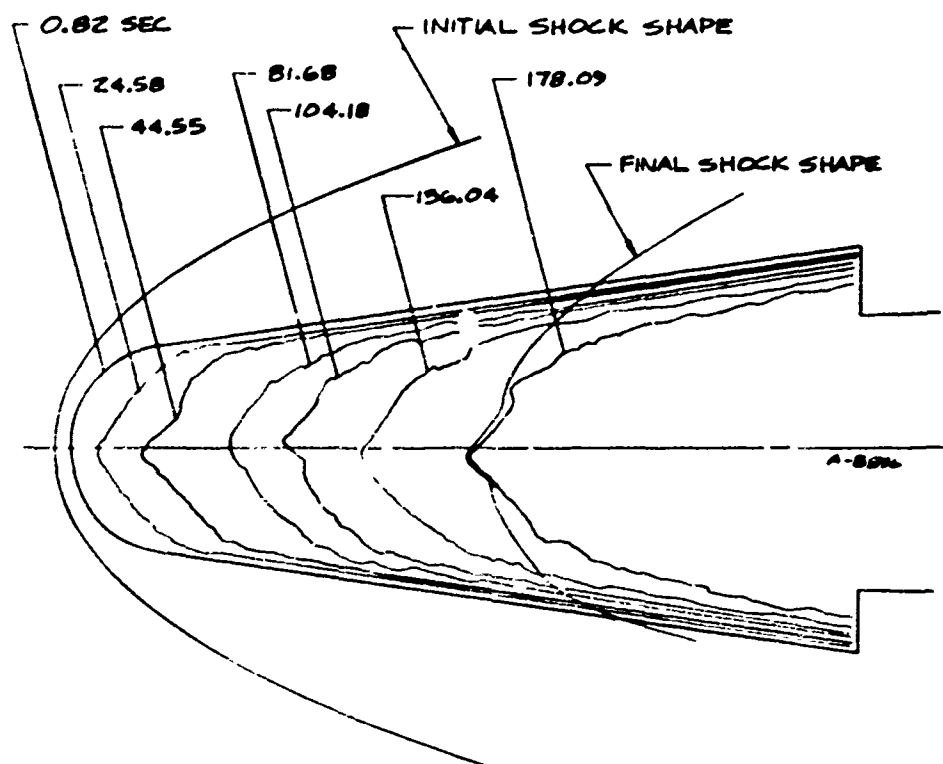


RUN 803, VERTICAL PLANE

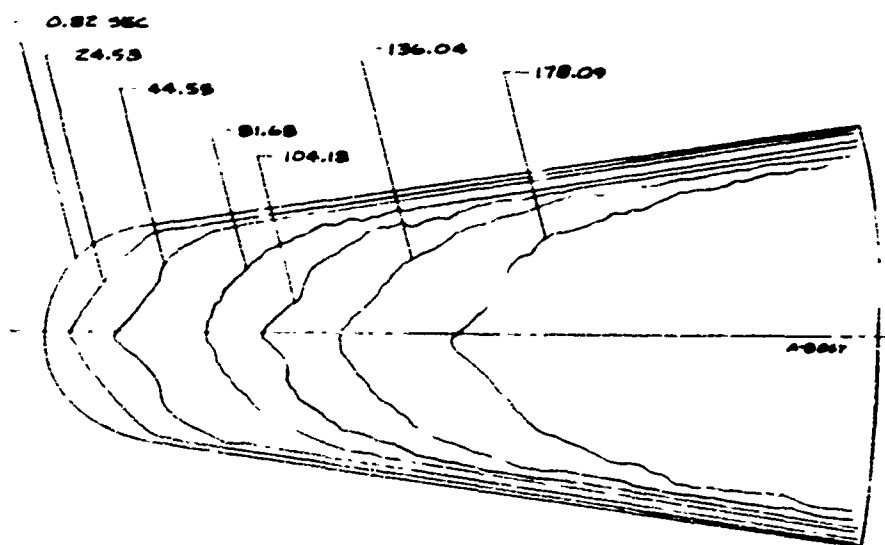


RUN 803, HORIZONTAL PLANE

Figure B-3. Shape Profile History for Run 803 (1.5-Inch R_N Sphere-Cone;
 $Re_\infty = 6.54 \times 10^6/\text{ft}$; $T_0 = 927^\circ\text{F}$)

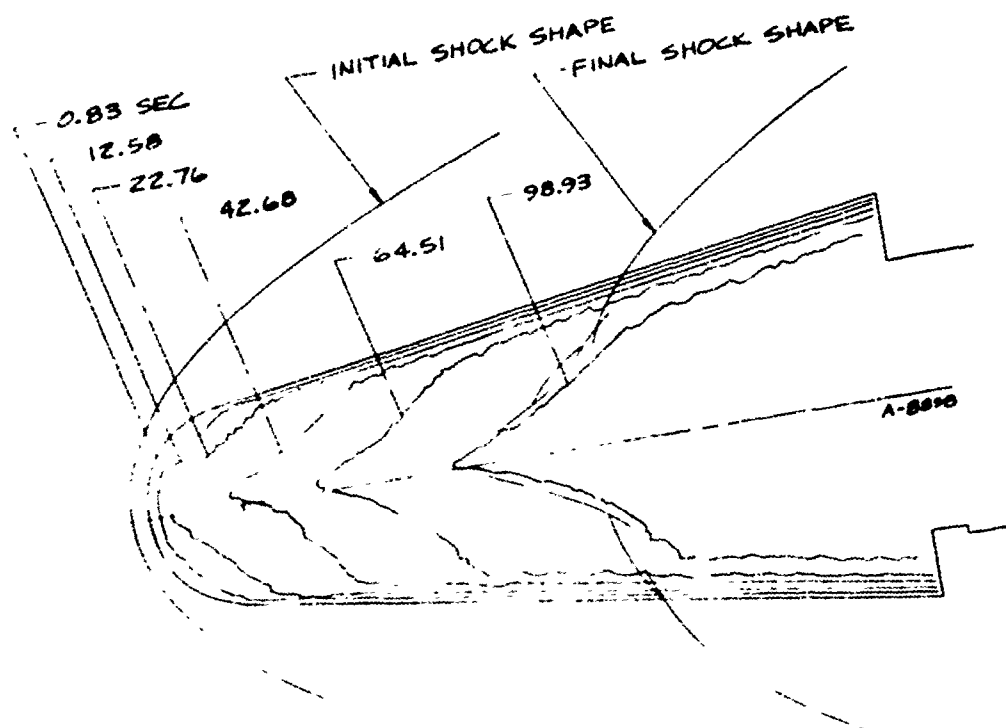


RUN 804, VERTICAL PLANE

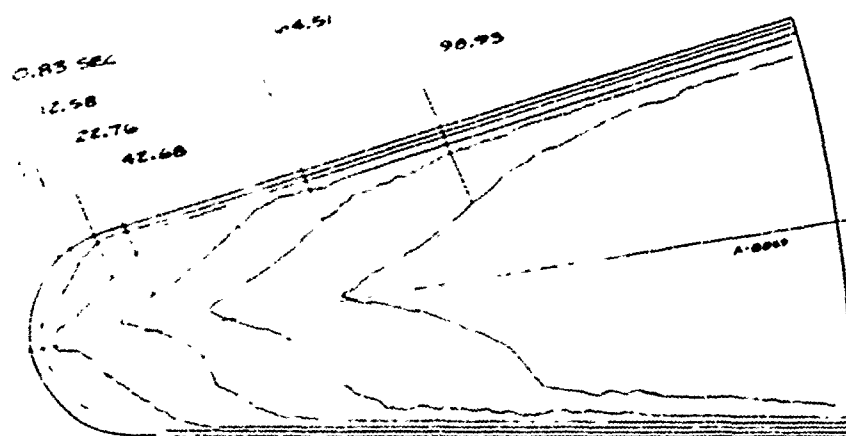


RUN 804, HORIZONTAL PLANE

Figure B-4. Shape Profile History for Run 804 (1.5-Inch R_N Sphere-Cone, Particle-Loaded; $Re_\infty = 2.51 \times 10^6/\text{ft}$; $T_0 = 983^\circ\text{F}$)

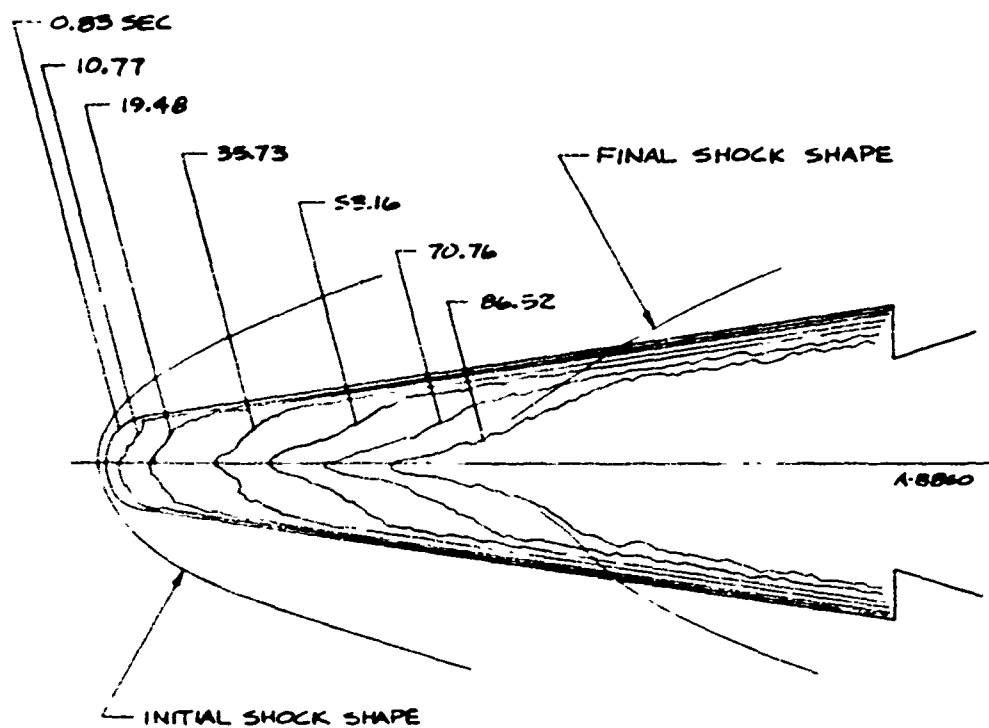


RUN 805, VERTICAL PLANE

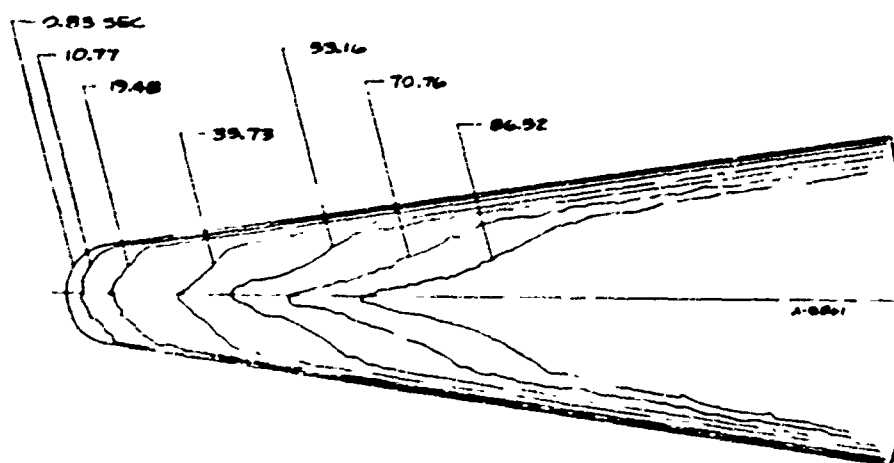


RUN 805, HORIZONTAL PLANE

Figure D-5. Shape Profile History for run 805 (1.5-Inch R_N Sphere-Cone;
 $Re_\infty = 6.56 \times 10^6/\text{ft}$; $T_0 = 987^\circ\text{F}$)

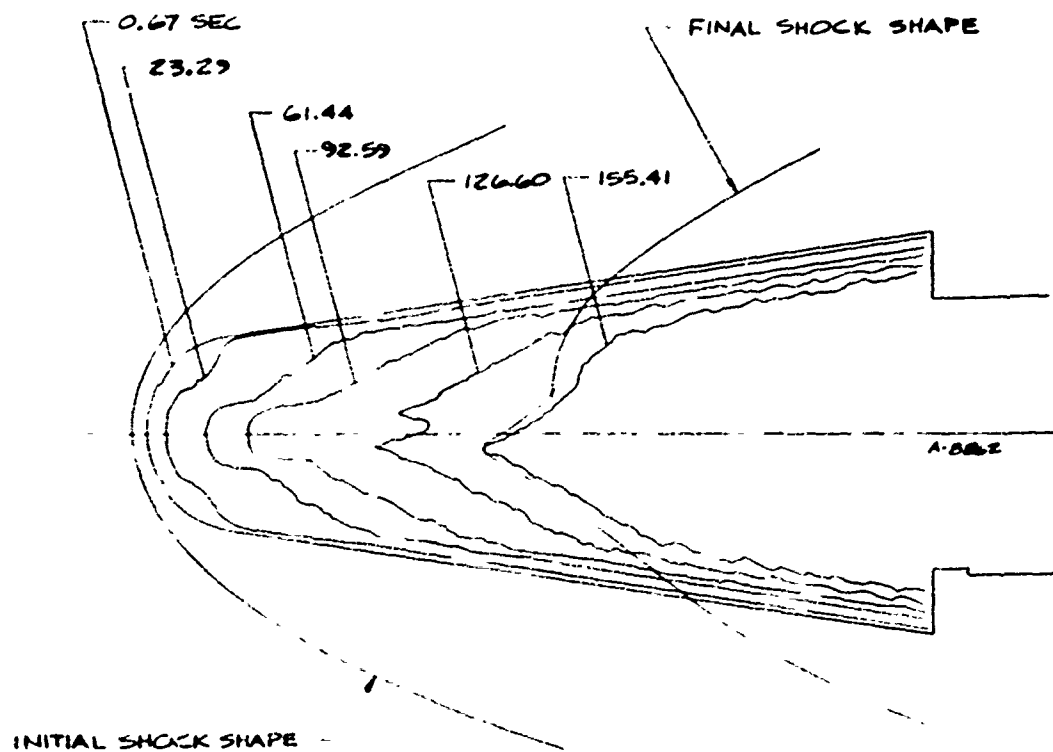


RUN 806, VERTICAL PLANE

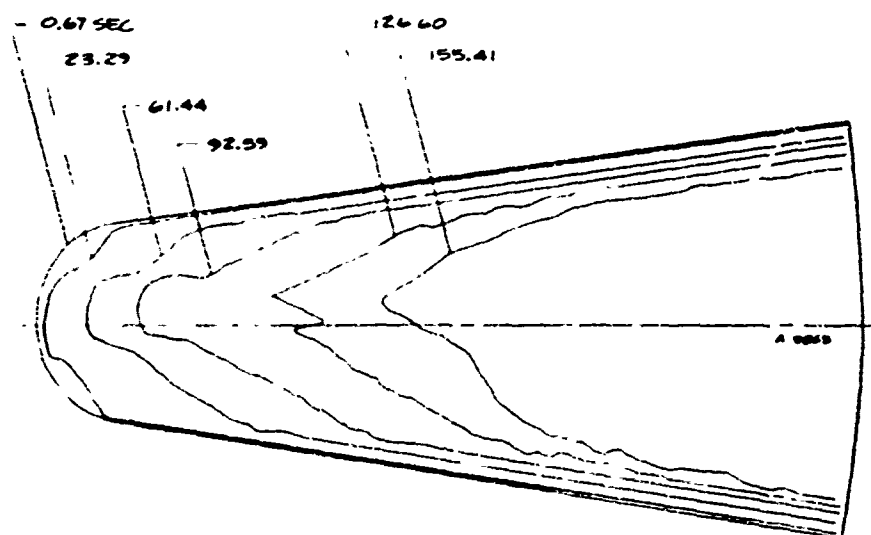


RUN 806, HORIZONTAL PLANE

Figure 8-6. Shape Profile History for Run 806 (0.75-Inch R_H Sphere-Cone;
 $Re_m = 7.36 \times 10^6/\text{ft}$; $T_0 = 921^\circ\text{F}$)

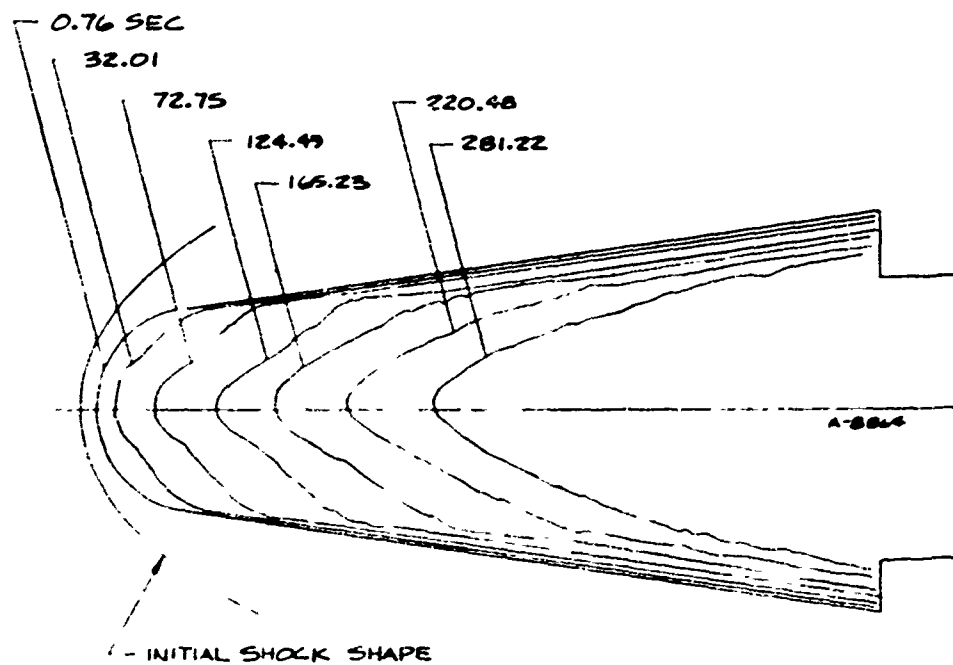


RUN 807, VERTICAL PLANE

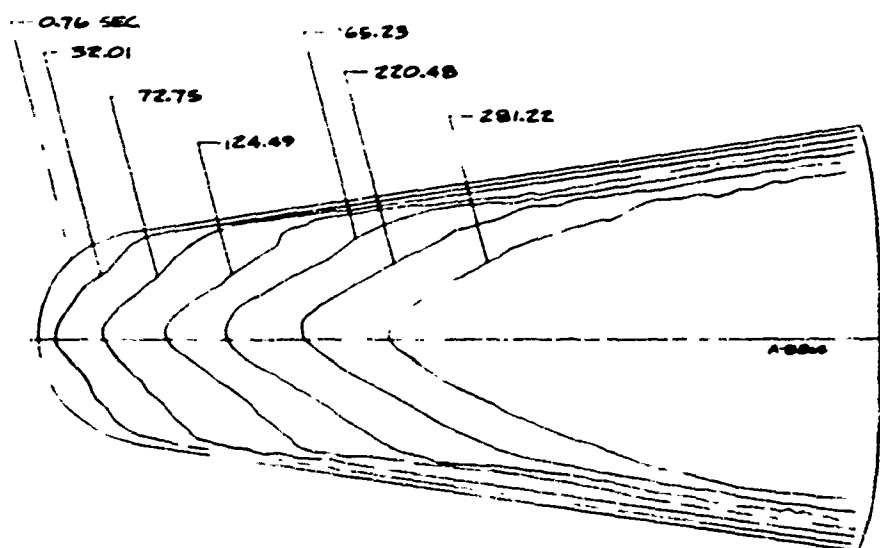


RUN 807, HORIZONTAL PLANE

Figure B-7. Shape Profile History for Run 807 (1.5-inch R_N Sphere-Cone with Groove; $Re_\infty = 4.08 \times 10^6/\text{ft}$; $T_0 = 1013^\circ\text{F}$)

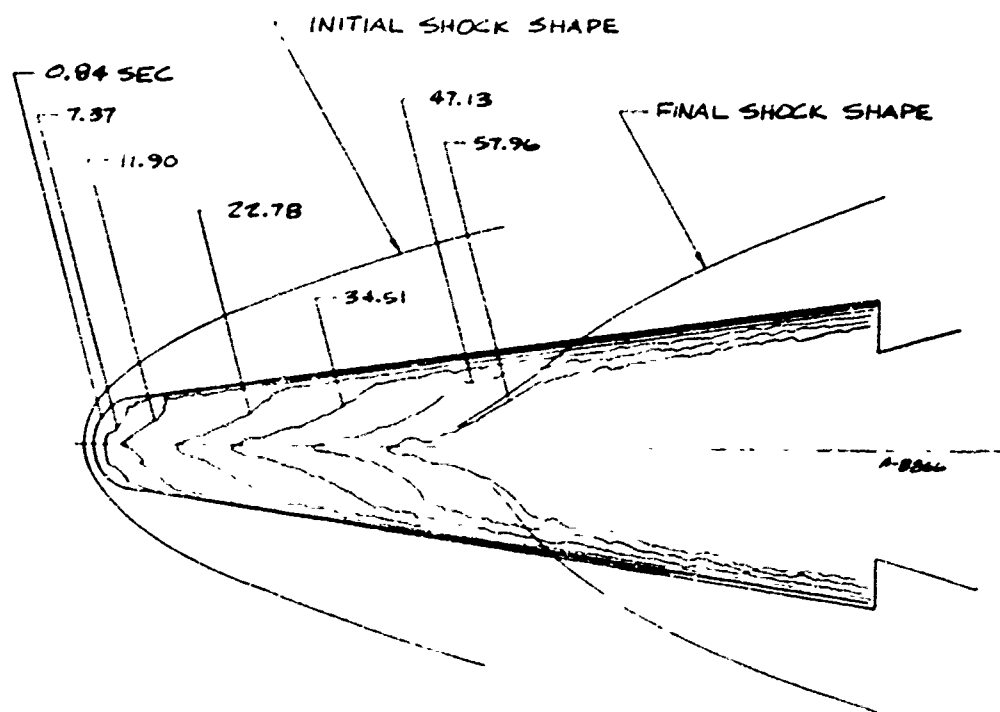


RUN 808, VERTICAL PLANE

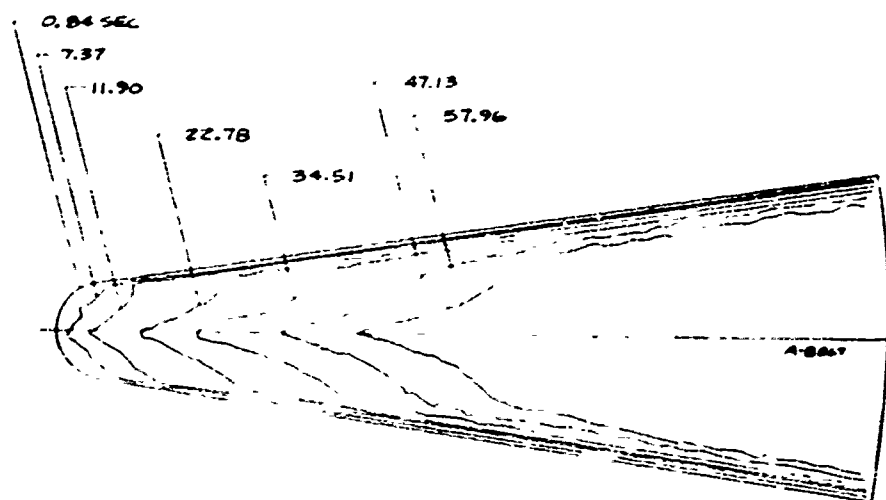


RUN 808, HORIZONTAL PLANE

Figure B-3. Shape Profile History for Run 808 (1.5-Inch R_N Sphere-Cone, Particle-Loaded; $Re_\infty = 1.50 \times 10^6/\text{ft}$; $T_0 = 996^\circ\text{F}$)

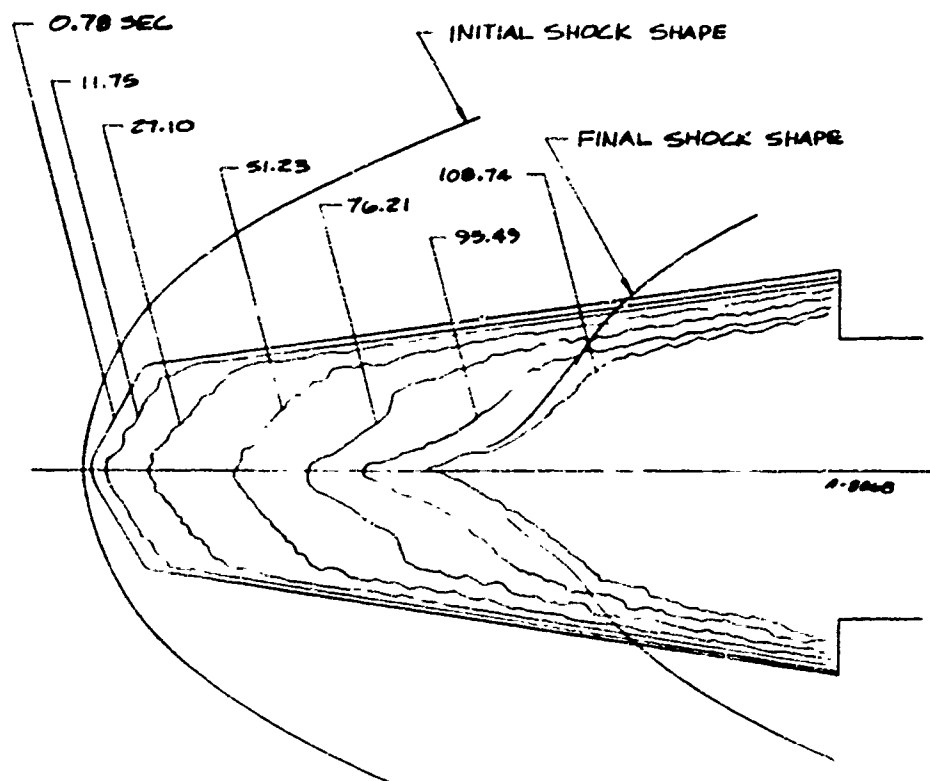


RUN 809, VERTICAL PLANE

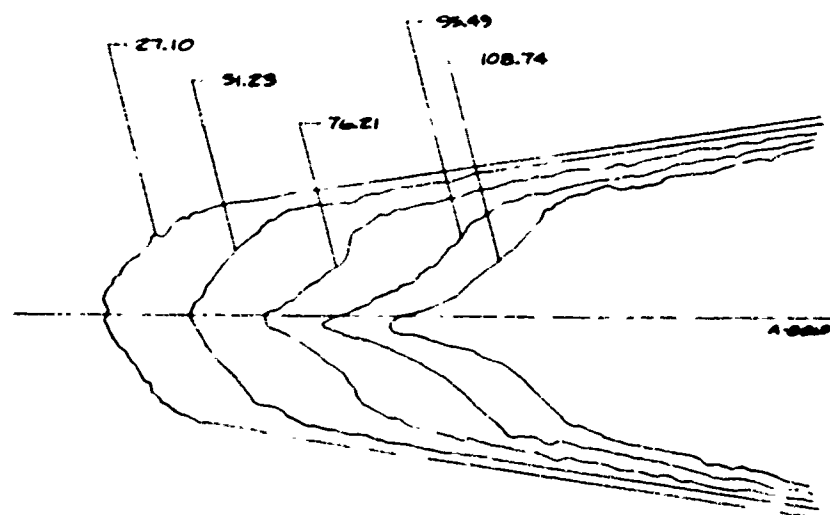


RUN 809, HORIZONTAL PLANE

Figure B-9. Shape Profile History for Run 809 (0.75-Inch R_N Sphere-Cone; $Re_{\infty} = 9.38 \times 10^4/\text{ft}$; $T_0 = 971^\circ\text{F}$)

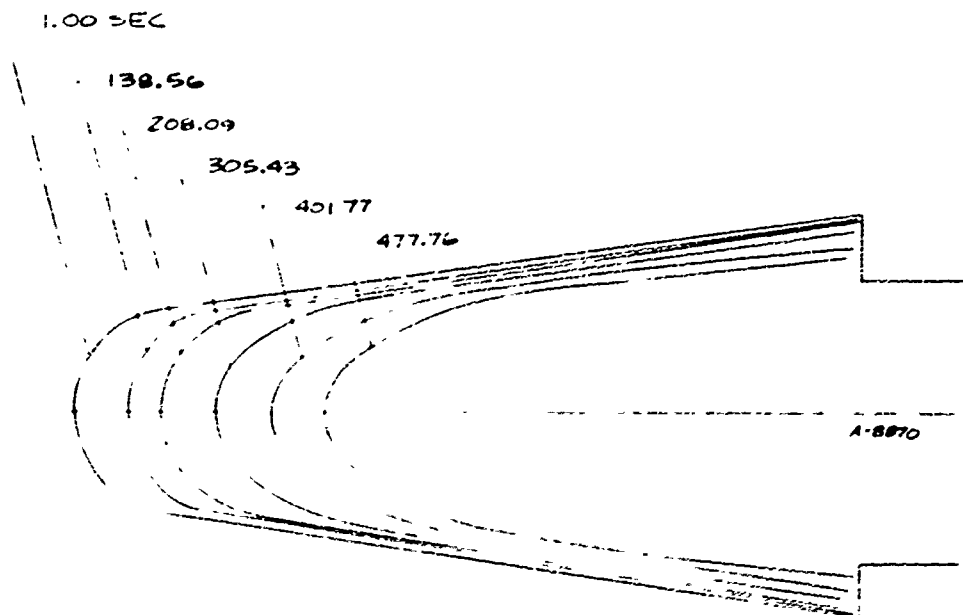


RUN 810, VERTICAL PLANE

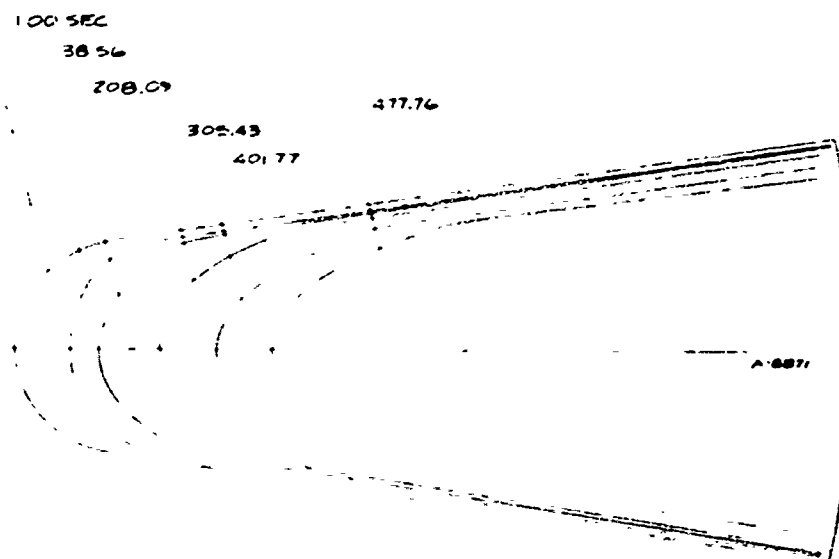


RUN 810, HORIZONTAL PLANE

Figure B-10. Shape Profile History for Run 810 (1.5-Inch $R_s/60^\circ/8^\circ$ Biconic;
 $Re_w = 6.73 \times 10^6/\text{ft}$; $T_0 = 964^\circ\text{F}$)

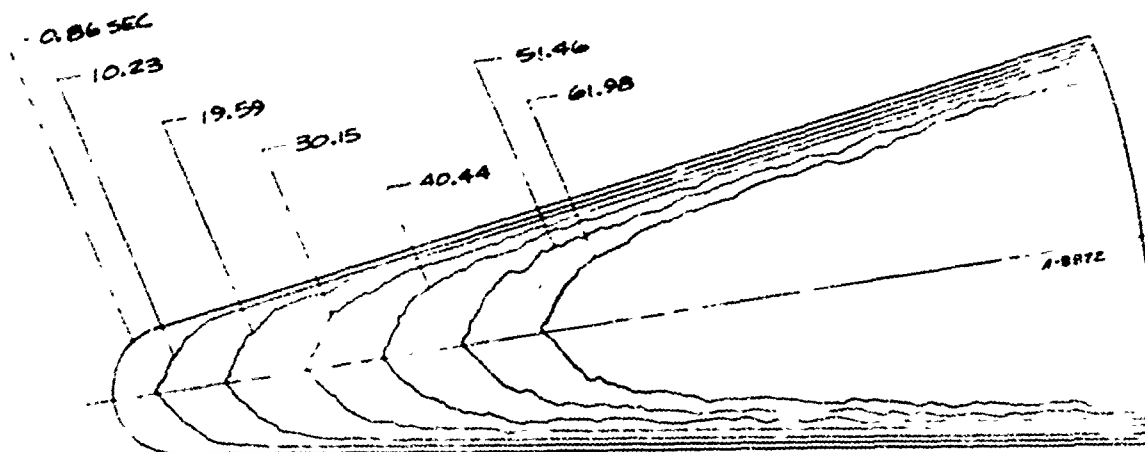


RUN 811, VERTICAL PLANE



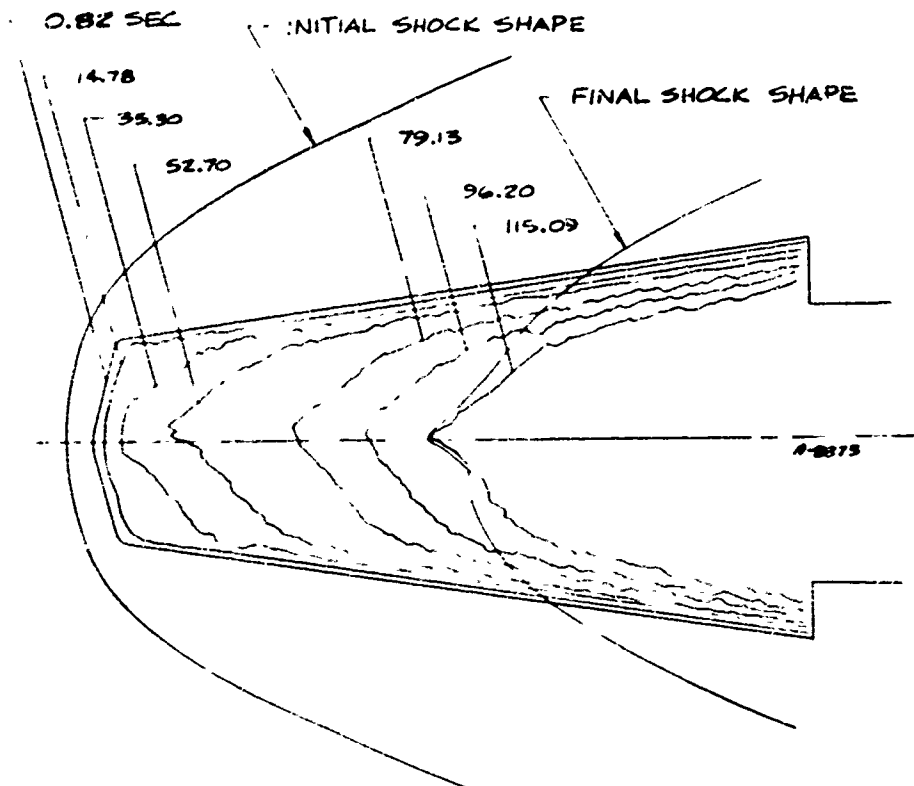
RUN 811 HORIZONTAL PLANE

Figure B-11. Shape Profile History for Run 811 (1.5-inch R_N Sphere-Cone, Particle-Loaded, $Pe_p = 0.77/12 \times 10^6/\text{ft}$, $T_0 = 972^\circ\text{F}$)_N

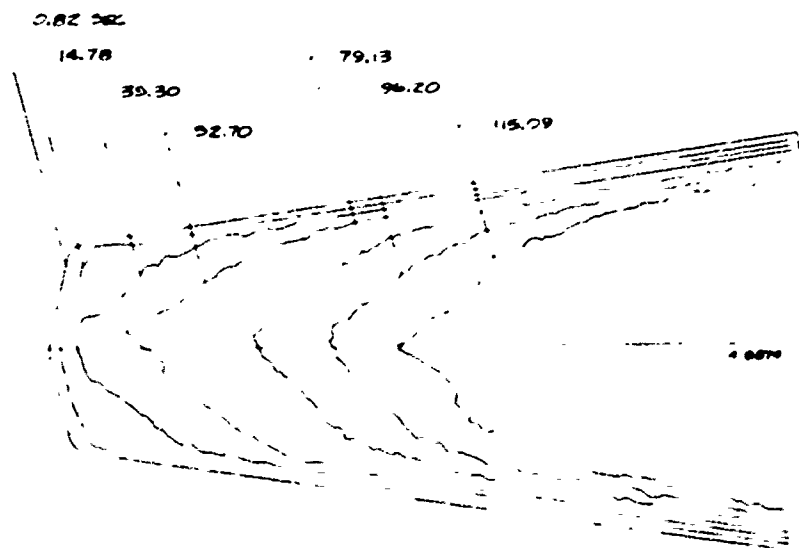


RUN 812, HORIZONTAL PLANE

Figure B-12. Shape Profile History for Run 812 (0.75-Inch R_H Sphere-Cone;
 $Re_\infty = 15.70 \times 10^5/\text{ft}$; $T_0 = 807^\circ\text{F}$)

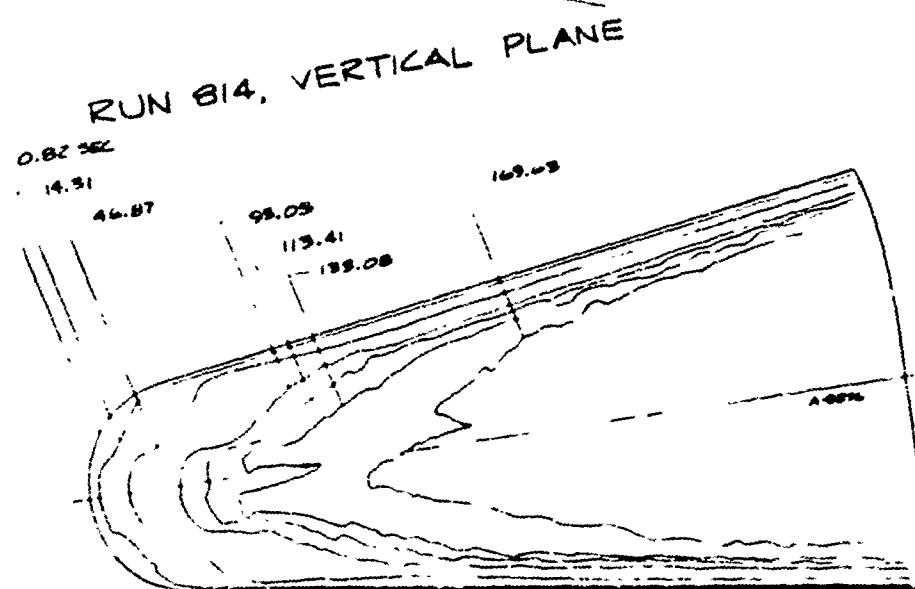
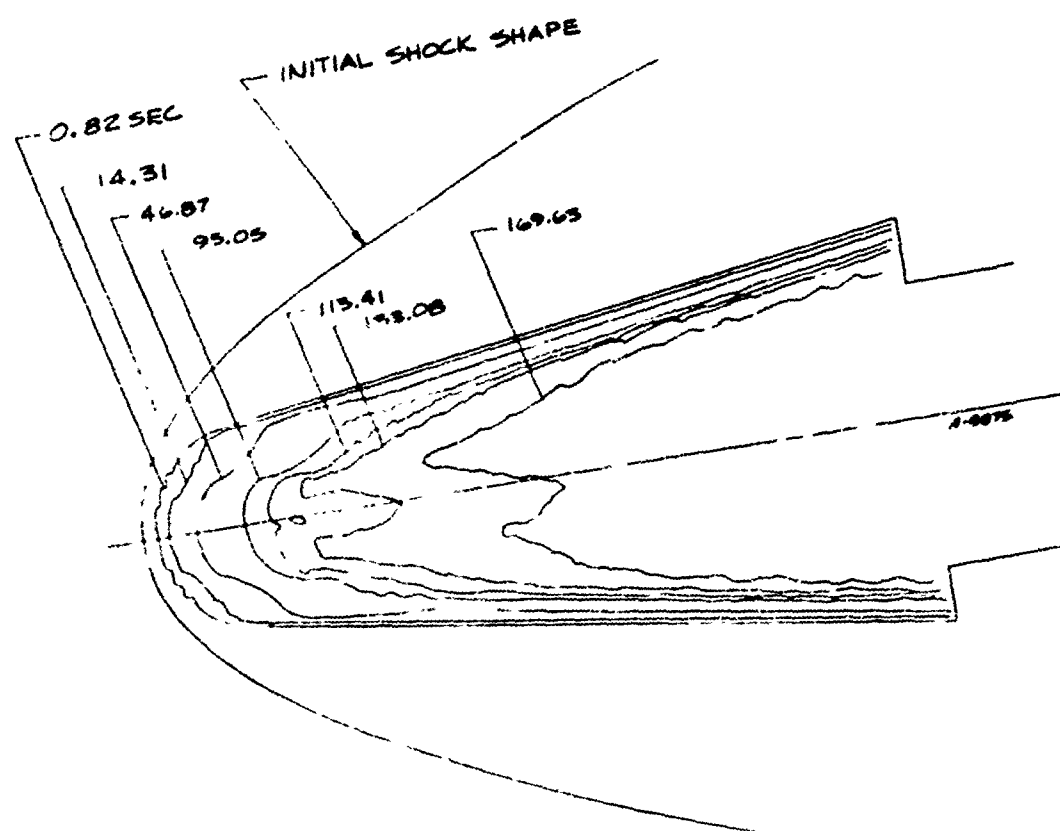


RUN 813, VERTICAL PLANE



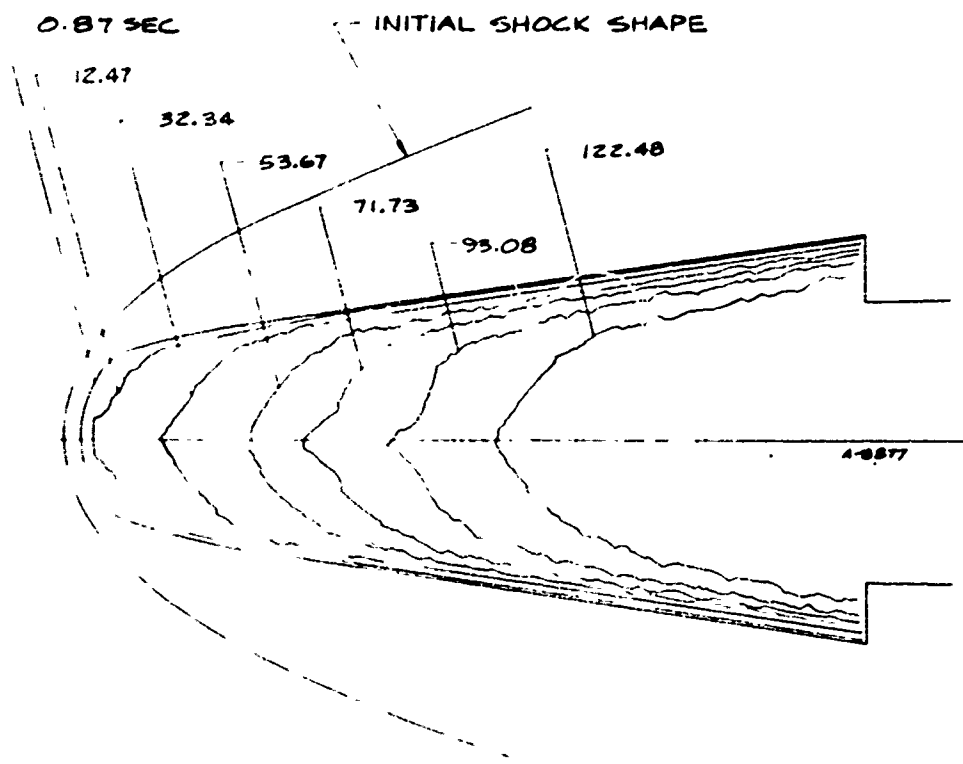
RUN 813, HORIZONTAL PLANE

Figure B-13. Shape Profile History for Run 813 (1.5-Inch $R_5/75^\circ/8^\circ$ Biconic, $Re_\infty = 6.70 \times 10^6/\text{ft}$; $T_0 = 970^\circ\text{F}$)

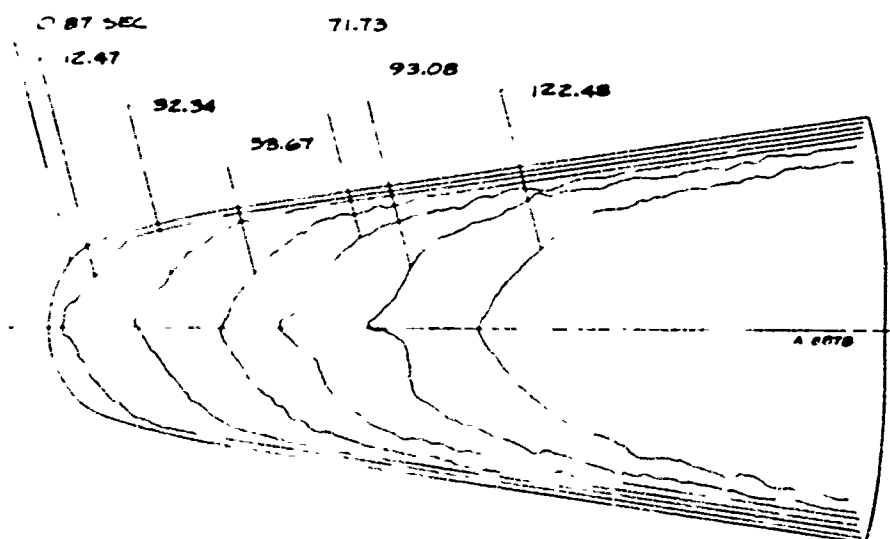


RUN 814, HORIZONTAL PLANE

Figure B-14. Shape Profile History for Run R14 (1.5-Inch R_N Sphere-Cone with Three Grooves; $Re_\infty = 4.15 \times 10^4$ /ft; $T_0 = 998^\circ\text{F}$)

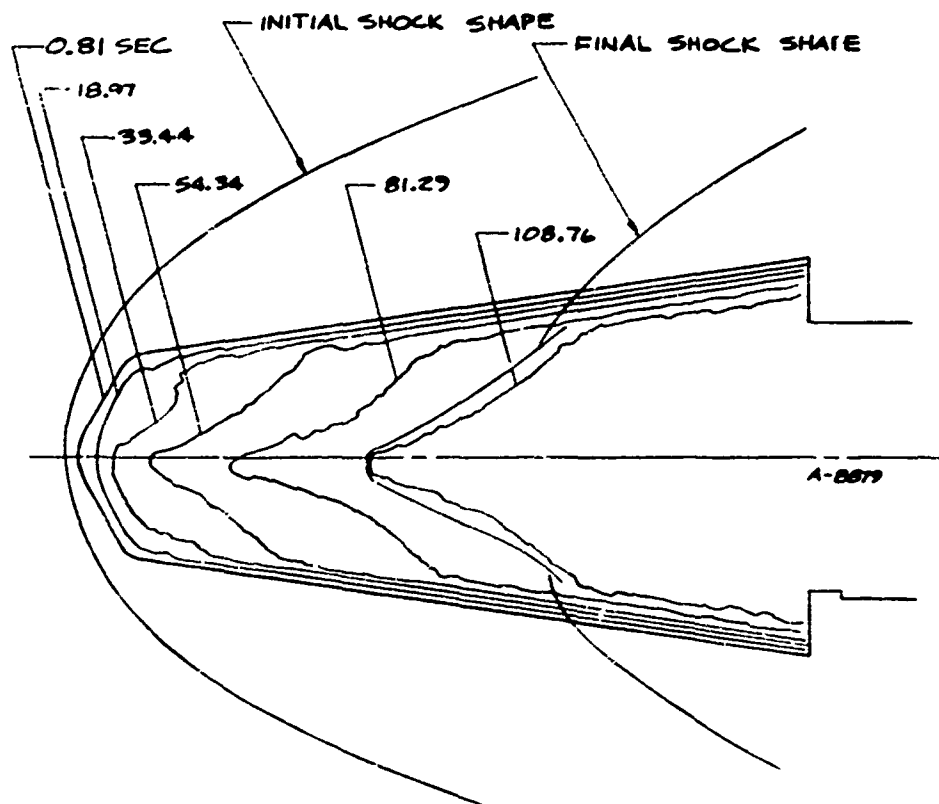


RUN 815, VERTICAL PLANE

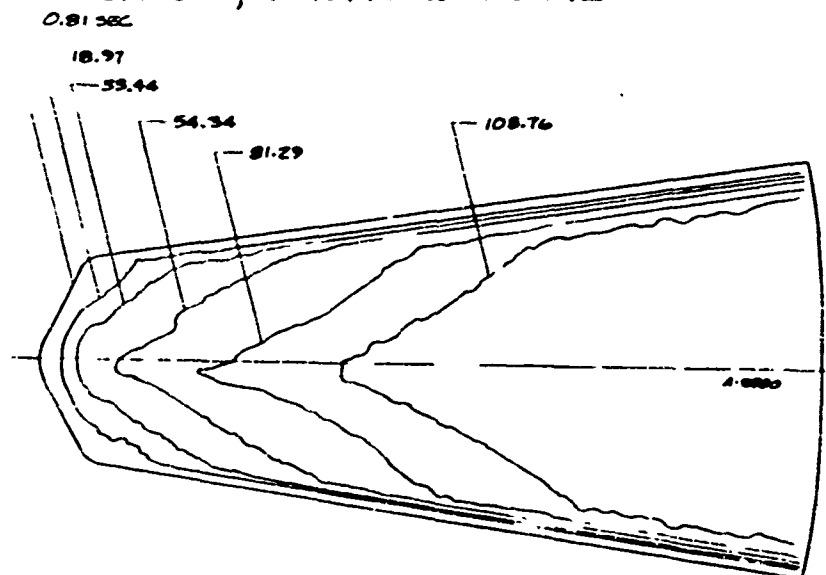


RUN 815, HORIZONTAL PLANE

Figure B-15. Shape Profile History for Run 815 (1.5-Inch R_S Laminar-Blunt; $Re_p = 6.72 \times 10^6/\text{ft}$; $T_0 = 944^\circ\text{F}$)



RUN 816, VERTICAL PLANE



RUN 816, HORIZONTAL PLANE

Figure B-16. Shape Profile History for Run 816 (1.5-Inch $R_5/60^\circ/8^\circ$ Biconic; $Re_\infty = 5.20 \times 10^6/\text{ft}$; $T_0 = 954^\circ\text{F}$)

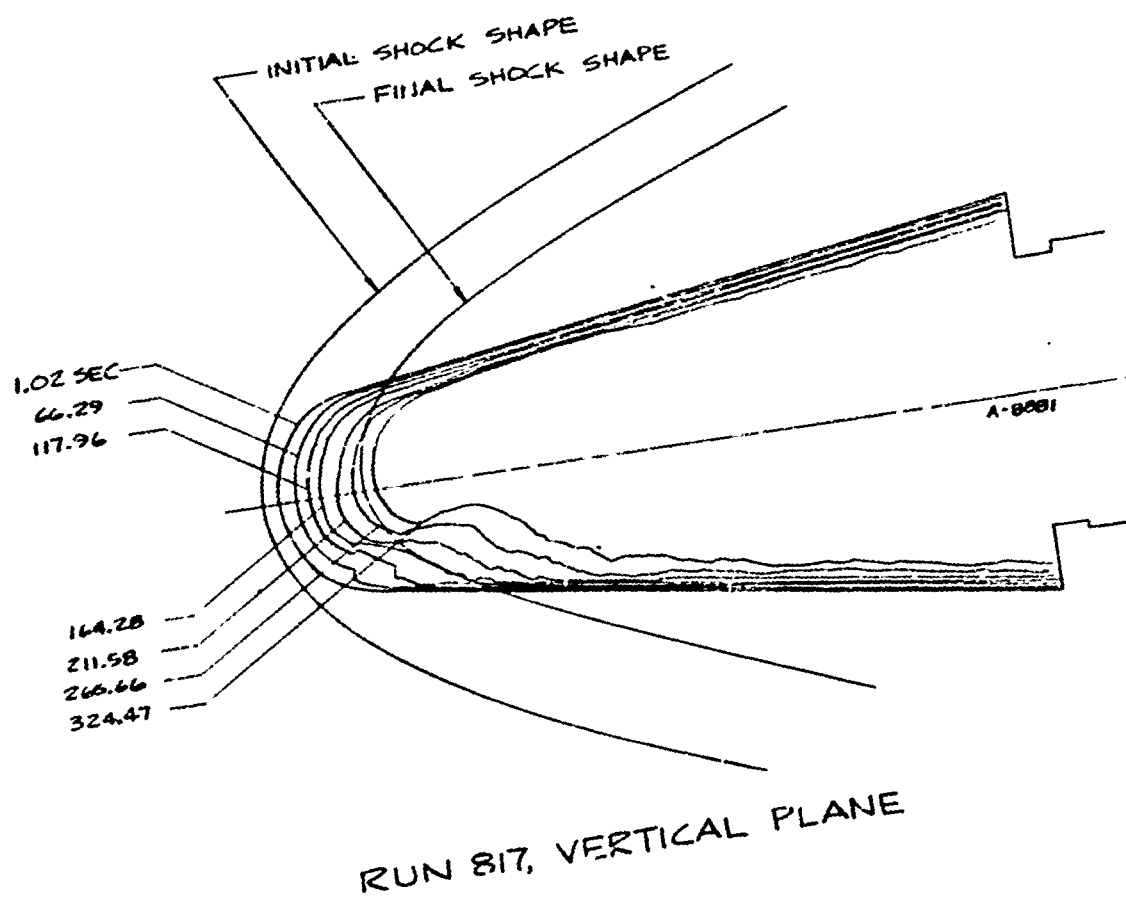
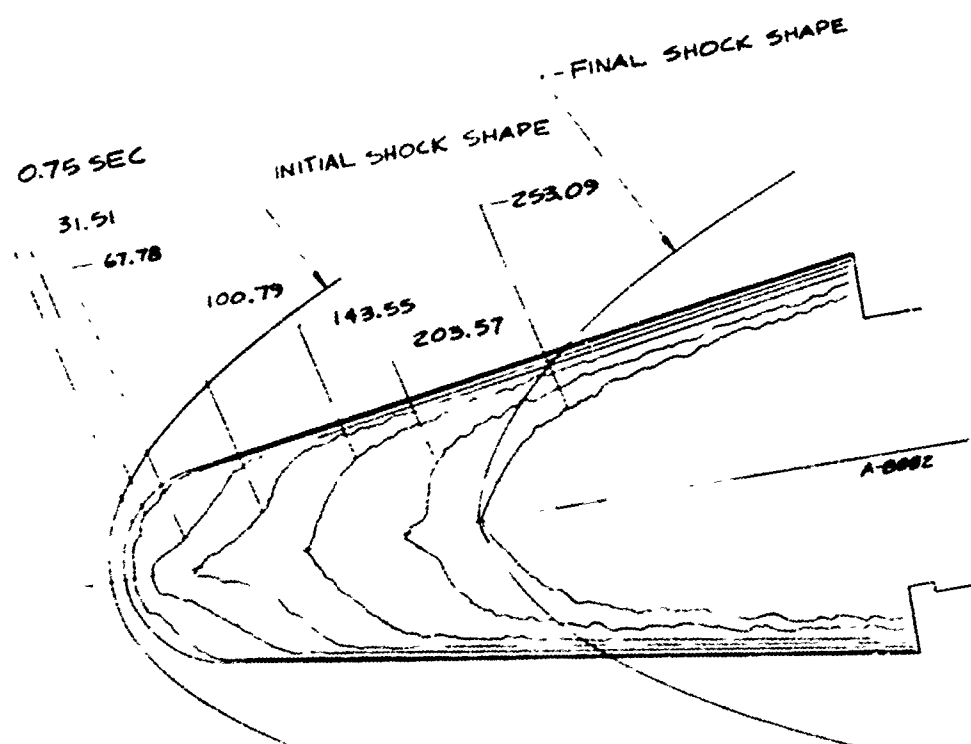
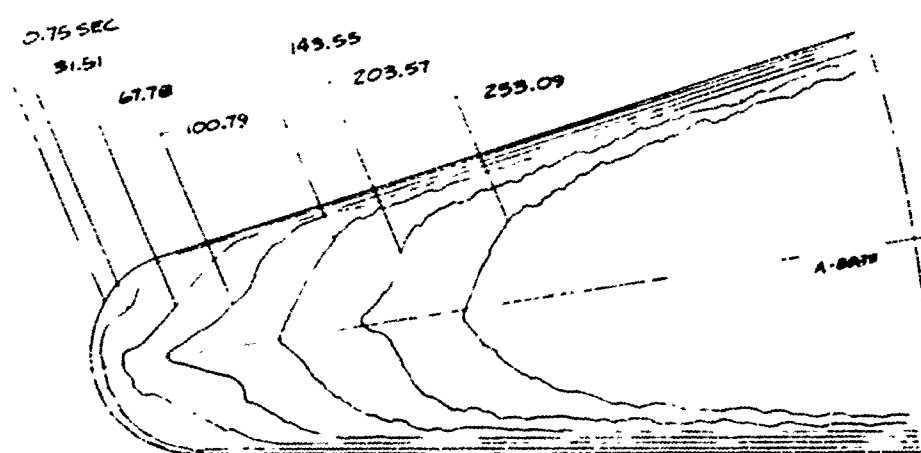


Figure B-17. Shape Profile History for Run 817 (1.5-Inch R_N Sphere-Cone;
 $Re_\infty = 6.52 \times 10^6/\text{ft}$; $T_0 = 493^\circ\text{F}$)

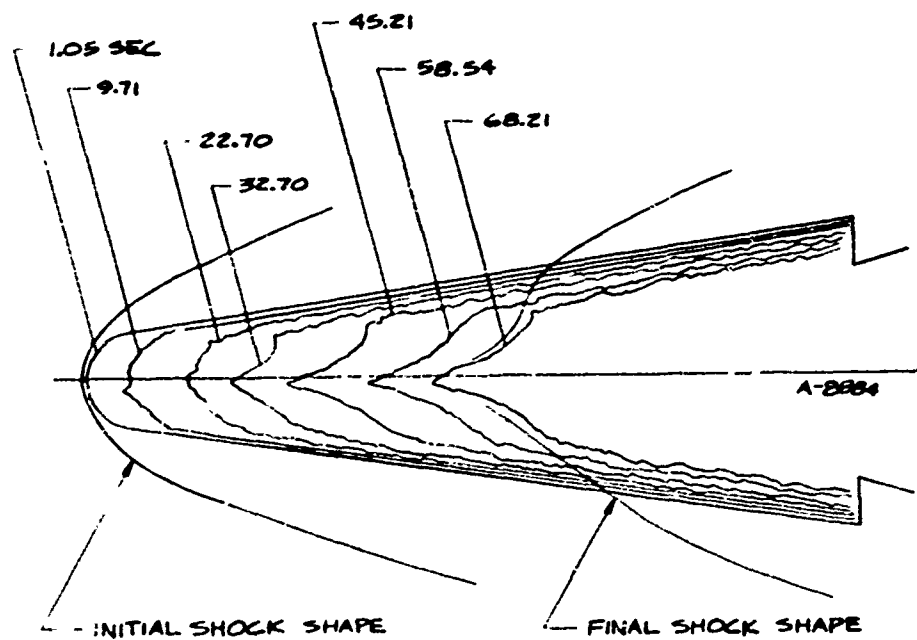


RUN 818, VERTICAL PLANE

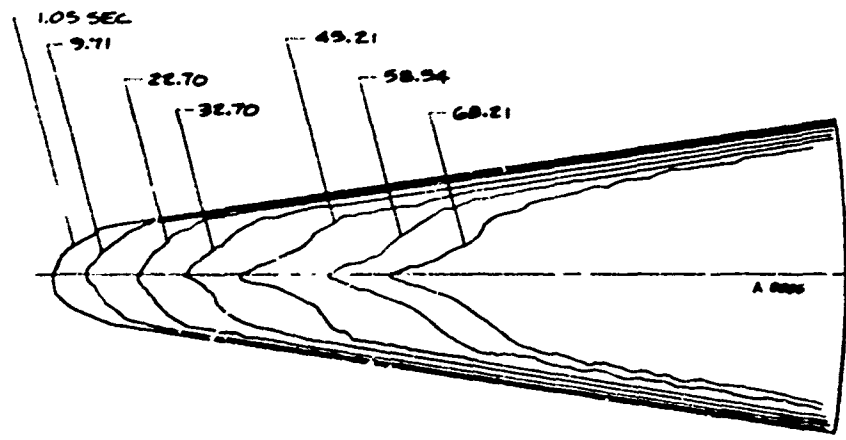


RUN 818, HORIZONTAL PLANE

Figure B-18. Shape Profile History for Run 818 (1.5-Inch R_N Sphere-Cone;
 $Re_\infty = 9.56 \times 10^6/\text{ft}$; $T_0 = 508^\circ\text{F}$)

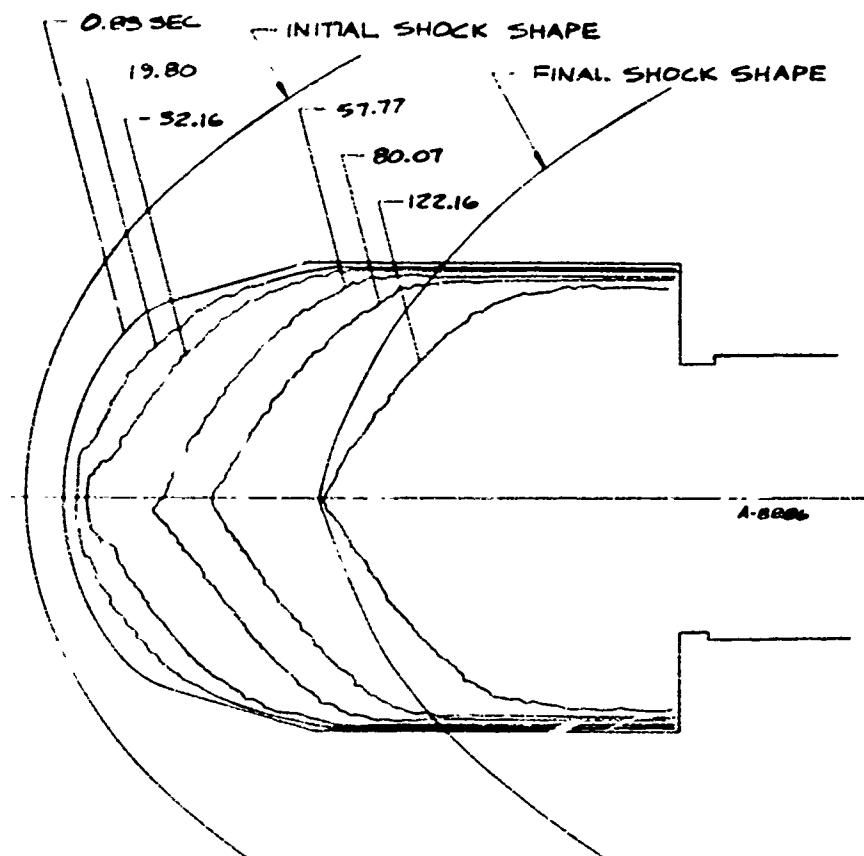


RUN 819, VERTICAL PLANE
(SECOND PORTION OF TEST SHOWN ONLY)

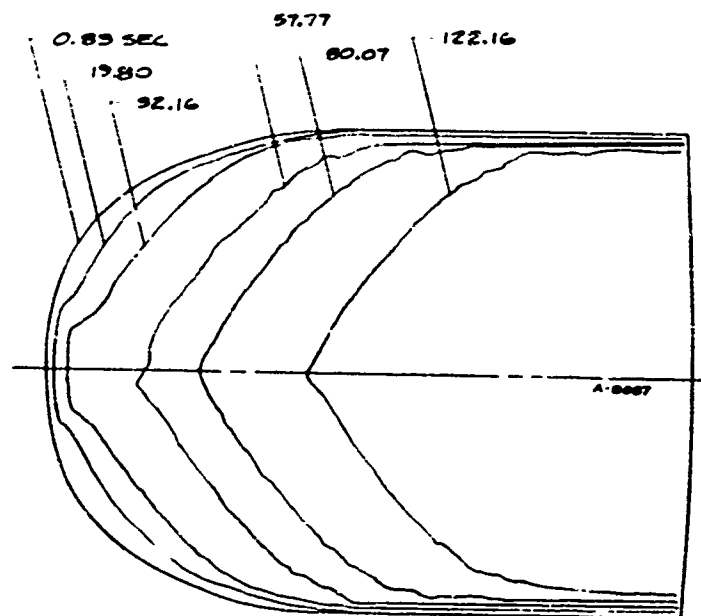


RUN 819, HORIZONTAL PLANE
(SECOND PORTION OF TEST SHOWN ONLY)

Figure B-19. Shape Profile History for Run 819 (0.75-Inch R_N Sphere-Cone;
 $Re_\infty = 12.96 \times 10^6/\text{ft}$; $T_0 = 804^\circ\text{F}$)

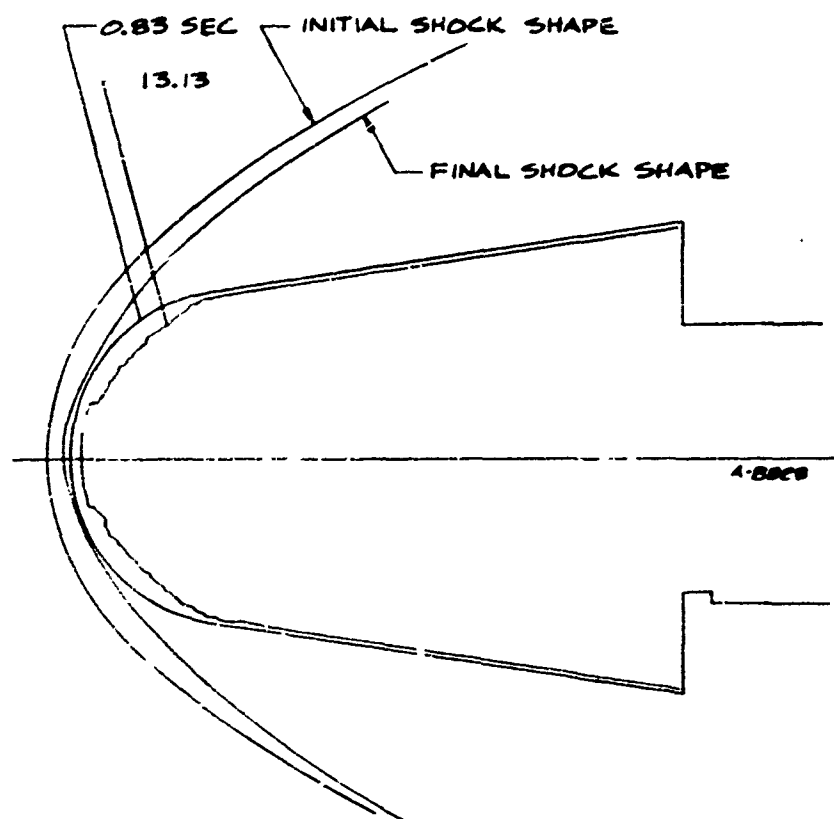


RUN 820, VERTICAL PLANE

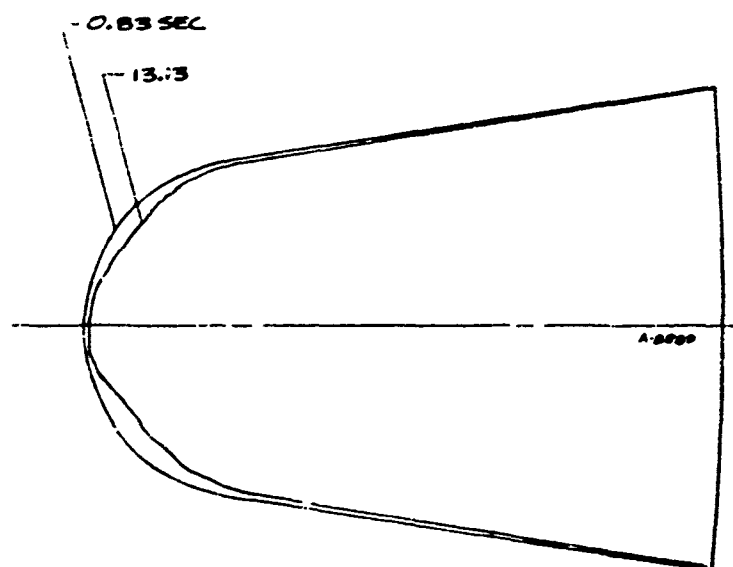


RUN 820, HORIZONTAL PLANE

Figure B-20. Shape Profile History for Run 820 (3.5-Inch R_S Laminar-Blunt; $Re_\infty = 4.90 \times 10^5/\text{ft}$; $T_0 = 986^\circ\text{F}$)

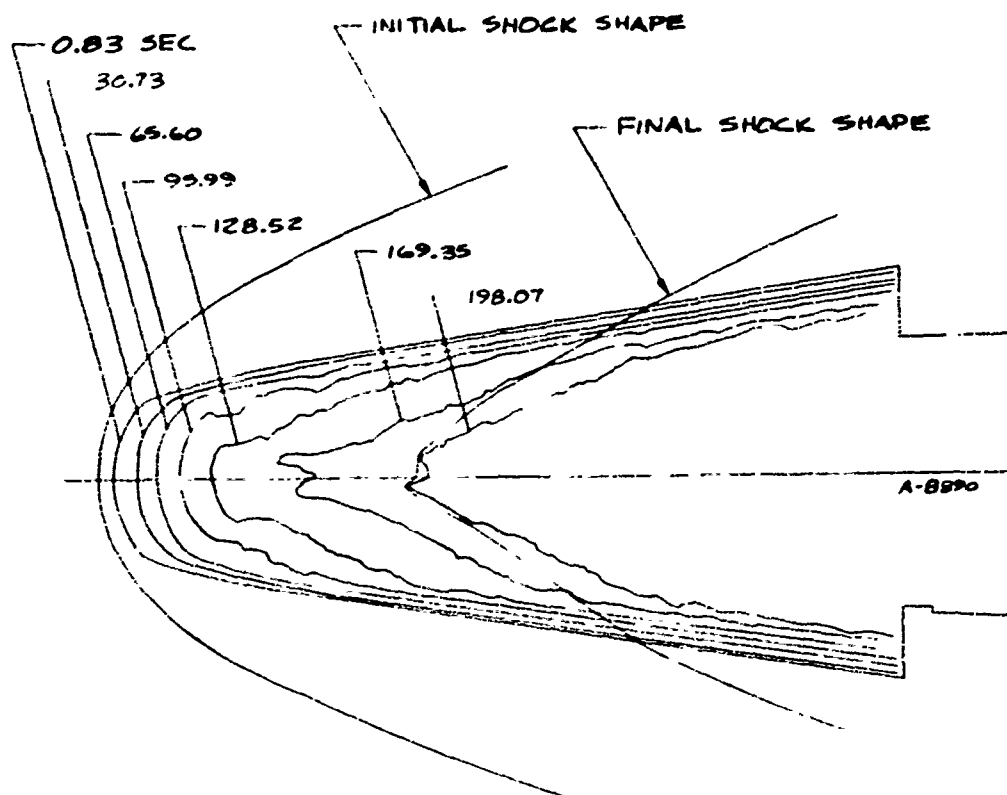


RUN 821, VERTICAL PLANE

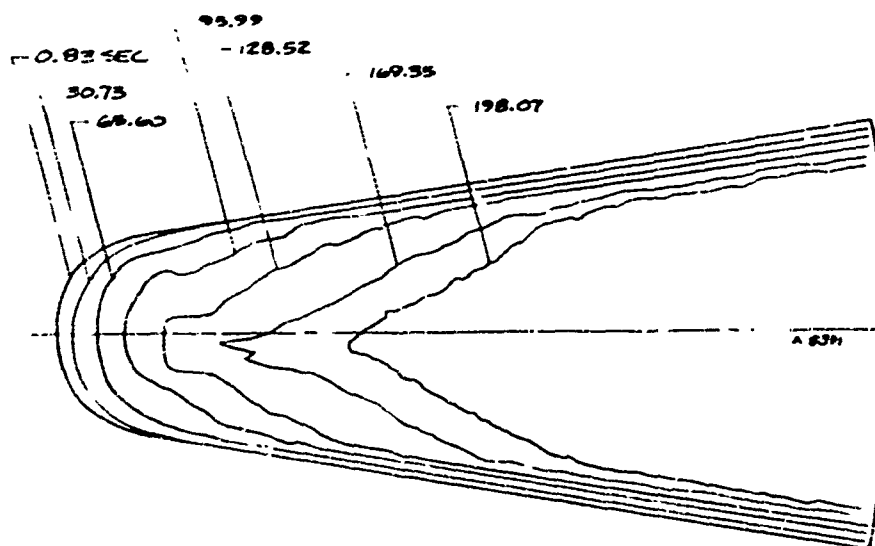


RUN 821, HORIZONTAL PLANE

Figure B-21. Shape Profile History for Run 821 (2.5-Inch R_N Sphere-Cone; $Re_\infty = 7.47 \times 10^6/\text{ft}$; $T_0 = 973^\circ\text{F}$)

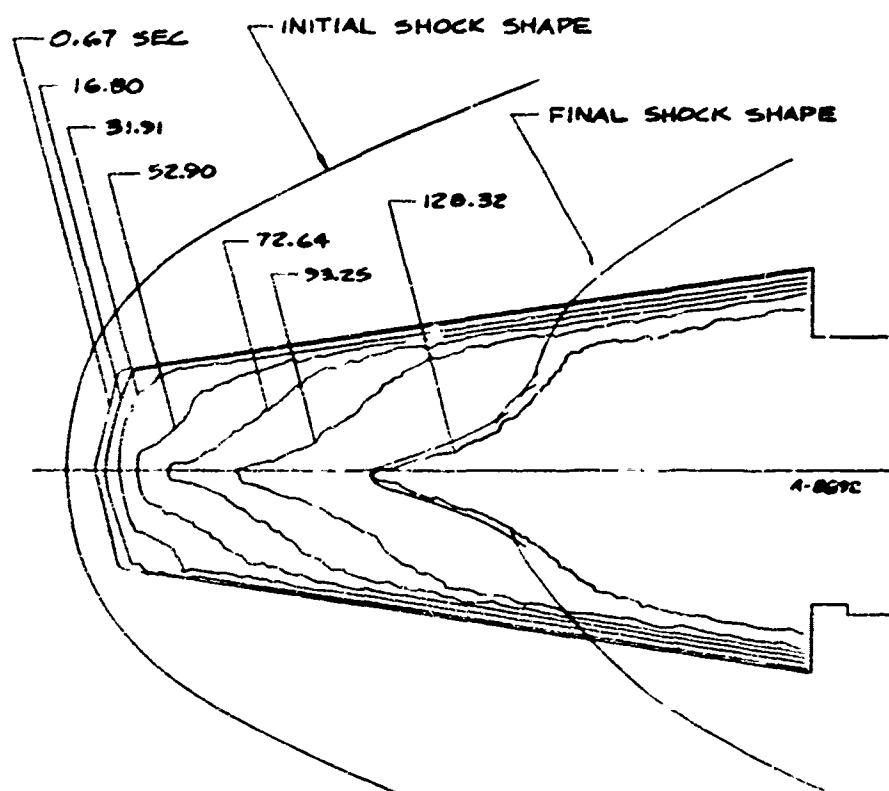


RUN 822, VERTICAL PLANE

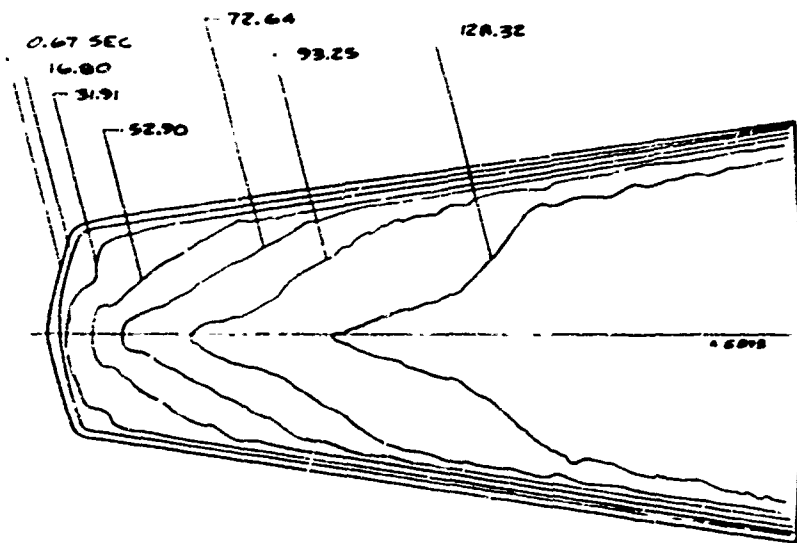


RUN 822, HORIZONTAL PLANE

Figure B-22. Shape Profile History for Run 822 (1.5-Inch R_S Laminar-Blunt; $Re_\infty = 4.02 \times 10^6/\text{ft}$; $T_0 = 960^\circ\text{F}$)

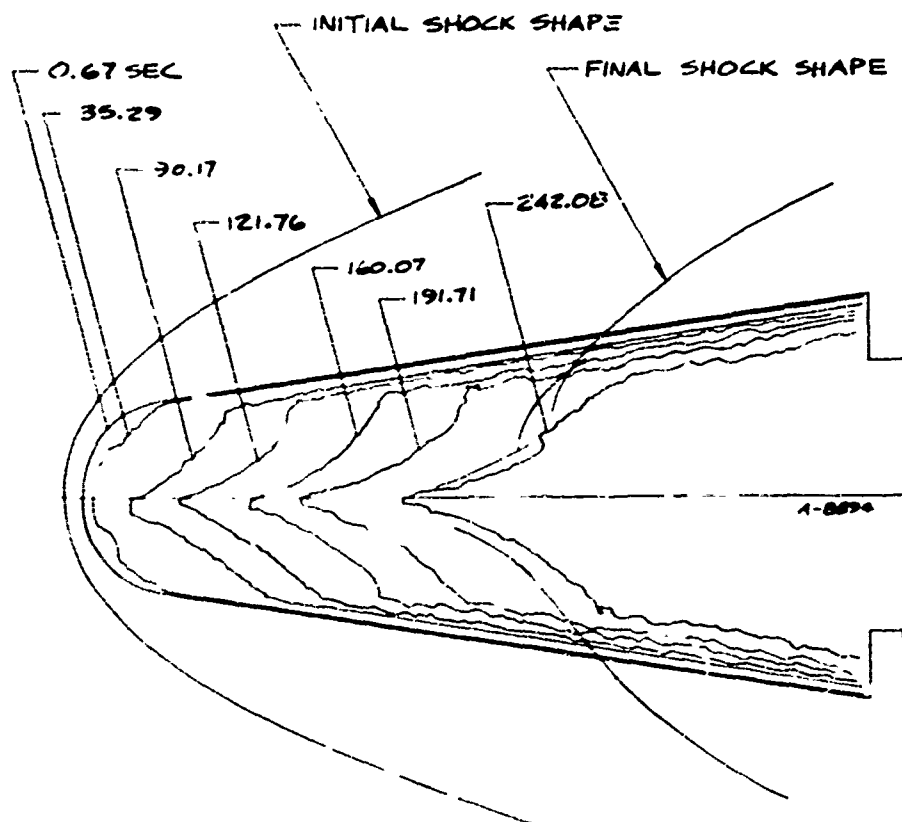


RUN 823, VERTICAL PLANE

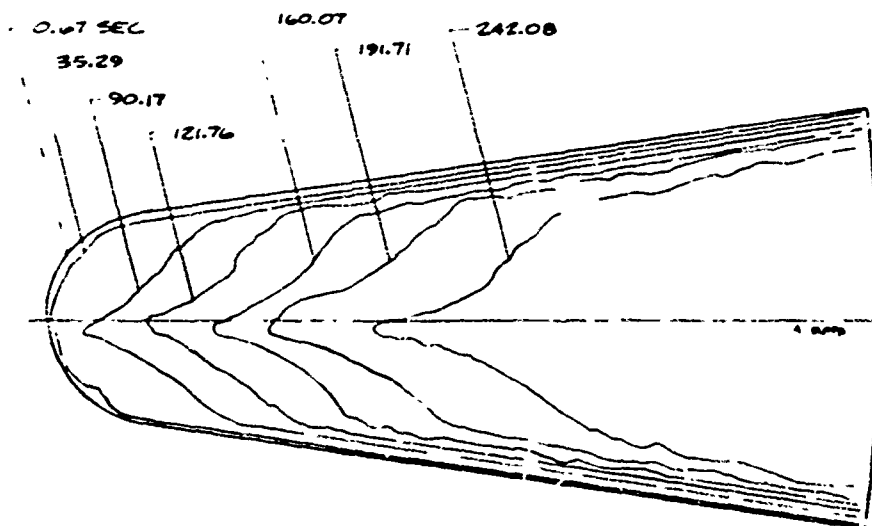


RUN 823, HORIZONTAL PLANE

Figure B-23. Shape Profile History for Run 823 (1.5-Inch $R_5/75^\circ/8^\circ$ Biconic; $Re_\infty = 5.18 \times 10^6/\text{ft}$; $T_0 = 986^\circ\text{F}$)

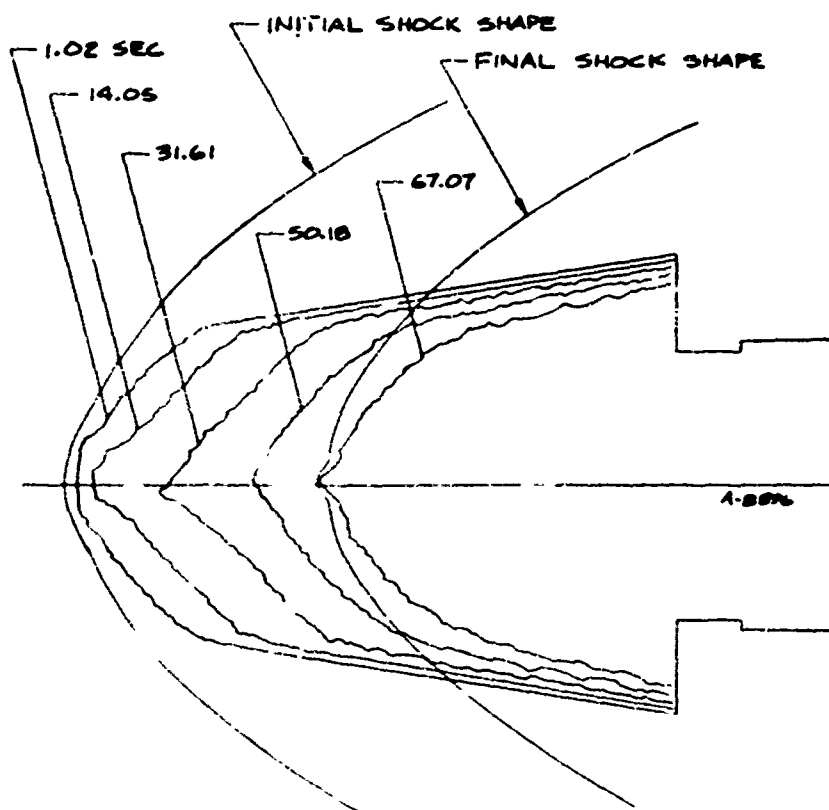


RUN 824, VERTICAL PLANE

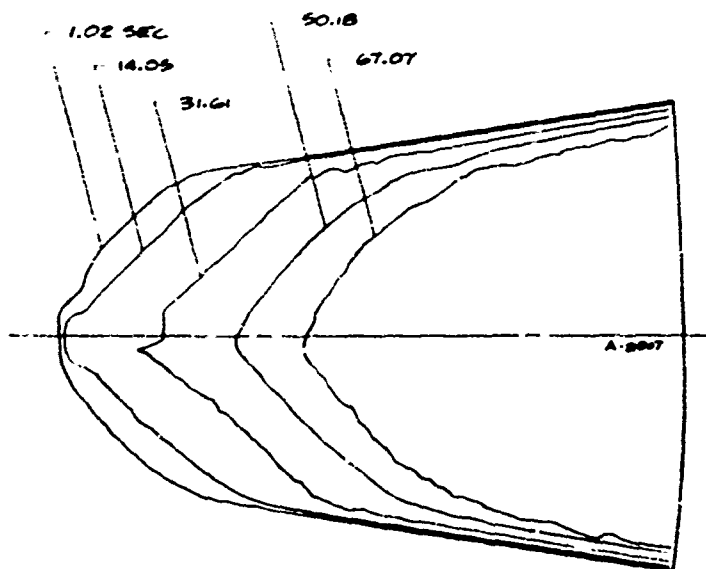


RUN 824, HORIZONTAL PLANE

Figure 8-24. Shape Profile History for Run 824 (1.5-Inch R_N Sphere-Cone; $\rho_{e_0} = 9.44 \times 10^4$ /ft; $T_0 = 535^\circ\text{F}$)

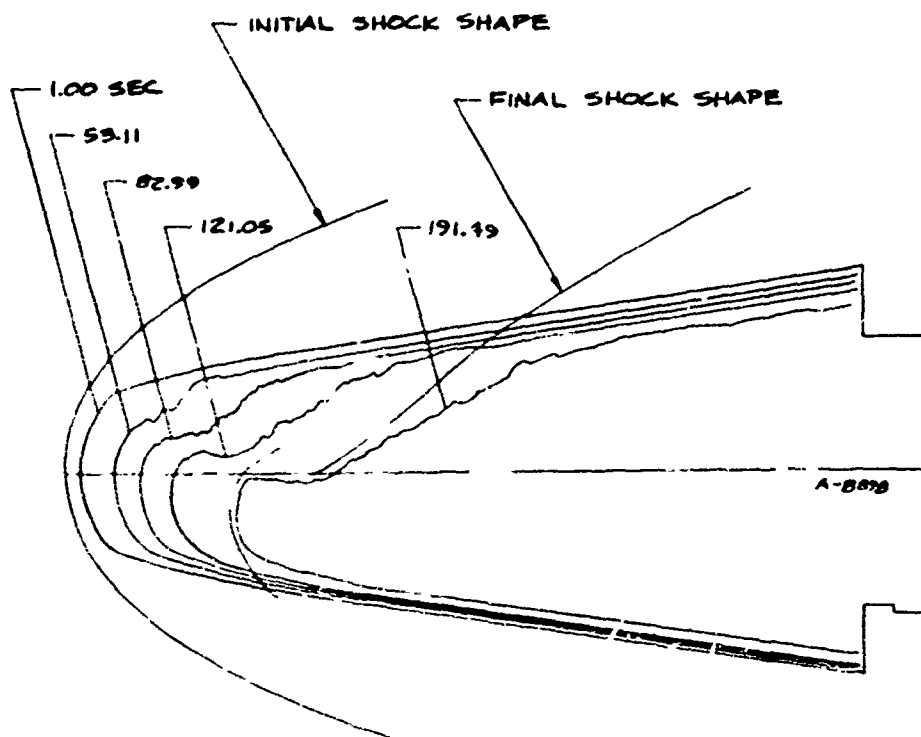


RUN 825, VERTICAL PLANE

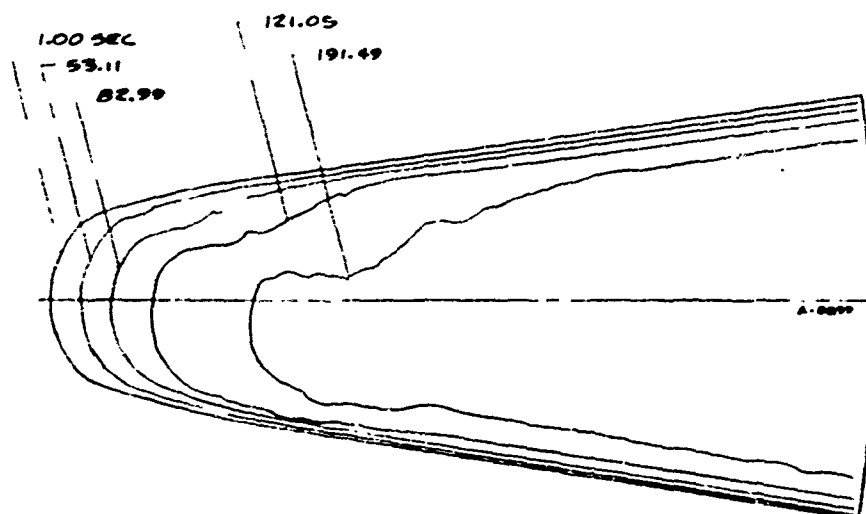


RUN 825, HORIZONTAL PLANE

Figure B-25. Shape Profile History for Run 825 (2.5-Inch R_N Sphere-Cone; $Re_\infty = 7.20 \times 10^5/\text{ft}$; $T_0 = 990^\circ\text{F}$)

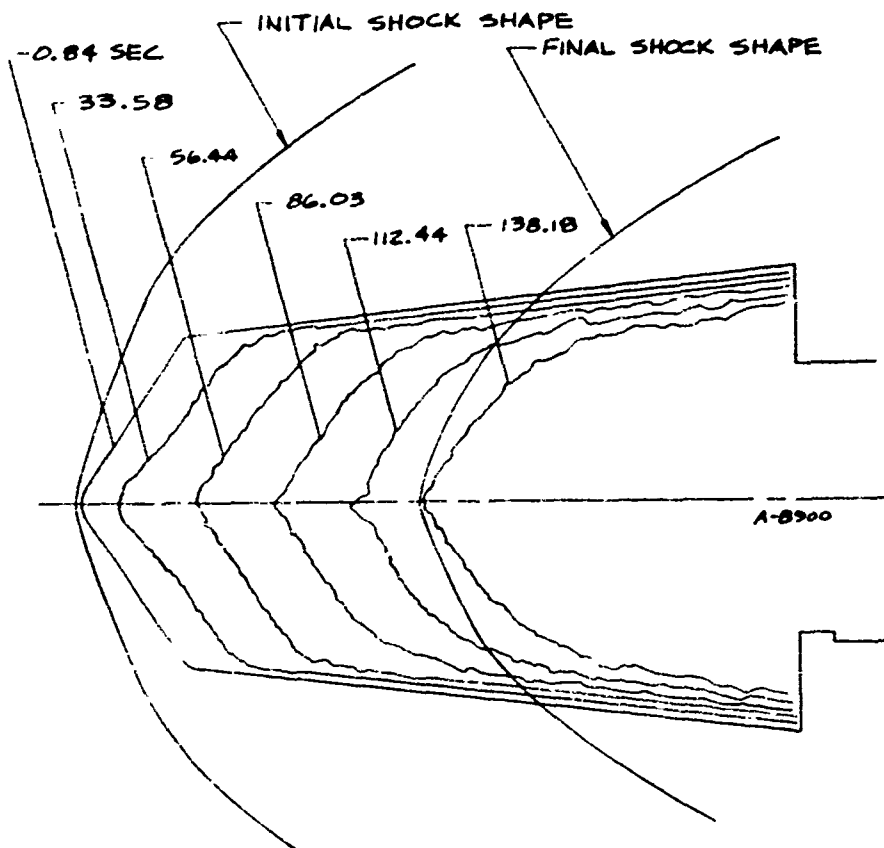


RUN 826, VERTICAL PLANE

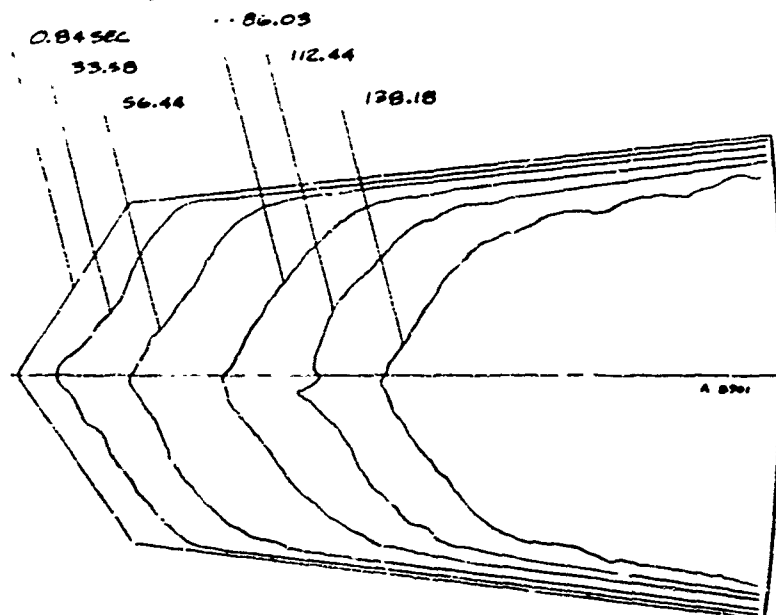


RUN 826, HORIZONTAL PLANE

Figure 8-26. Shape Profile History for Run 826 (1.5-Inch R_S Laminar-Blunt; $Re_\infty = 3.41 \times 10^6/\text{ft}$; $T_0 = 987^\circ\text{F}$)



RUN 827, VERTICAL PLANE



RUN 827, HORIZONTAL PLANE

Figure B-27. Shape Profile History for Run 827 (2.5-Inch $R_S/55^\circ/6^\circ$ Biconic; $Re_\infty = 4.76 \times 10^6/\text{ft}$; $T_0 = 1008^\circ\text{F}$)

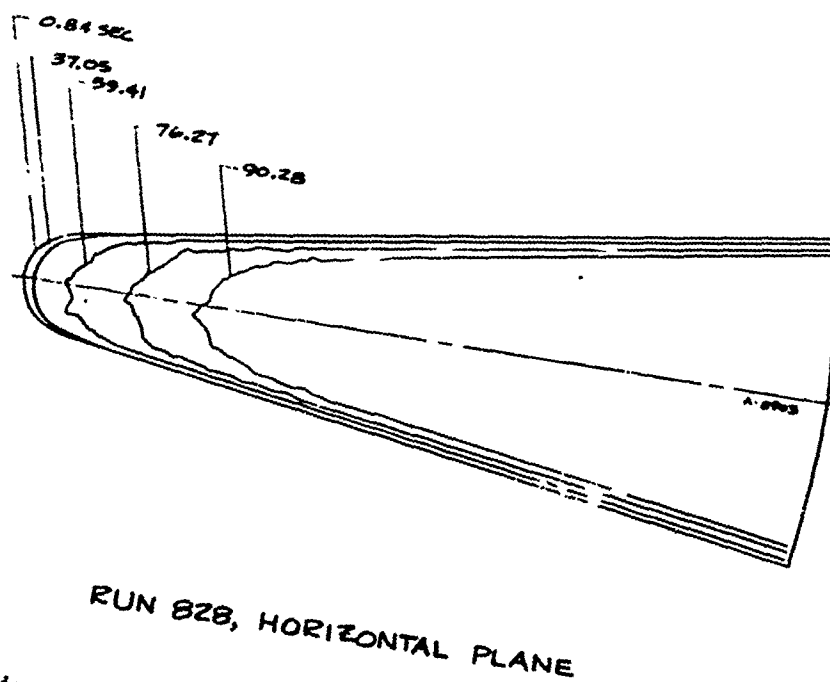
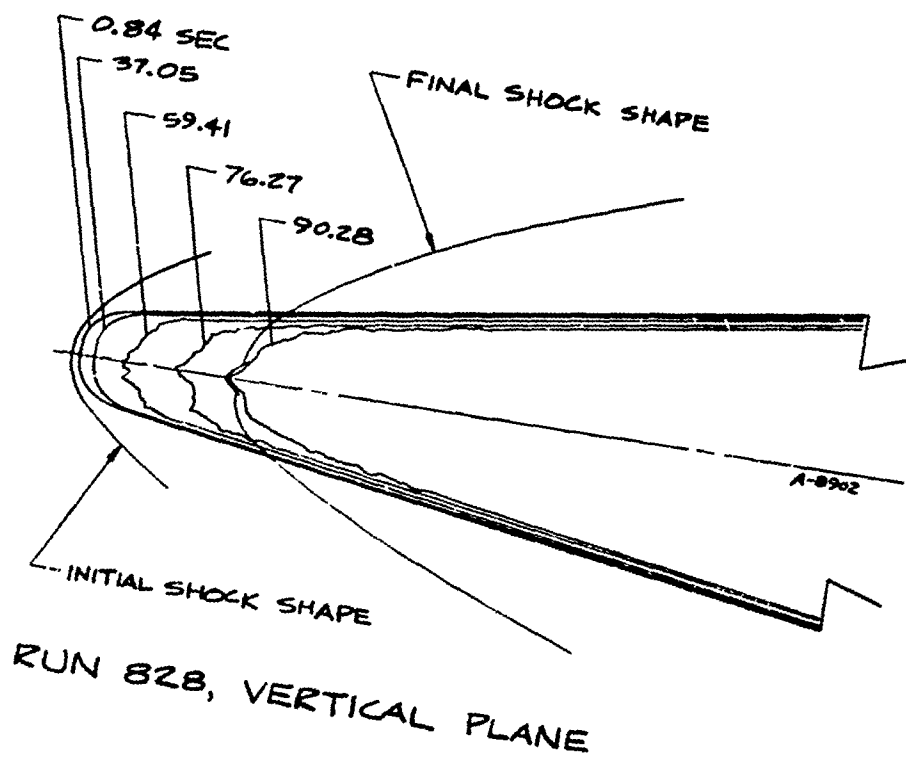
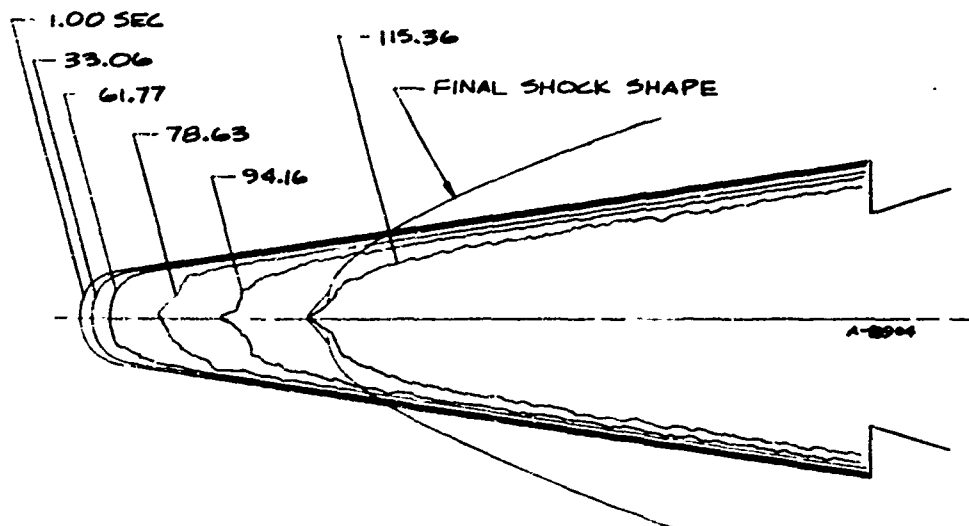
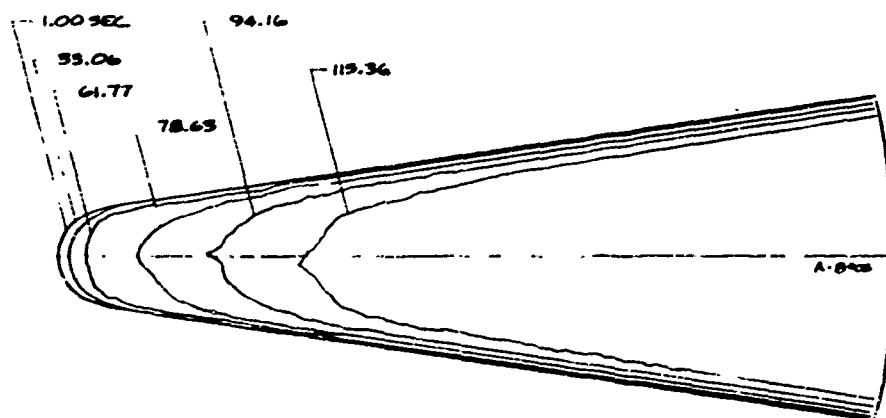


Figure B-28. Shape Profile History for Run 828 (0.75-Inch R_N Sphere-Cone;
Variable Re_∞)

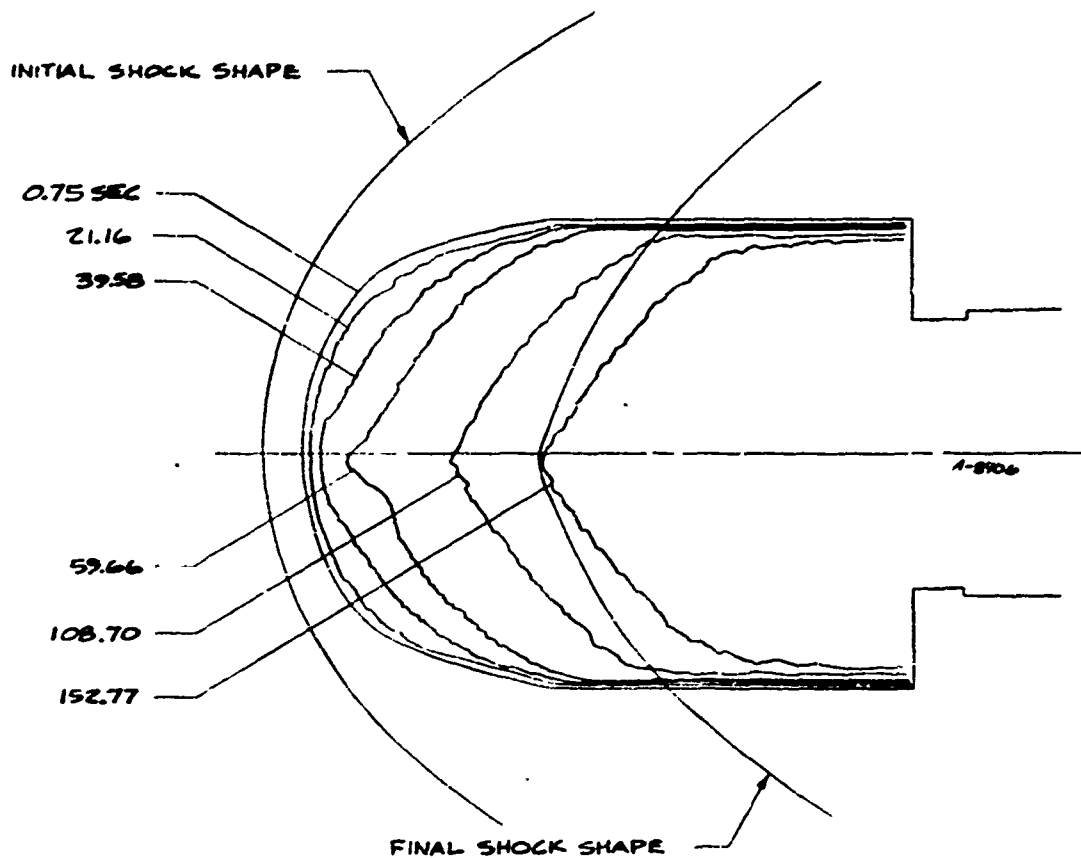


RUN 829, VERTICAL PLANE

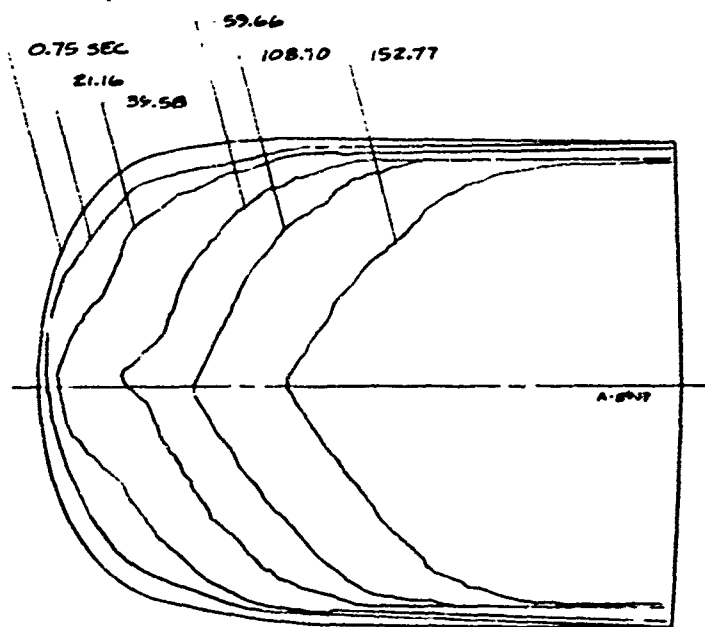


RUN 829, HORIZONTAL PLANE

Figure B-29. Shape Profile History for Run 829 (0.75-Inch R_N Sphere-Cone; Variable Re_m)

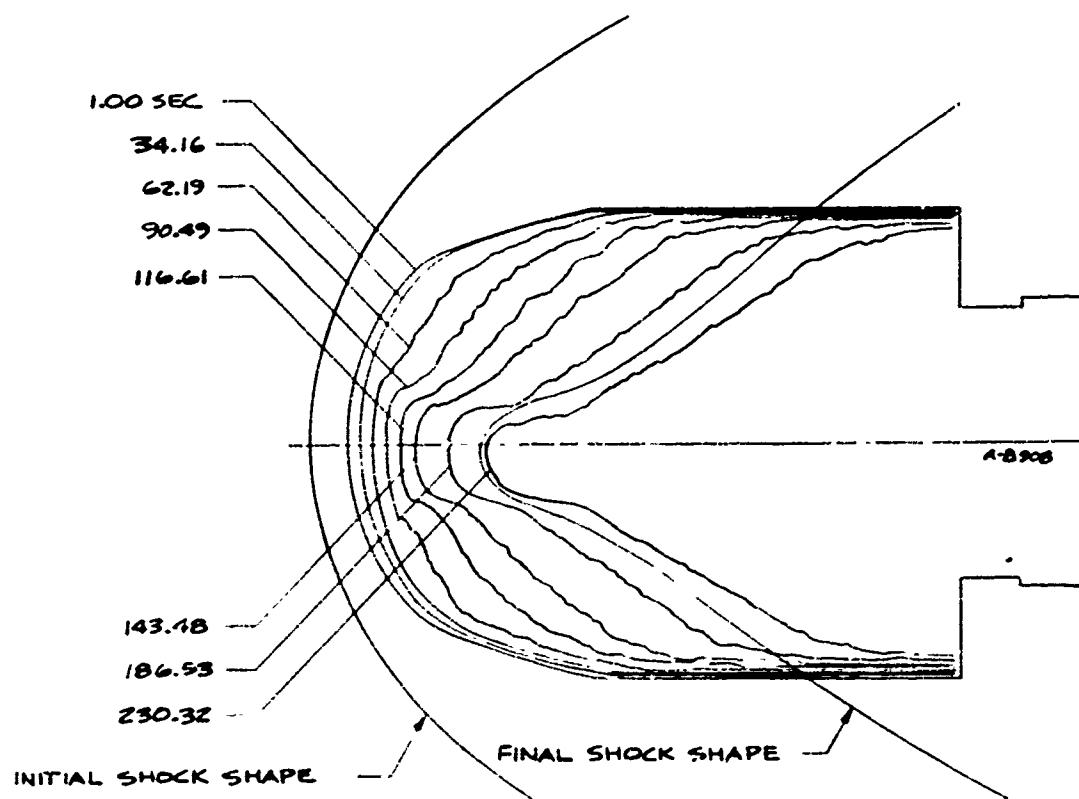


RUN 830, VERTICAL PLANE

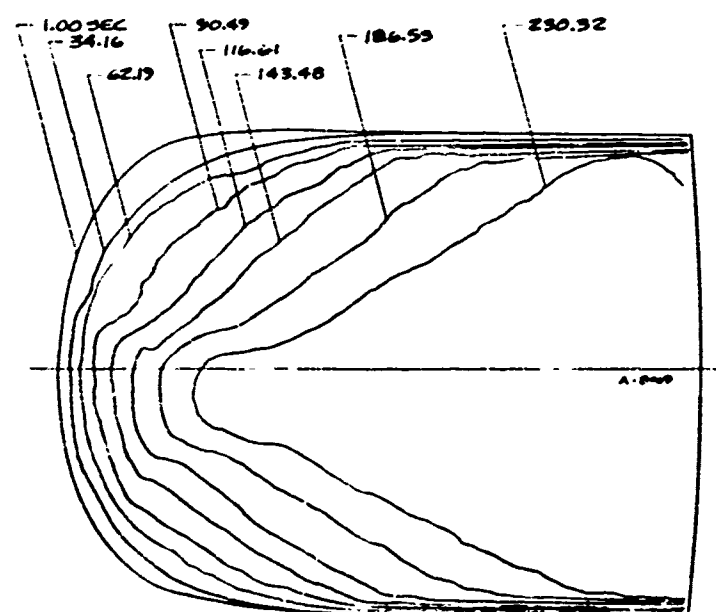


RUN 830, HORIZONTAL PLANE

Figure B-30. Shape Profile History for Run 830 (3.5-Inch R_S Laminar-Blunt; $Re_\infty = 3.47 \times 10^6/\text{ft}$; $T_0 = 985^\circ\text{F}$)



RUN 831, VERTICAL PLANE



RUN 831, HORIZONTAL PLANE

Figure B-31. Shape Profile History for Run 831 (3.5-Inch R_S Laminar-Blunt;
 $Re_\infty = 2.52 \times 10^5/\text{ft}$; $T_0 = 998^\circ\text{F}$)

APPENDIX C

STAGNATION POINT AXIAL RECESSION PLOTS
RUNS 801-831

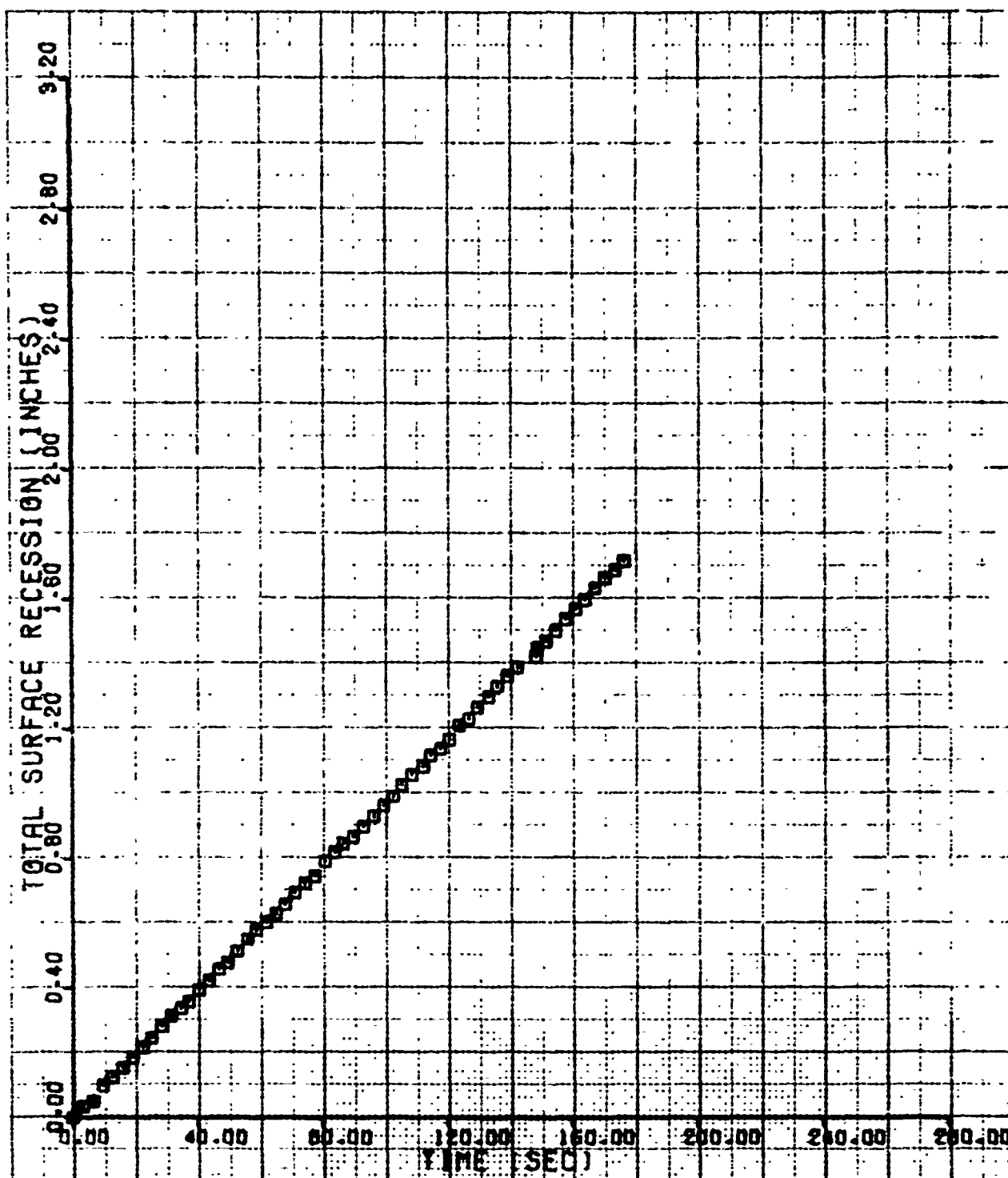


Figure C-1. Stagnation Point Axial Recession for Run 801 (1.5-Inch R_N Sphere-Cone; $Re_\infty = 3.44 \times 10^5/\text{ft}$; $T_0 = 953^\circ\text{F}$)

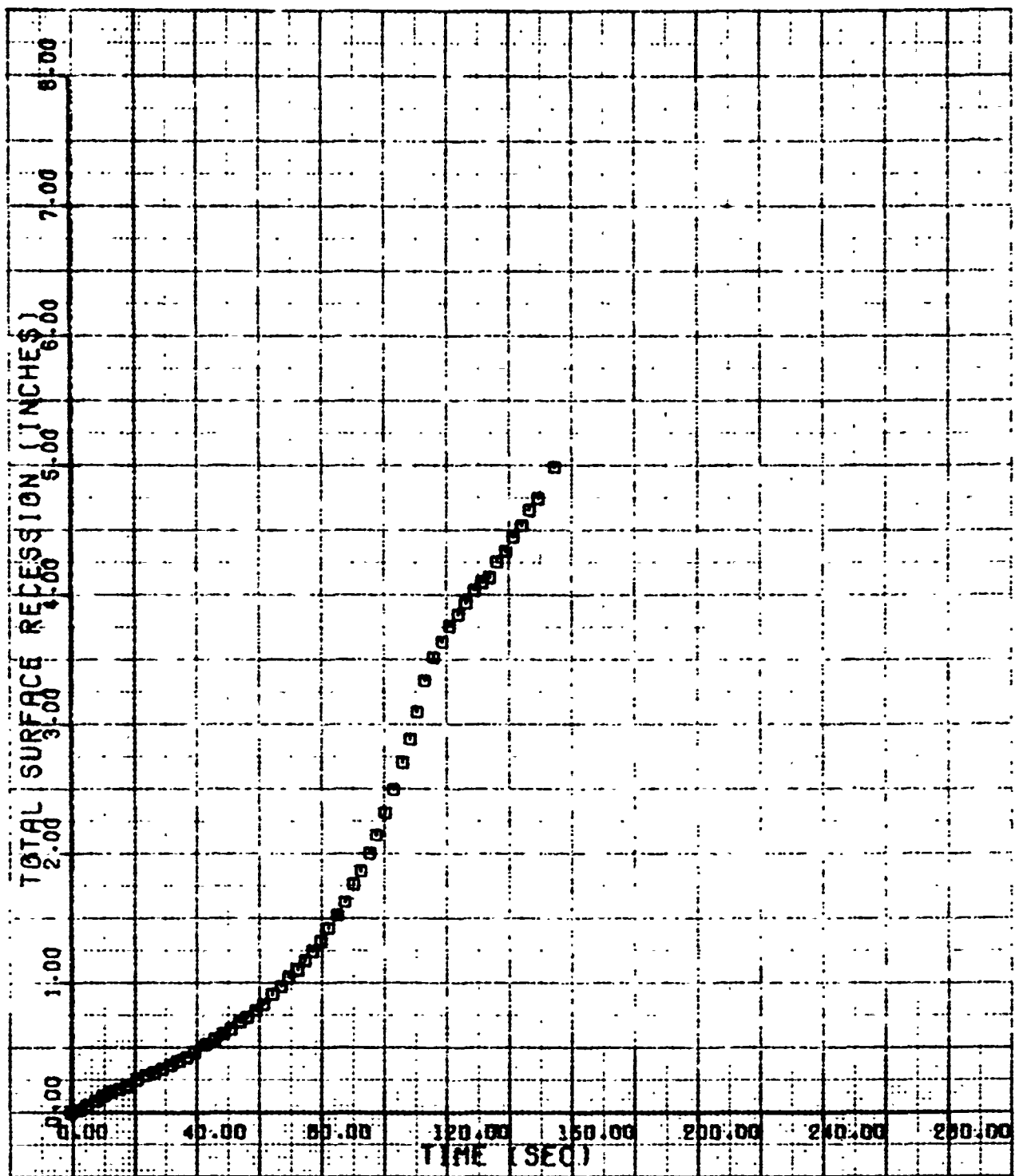


Figure C-2. Stagnation Point Axial Recession for Run 802 (1.5-Inch R_N Sphere-Cone; $Re_\infty = 4.69 \times 10^6/\text{ft}$; $T_0 = 970^\circ\text{F}$) Data from 35mm Overhead Camera

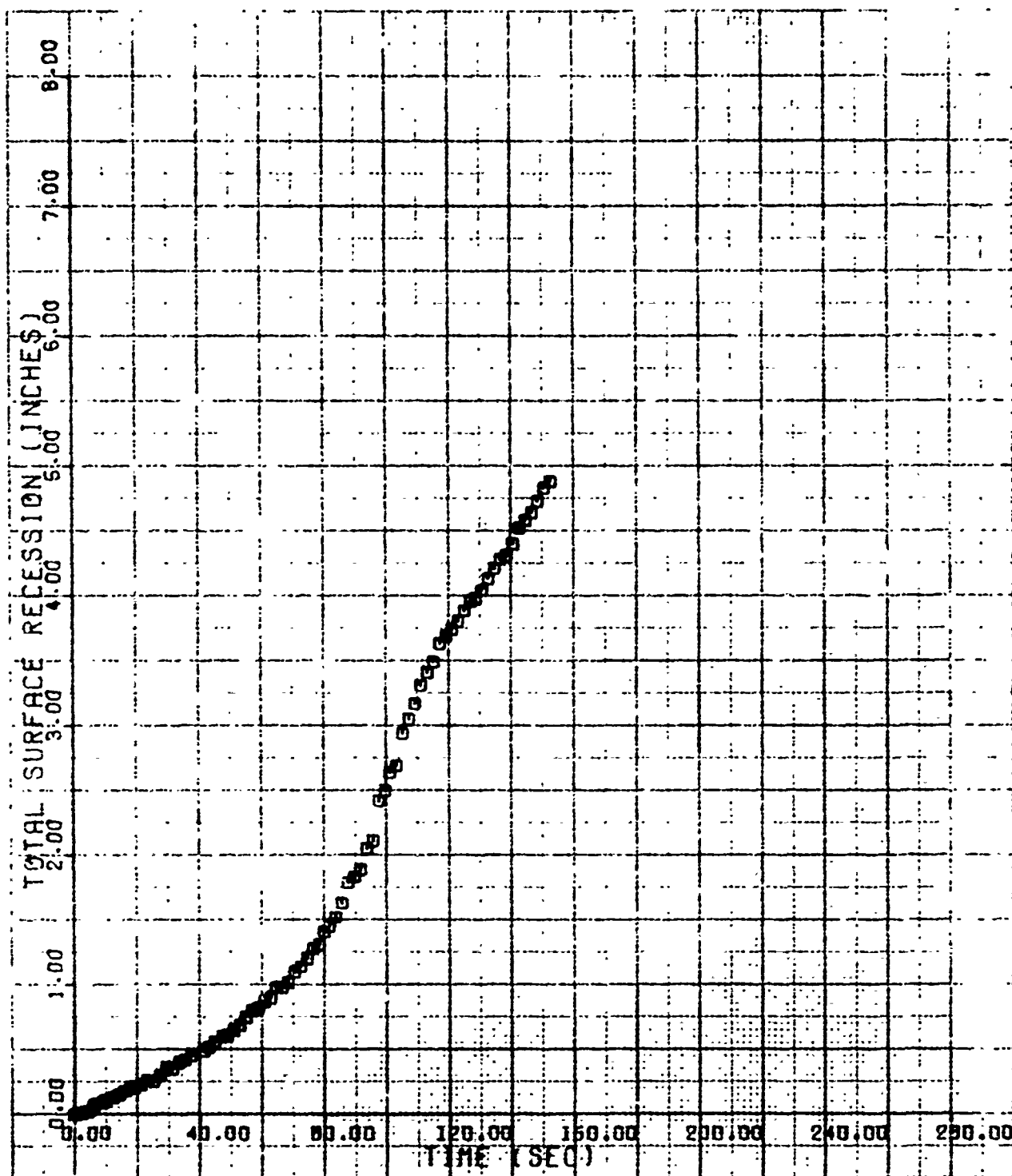


Figure C-3. Stagnation Point Axial Recession for Run 802 (1.5-Inch R_N Sphere-Cone; $Re_\infty = 4.09 \times 10^5/\text{ft}$; $T_0 = 970^\circ\text{F}$) Data from 35mm Sideview Shadowgraph Camera

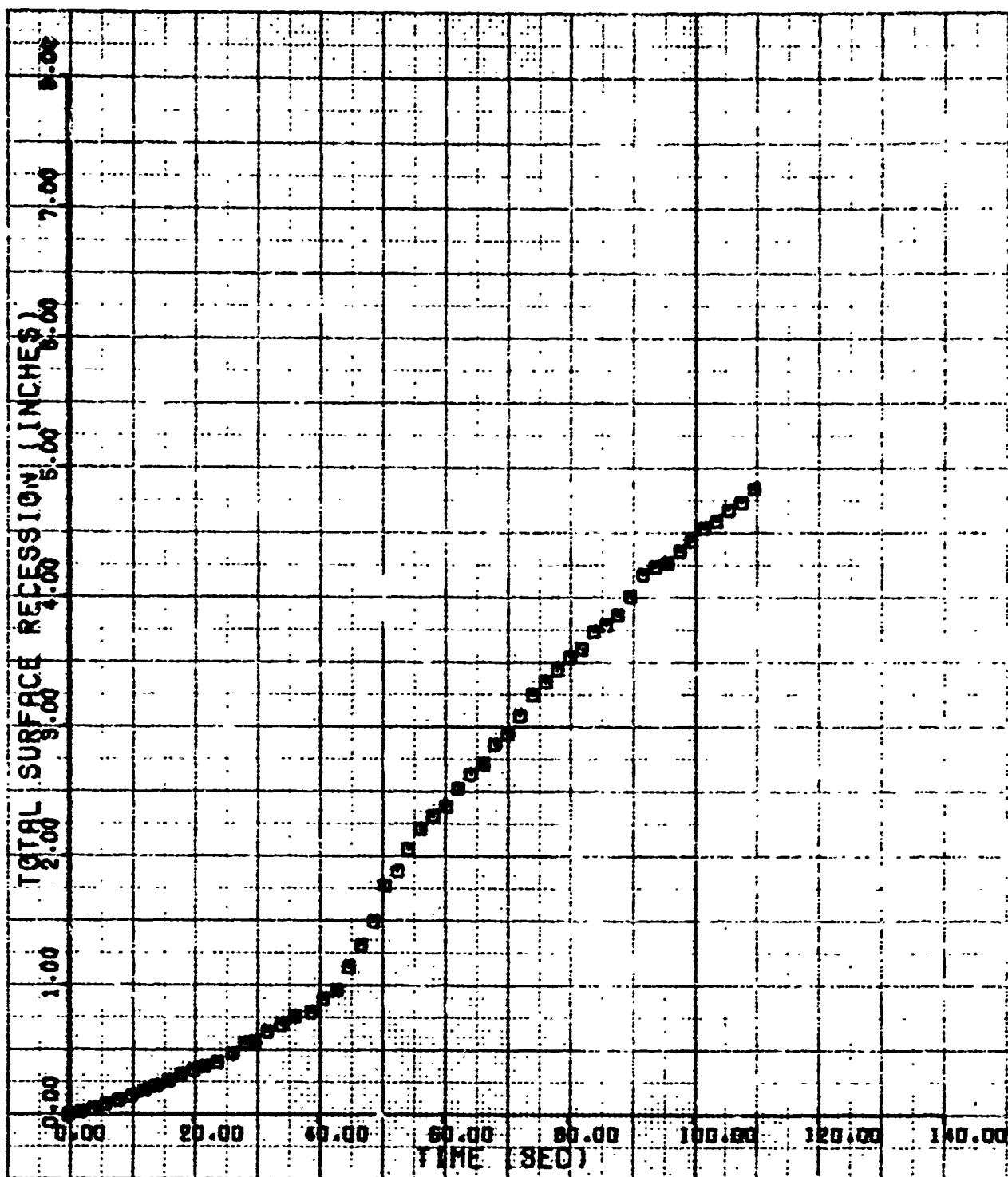


Figure C-4. Stagnation Point Axial Recession for Run 803 (1.5-Inch R_N Sphere-Cone;
 $Re_\infty = 6.54 \times 10^5/\text{ft}$; $T_0 = 475^\circ\text{F}$)

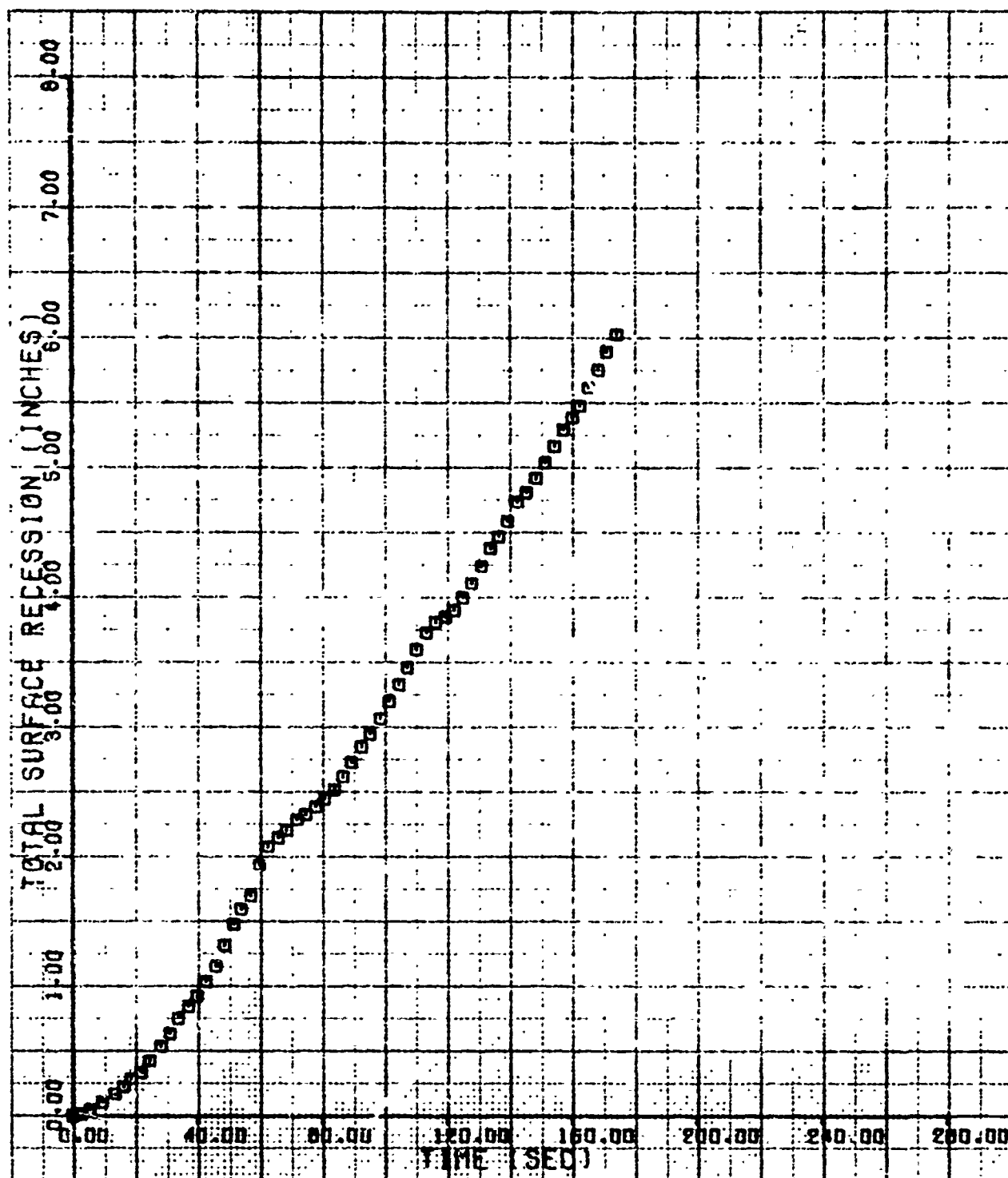


Figure C-5. Stagnation Point Axial Recession for Run 804 (1.5-Inch R_N Sphere-Cone, Particle-Loaded; $Re_m = 2.51 \times 10^6/\text{ft}$; $T_o = 983^\circ\text{F}$)

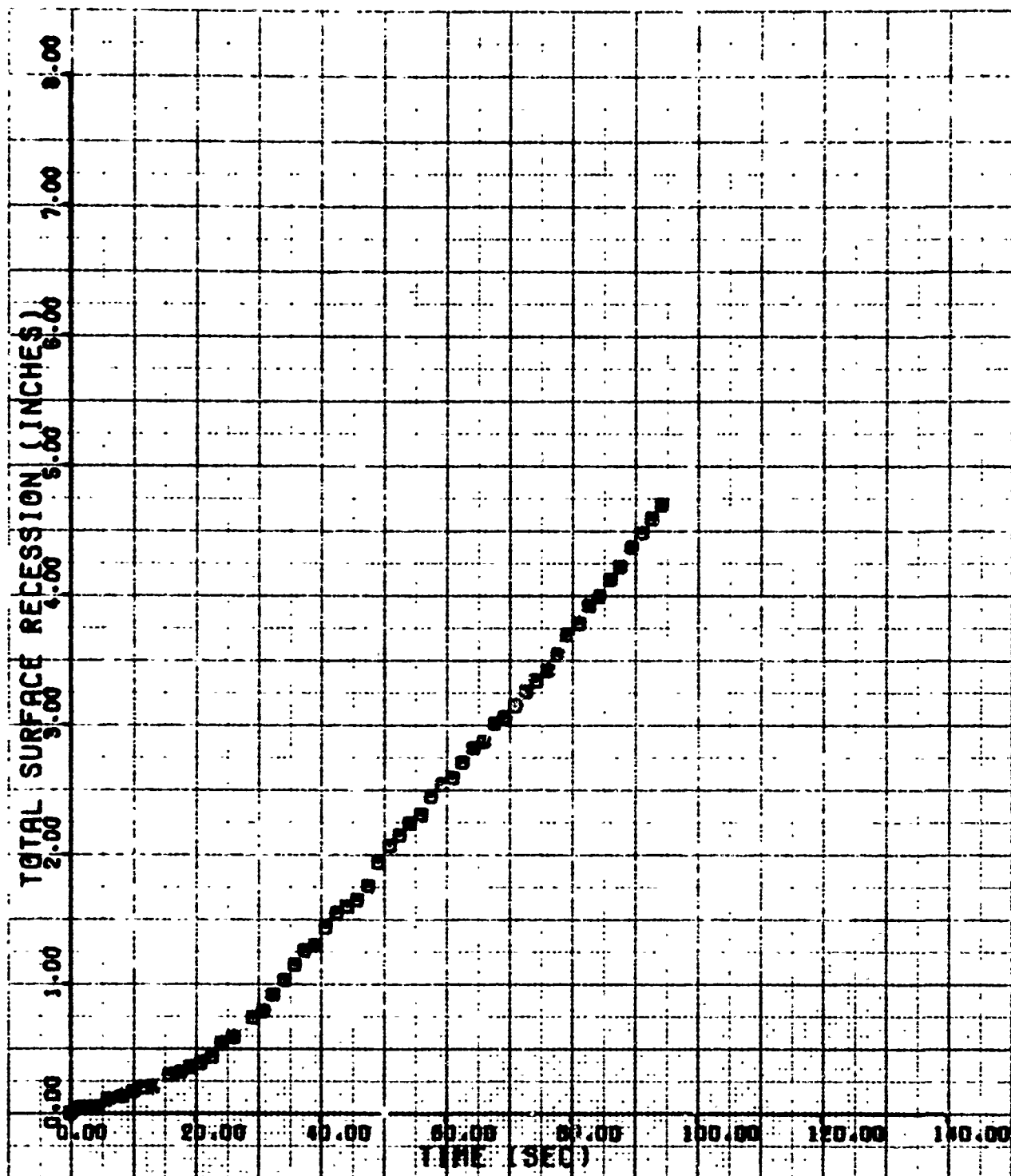


Figure C-6. Stagnation Point Axial Recession for Run 805 (1.5-Inch R_N Sphere-Cone;
 $Re_\infty = 6.56 \times 10^6/\text{ft}$; $T_0 = 987^\circ\text{F}$)

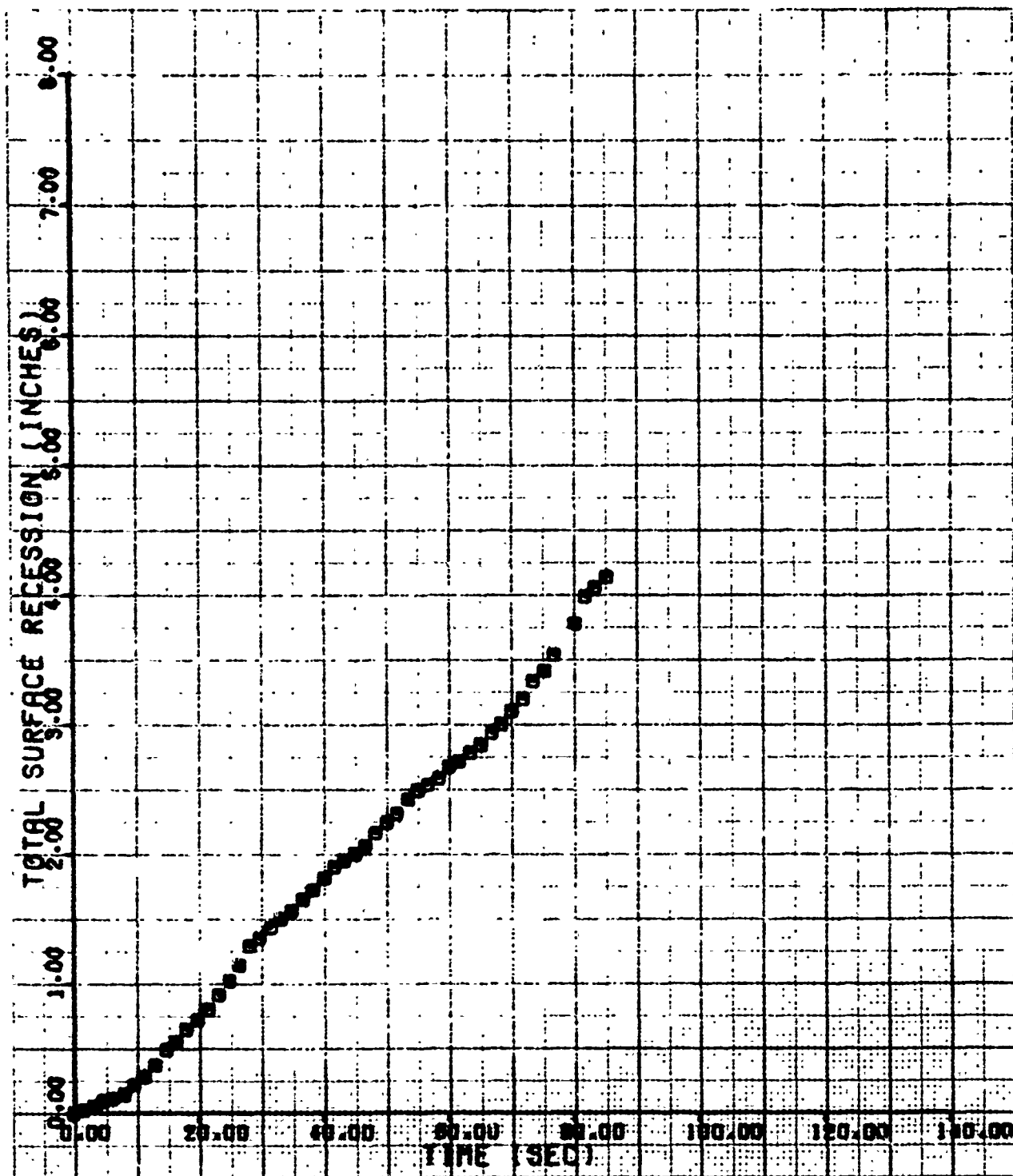


Figure C-7. Stagnation Point Axial Recession for Run 806 (0.75-Inch R_N Sphere-Cone;
 $Re_\infty = 7.36 \times 10^6/\text{ft}$; $T_0 = 921^\circ\text{F}$)

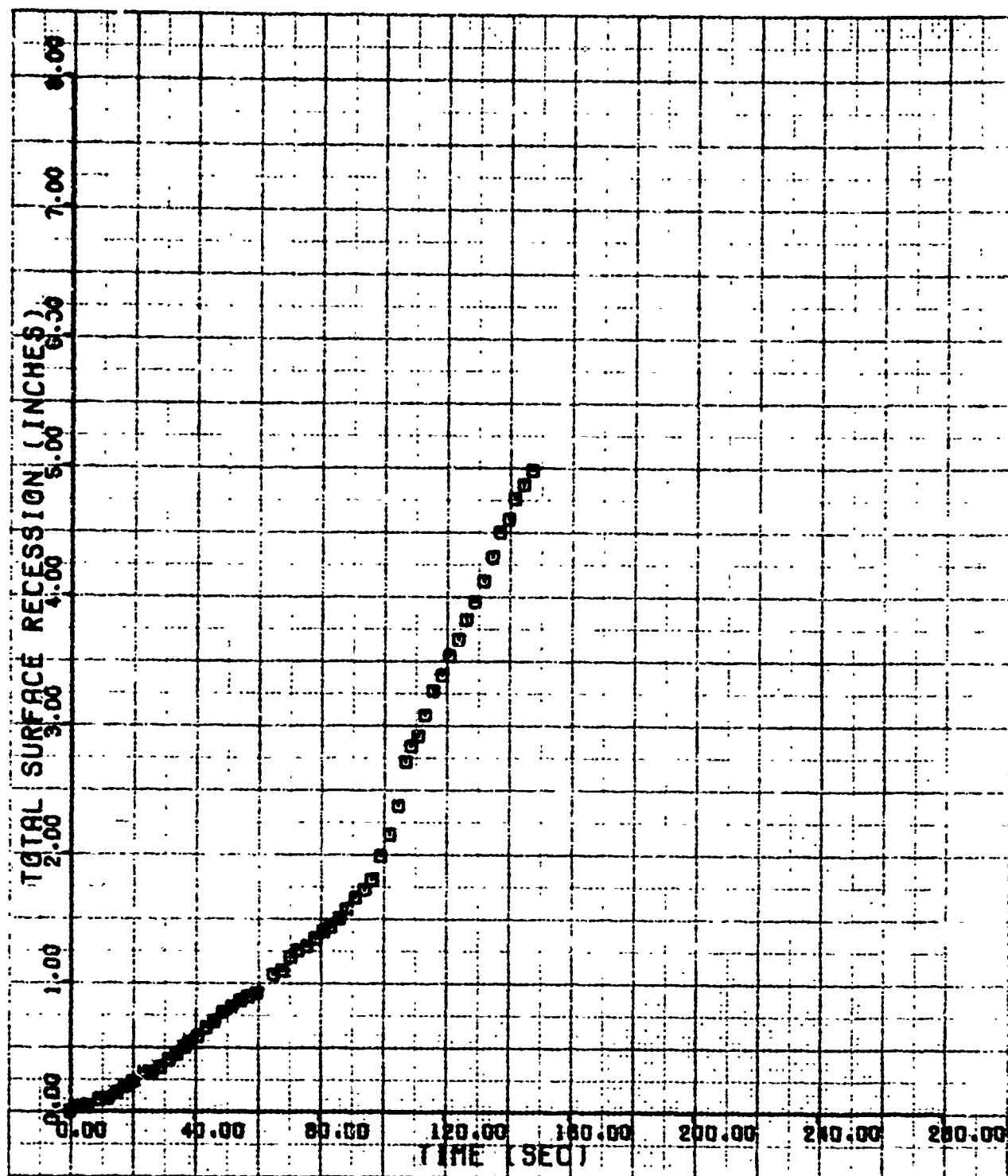


Figure C-8. Stagnation Point Axial Recession for Run 807 (1.5-Inch R_N Sphere-Cone with Groove; $Re_\infty = 4.08 \times 10^5/\text{ft}$; $T_0 = 1013^\circ\text{F}$)

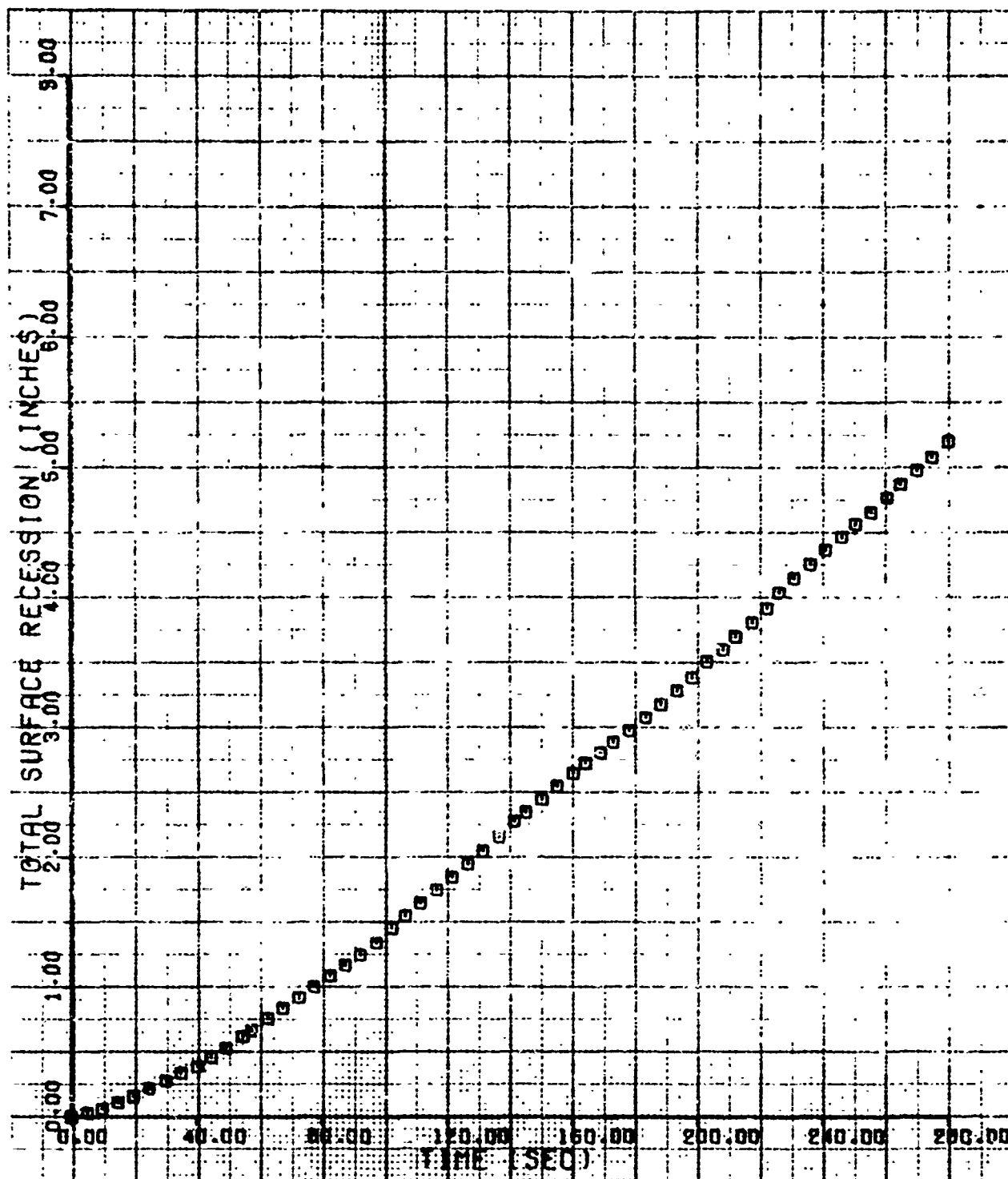


Figure C-9. Stagnation Point Axial Recession for Run 808 (1.5-Inch R_N Sphere-Cone, Particle-Loaded; $Re_\infty = 1.50 \times 10^6/\text{ft}$; $T_0 = 996^\circ\text{F}$)

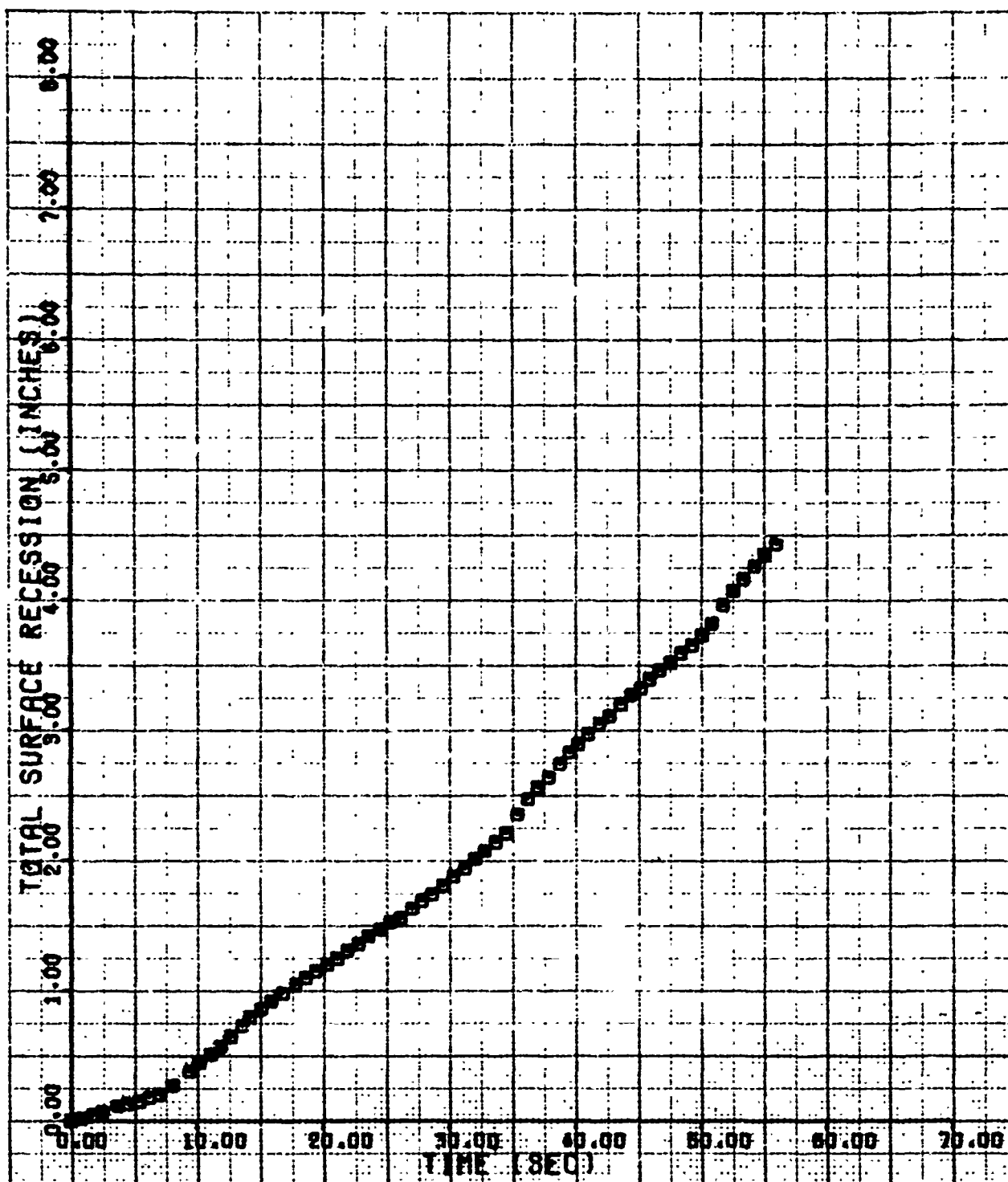


Figure C-10. Stagnation Point Axial Recession for Run 809 (0.75-Inch R_N Sphere-Cone; $Re_\infty = 9.38 \times 10^6/\text{ft}$; $T_0 = 971^\circ\text{F}$)

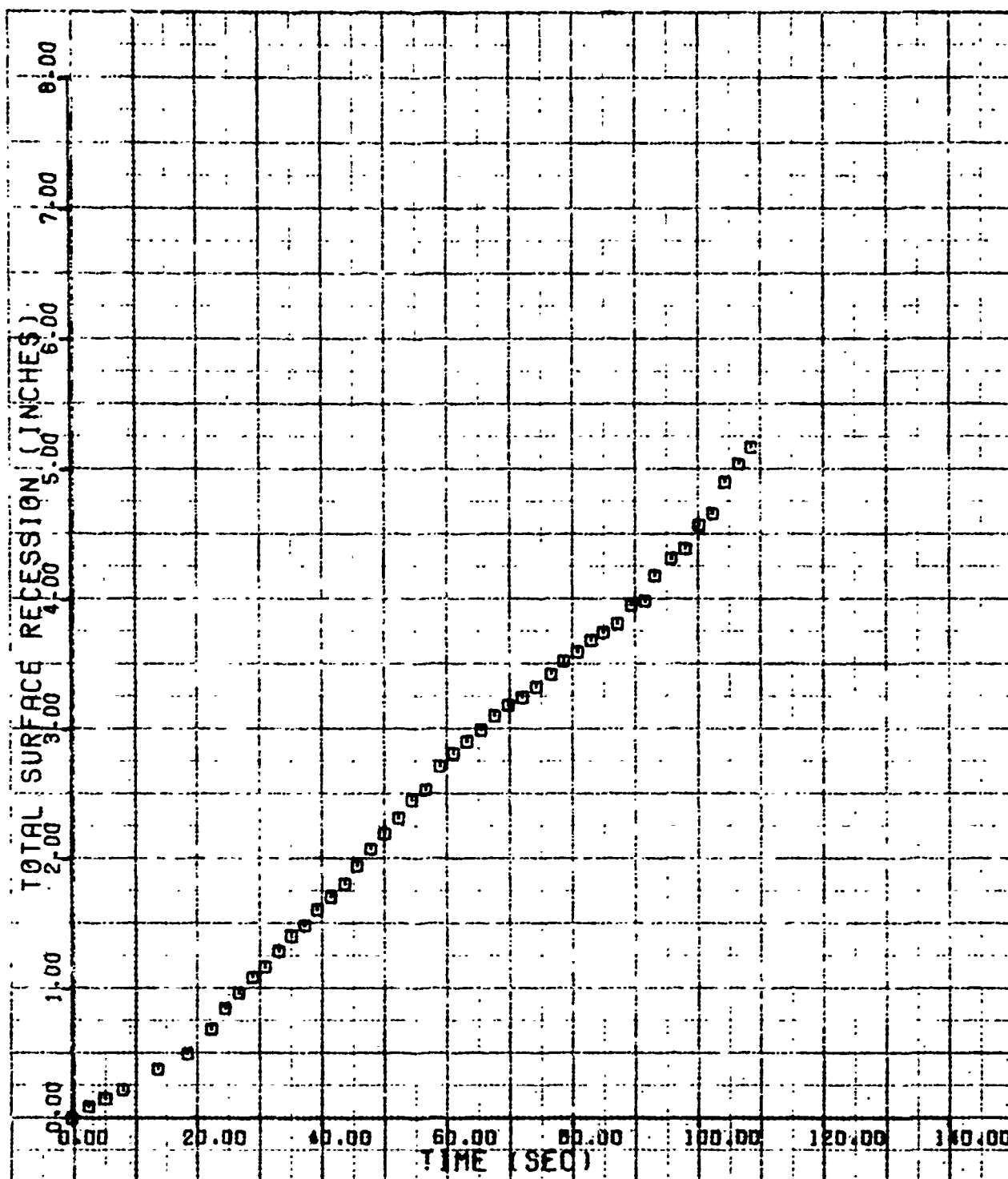


Figure C-11. Stagnation Point Axial Recession for Run 810 (1.5-Inch $R_s/60^\circ/8^\circ$ Biconic; $Re_\infty = 6.73 \times 10^5/\text{ft}$; $T_0 = 964^\circ\text{F}$)

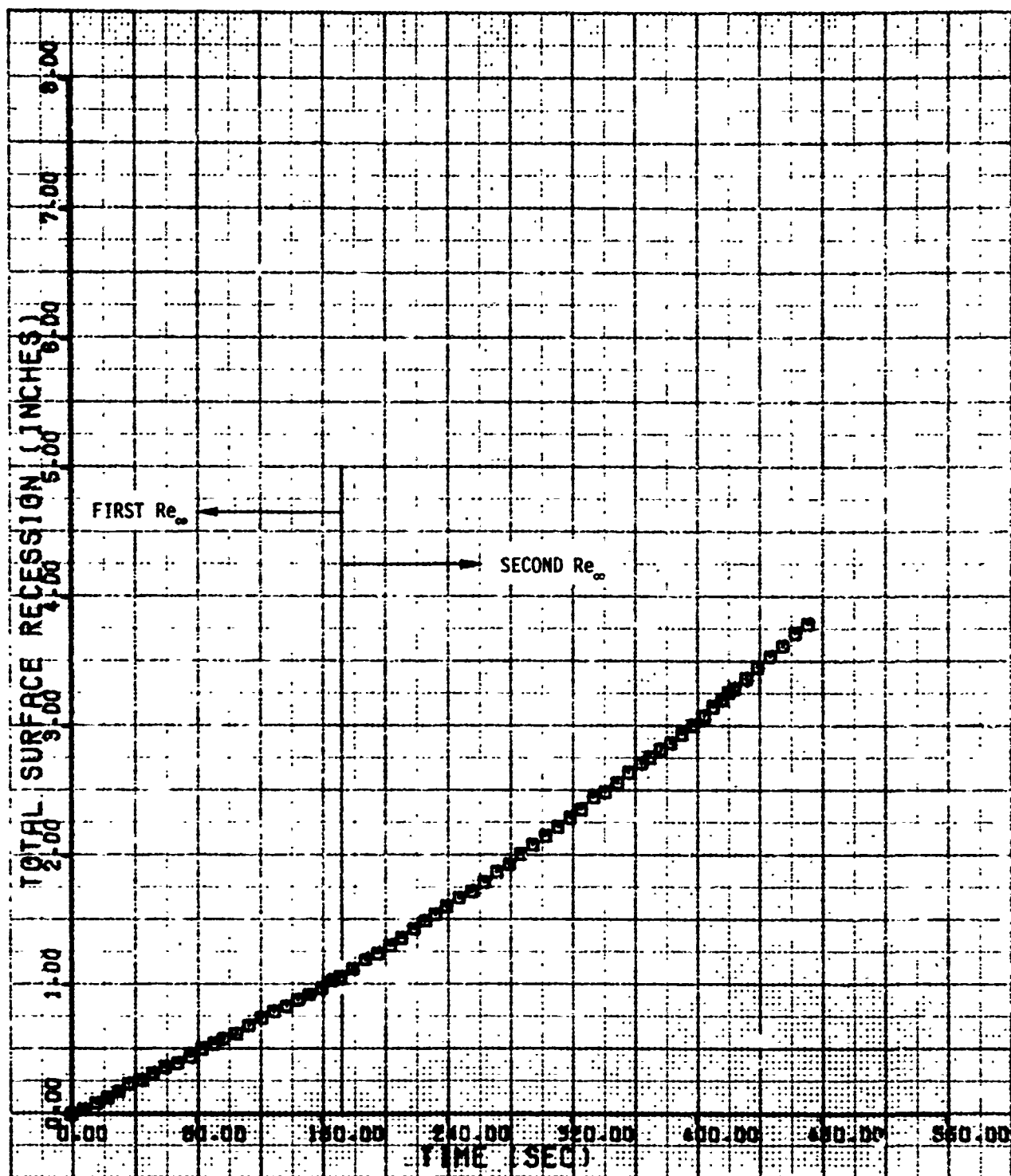


Figure C-12. Stagnation Point Axial Recession for Run 811 (1.5-Inch R_N Sphere-Cone, Particle-Loaded; $Re_{\infty} = 0.77/1.12 \times 10^6/\text{ft}$; $T_0 = 972^\circ\text{F}$)

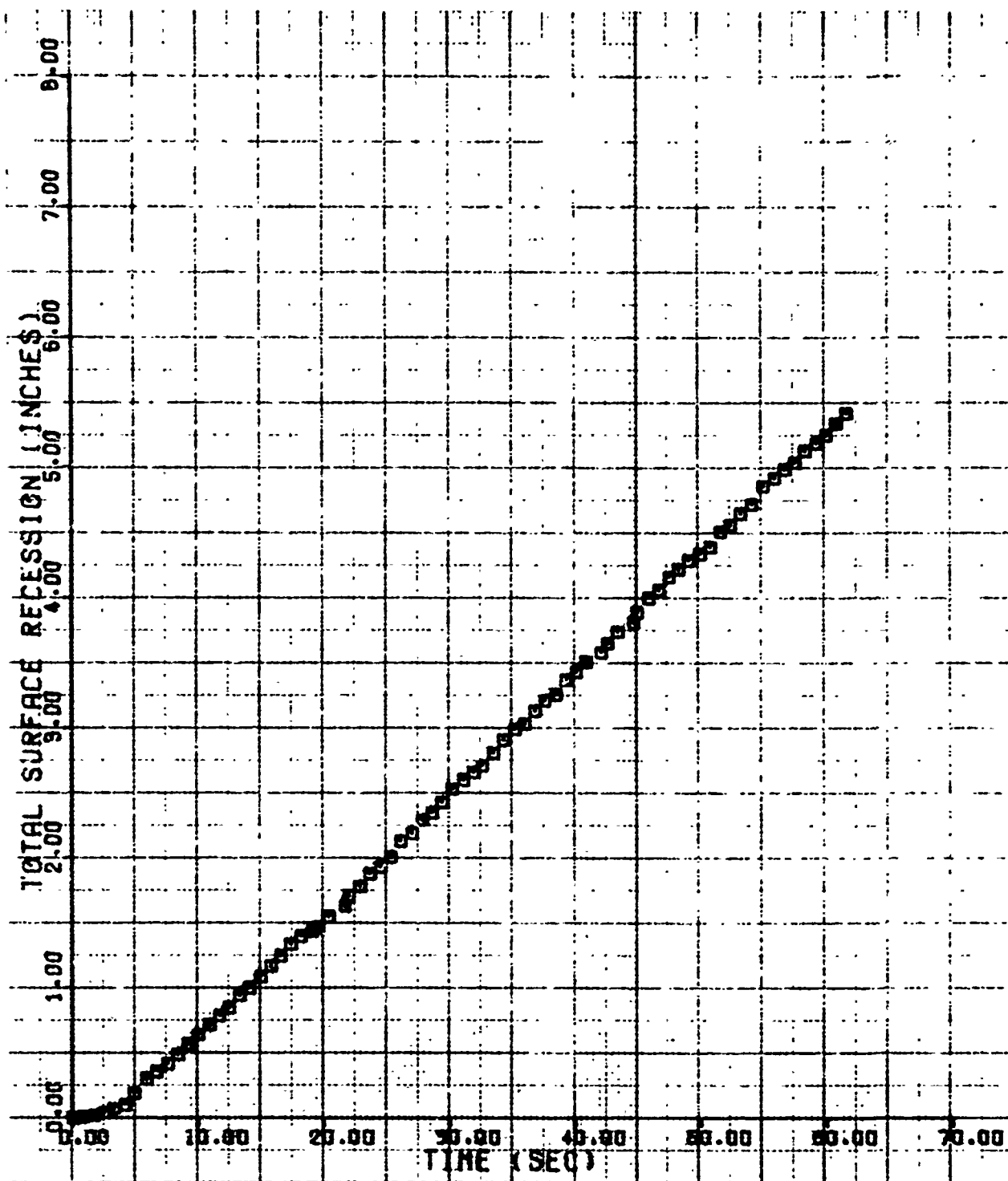


Figure C-13. Stagnation Point Axial Recession for Run 812 (0.75-Inch R_N Sphere-Cone; $Re_\infty = 15.70 \times 10^6/\text{ft}$; $T_0 = 807^\circ\text{F}$)

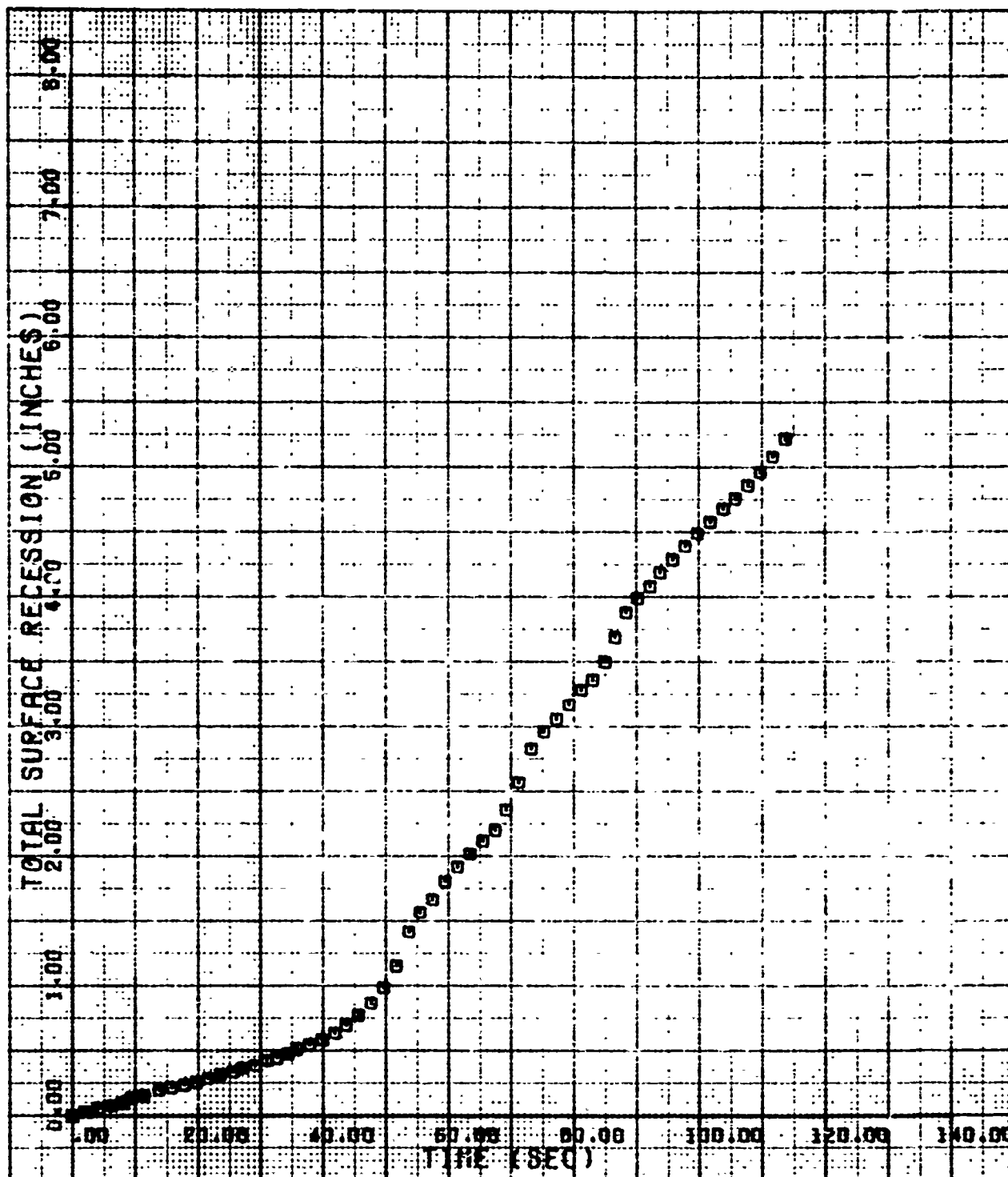


Figure C-14. Stagnation Point Axial Recession for Run 813 (1.5-Inch $R_5/75^\circ/8^\circ$ Biconic; $Re_\infty = 6.70 \times 10^5/\text{ft}$; $T_0 = 970^\circ\text{F}$)

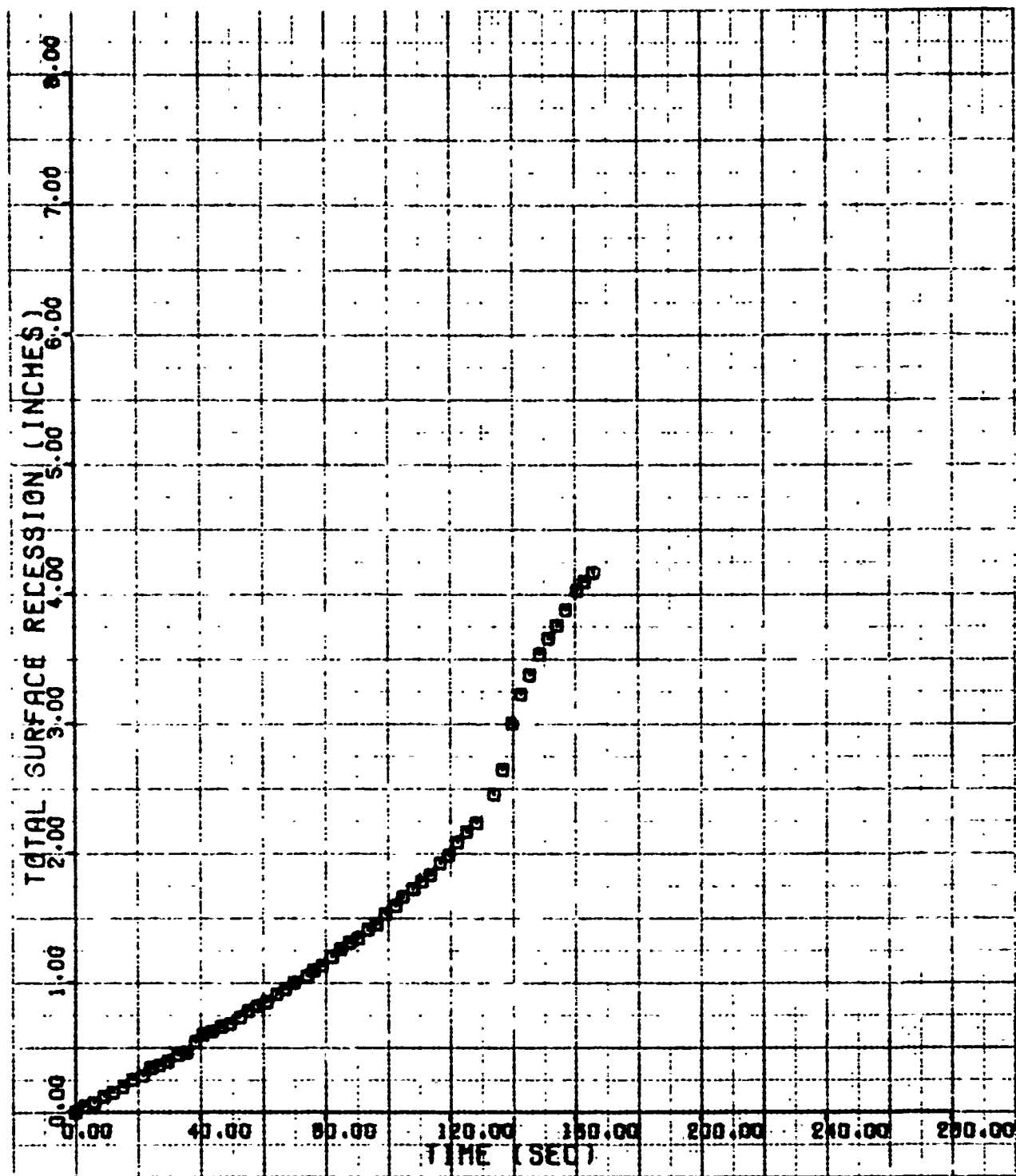


Figure C-15. Stagnation Point Axial Recession for Run 814 (1.5-Inch R_N Sphere-Cone with Three Grooves; $Re_\infty = 4.15 \times 10^6/\text{ft}$; $T_0 = 998^\circ\text{F}$)

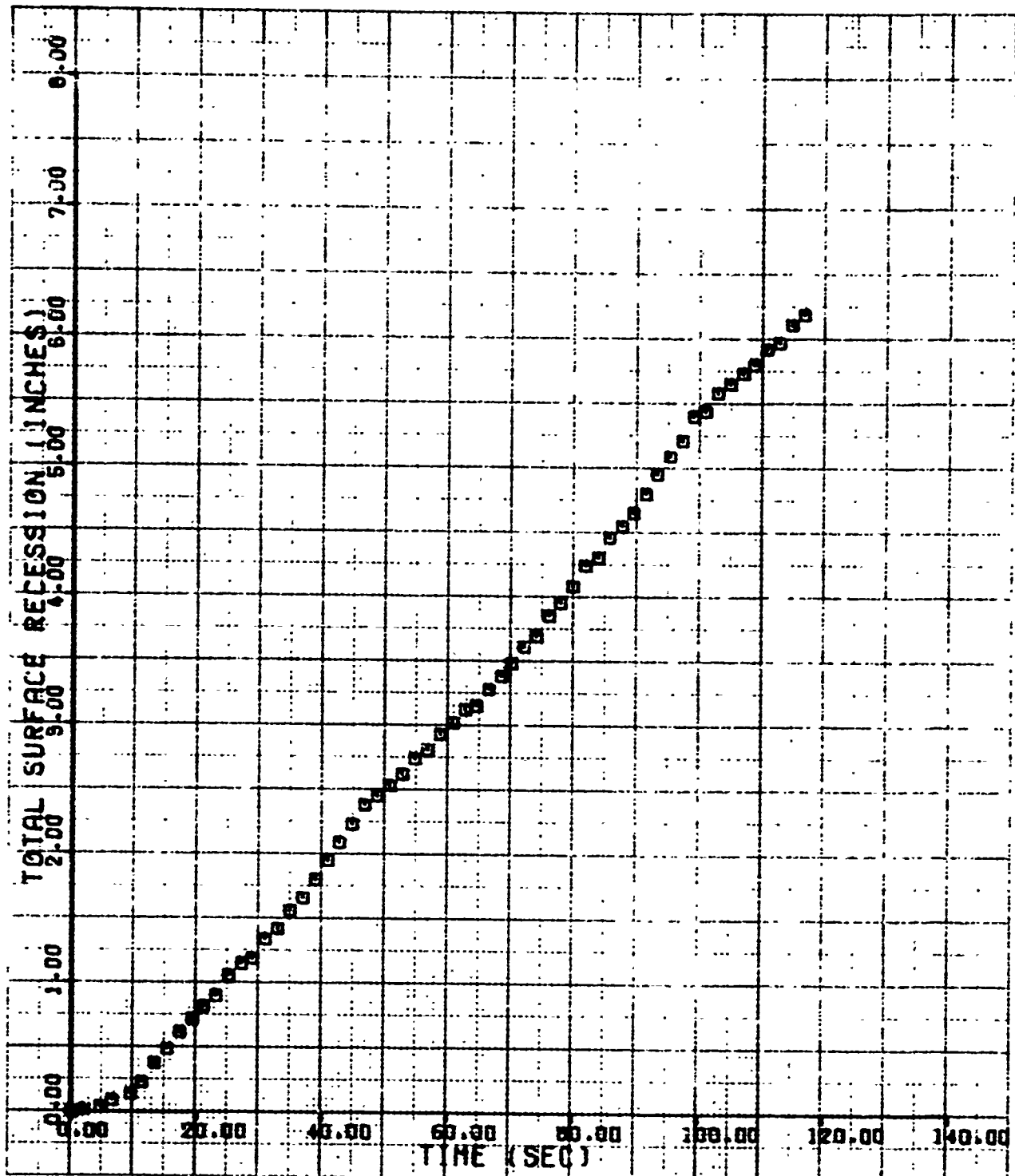


Figure C-16. Signation Point Axial Recession for Run 815 (1.5-Inch R_S Laminar-Blunt;
 $Re_\infty = 6.72 \times 10^4/\text{ft}$; $T_0 = 944^\circ\text{F}$)

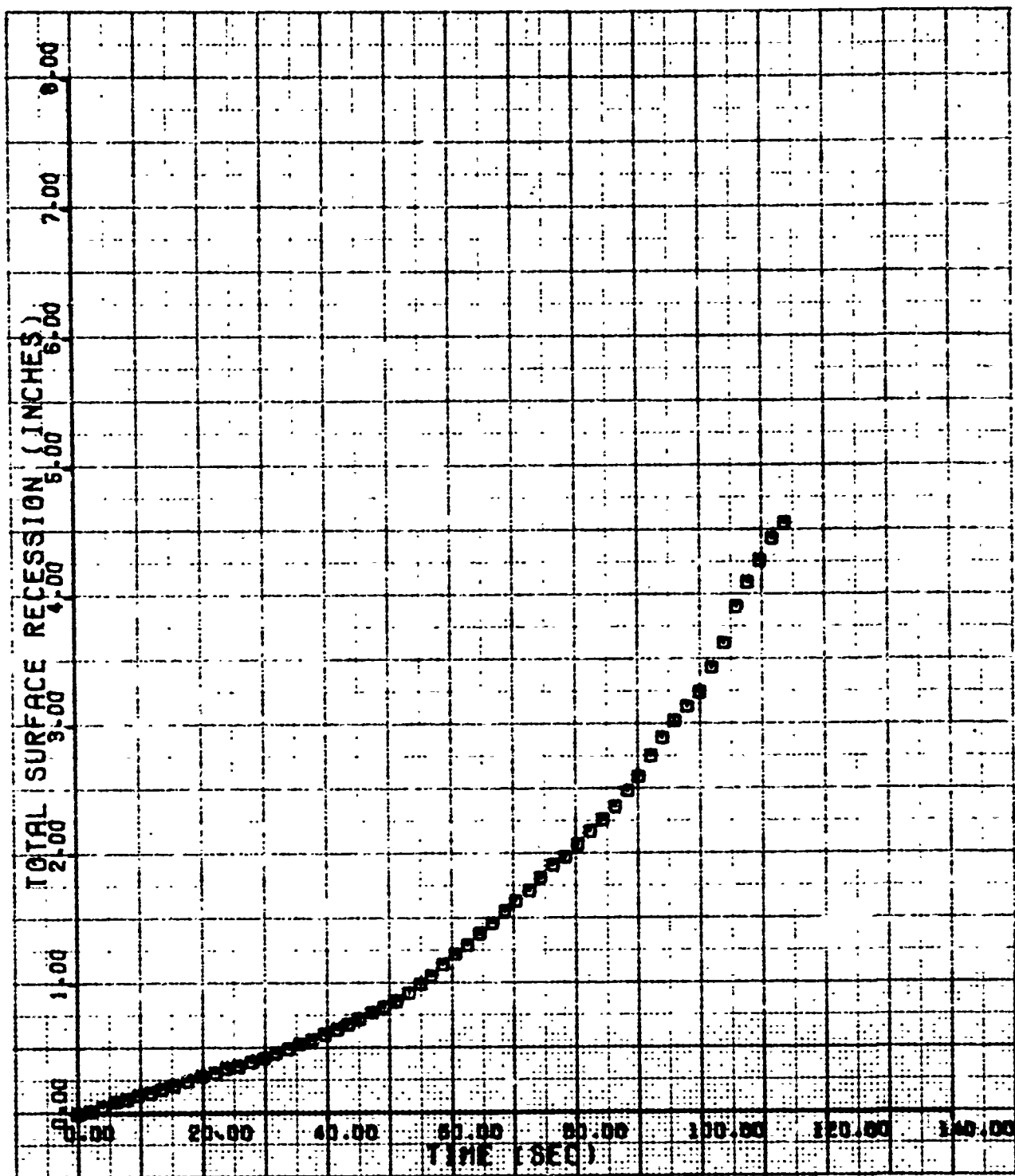


Figure C-17. Stagnation Point Axial Recession for Run 816 (1.5-Inch $R_S/60^\circ/8^\circ$ Biconic; $Re_\infty = 5.20 \times 10^6/\text{ft}$; $T_0 = 954^\circ\text{F}$)

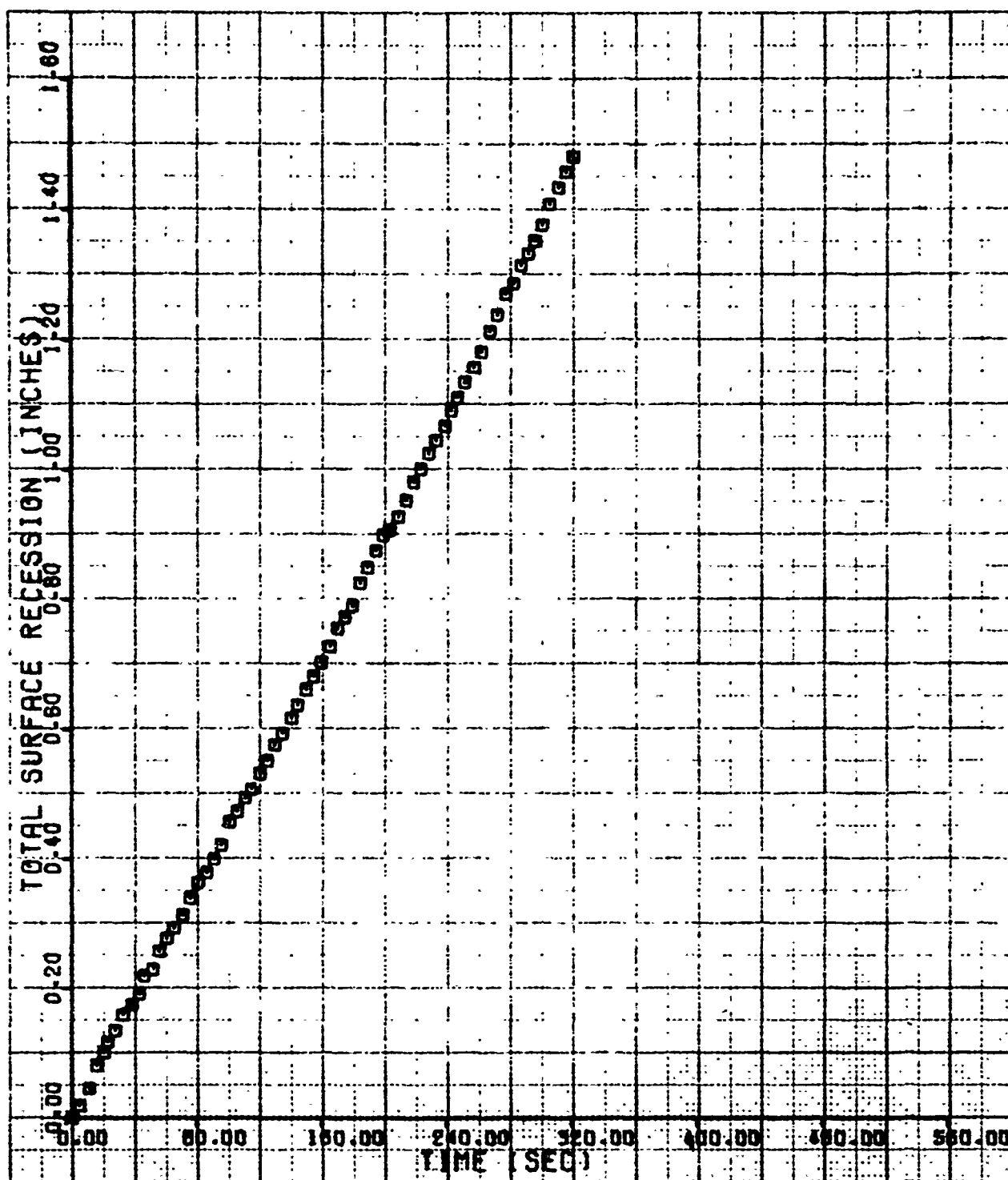


Figure C-18. Stagnation Point Axial Recession for Run 817 (1.5-Inch R_N Sphere-Cone; $Re_w = 6.52 \times 10^6/\text{ft}$; $T_0 = 493^\circ\text{F}$)

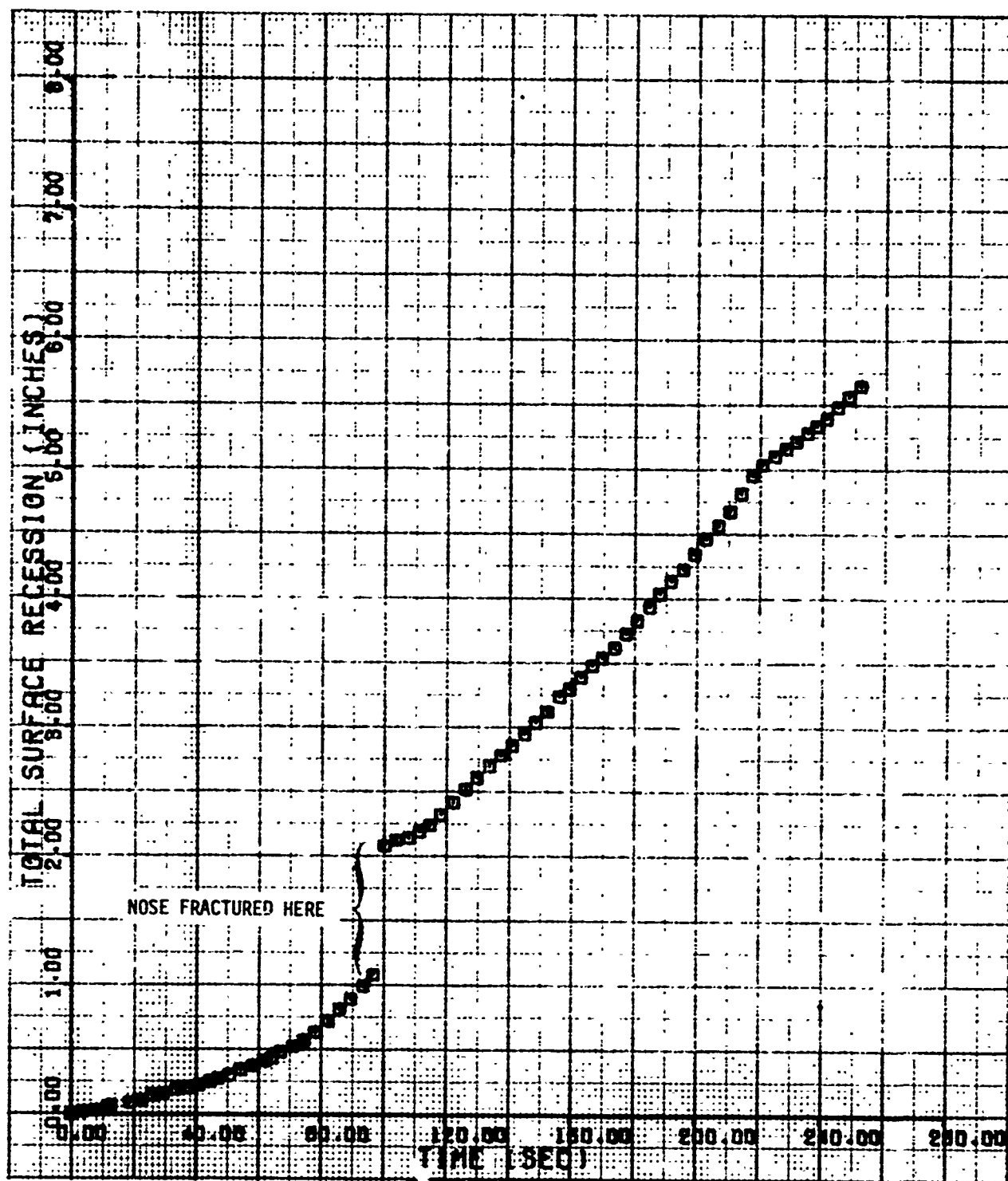


Figure C-19. Stagnation Point Axial Recession for Run 818 (1.5-Inch R_N Sphere-Cone; $Re_\infty = 9.56 \times 10^5/\text{ft}$; $T_0 = 508^\circ\text{F}$)

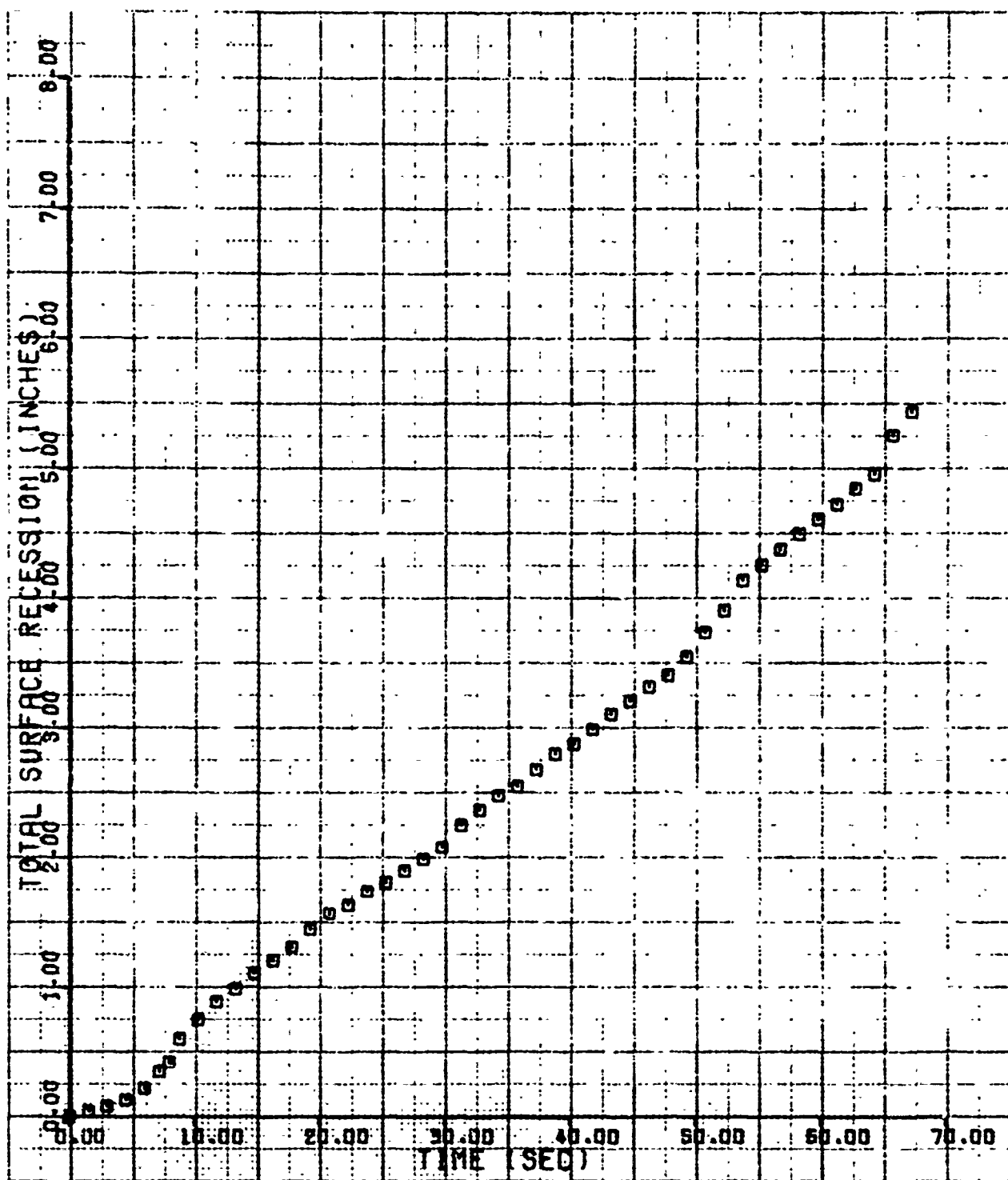


Figure C-20. Stagnation Point Axial Recession for Run 819 (0.75-Inch R_N Sphere-Cone; $Re_\infty = 12.96 \times 10^6/\text{ft}$; $T_0 = 804^\circ\text{F}$)

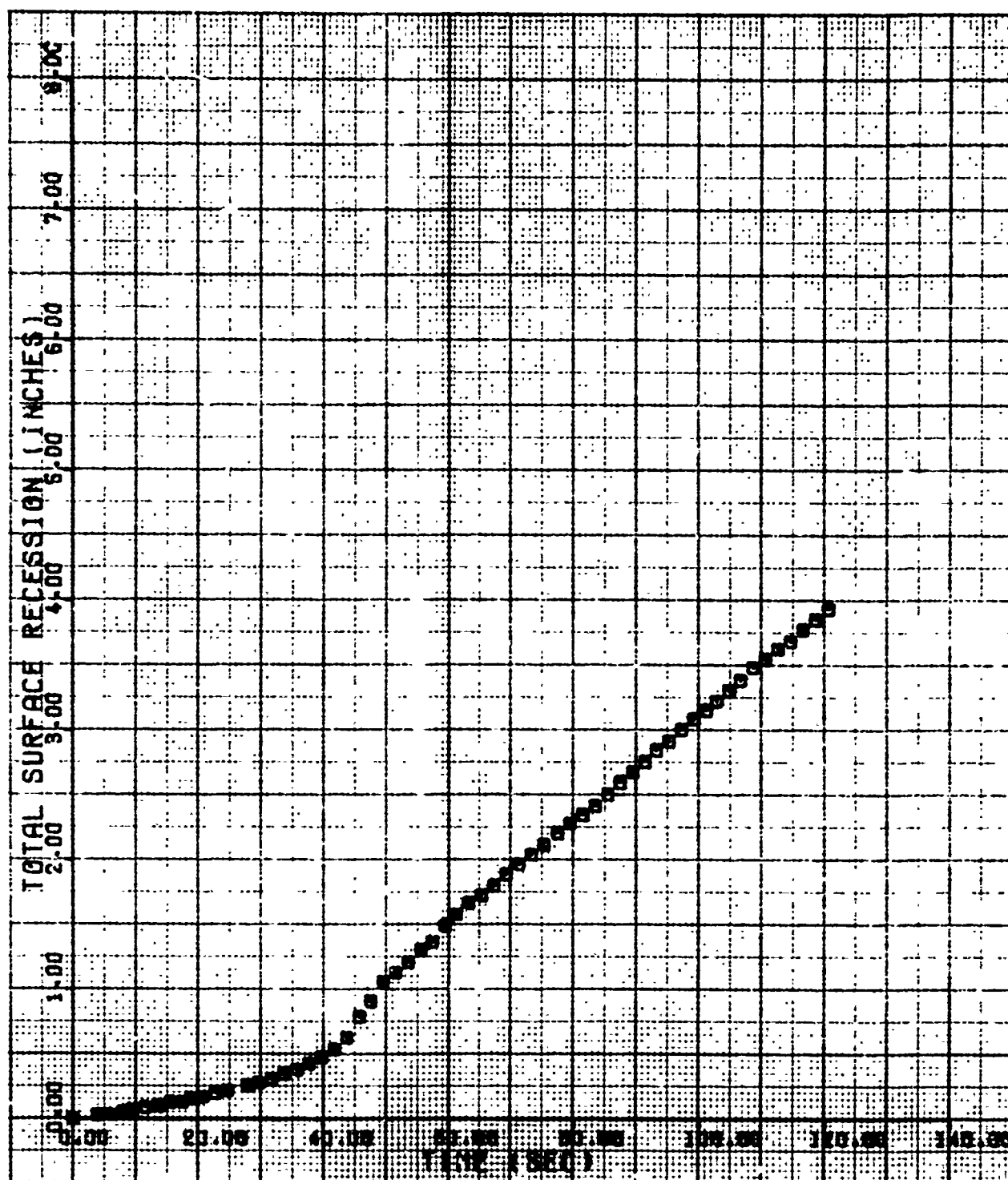


Figure C-21. Stagnation Point Axial Recession for Run 820 (3.5-Inch R_S Laminar-Blunt; $Re_\infty = 4.90 \times 10^5/\text{ft}$; $T_0 = 986^\circ\text{F}$)

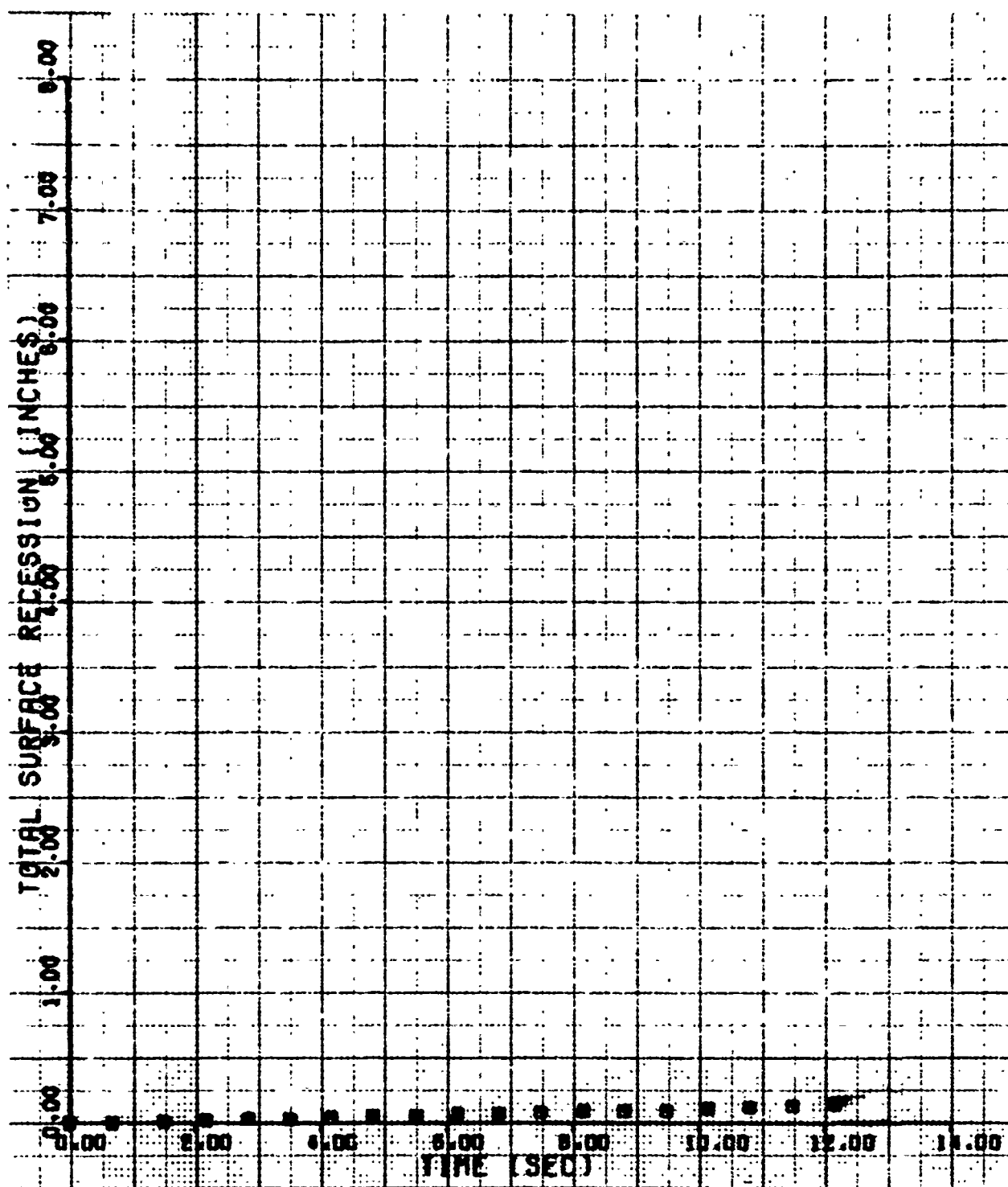


Figure C-22. Stagnation Point Axial Recession for Run 821 (2.5-Inch R_N Sphere-Cone;
 $Re_\infty = 7.47 \times 10^6/\text{ft}$; $T_0 = 973^\circ\text{F}$)

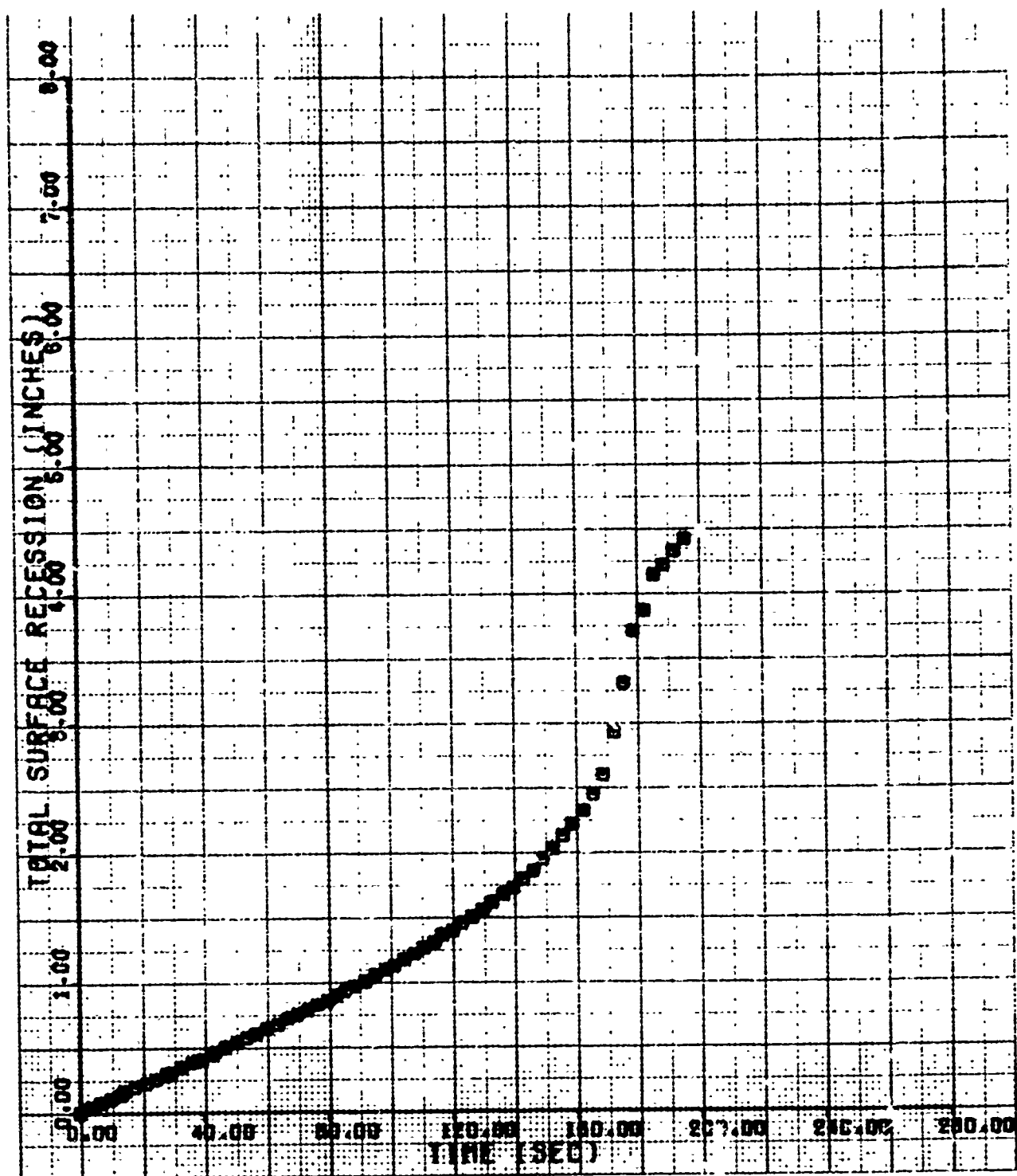


Figure C-23. Stagnation Point Axial Recession for Run 822 (1.5-Inch R_S Laminar-Blunt; $Re_\infty = 4.02 \times 10^5/\text{ft}$; $T_0 = 960^\circ\text{F}$)

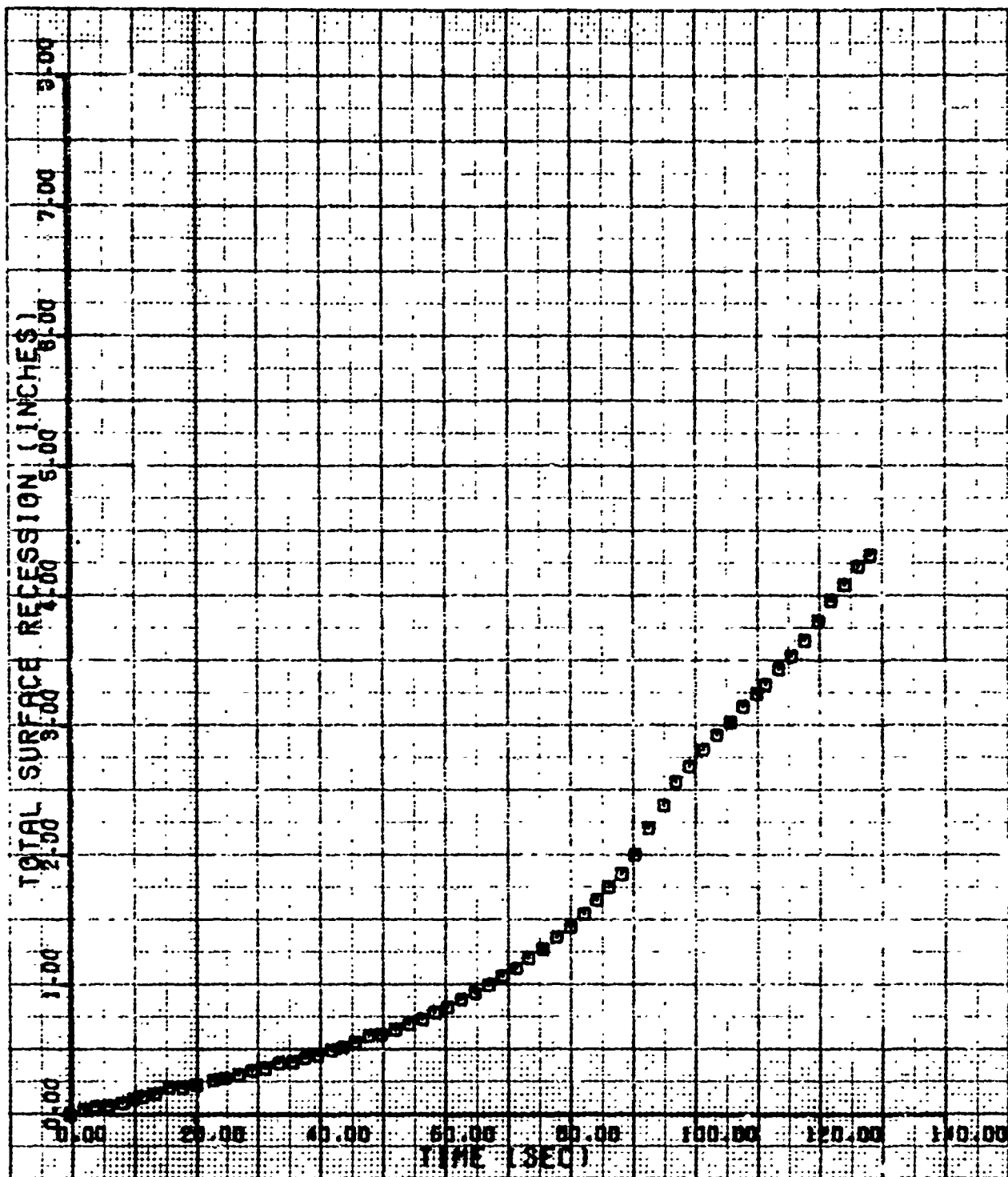


Figure C-24. Stagnation Point Axial Recession for Run 823 (1.5-Inch $R_s/75^\circ/8^\circ$ Biconic; $Re_\infty = 5.18 \times 10^6/\text{ft}$; $T_0 = 986^\circ\text{F}$)

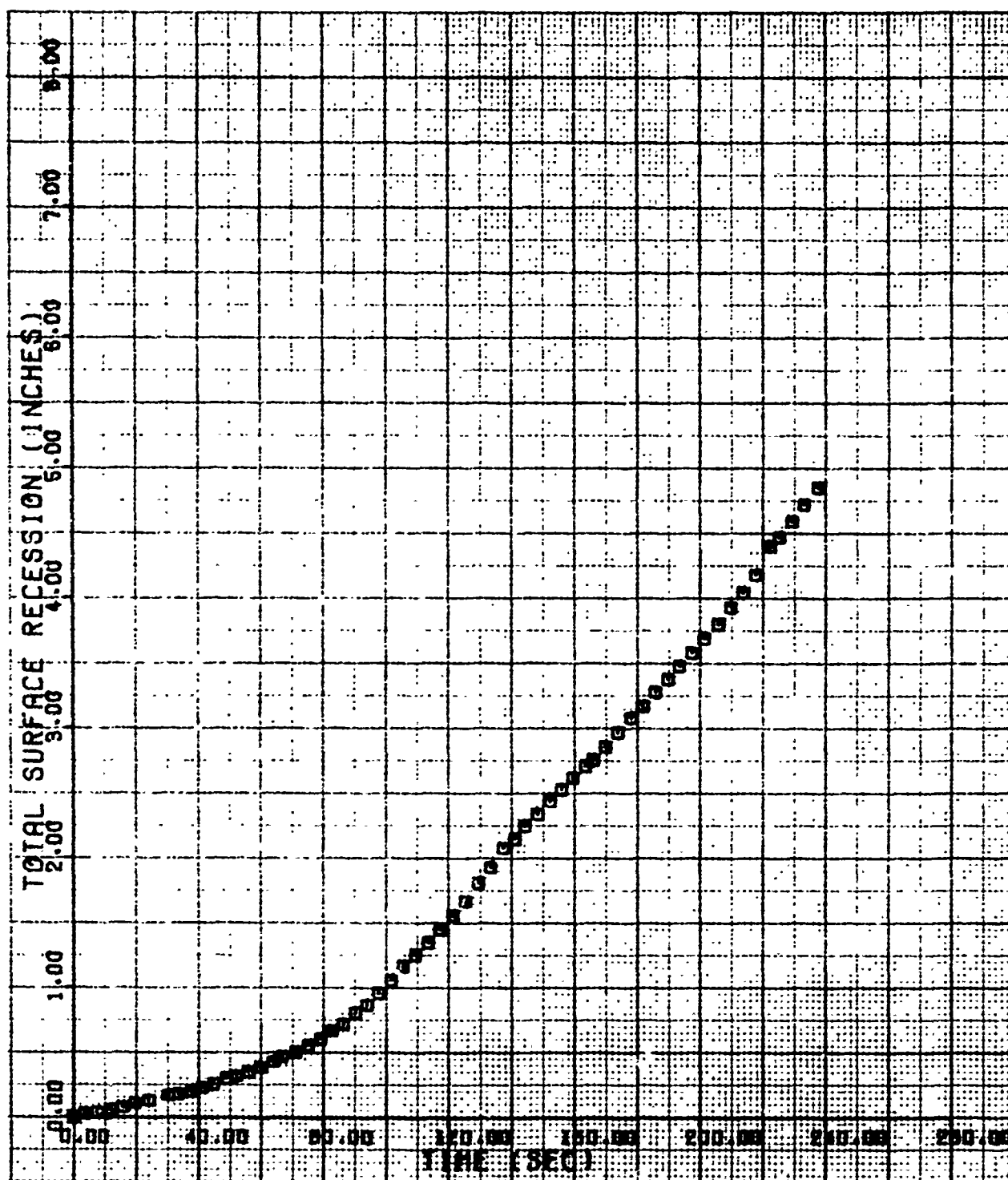


Figure C-25. Stagnation Point Axial Recession for Run 824 (1.5-Inch R_N Sphere-Cone;
 $Re_\infty = 9.44 \times 10^6/\text{ft}$; $T_0 = 535^\circ\text{F}$)

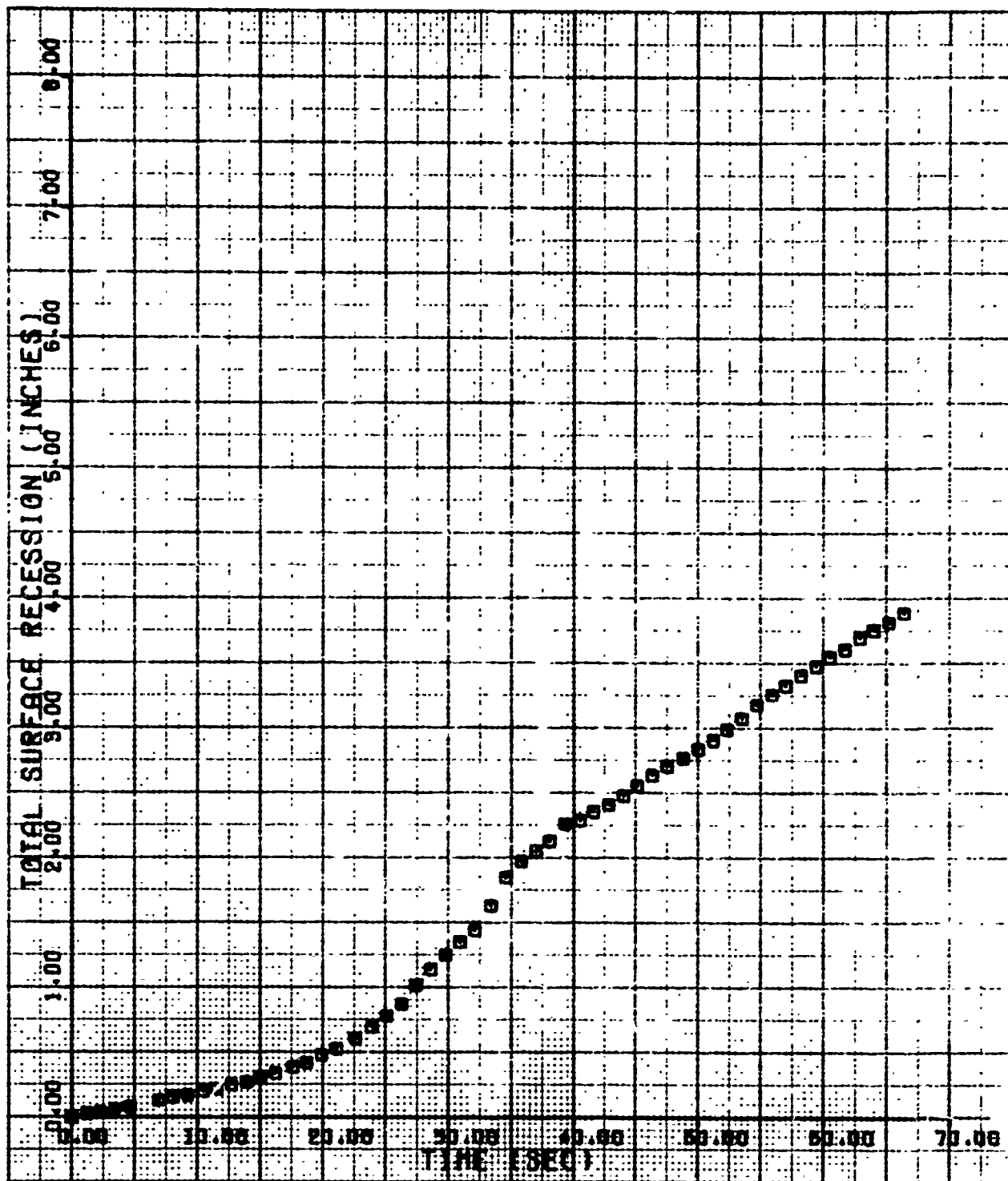


Figure C-26. Stagnation Point Axial Recession for Run 825 (2.5-Inch R_N Sphere-Cone;
 $Re_\infty = 7.20 \times 10^6/\text{ft}$; $T_0 = 990^\circ\text{F}$)

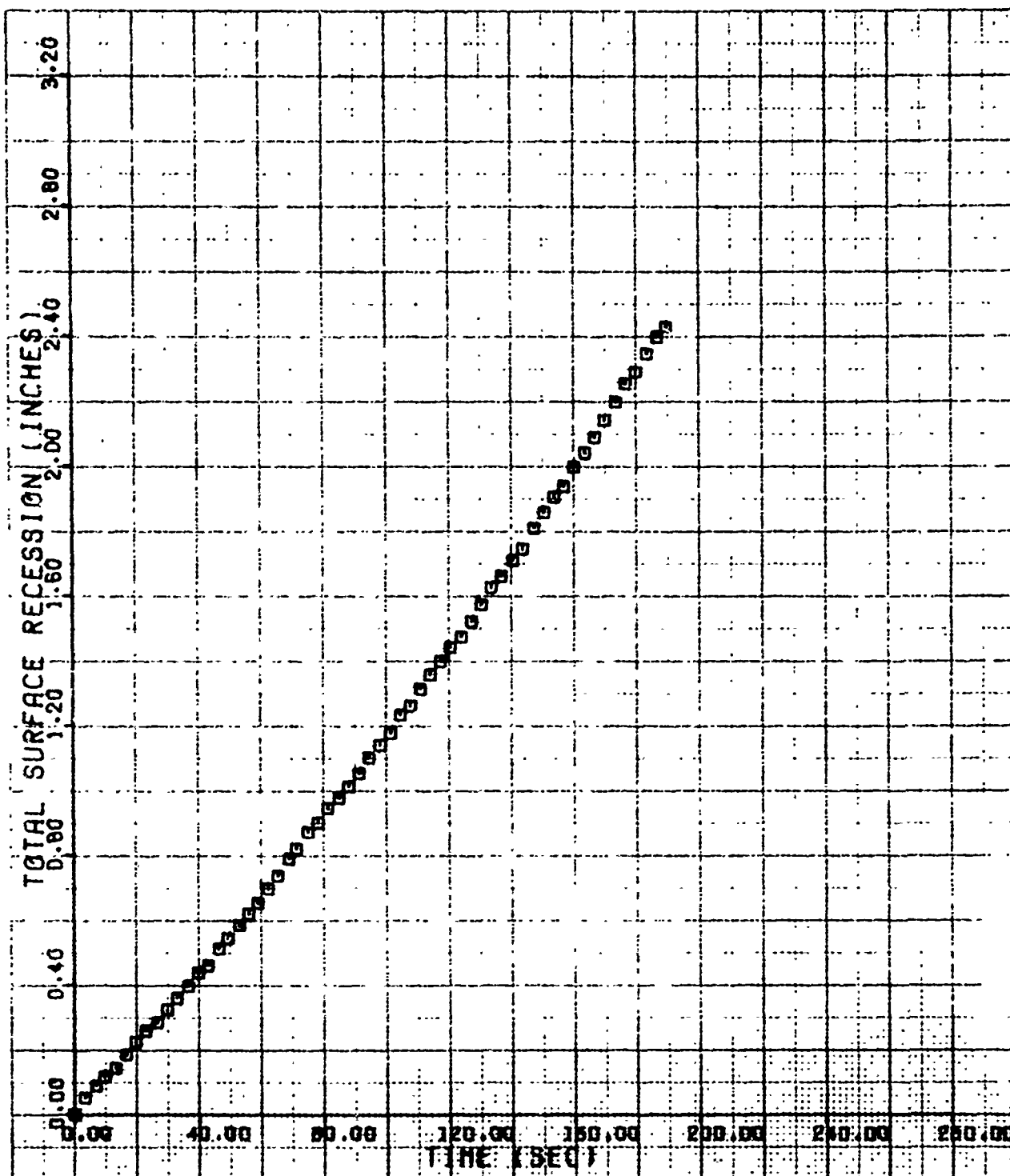


Figure C-27. Stagnation Point Axial Recession for Run 826 (1.5-Inch R_S Laminar-Blunt;
 $Re_\infty = 3.41 \times 10^6/\text{ft}$; $T_0 = 987^\circ\text{F}$)

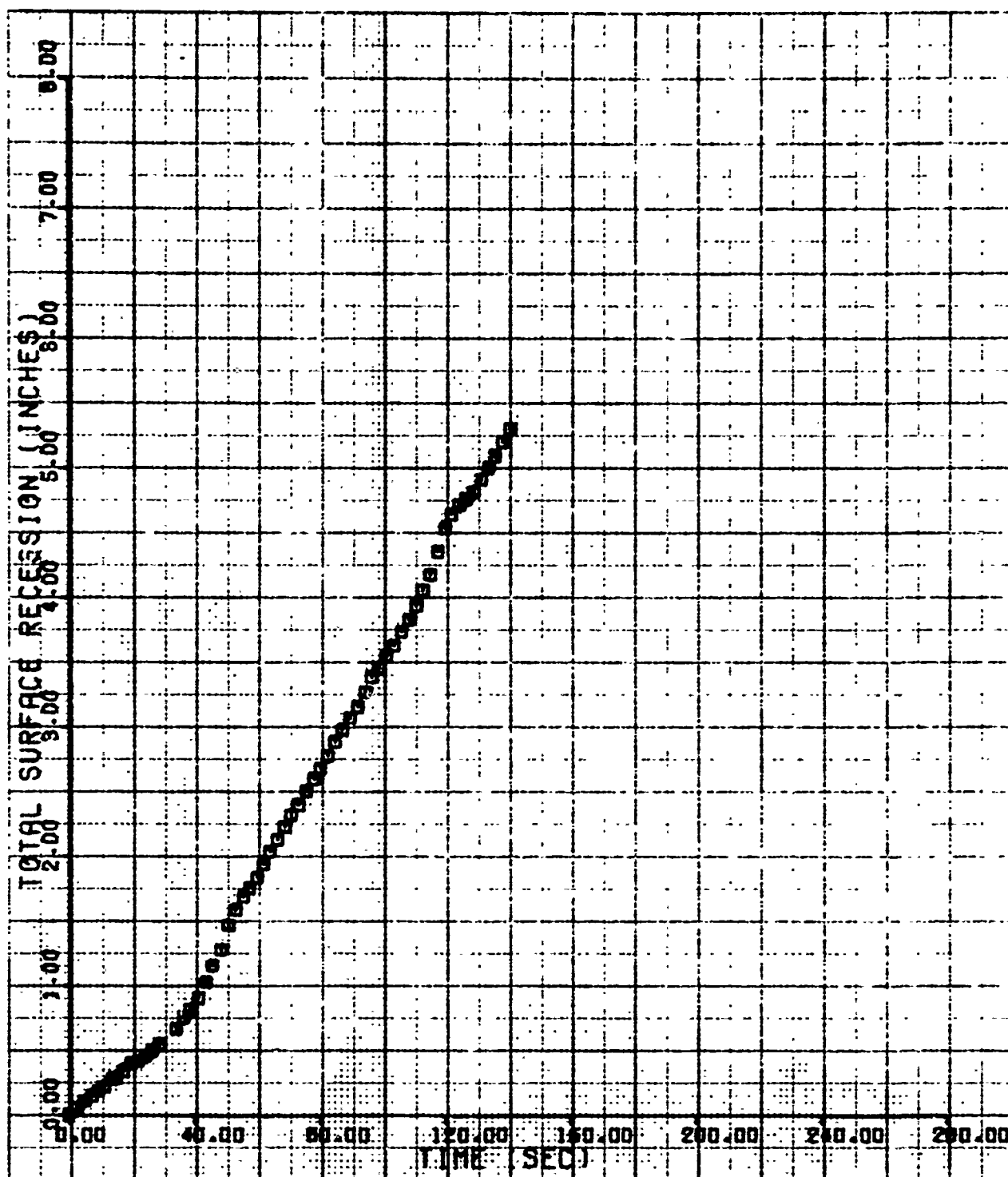


Figure C-28. Stagnation Point Axial Recession for Run 827 (2.5-Inch $R_s/55^\circ/6^\circ$ Biconic;
 $Re_\infty = 4.76 \times 10^6/\text{ft}$; $T_0 = 1008^\circ\text{F}$)

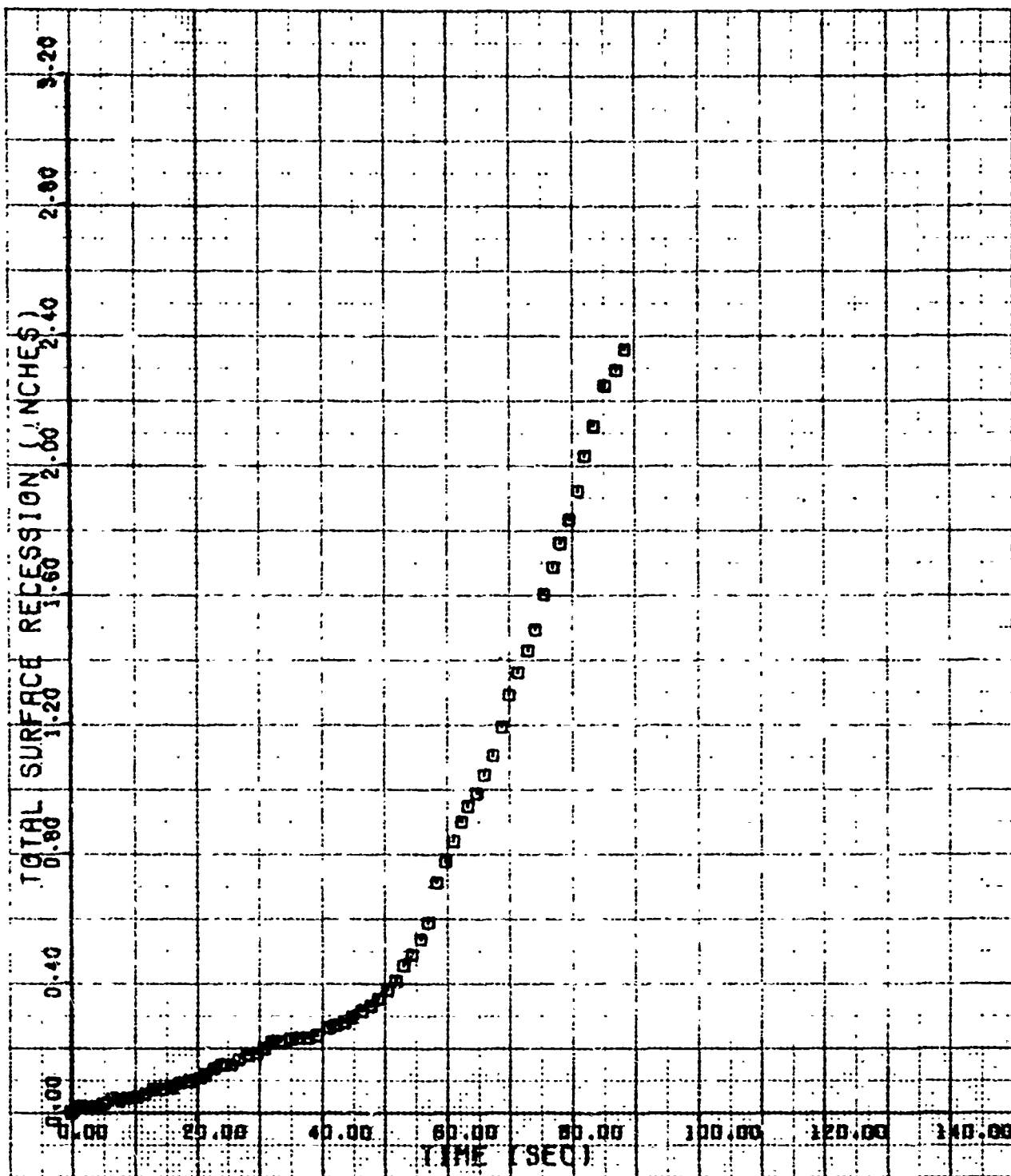


Figure C-29. Stagnation Point Axial Recession for Run 828 (0.75-Inch R_N Sphere-Cone; Variable Re_∞)

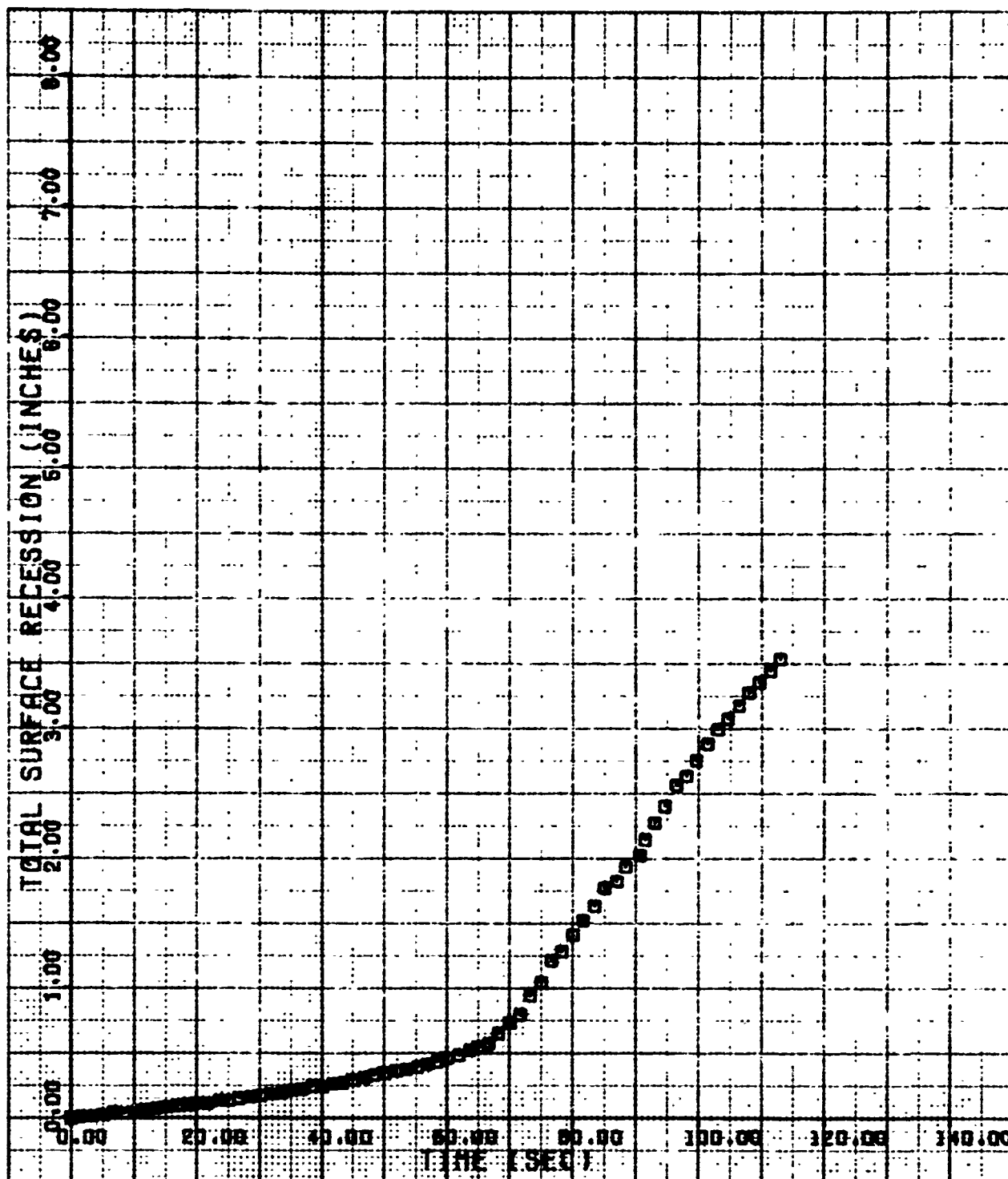


Figure C-30. Stagnation Point Axial Recession for Run 829 (0.75-Inch R_N Sphere-Cone; Variable Re_∞)

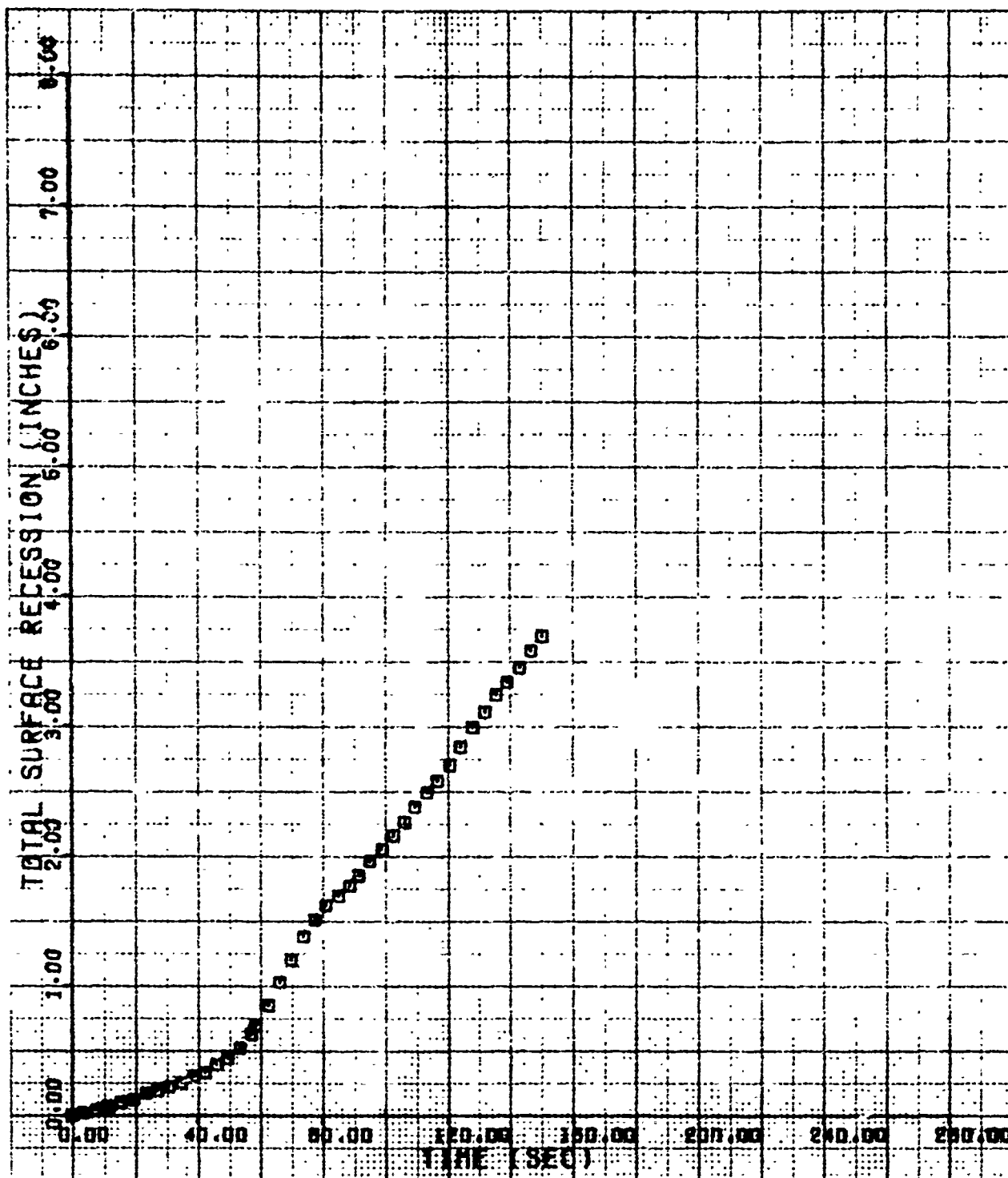


Figure C-31. Stagnation Point Axial Recession for Run 830 (3.5-Inch R_S Laminar-Blunt; $Re_\infty = 3.47 \times 10^6/\text{ft}$; $T_0 = 985^\circ\text{F}$)

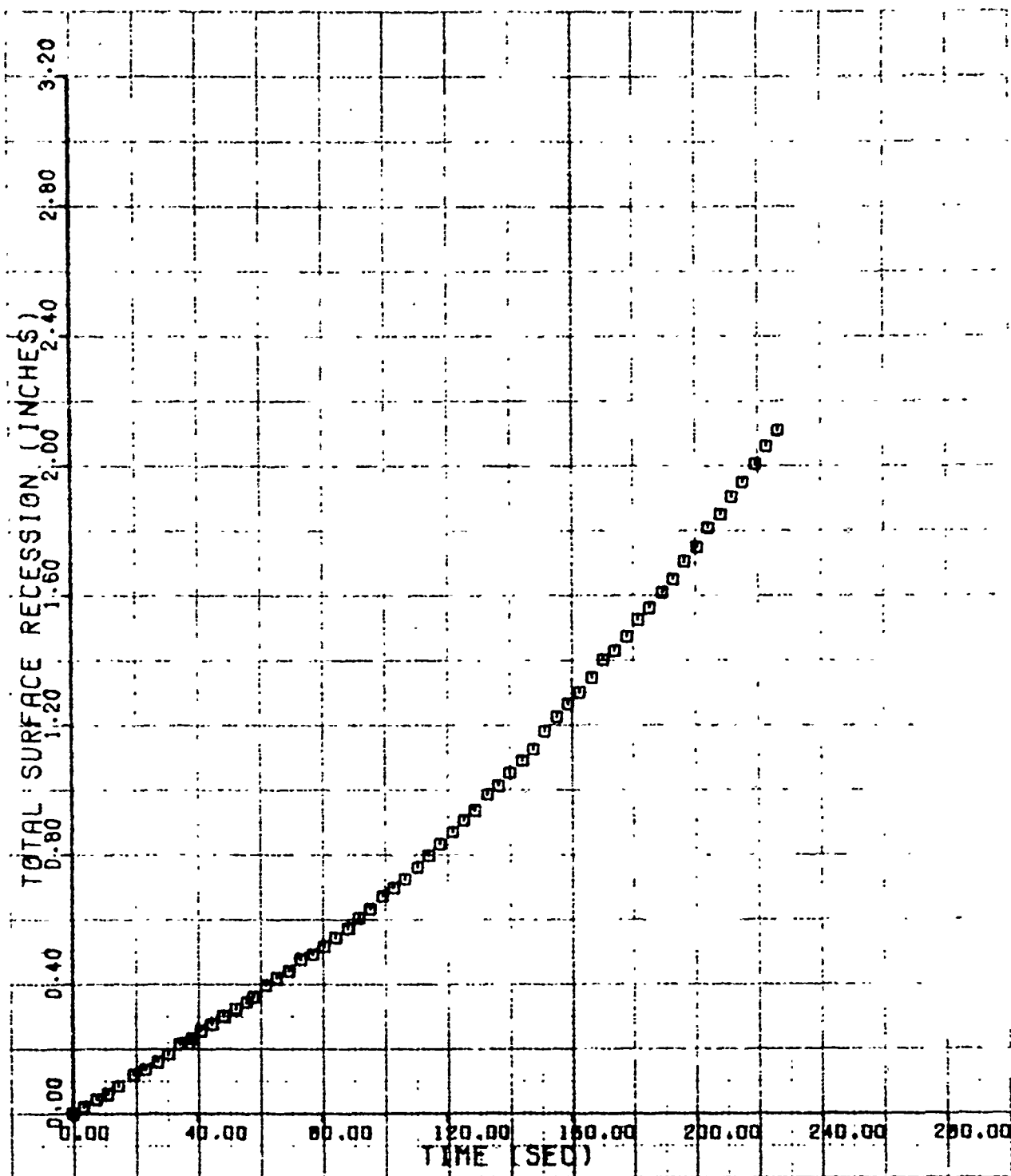


Figure C-32. Stagnation Point Axial Recession for Run 831 (3.5-Inch R_S Laminar-Blunt; $Re_\infty = 2.52 \times 10^6/\text{ft}$; $T_0 = 998^\circ\text{F}$)

APPENDIX D

SELECTED 70MM FRONT-VIEW PHOTOGRAPHS

RUNS 801-803, 805-807, 809, 810,
813-816, 818-828, 830, 831



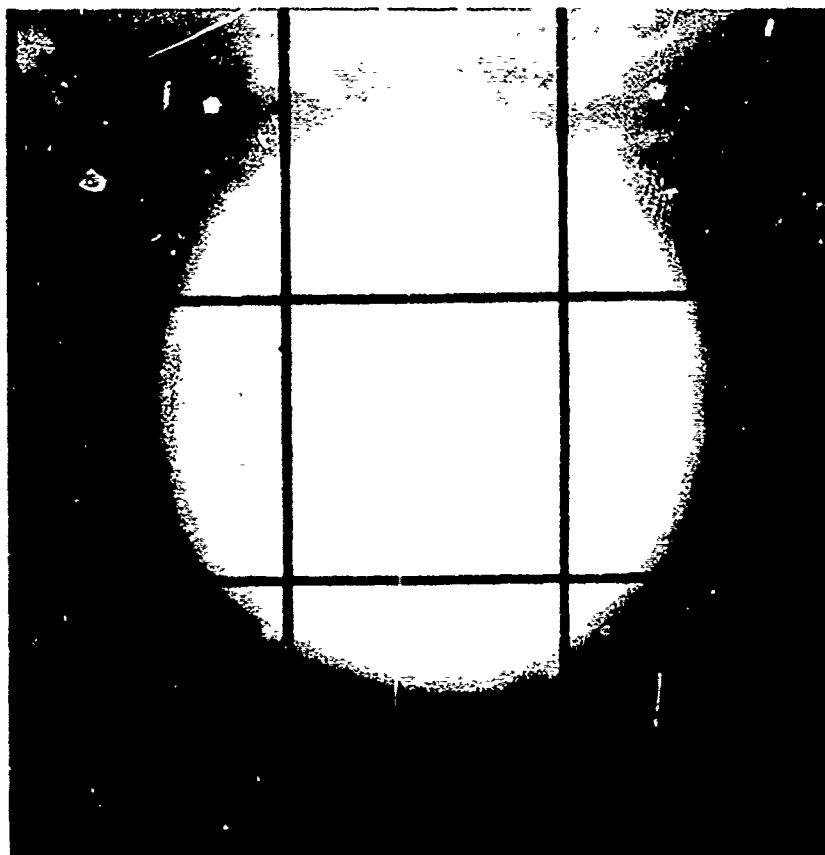
1a. 15.82 seconds

Run 801
1.5-inch RN Sphere-Cone
 $Re_{\infty} = 3.44 \times 10^6 / ft$, $T_0 = 953^{\circ}F$



1b. 10.35 seconds

Run 802
1.5-inch RN Sphere-Cone
 $Re_{\infty} = 4.09 \times 10^6 / ft$, $T_0 = 970^{\circ}F$



2a.

21.52 seconds



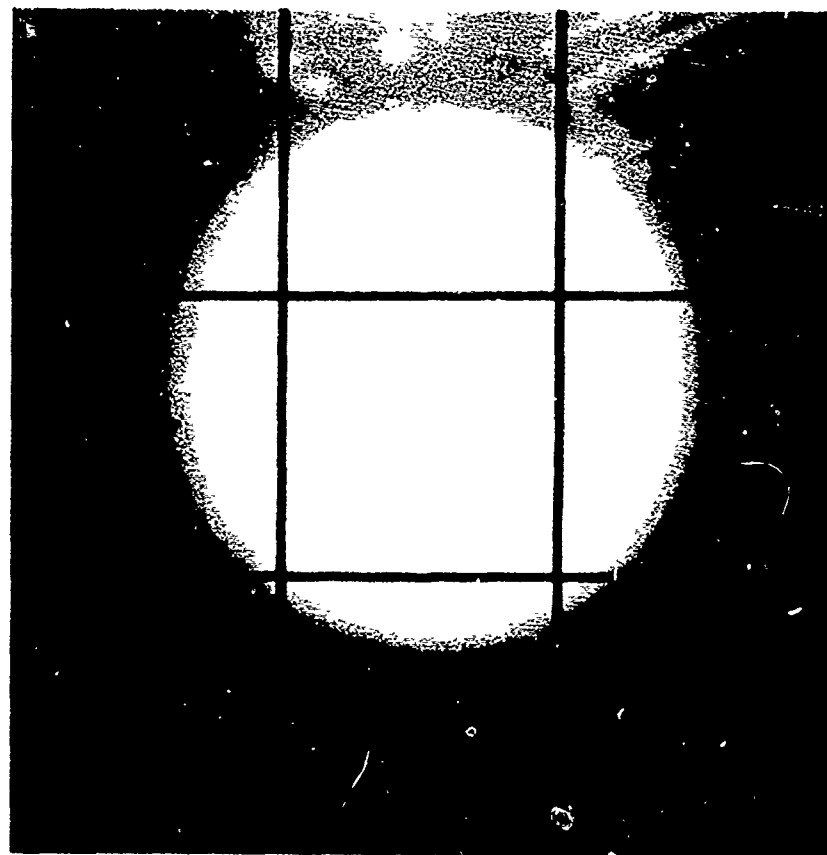
2b.

43.19 seconds

Run 802
1.5-inch R_g Sphere-Cone
 $Re_{\infty} = 4.09 \times 10^6/\text{ft}$, $T_0 = 970^\circ\text{F}$



3a. 10.53 seconds



3b. 30.60 seconds

Run 803
1.5-inch RN Sphere-Cone
 $Re_{\infty} = 6.54 \times 10^6 / ft$, $T_o = 927^{\circ}F$



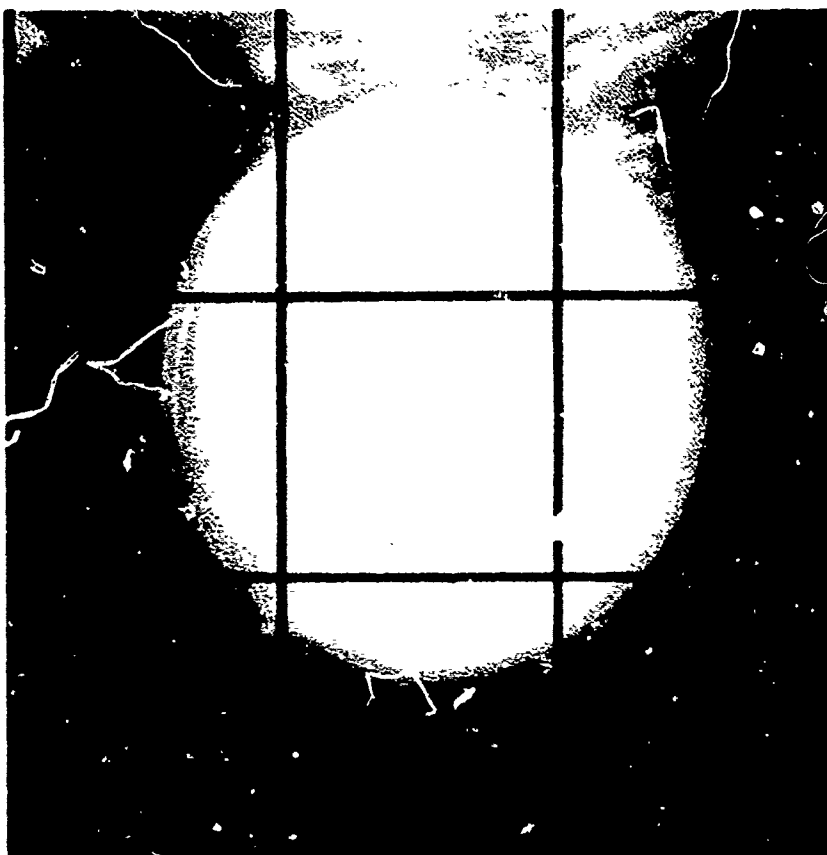
4a.

58.89 seconds

Run 803

1.5-inch RN Sphere-Cone

$Re_{\infty} = 6.54 \times 10^6 / ft, T_o = 927^{\circ}F$



4b.

6.20 seconds

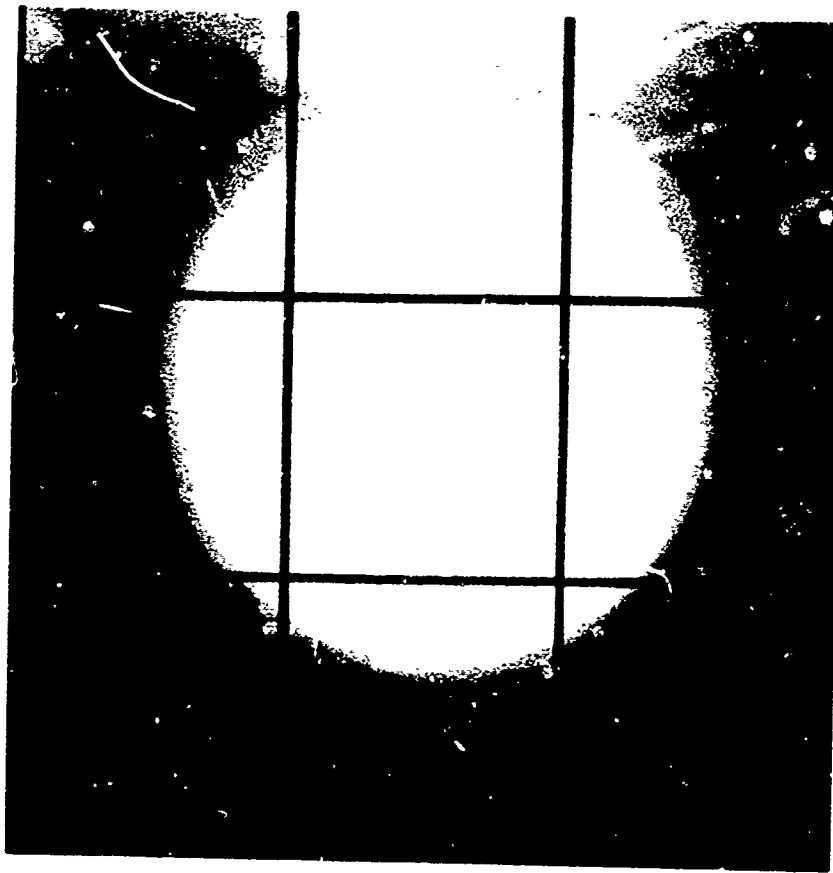
Run 805

1.5-inch RN Sphere-Cone

$Re_{\infty} = 6.56 \times 10^6 / ft, T_o = 987^{\circ}F$

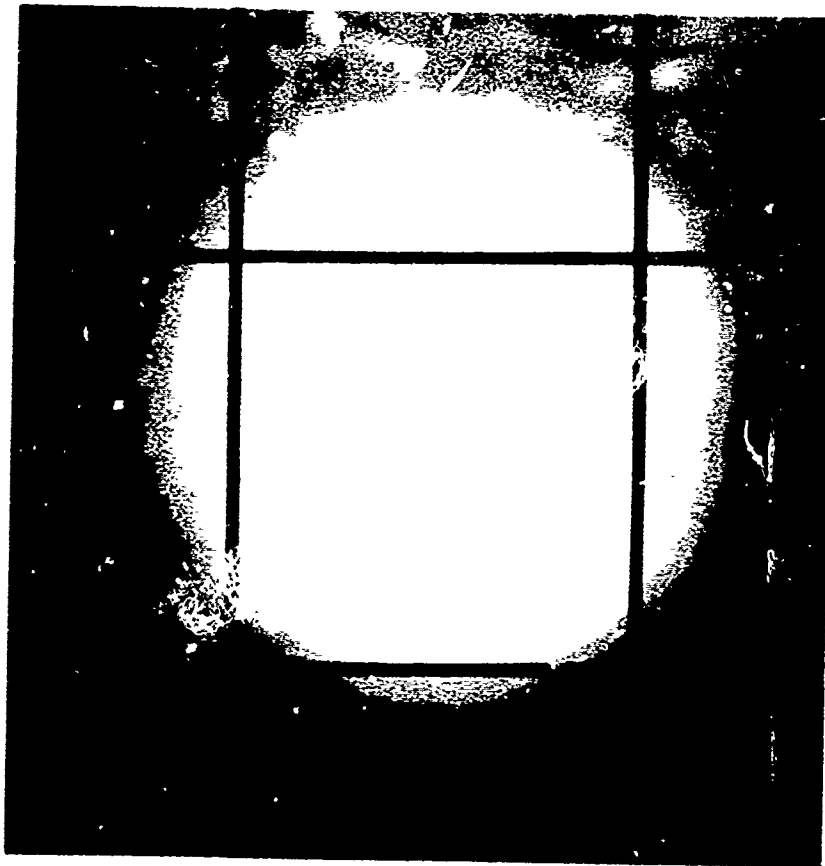


5a. 11.74 seconds

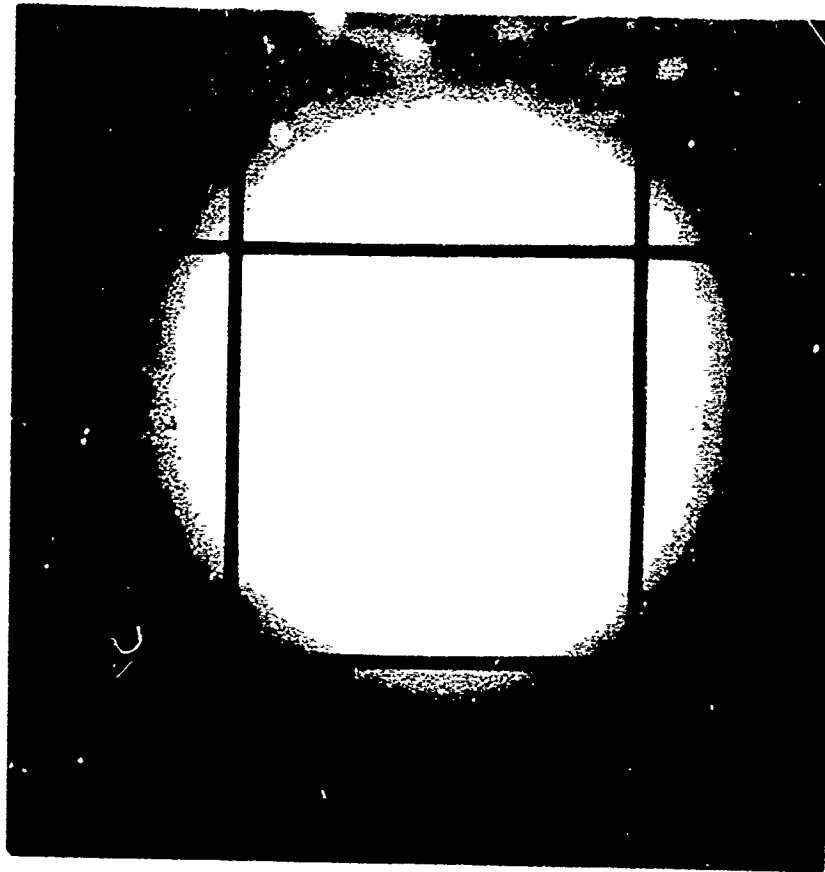


5b. 19.13 seconds

Run 805
1.5-inch RN Sphere-Cone
 $Re_{\infty} = 6.56 \times 10^6 / ft, T_o = 987^{\circ}F$

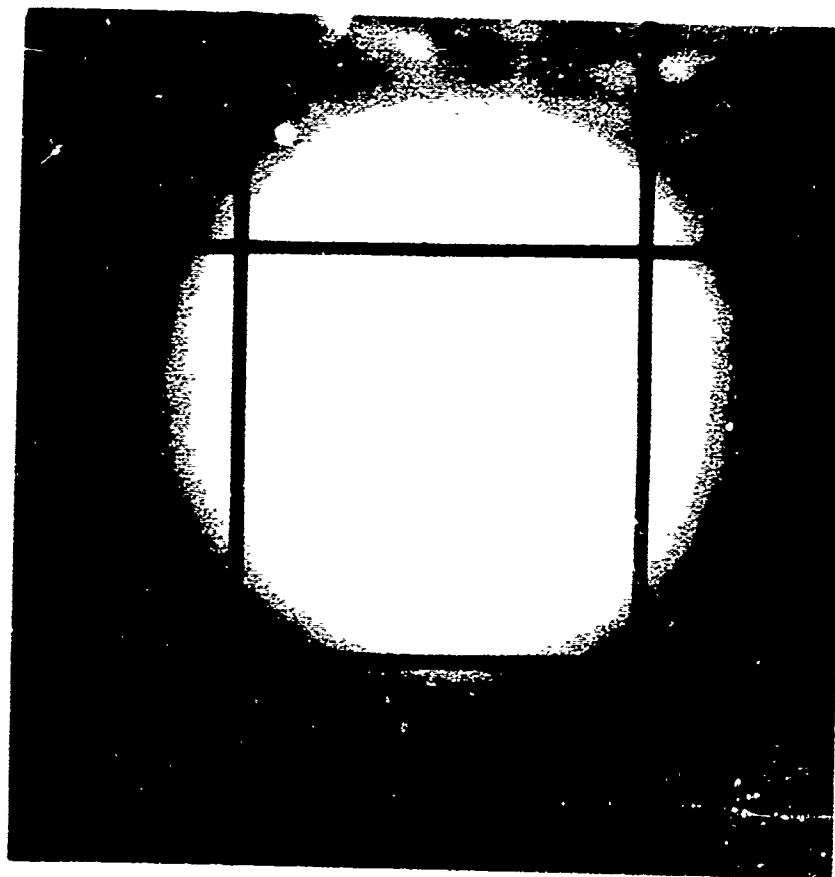


6a. 4.70 seconds



6b. 9.73 seconds

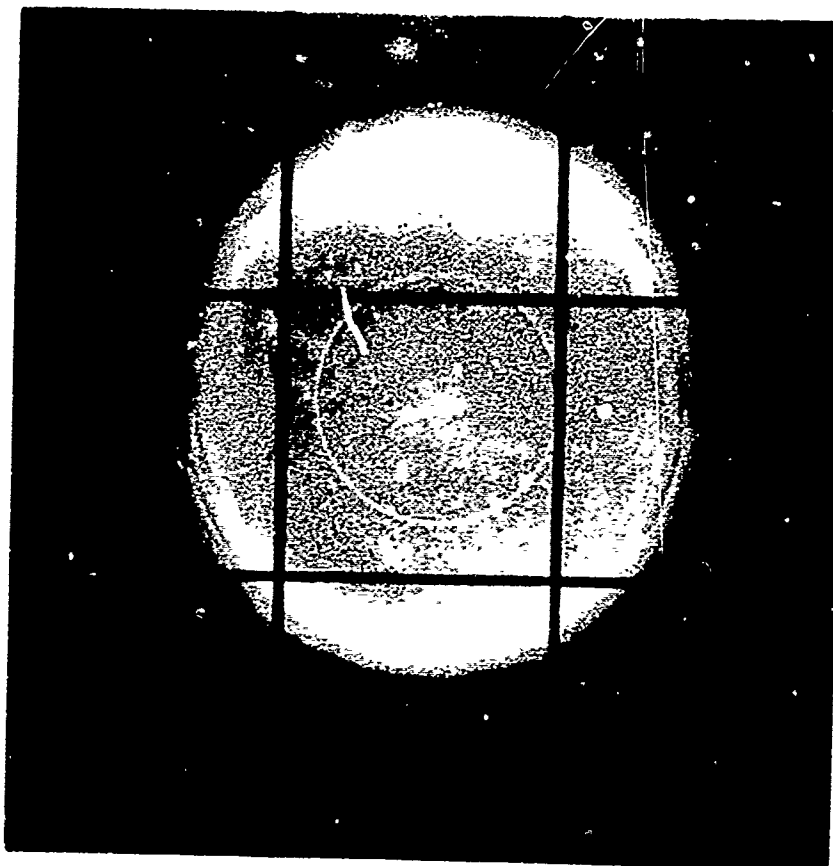
Run 806
0.75-inch R_N Sphere-Cone
 $Re_{\infty} = 7.36 \times 10^6$, $T_0 = 921^{\circ}F$



7a.

14.79 seconds

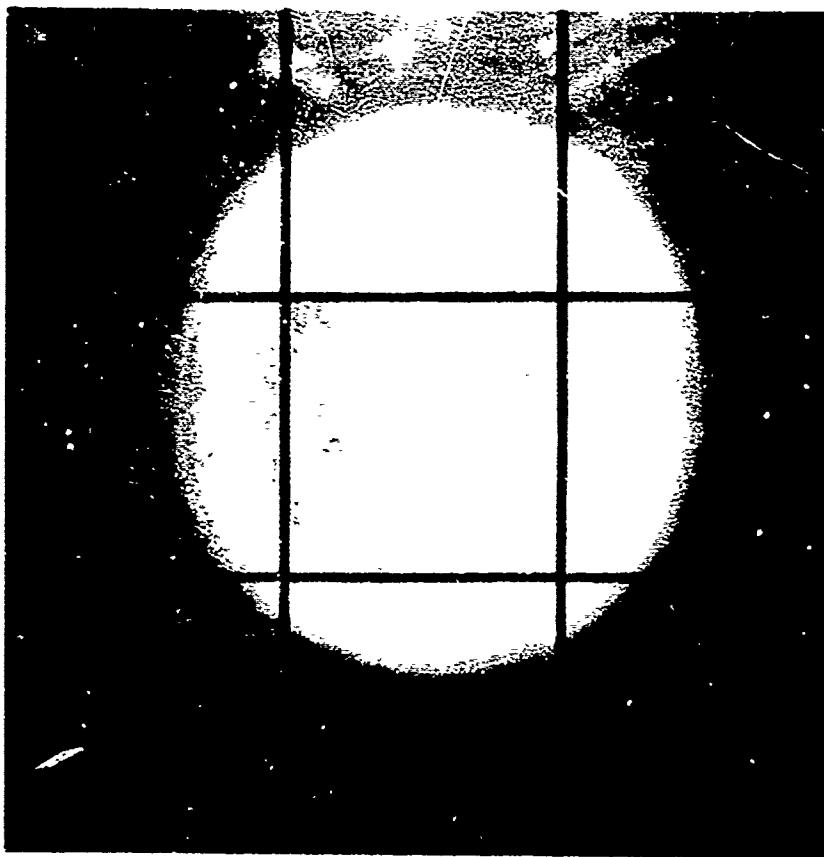
Run 806
0.75-inch R_N Sphere-Cone
 $Re_\infty = 7.36 \times 10^6/\text{ft}$, $T_0 = 921^\circ\text{F}$



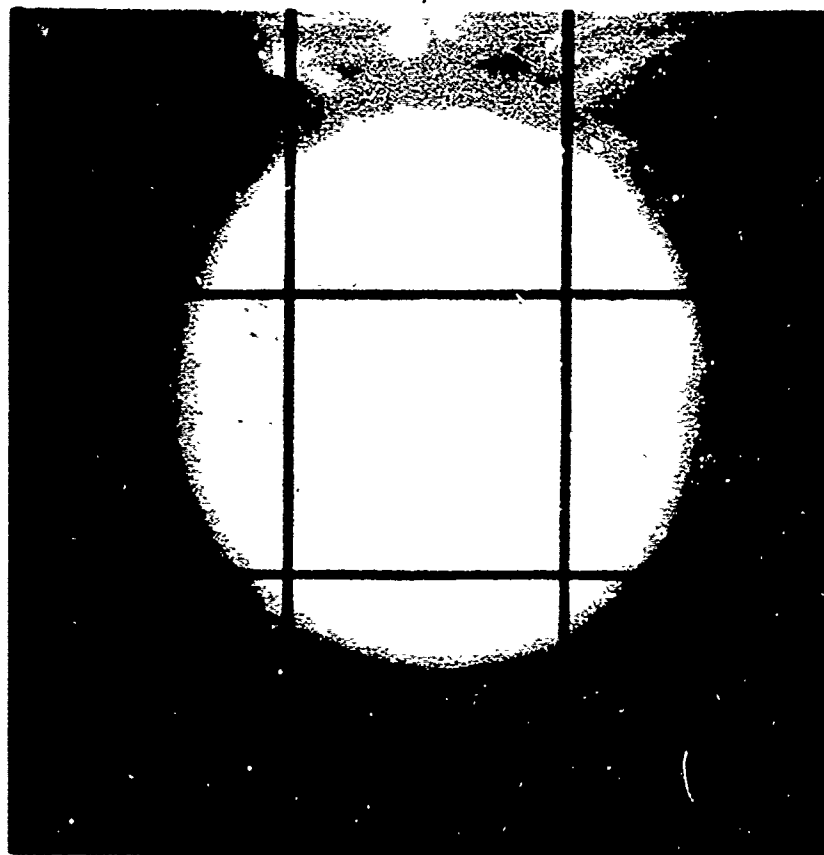
7b.

0 seconds

Run 807
1.5-inch R_N Sphere-Cone with Groove
 $Re_\infty = 4.08 \times 10^6/\text{ft}$, $T_0 = 1013^\circ\text{F}$

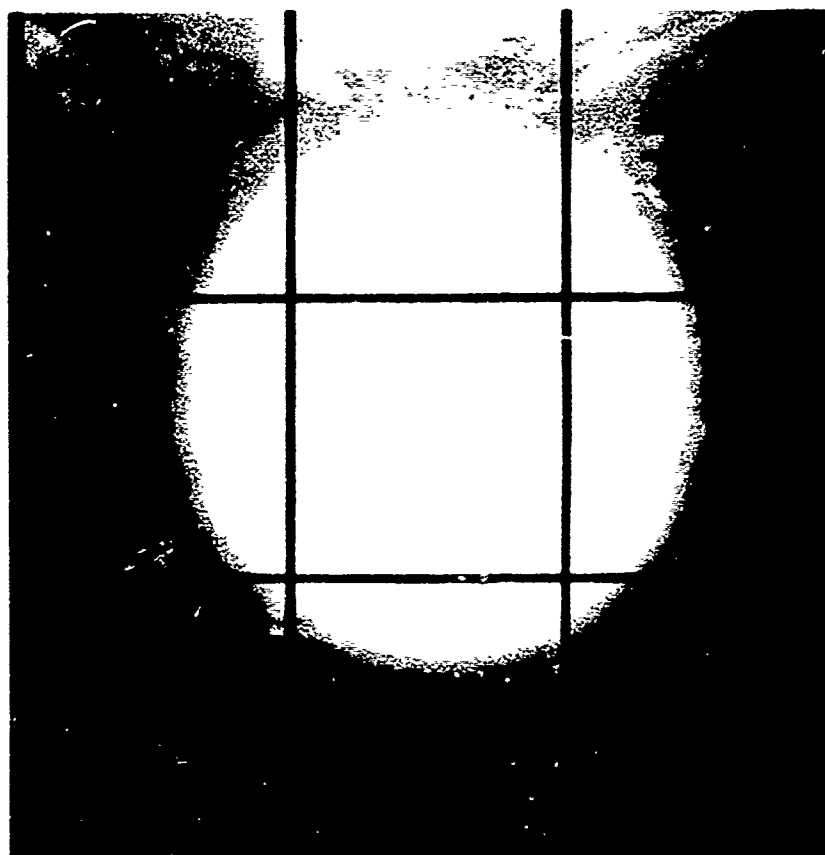


8a. 14.90 seconds



8b. 29.13 seconds

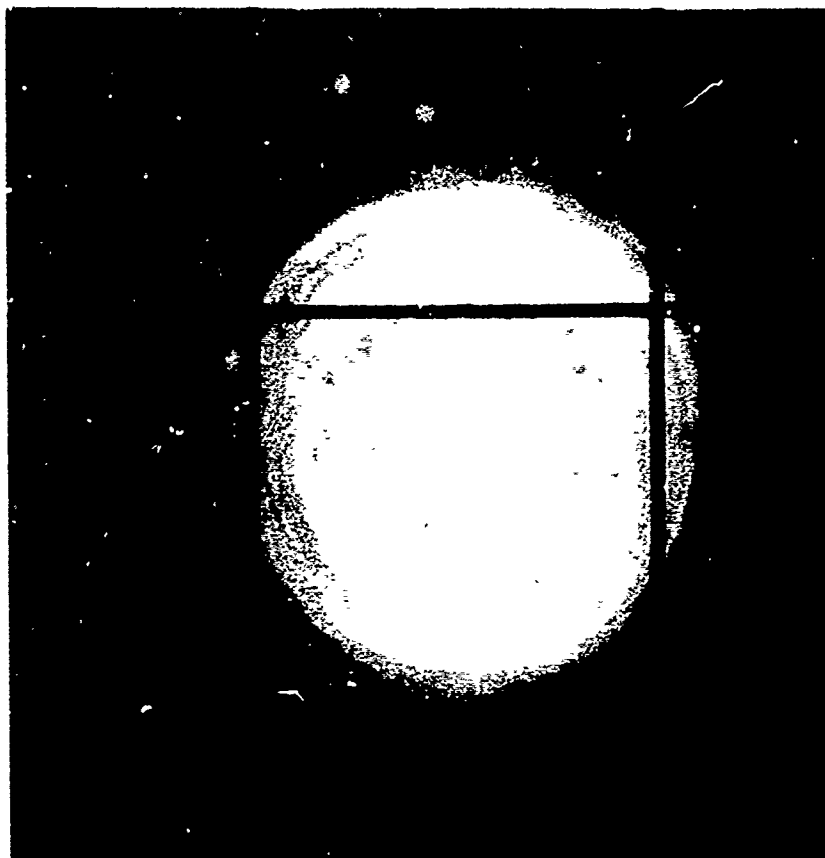
Run 807
1.5-inch R_N Sphere-Cone with Groove
 $Re_\infty = 4.08 \times 10^6/\text{ft}$, $T_o = 1013^\circ\text{F}$



9a.

43.52 seconds

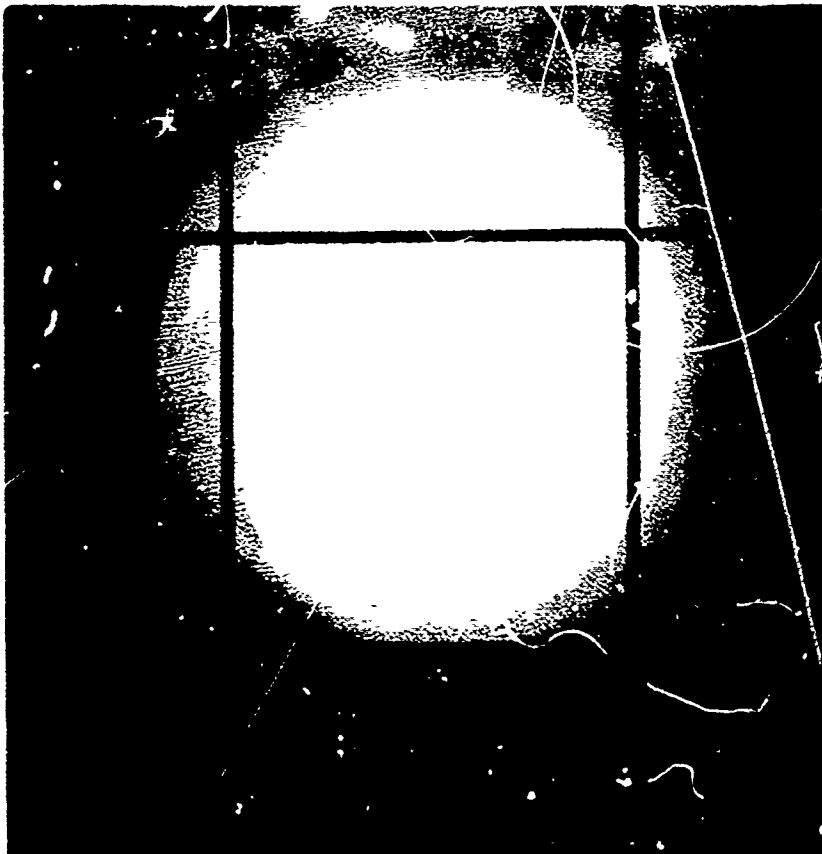
Run 807
1.5-inch RN Sphere-Cone with Groove
 $Re_{\infty} = 4.08 \times 10^6/\text{ft}$, $T_o = 1013^{\circ}\text{F}$



9b.

3.52 seconds

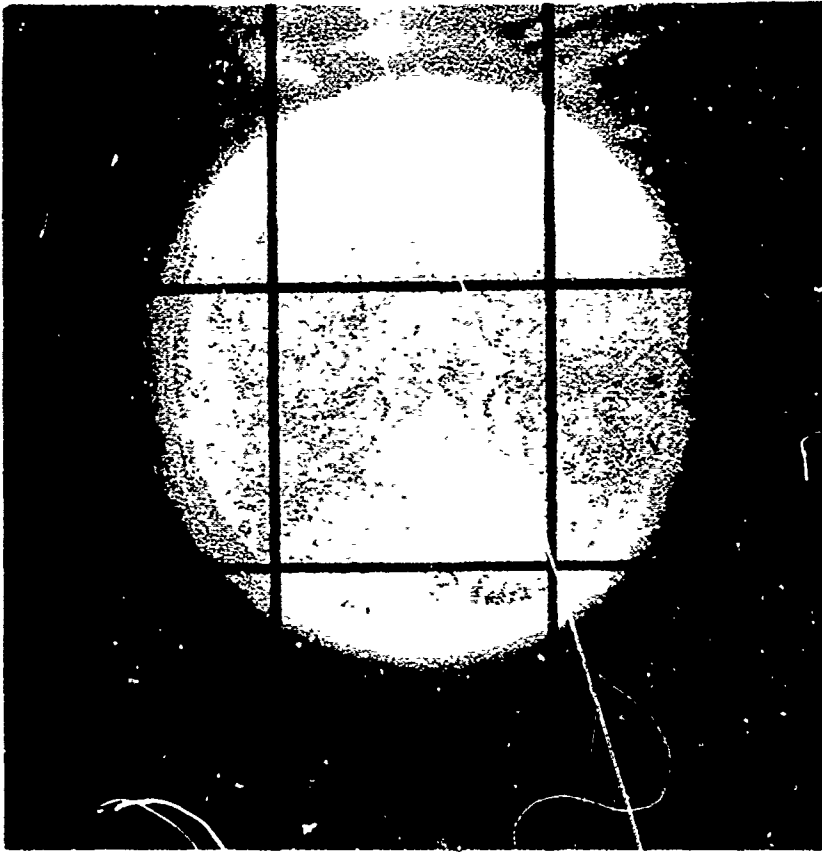
Run 809
0.75-inch RN Sphere-Cone
 $Re_{\infty} = 9.38 \times 10^6/\text{ft}$, $T_o = 971^{\circ}\text{F}$



10a.

9.21 seconds

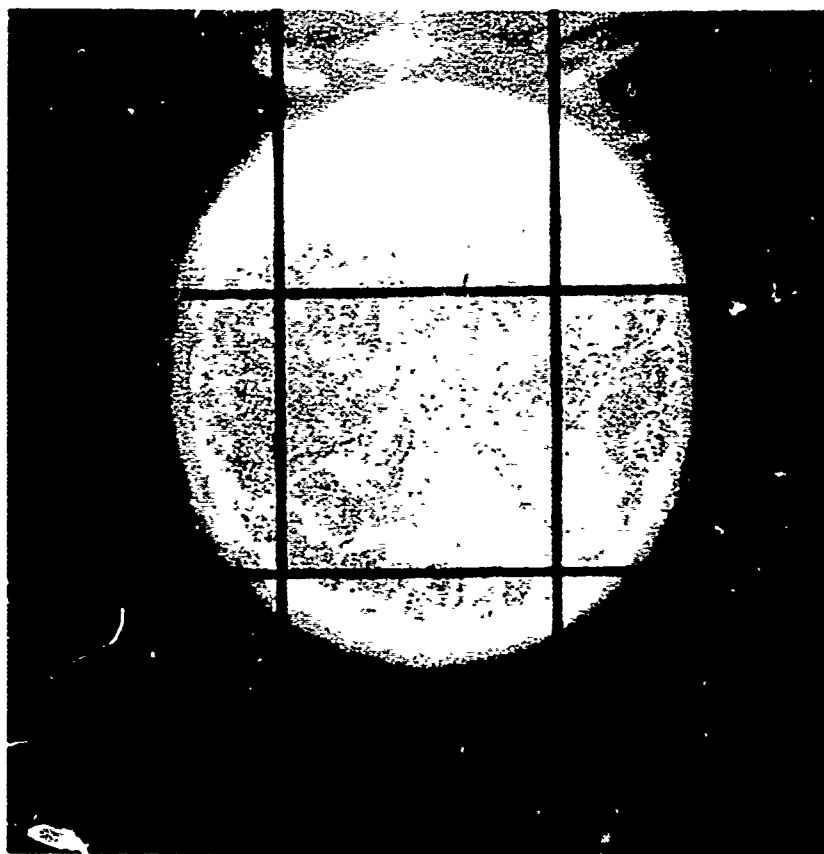
Run 809
0.75 inch RN Sphere-Cone
 $Re_{\infty} = 9.38 \times 10^6 / ft$, $T_0 = 971^{\circ}F$



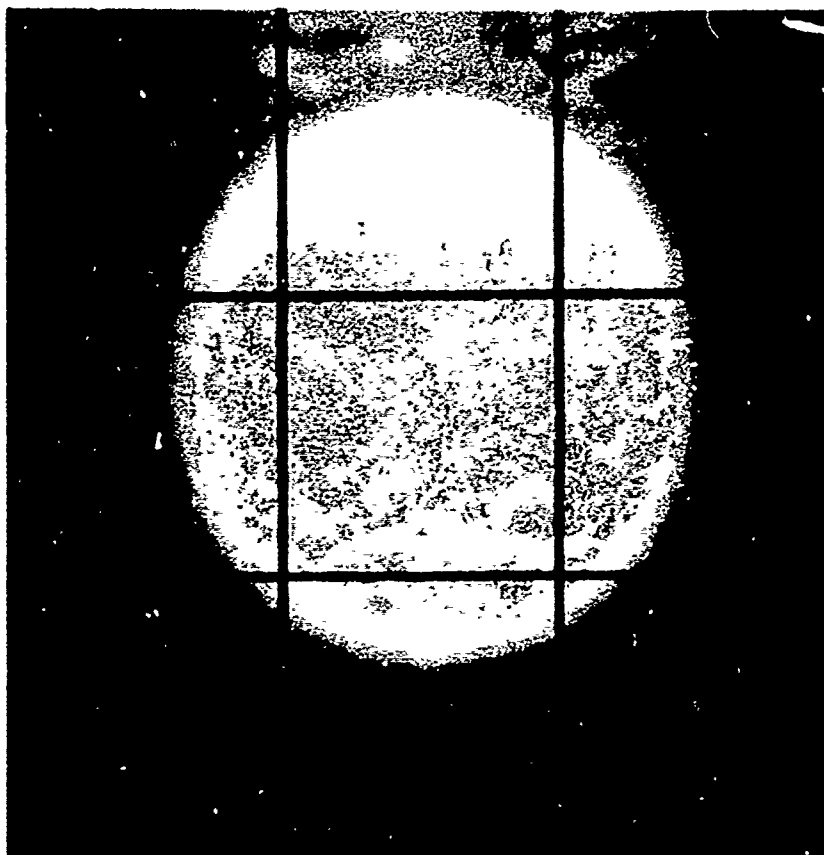
10b.

4.77 seconds

Run 810
1.5-inch RN $60^{\circ}/8^{\circ}$ Biconic
 $Re_{\infty} = 6.73 \times 10^6 / ft$, $T_0 = 964^{\circ}F$

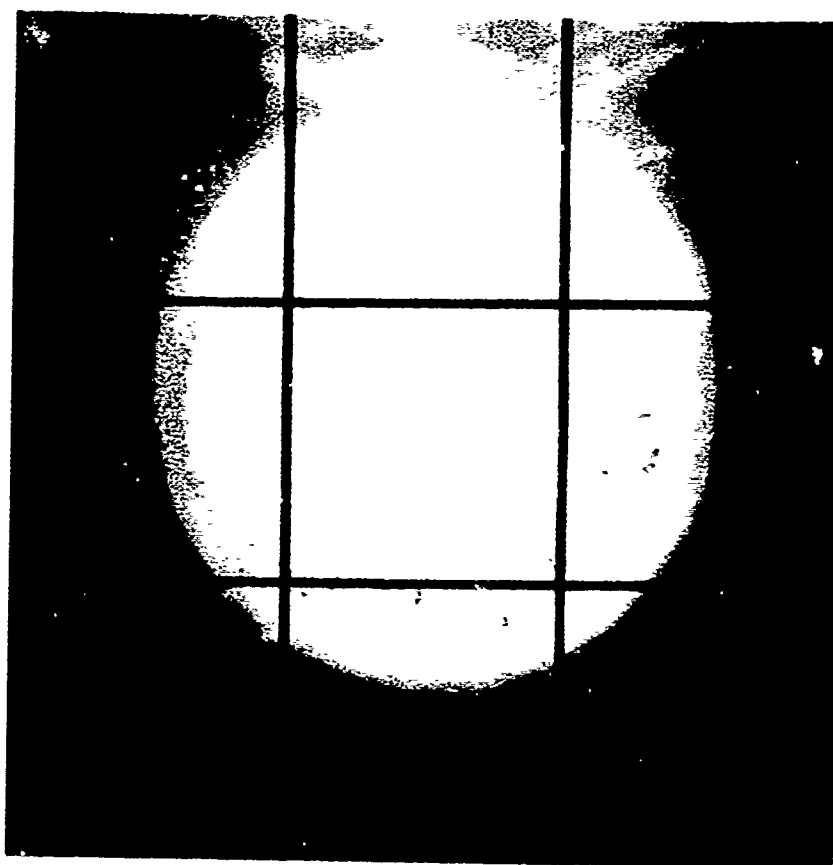


11a. 10.30 seconds

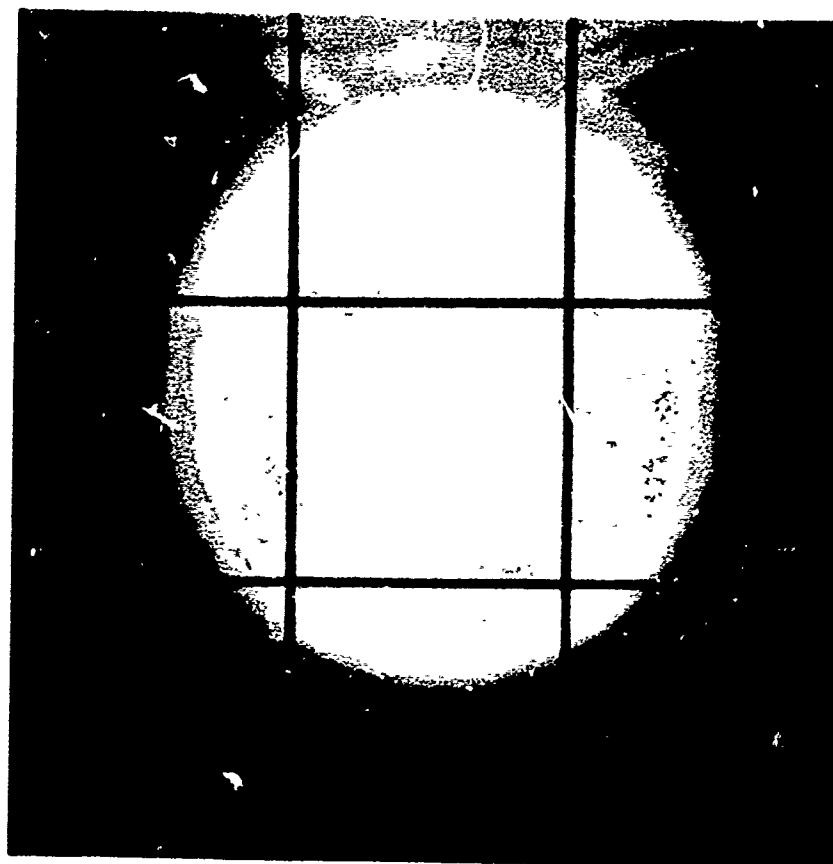


11b. 17.84 seconds

Run 810
 1.5-inch R_s 60°/8° Biconic
 $Re_\infty = 6.73 \times 10^6/\text{ft}$, $T_o = 964^\circ\text{F}$



12a. 9.35 seconds

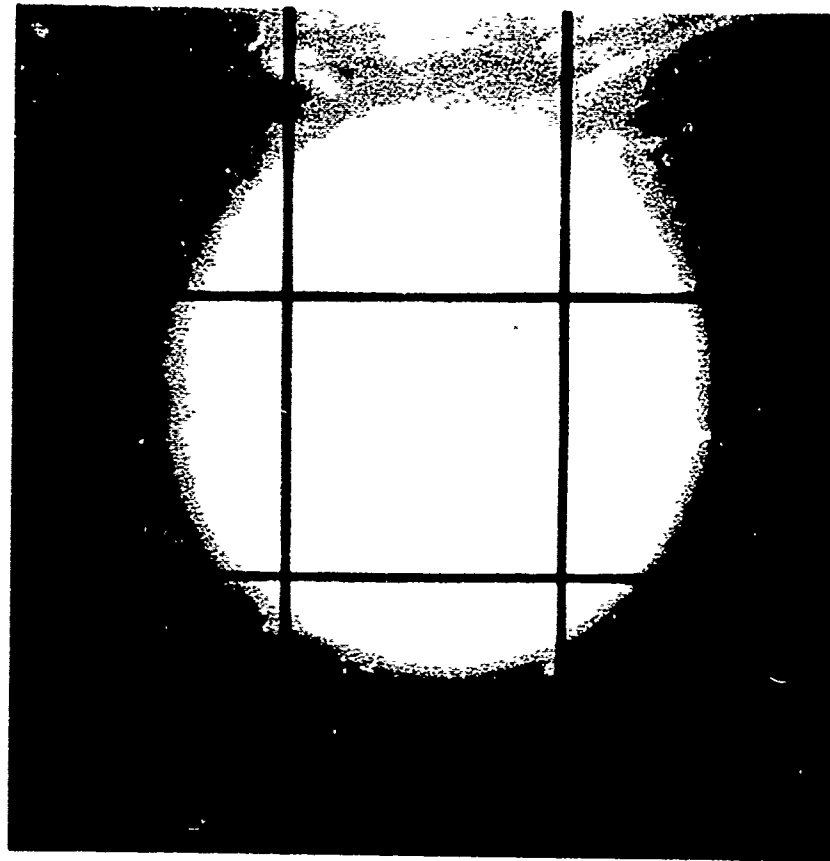


12b. 13.79 seconds

Run 813
 1.5 inch R_s 75°/8° Biconic
 $Re_{cr} = 6.70 \times 10^6$ /ft, $T_o = 970^\circ F$



13a. 0 seconds



13b. 29.86 seconds

Run 814
1.5-inch R_N Sphere-Cone with Grooves
 $Re_{\infty} = 4.15 \times 10^6/\text{ft}$, $T_0 = 998^\circ\text{F}$

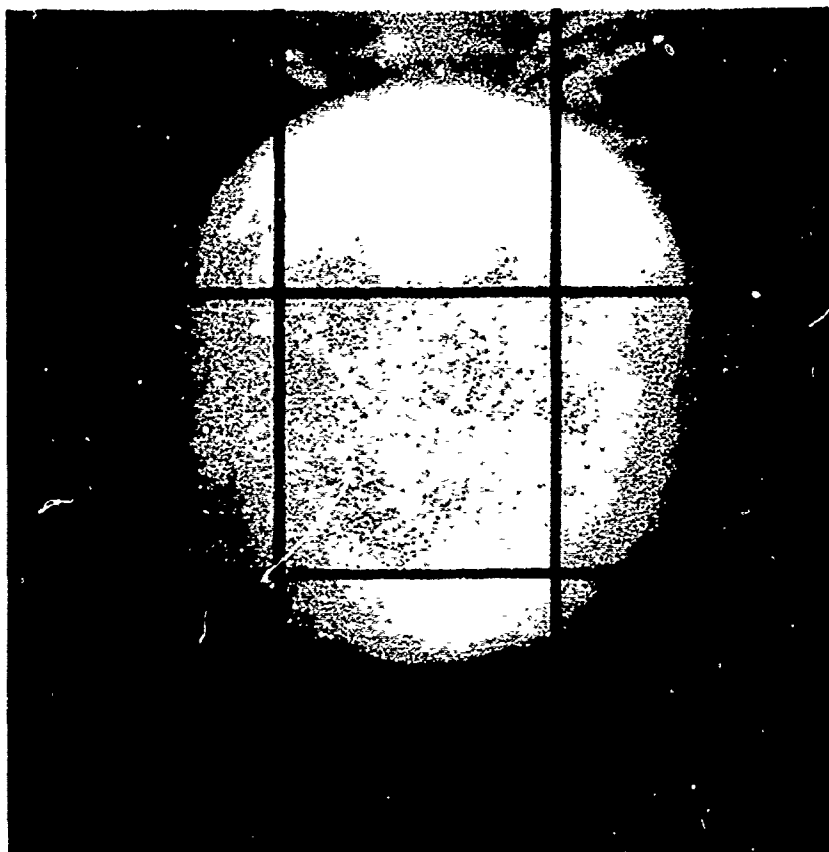


14a.

44.26 seconds

Run 814

1.5-inch R_N Sphere-Cone with Grooves
 $Re_\infty = 4.15 \times 10^6 / ft, T_0 = 998^\circ F$

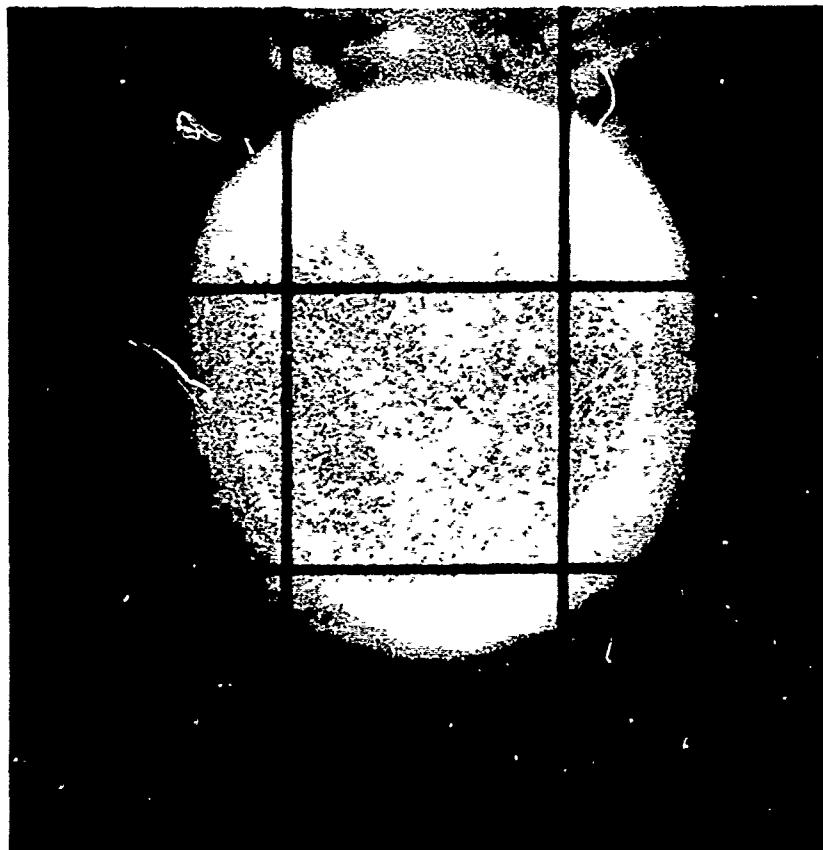


14b.

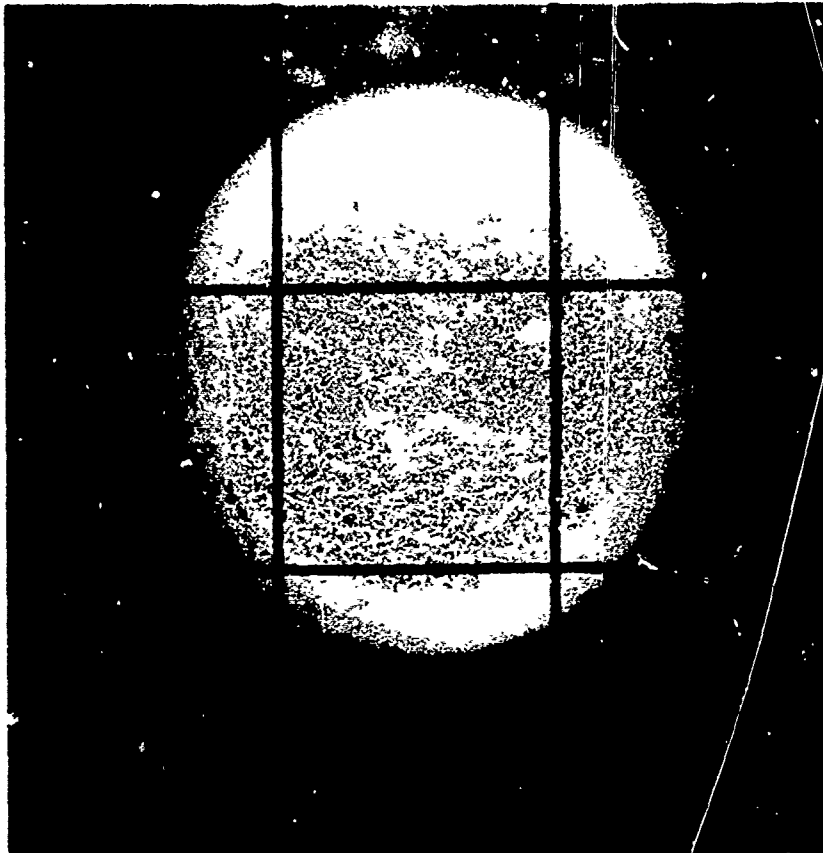
4.11 seconds

Run 815

1.5-inch P_S Laminar-Blunt
 $Re_\infty = 6.72 \times 10^6 / ft, T_0 = 944^\circ F$

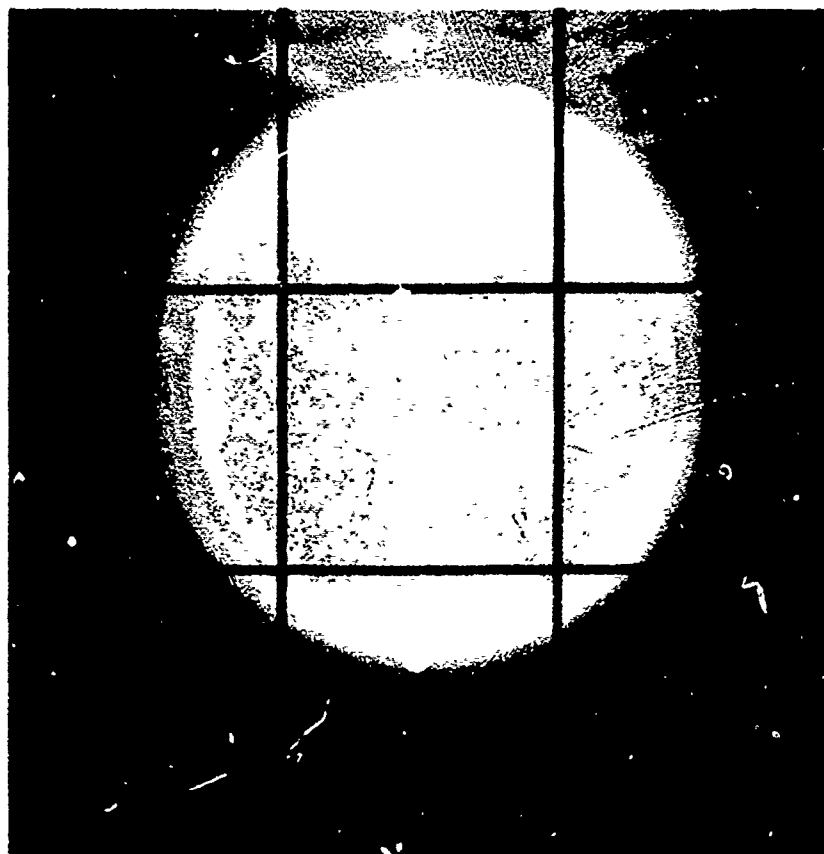


15a. 8.71 seconds

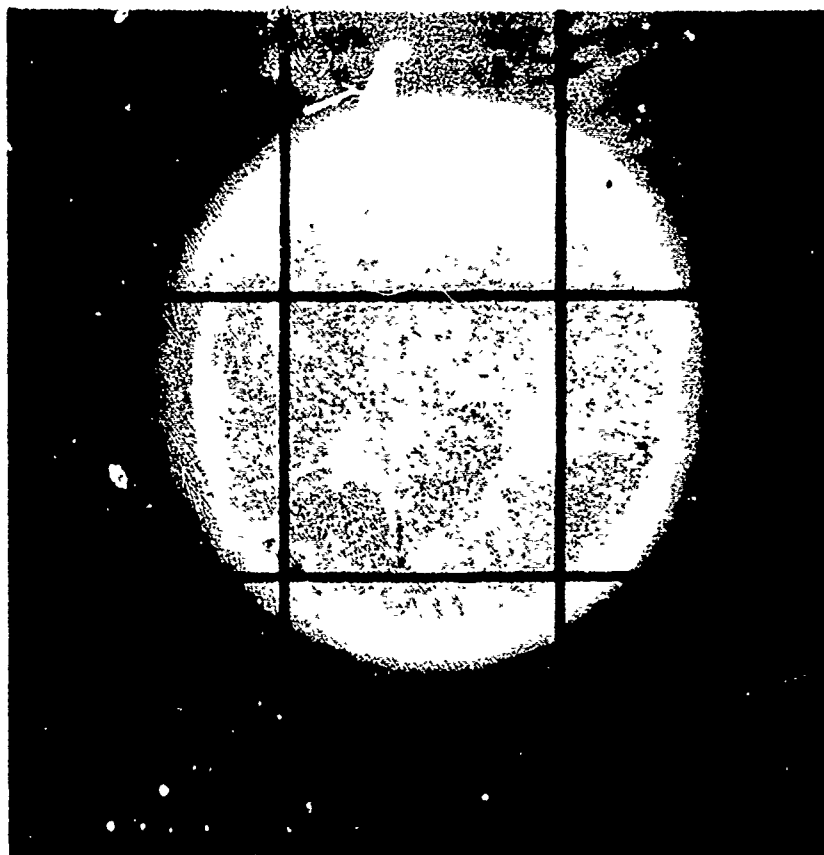


15b. 13.14 seconds

Run 815
1.5 inch R_s Laminar-Blunt
 $Re_\infty = 6.72 \times 10^6 / ft, T_o = 944^\circ F$

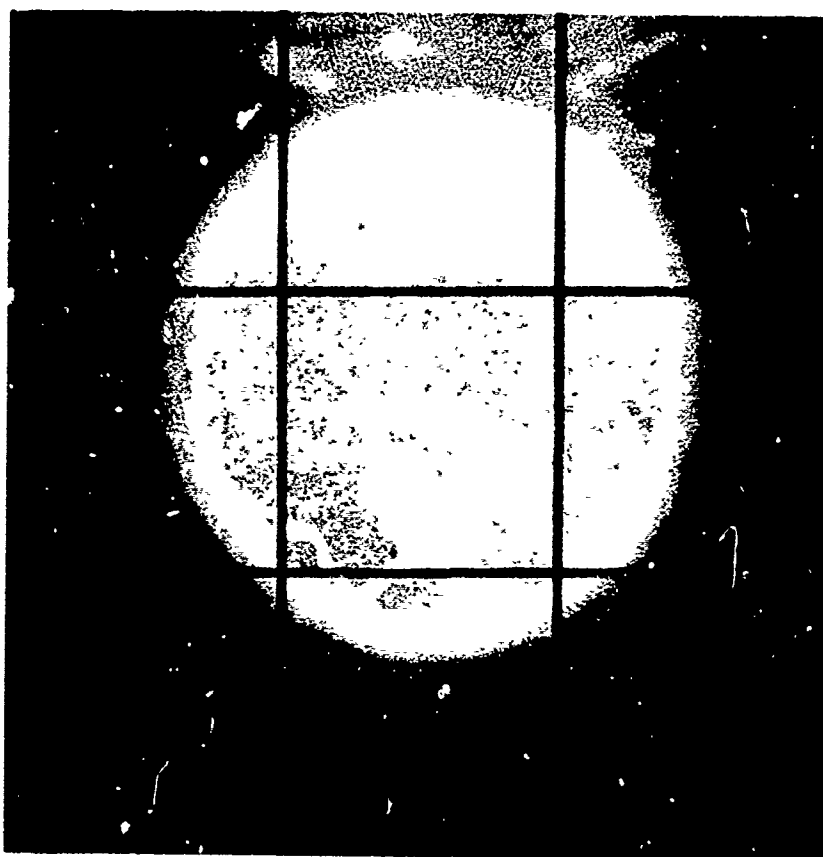


16a. 10.34 seconds



16b. 20.05 seconds

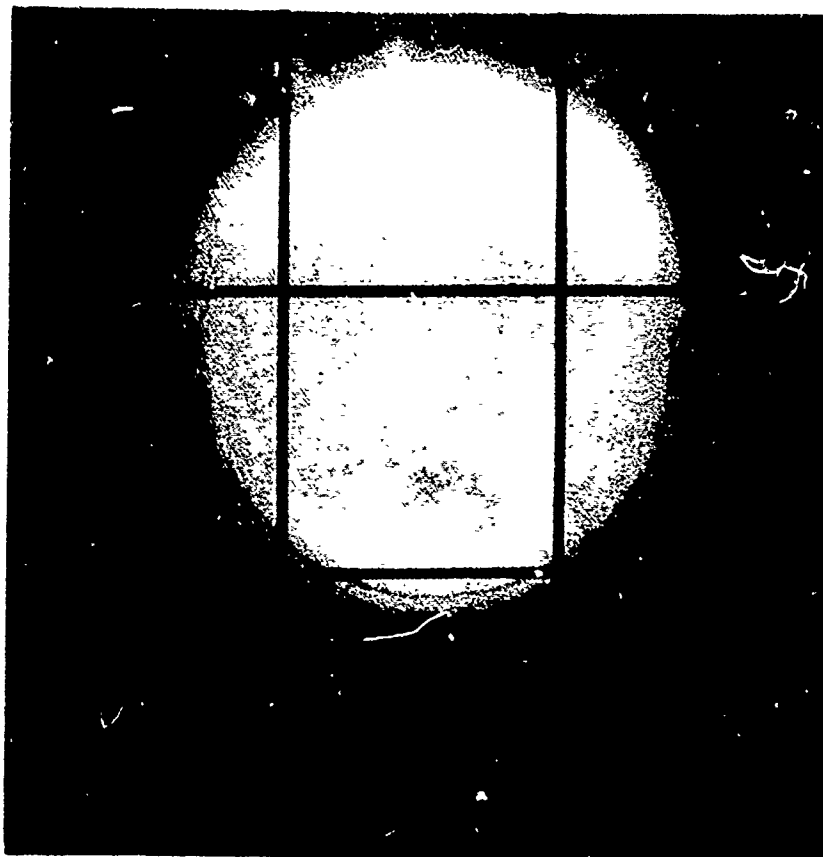
Run 816
1.5-inch R_5 60°/8° Biconic
 $Re_\infty = 5.20 \times 10^6/\text{ft}$, $T_0 = 954^\circ\text{F}$



17a.

30.41 seconds

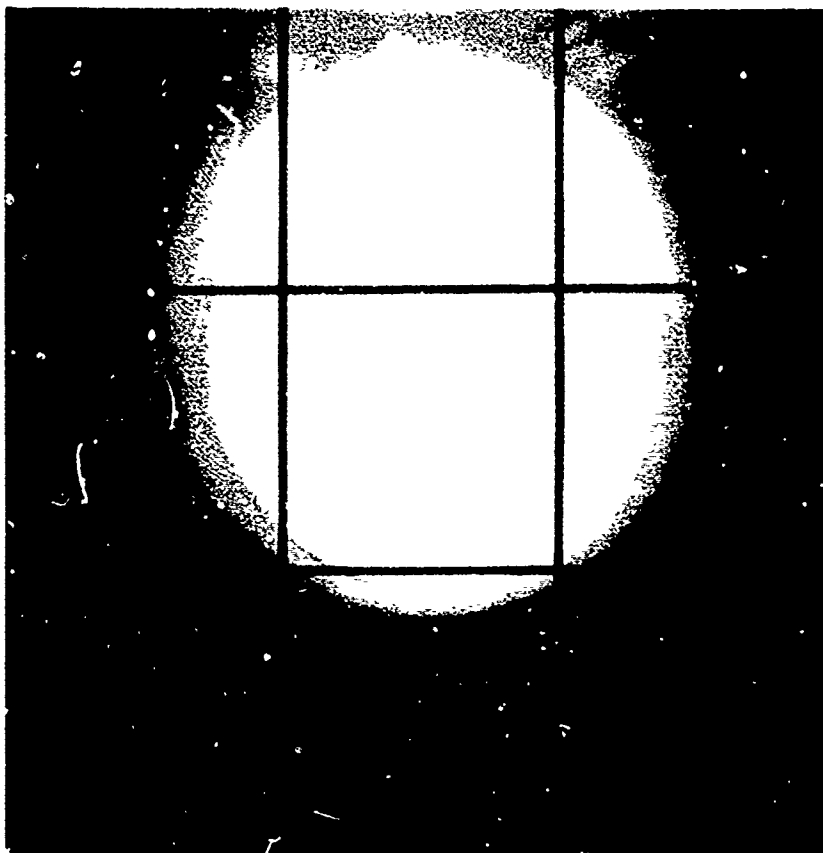
Run 816
1.5 inch R_5 60°/8° Biconic
 $Re_\infty = 5.20 \times 10^6$ /ft, $T_0 = 954^\circ F$



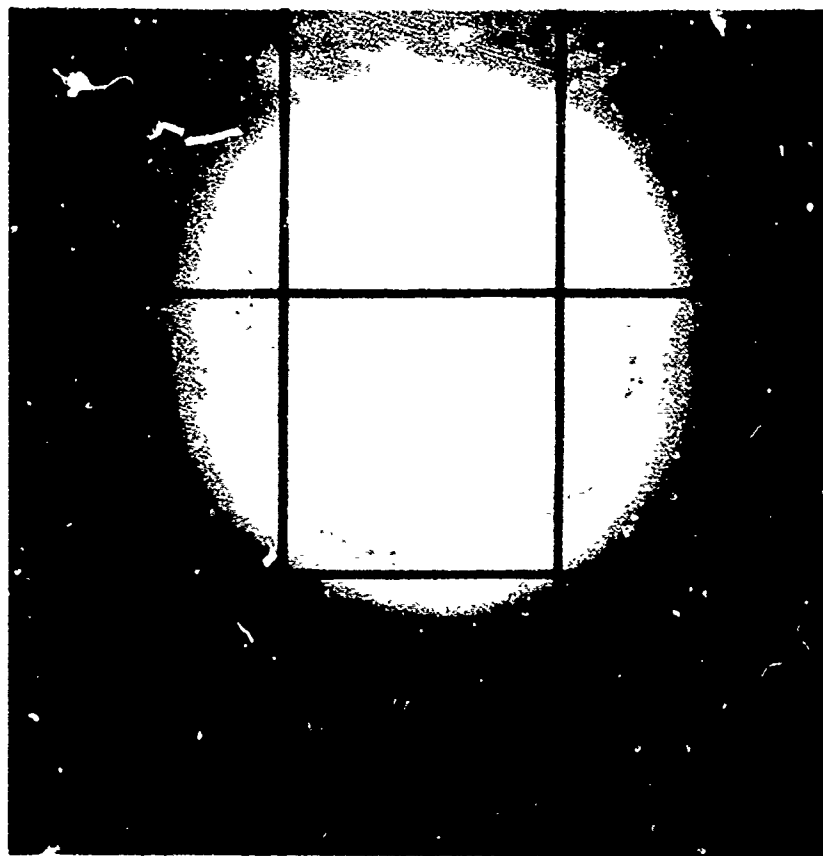
17b.

11.50 seconds

Run 818
1.5-inch RN Sphere-Cone
 $Re_\infty = 9.56 \times 10^6$ /ft, $T_0 = 508^\circ F$

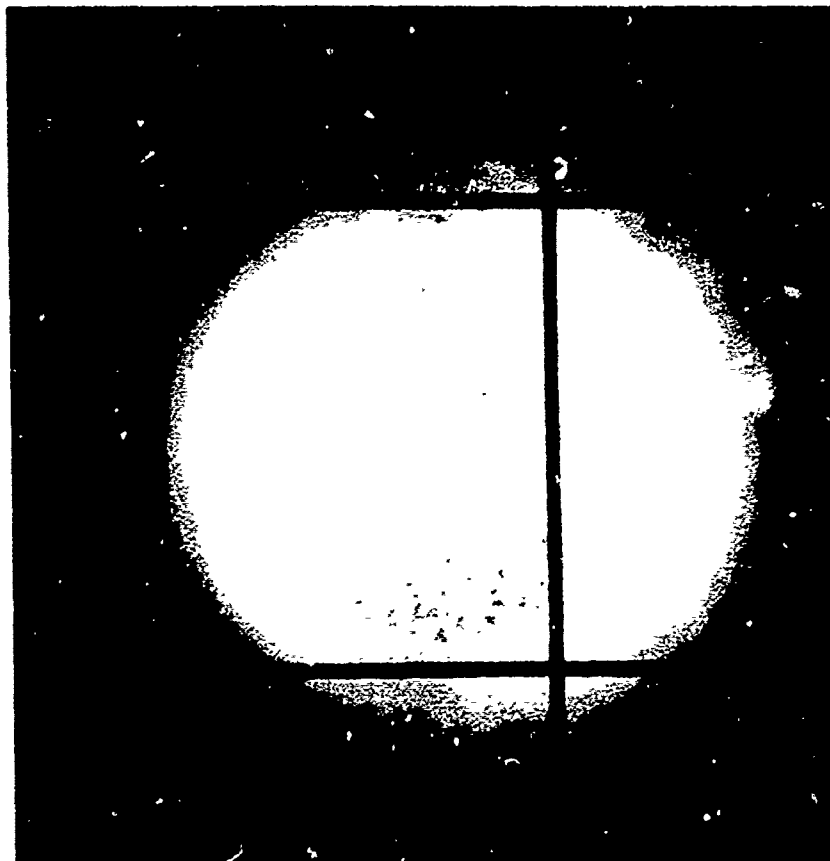


18a. 22.75 seconds

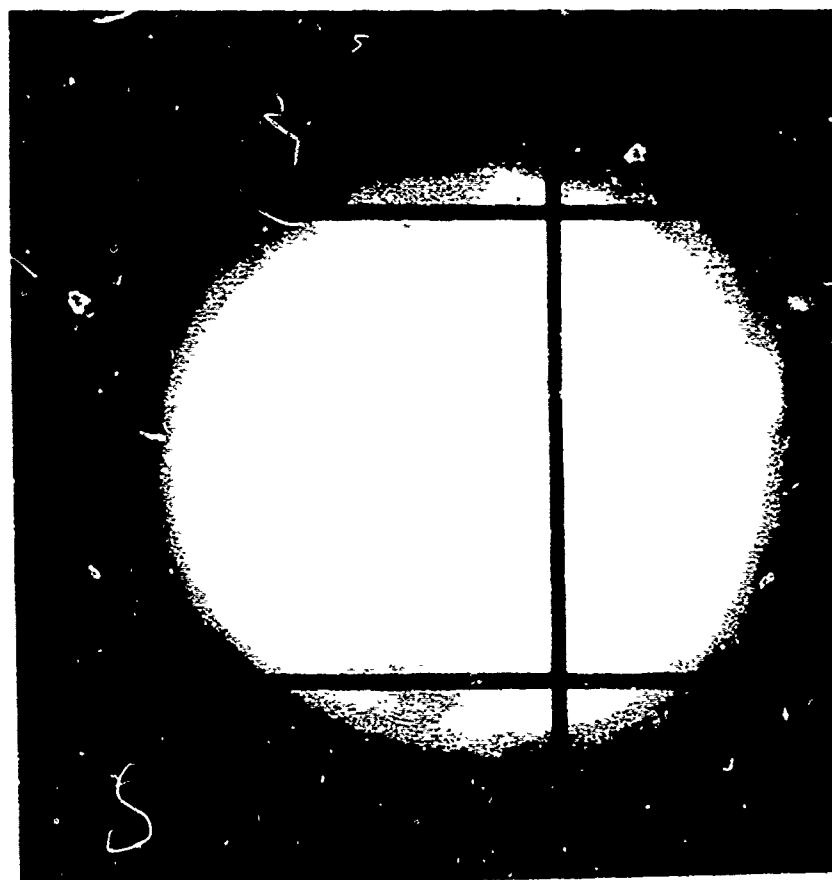


18b. 47.02 seconds

Run 818
1.5-inch RN Sphere-Cone
 $Re_{\infty} = 9.56 \times 10^6 / ft, T_0 = 508^{\circ}F$

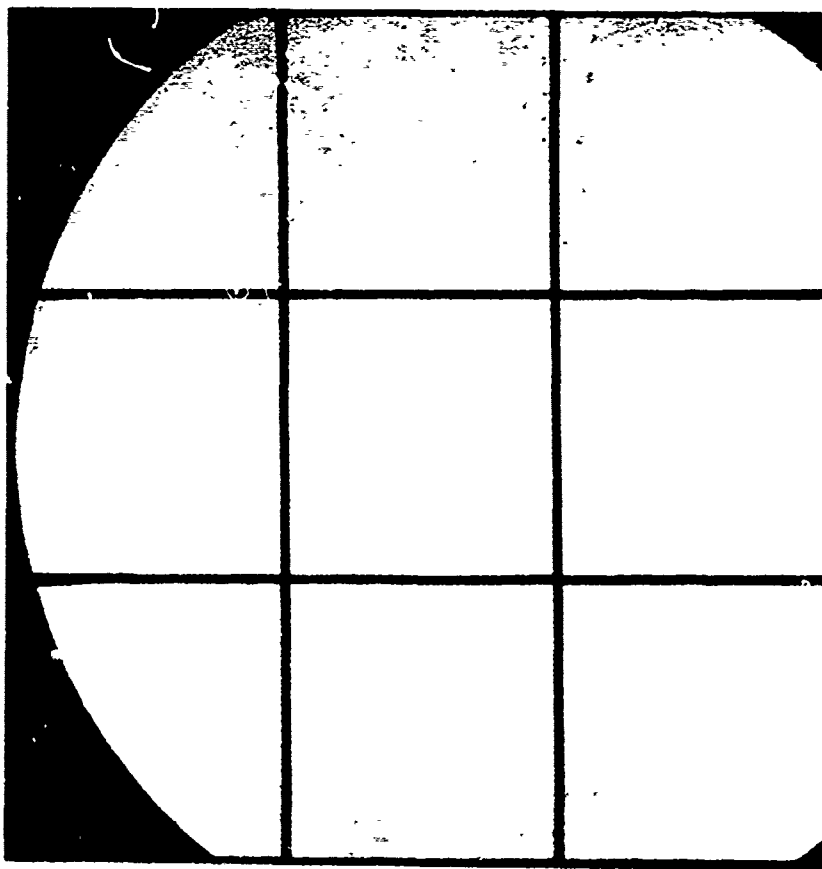


19b. 29.55 seconds



19a. 20.84 seconds

Run 819
0.75-inch RN Sphere-Cone
 $Re_{\infty} = 5.69/12.96 \times 10^6/\text{ft}$, $T_0 = 812/804^{\circ}\text{F}$

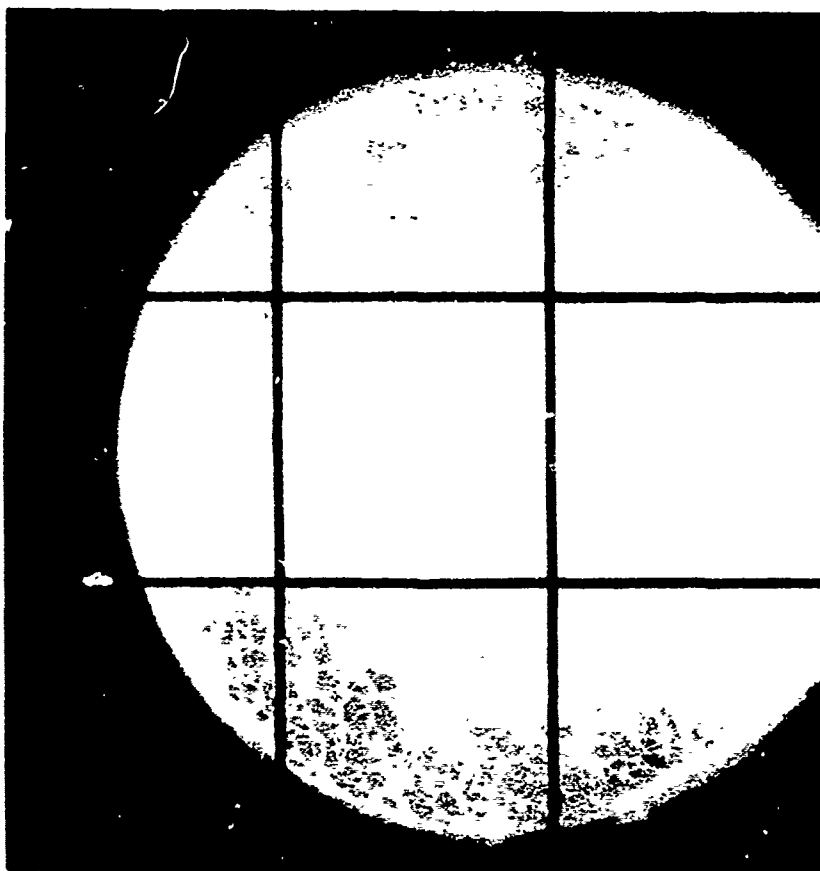


20a. 9.48 seconds

Run 820

3.5-inch R_S Laminar-Blunt

$$Re_{\infty} = 4.90 \times 10^6 / ft, T_0 = 986^{\circ}F$$

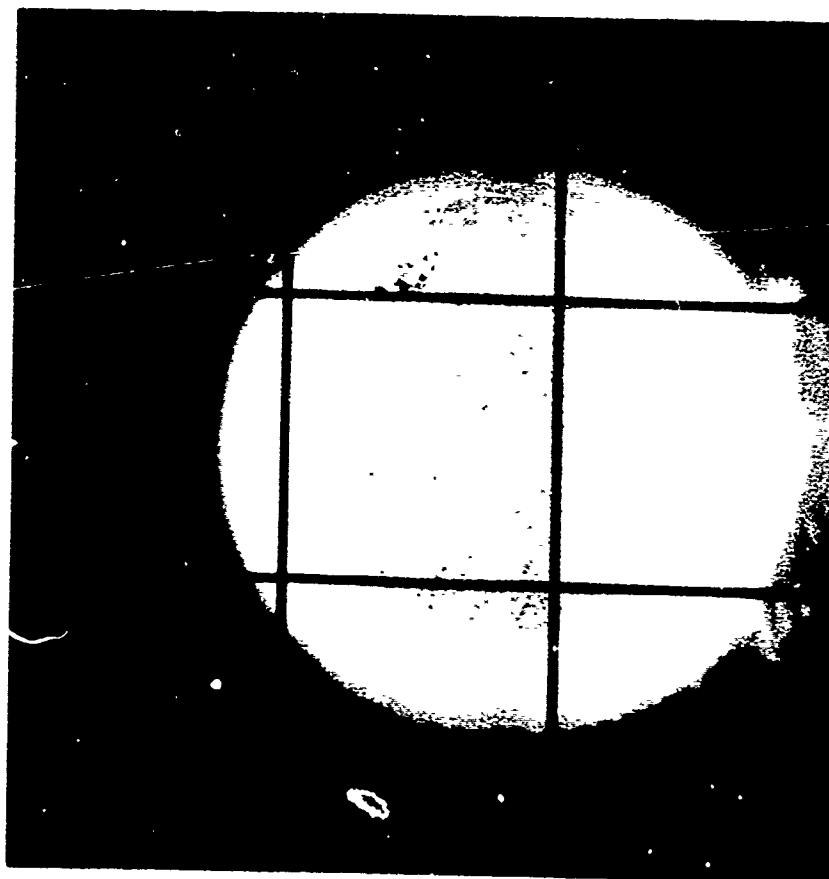


20b. 13.47 seconds

Run 821

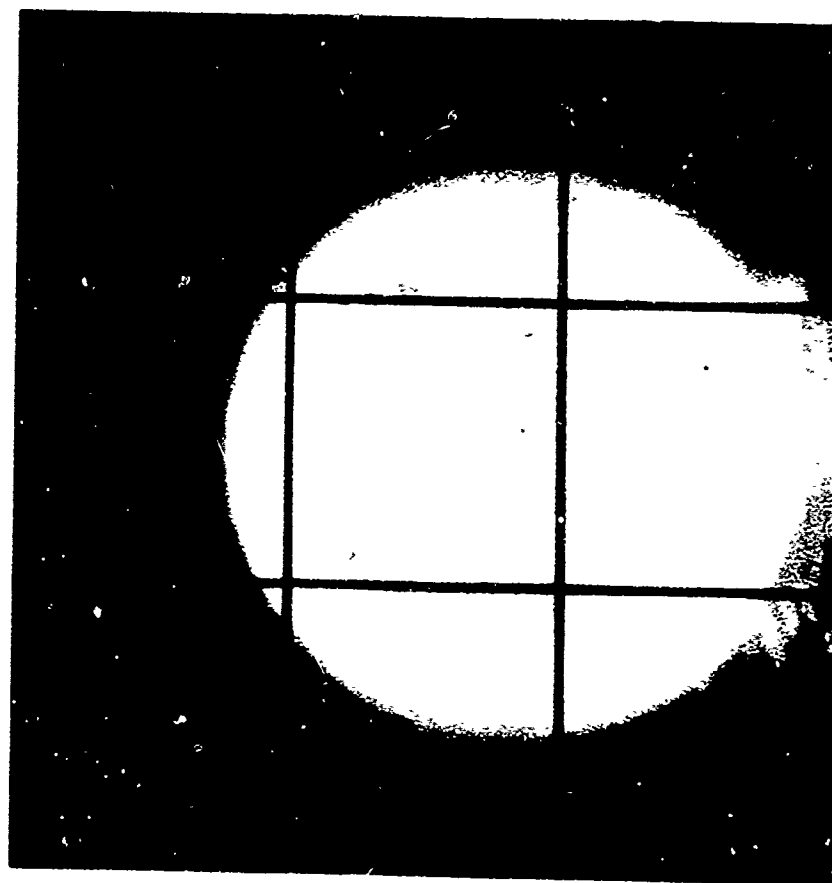
2.5-inch R_N Sphere-Cone

$$Re_{\infty} = 7.47 \times 10^6 / ft, T_0 = 973^{\circ}F$$



21a.

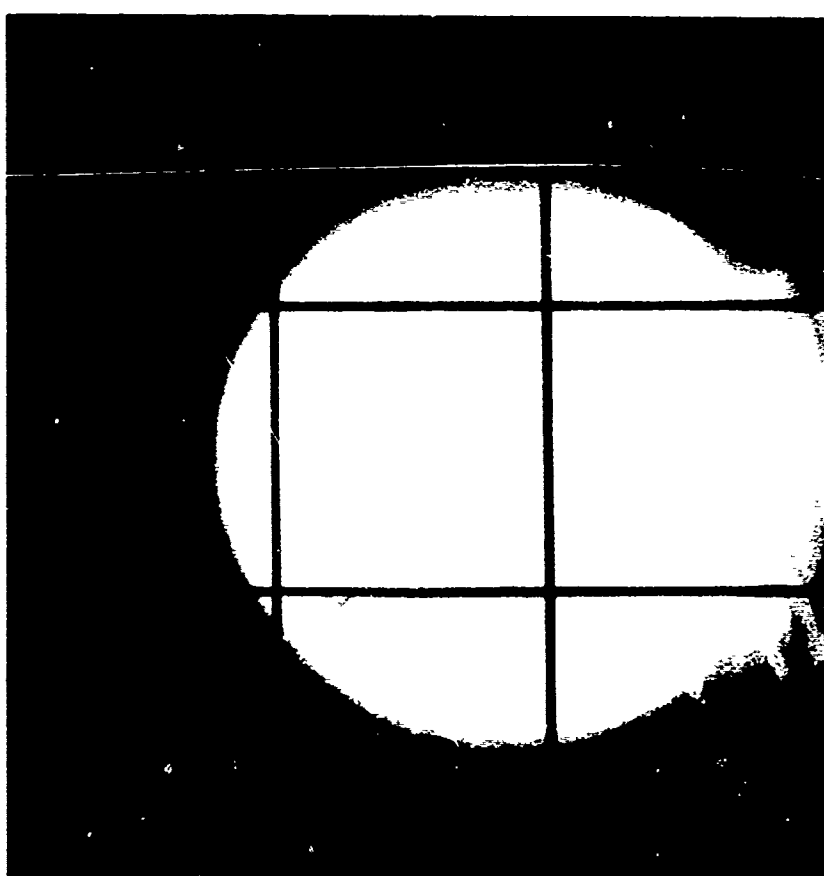
14.29 seconds



21b.

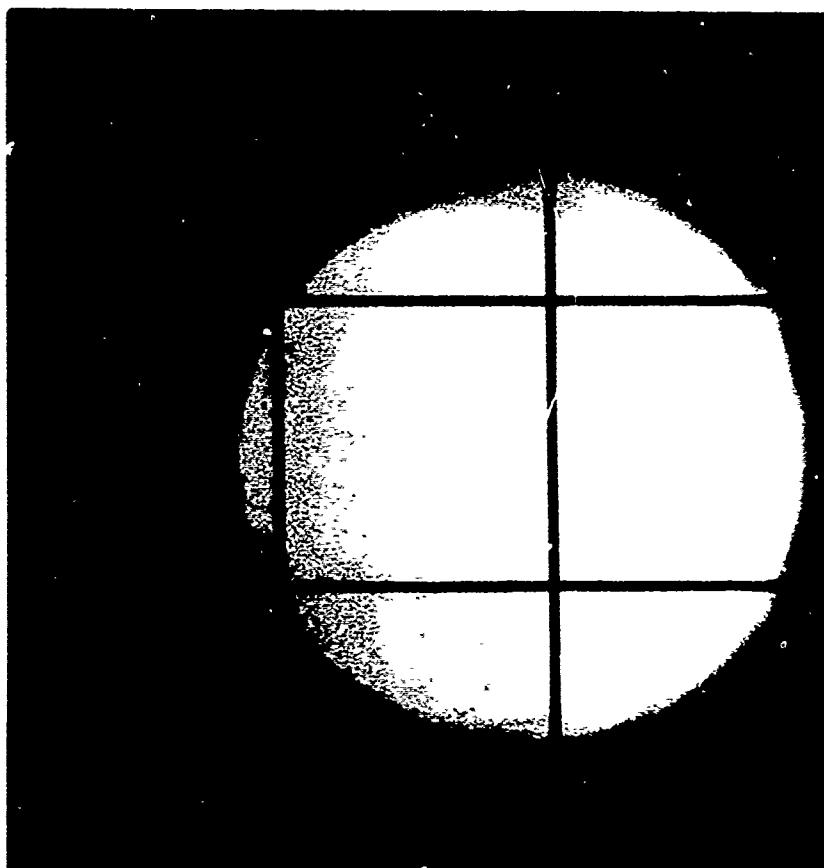
29.24 seconds

Run 822
1.5-inch R_s Laminar-Blunt
 $Re_\infty = 4.02 \times 10^6/\text{ft}$, $T_0 = 960^\circ\text{F}$



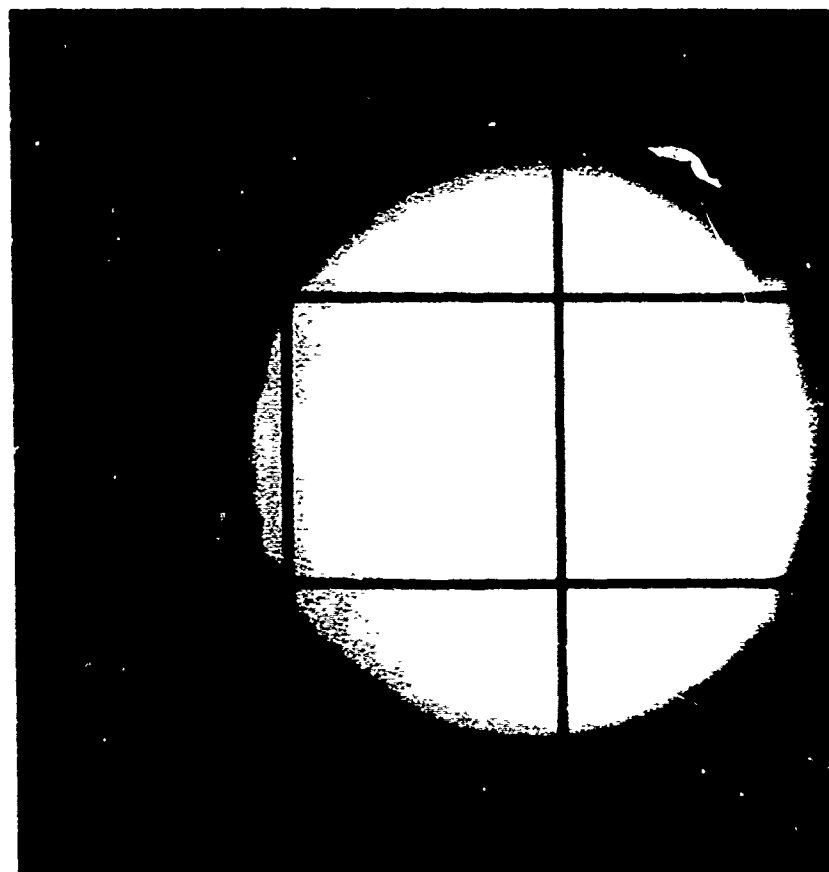
22a. 43.85 seconds

Run 822
1.5-inch R_s Laminar-Blunt
 $Re_\infty = 4.02 \times 10^6/\text{ft}$, $T_o = 960^\circ\text{F}$



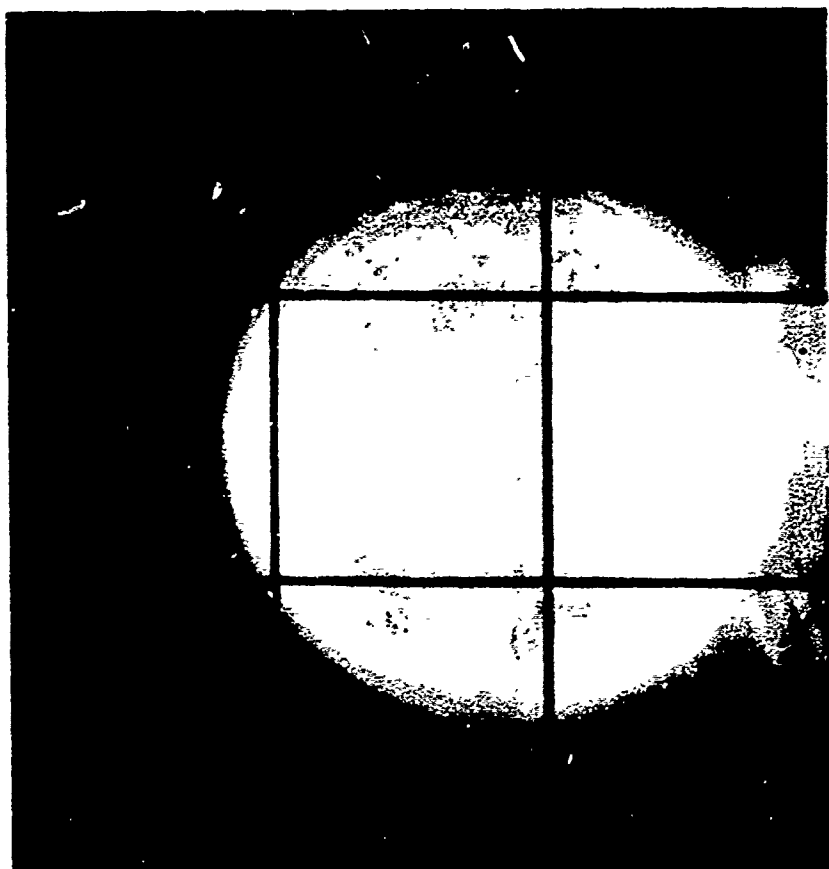
22b. 11.81 seconds

Run 823
1.5-inch R_s $75^\circ/8^\circ$ Biconic
 $Re_\infty = 5.18 \times 10^6/\text{ft}$, $T_o = 986^\circ\text{F}$



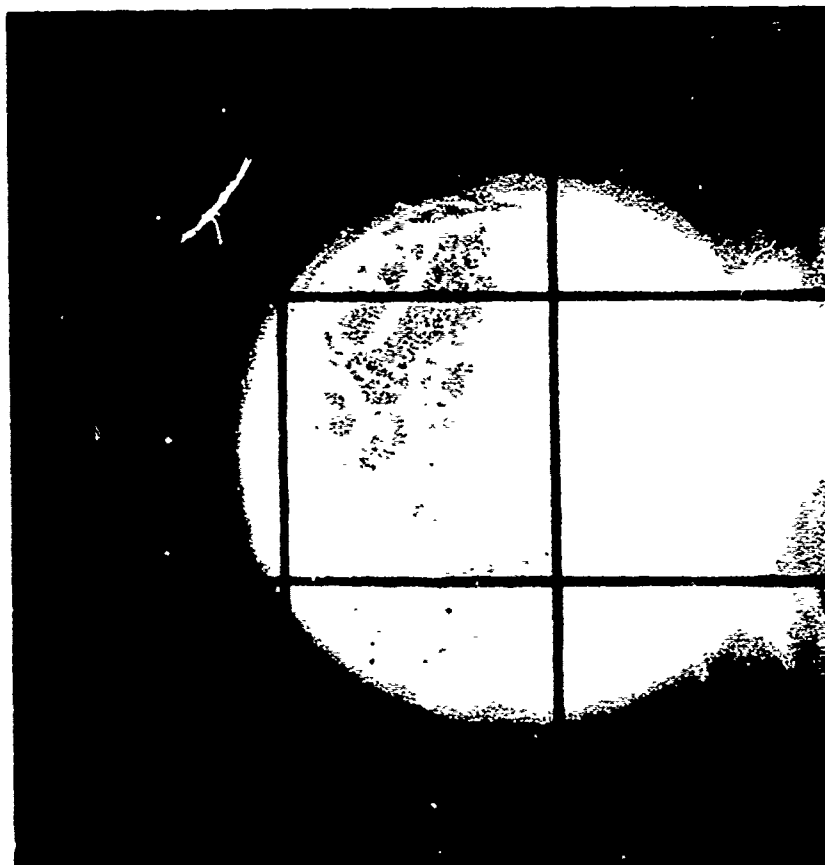
23a. 22.94 seconds

Run 823
1.5-inch R_s $75^\circ/8^\circ$ Biconic
 $Re_\infty = 5.18 \times 10^6/\text{ft}$, $T_0 = 986^\circ\text{F}$

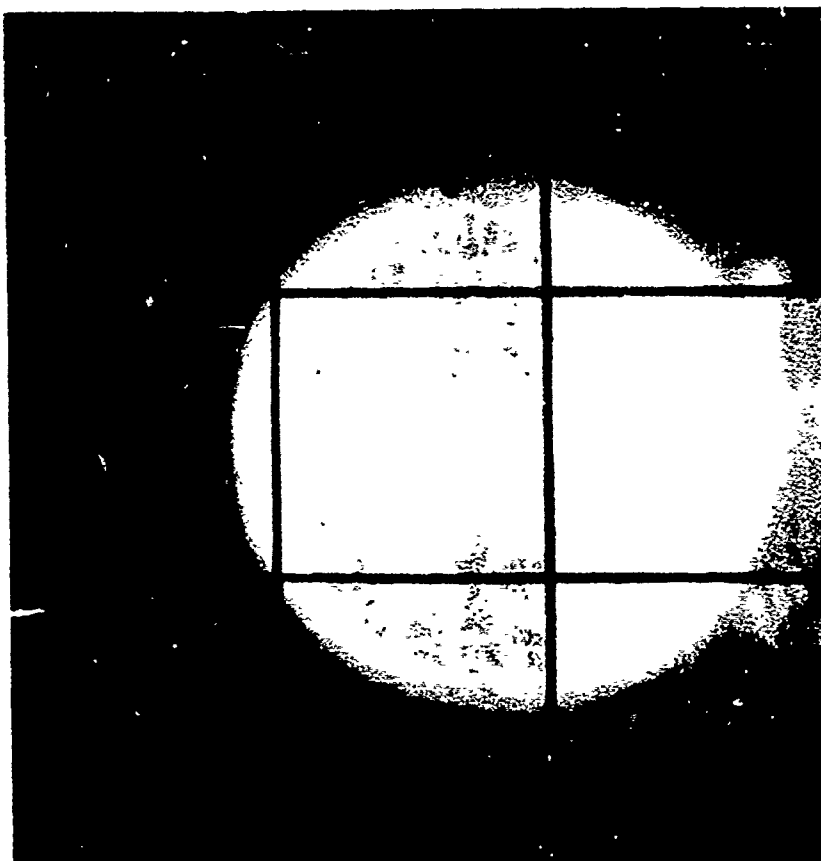


23b. 15.13 seconds

Run 824
1.5-inch R_N Sphere-Cone
 $Re_\infty = 9.44 \times 10^6/\text{ft}$, $T_0 = 535^\circ\text{F}$

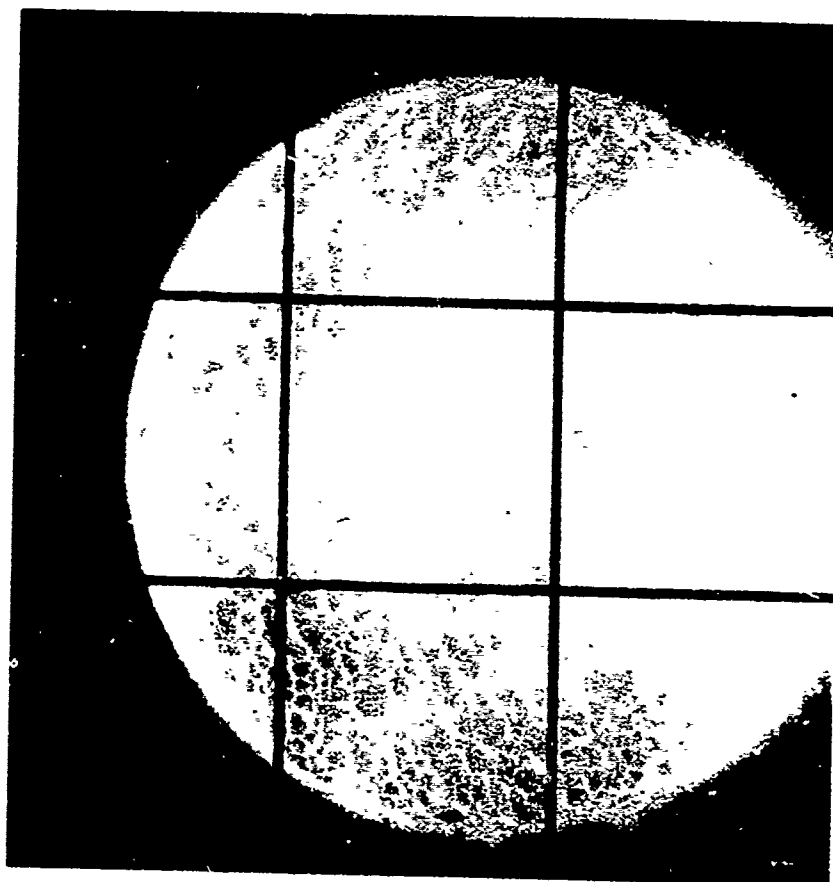


24a. 29.58 seconds



24b. 44.03 seconds

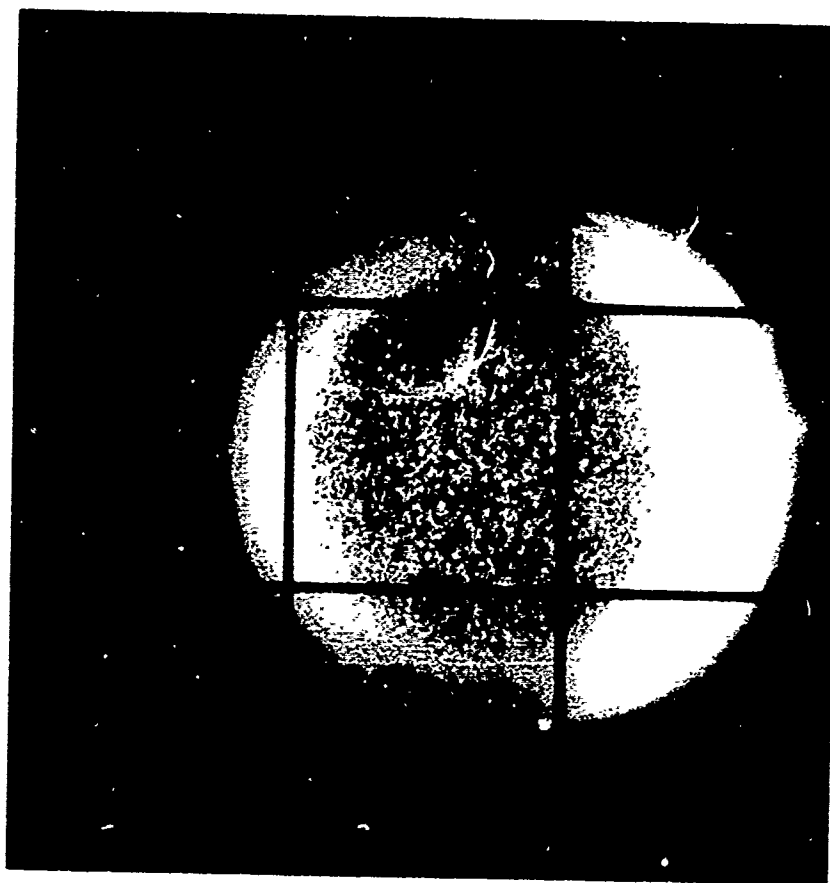
Run 824
1.5-inch R_N Sphere-Cone
 $Re_\infty = 9.44 \times 10^6/\text{ft}$, $T_0 = 535^\circ\text{F}$



25a.

6.53 seconds

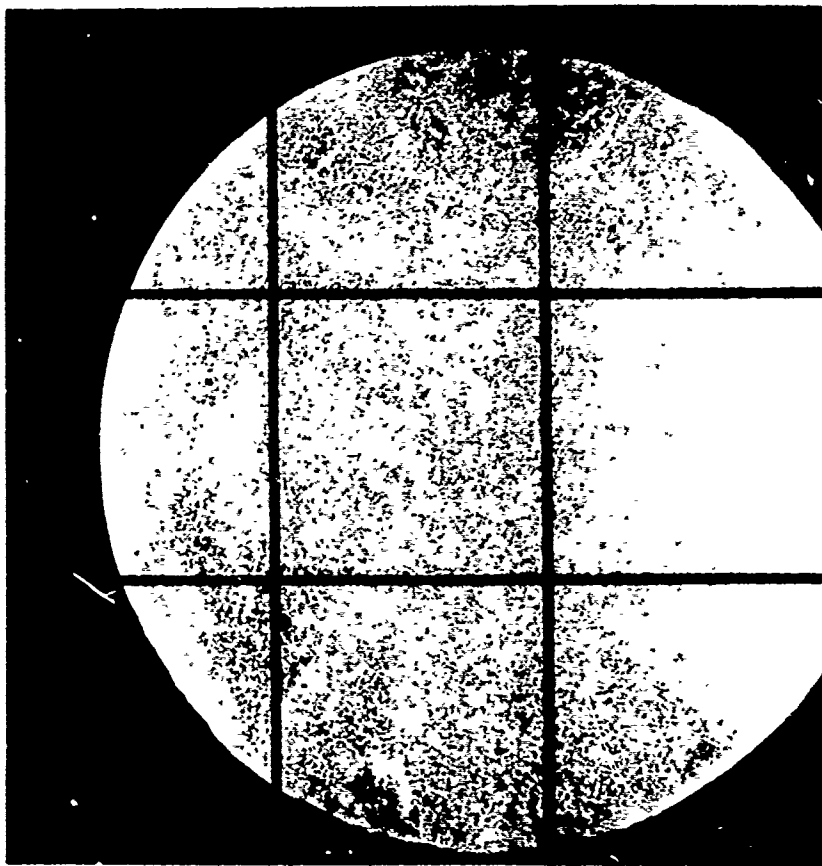
Run 825
2.5-inch R_N Sphere-Cone
 $Re_\infty = 7.20 \times 10^6 / ft$, $T_0 = 990^\circ F$



25b.

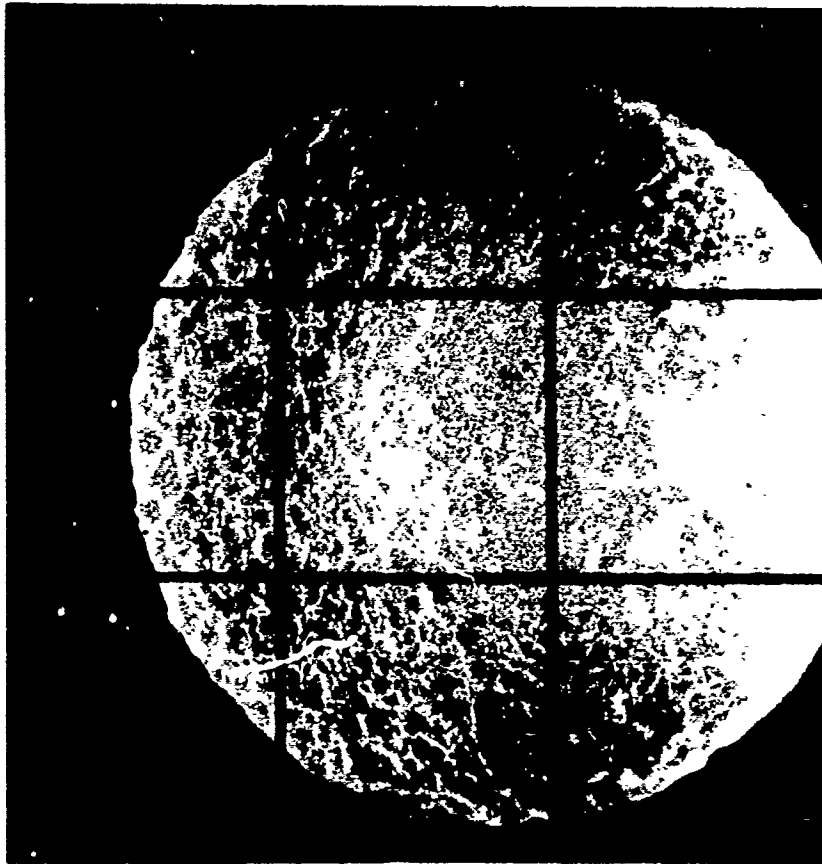
19.72 seconds

Run 826
1.5-inch R_N Laminar-Blunt
 $Re_\infty = 3.41 \times 10^6 / ft$, $T_0 = 987^\circ F$



26a.

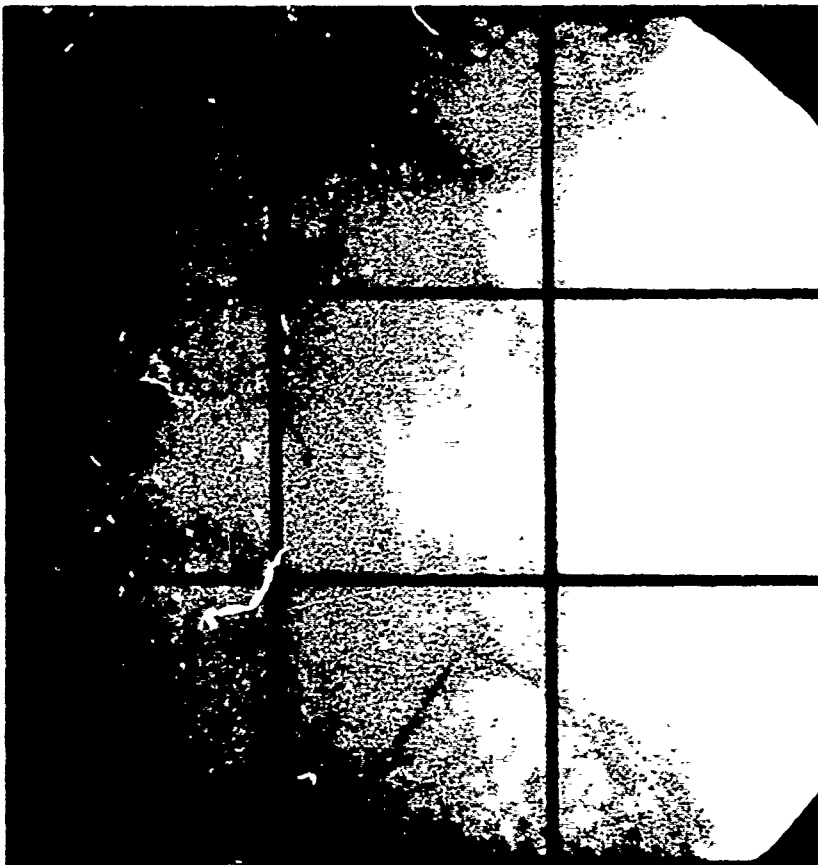
14.87 seconds



26b.

44.28 seconds

Run 827
 2.5-inch R_s 55°/6° Biconic
 $Re_\infty = 4.76 \times 10^6$ /ft, $T_o = 1008^\circ F$

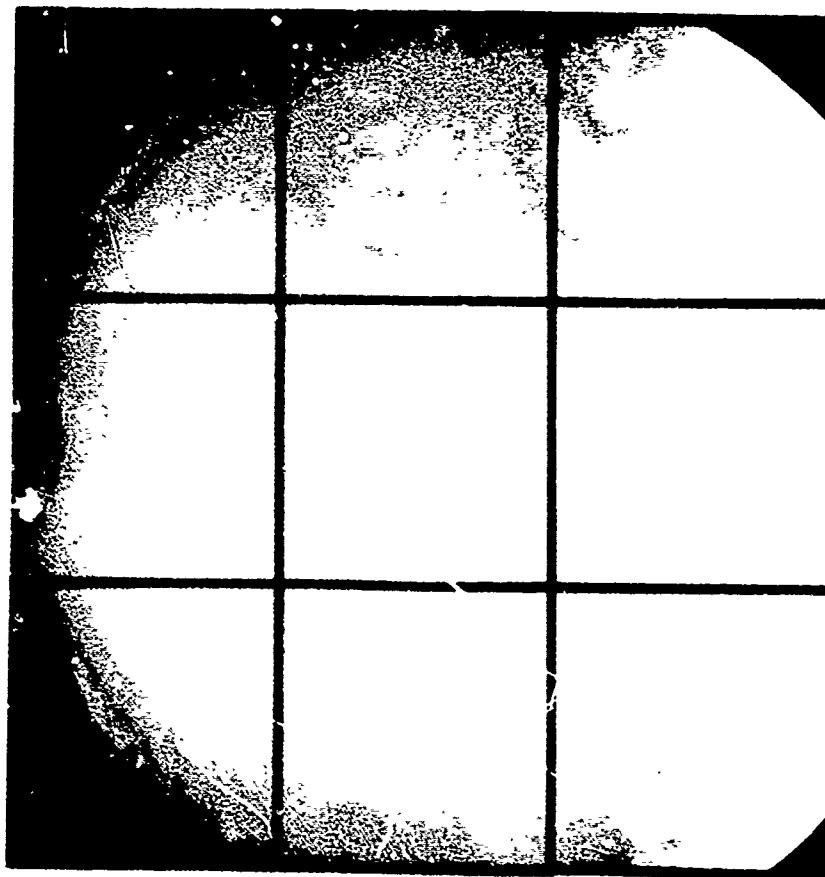


27a. 19.42 seconds



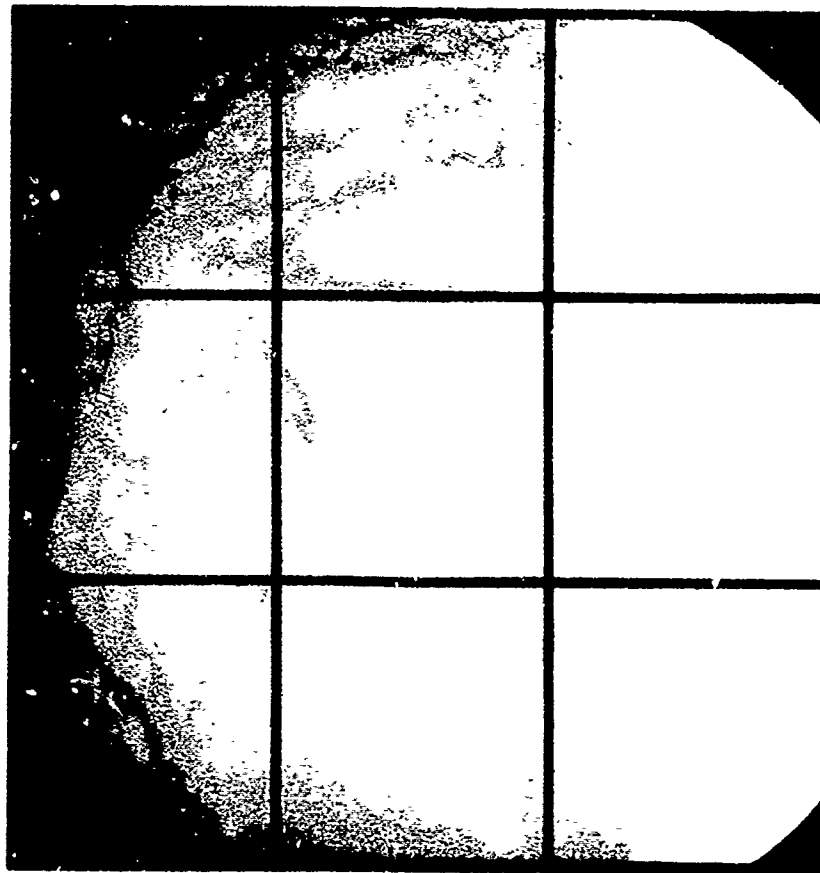
27b. 38.84 seconds

Run 830
3.5-inch R_S Laminar-Blunt
 $Re_\infty = 3.47 \times 10^6/\text{ft}$, $T_0 = 985^\circ\text{F}$



28a.

38.10 seconds



28b.

58.01 seconds

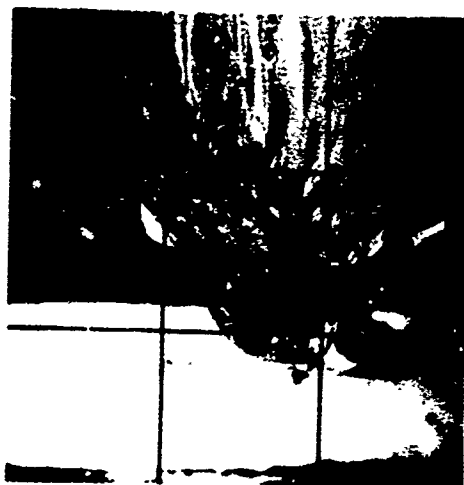
Run 831
3.5-inch R_S Laminar-Blunt
 $Re_\infty = 2.52 \times 10^6 / ft$, $T_0 = 998^\circ F$

APPENDIX E

SELECTED 70MM PROFILE-VIEW PHOTOGRAPHS
RUNS 802-816, 818-831



3.68 seconds



74.99 seconds

Run 802

$Re_{\infty} = 4.09 \times 10^6 / ft$, $T_0 = 970^{\circ}F$



99.86 seconds



5.58 seconds



41.24 seconds

Run 803

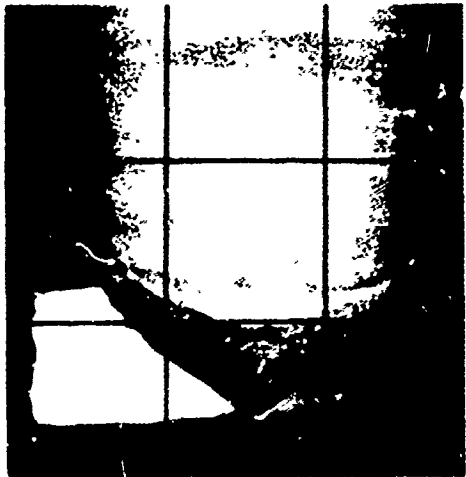
$Re_{\infty} = 6.54 \times 10^6 / ft$, $T_0 = 927^{\circ}F$



63.20 seconds



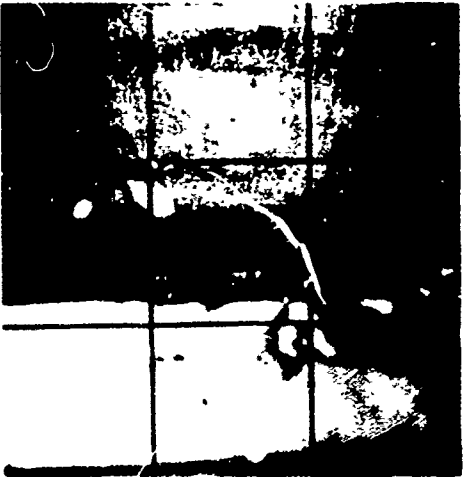
7.21 seconds



29.87 seconds

Run 804

$Re_{\infty} = 2.51 \times 10^6/\text{ft}$, $T_0 = 983^{\circ}\text{F}$



57.09 seconds



3.85 seconds



33.57 seconds

Run 805

$Re_{\infty} = 6.56 \times 10^6/\text{ft}$, $T_0 = 987^{\circ}\text{F}$



49.68 seconds



7.18 seconds



20.70 seconds

Run 806

$Re_{\infty} = 7.36 \times 10^6/\text{ft}$, $T_o = 921^\circ\text{F}$



44.83 seconds



11.87 seconds



69.94 seconds

Run 807

$Re_{\infty} = 4.08 \times 10^6/\text{ft}$, $T_o = 1013^\circ\text{F}$



108.63 seconds



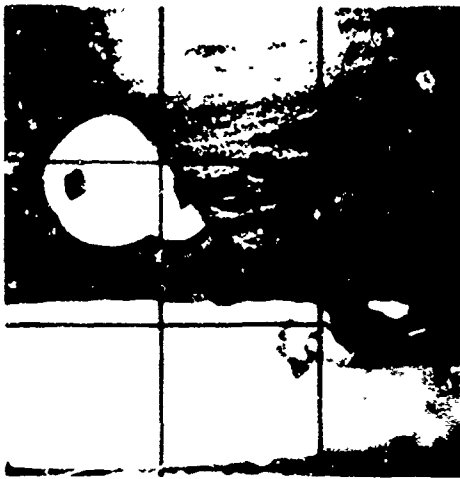
25.92 seconds



87.18 seconds

Run 808

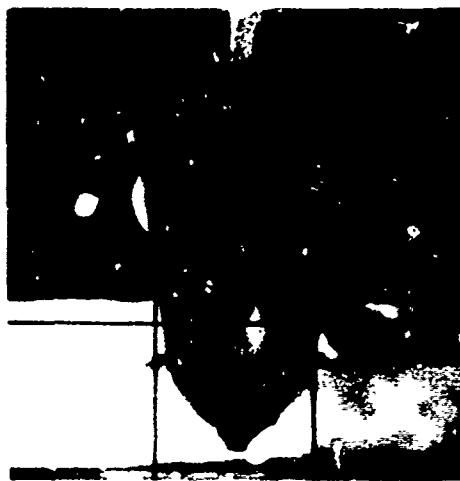
$Re_{\infty} = 1.50 \times 10^6 / ft, T_o = 996^{\circ}F$



130.67 seconds



1.81 seconds



8.02 seconds

Run 809

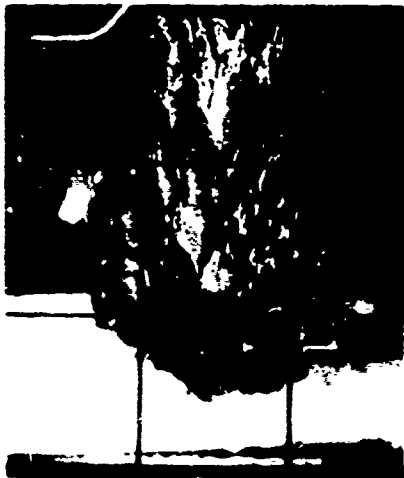
$Re_{\infty} = 9.38 \times 10^6 / ft, T_o = 971^{\circ}F$



27.45 seconds



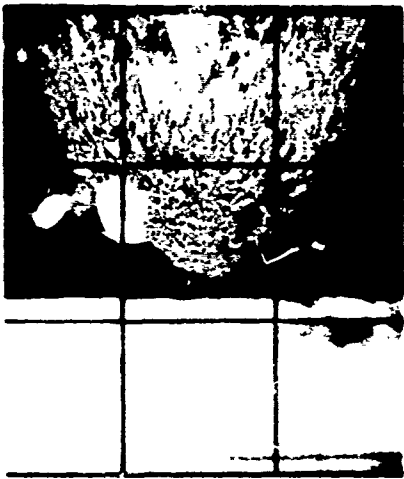
1.81 seconds



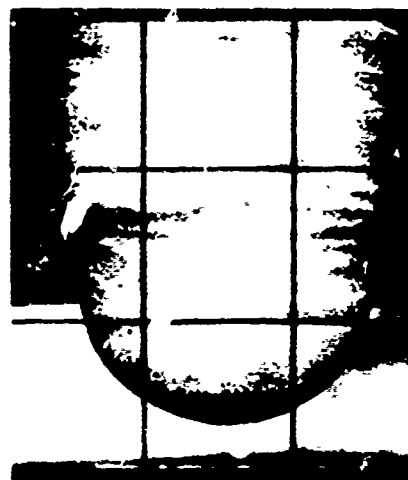
25.44 seconds

Run 810

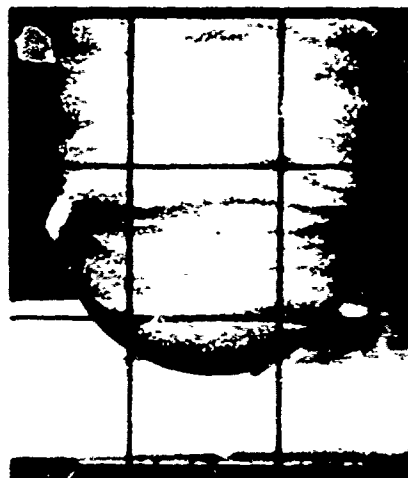
$Re_w = 6.73 \times 10^6 / ft, T_o = 964^\circ F$



48.36 seconds



69.87 seconds (1st portion)



146.45 seconds (1st portion)

Run 811

$Re_w = 0.77 / 1.12 \times 10^6 / ft, T_o = 972^\circ F$



194.32 seconds (2nd portion)



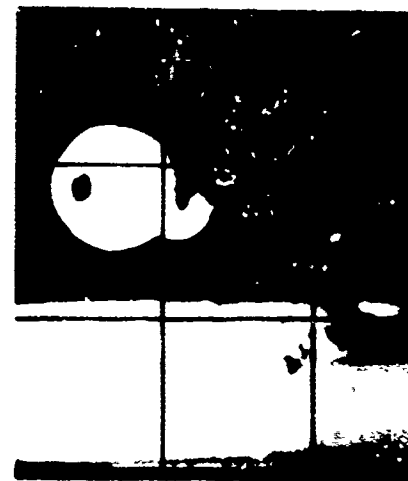
1.70 seconds



15.50 seconds

Run 812

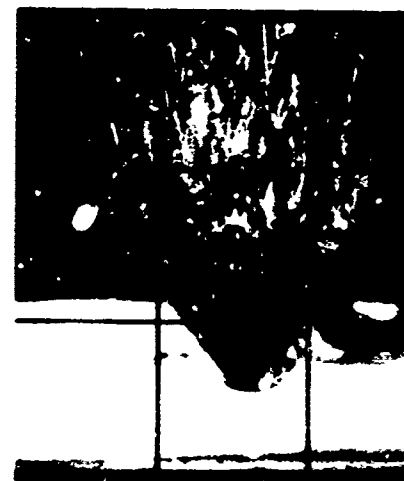
$Re_{\infty} = 15.70 \times 10^6 / ft, T_0 = 807^{\circ}F$



28.98 seconds



6.24 seconds



45.15 seconds

Run 813

$Re_{\infty} = 6.70 \times 10^6 / ft, T_0 = 970^{\circ}F$



56.49 seconds



10.41 seconds



95.37 seconds
Run 814
 $Re_{\infty} = 4.15 \times 10^6 / \text{ft}$, $T_0 = 998^\circ\text{F}$



126.18 seconds



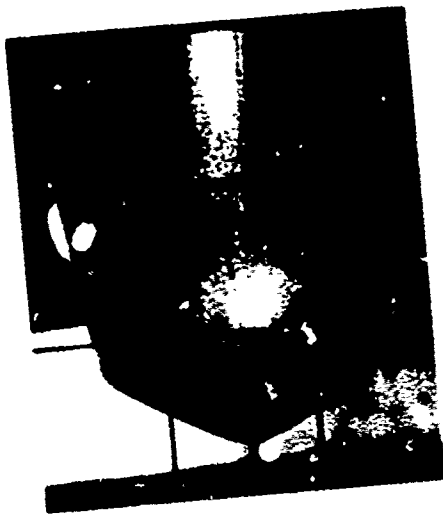
6.51 seconds



10.76 seconds
Run 815
 $Re_{\infty} = 6.72 \times 10^6 / \text{ft}$, $T_0 = 944^\circ\text{F}$



45.30 seconds



6.37 seconds



57.23 seconds
Run 81b
 $Re_{cr} = 5.20 \times 10^6 / ft, T_o = 954^\circ F$



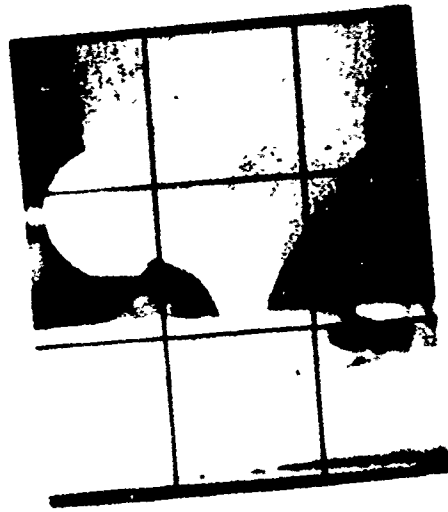
74.99 seconds



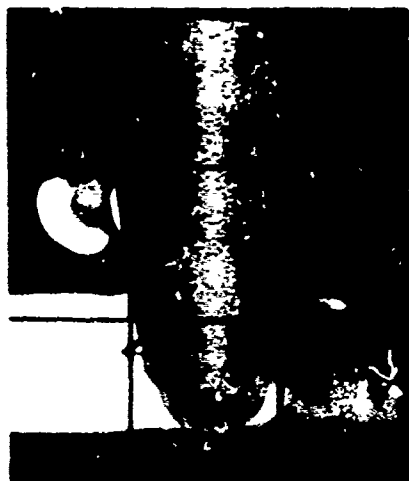
26.04 seconds



67.09 seconds
Run 818
 $Re_{cr} = 9.56 \times 10^6 / ft, T_o = 508^\circ F$



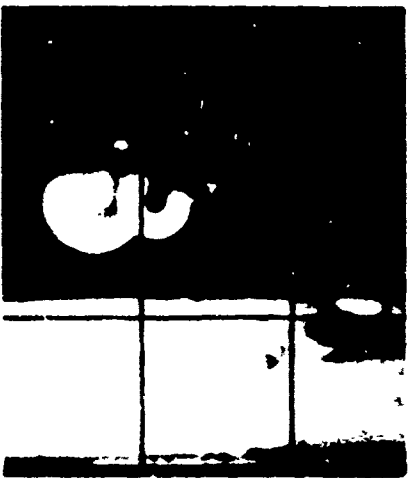
101.10 seconds



20.93 seconds



26.83 seconds
Run 819, Second Portion
 $Re_{\infty} = 12.96 \times 10^6 / ft, T_0 = 804^{\circ}F$



49.82 seconds



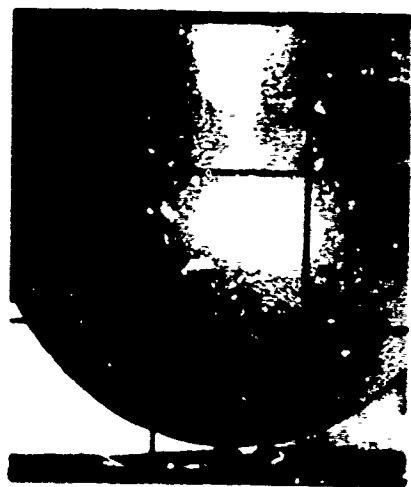
8.89 seconds



39.84 seconds
Run 820
 $Re_{\infty} = 4.90 \times 10^6 / ft, T_0 = 986^{\circ}F$



79.43 seconds



4. seconds



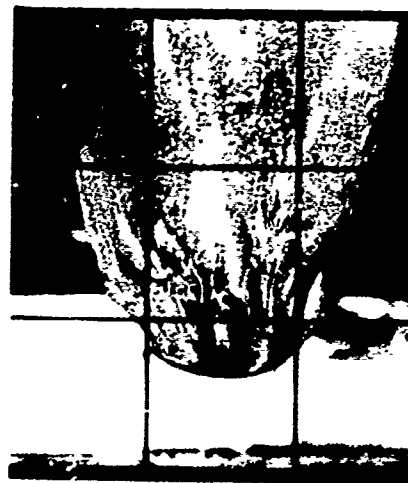
8.47 seconds
Run 821
 $Re_m = 7.47 \times 10^6 / ft, T_o = 973^\circ F$



12.46 seconds



53.90 seconds



77.81 seconds
Run 822
 $Re_m = 4.02 \times 10^6 / ft, T_o = 960^\circ F$



118.48 seconds



16.66 seconds



64.58 seconds

Run 823

$Re_{in} = 5.18 \times 10^6 / ft, T_o = 986^\circ F$



88.51 seconds



5.76 seconds



76.62 seconds

Run 824

$Re_{co} = 9.44 \times 10^6 / ft, T_o = 93^\circ F$



137.79 seconds



2.13 seconds



22.89 seconds
Run 825

$Re_{\infty} = 7.20 \times 10^6 / \text{ft}$, $T_0 = 990^\circ\text{F}$



33.76 seconds



1.93 seconds



76.98 seconds
Run 826

$Re_{\infty} = 3.41 \times 10^6 / \text{ft}$, $T_0 = 987^\circ\text{F}$



125.05 seconds



5.80 seconds



33.16 seconds
Run 827
 $Re_{\infty} = 4.76 \times 10^6 / ft, T_0 = 1008^\circ F$



52.52 seconds



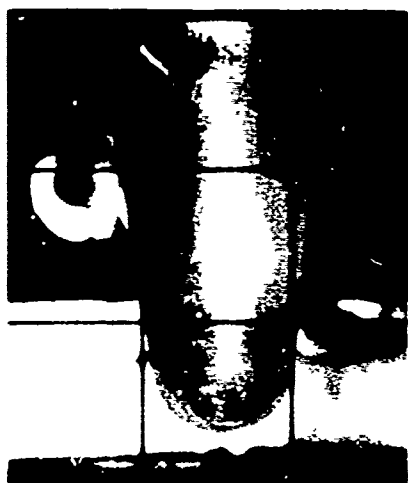
44.20 seconds



56.22 seconds
Run 828
Variable Re_{∞}



78.25 seconds



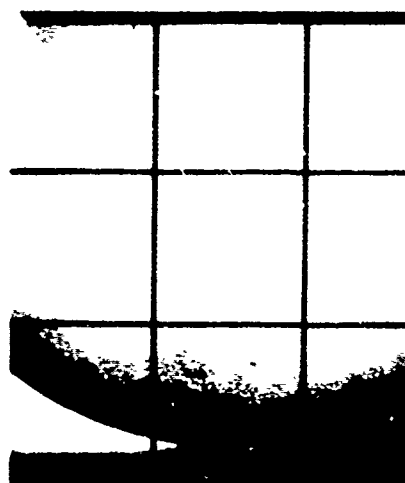
45.81 seconds



65.84 seconds
Run 829
Variable Re_{∞}



92.06 seconds



11.67 seconds



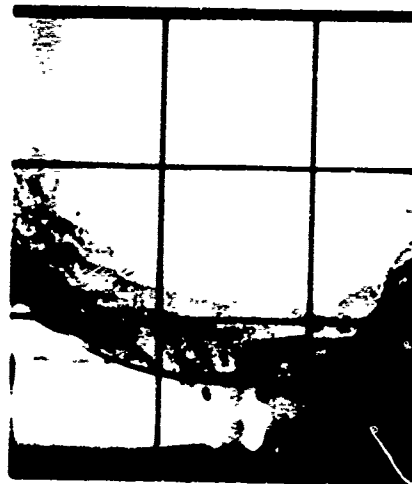
48.23 seconds
Run 830
 $Re_{\infty} = 3.47 \times 10^6 / ft, T_o = 985^{\circ}F$



67.55 seconds



68.54 seconds



89.18 seconds

Run 831

$Re_{cr} = 2.52 \times 10^6 / ft, T_o = 998^\circ F$



123.01 seconds

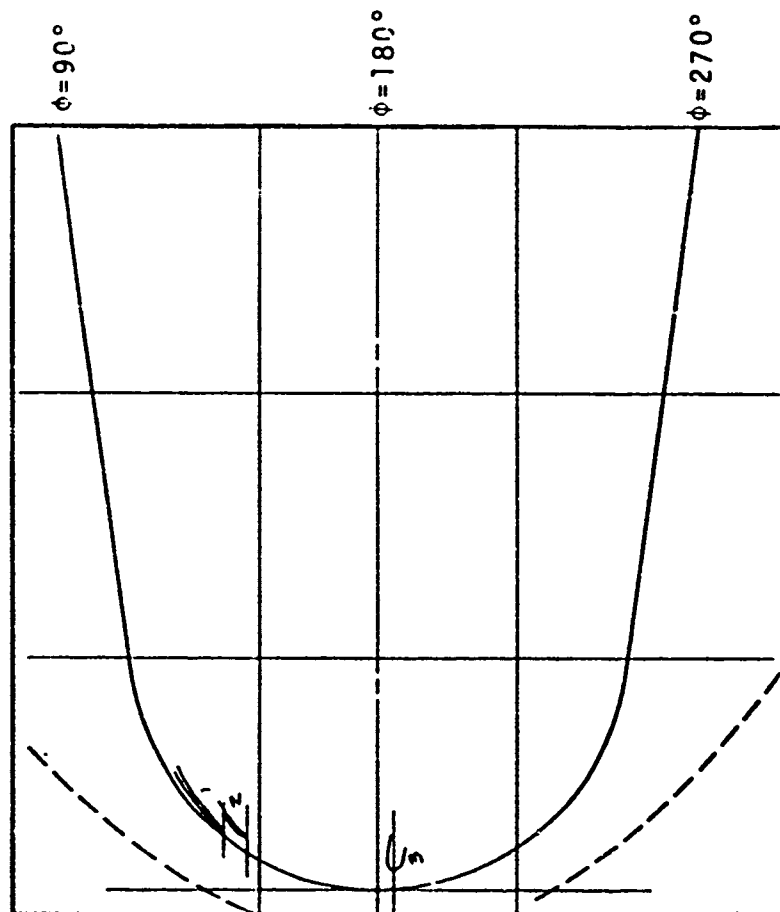
APPENDIX F

**INITIAL TRANSITION LOCATION TRACINGS AND
INITIAL TRANSITION LOCATION PLOTS**

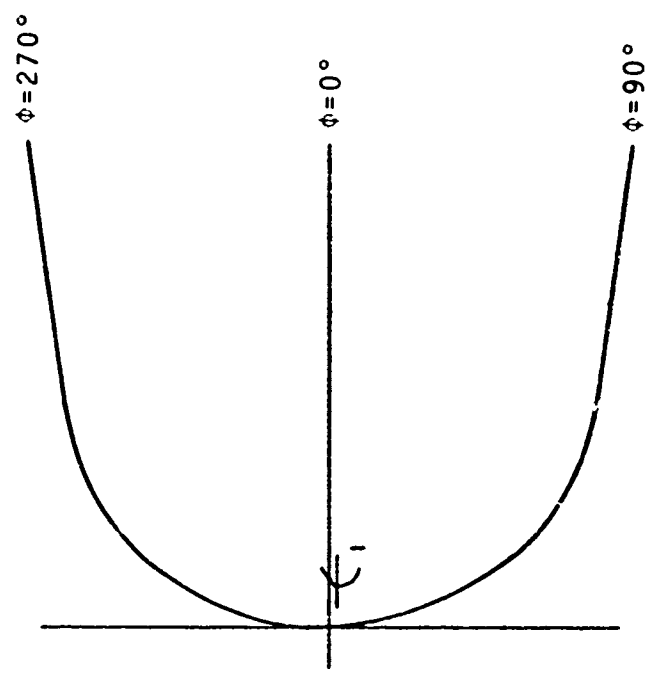
**RUNS 802, 803, 805, 806, 809, 810, 813,
816, 818, 823, 824, 827, 828, 829**

TABLE F-1
MODEL EXPOSURE TIMES
CORRESPONDING TO INITIAL
TRANSITION LOCATIONS

Run No.	Model Exposure Time (Sec)	
	70mm Profile-View (Lower Side)	35mm Overhead (Upper Side)
802	1.71	8.39
803	5.58	5.60
805	1.83	1.93
806	3.72	3.69
809	1.81	1.85
810	1.81	-
813	3.99	3.95
816	2.42	11.84
818	13.98	11.01
823	7.80	7.83
824	2.73	4.38
827	5.80	5.86
828	34.20	34.21
829	25.78	25.72

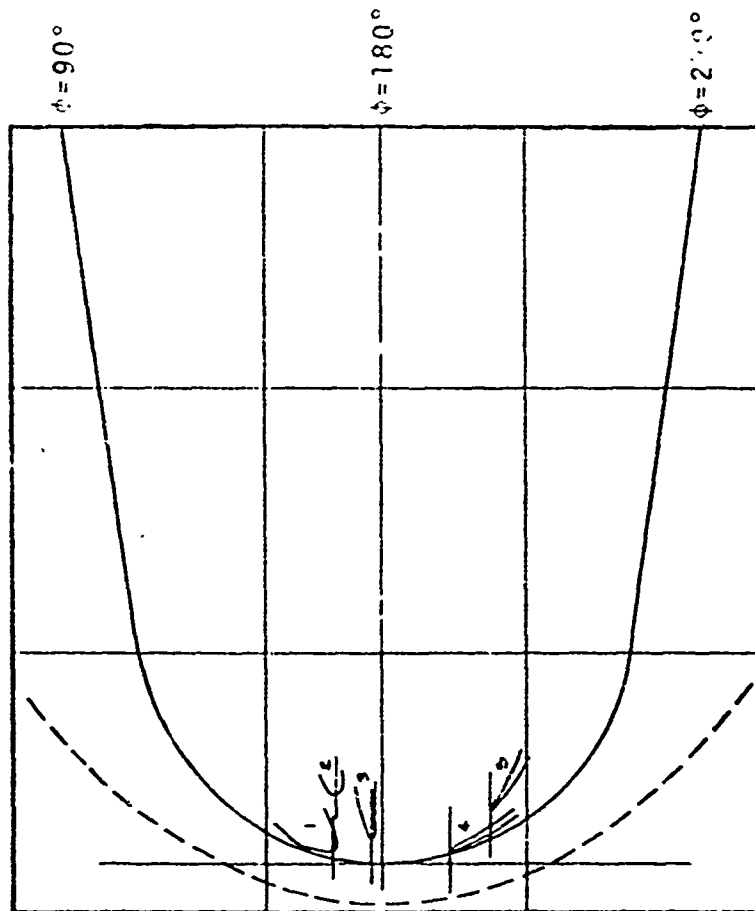


Lower Side
70mm Profile-view Camera

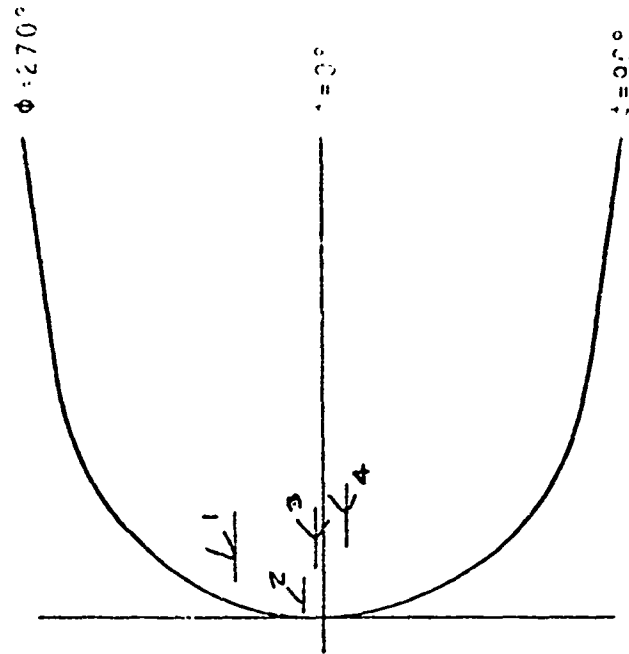


Upper Side
35mm Overhead Camera

Figure F-1. Initial Transition Location Tracings for Run 802 (1.5-Inch R_N Sphere-Cone;
 $Re_\infty = 4.09 \times 10^6/\text{ft}$, $T_0 = 970^\circ\text{F}$)

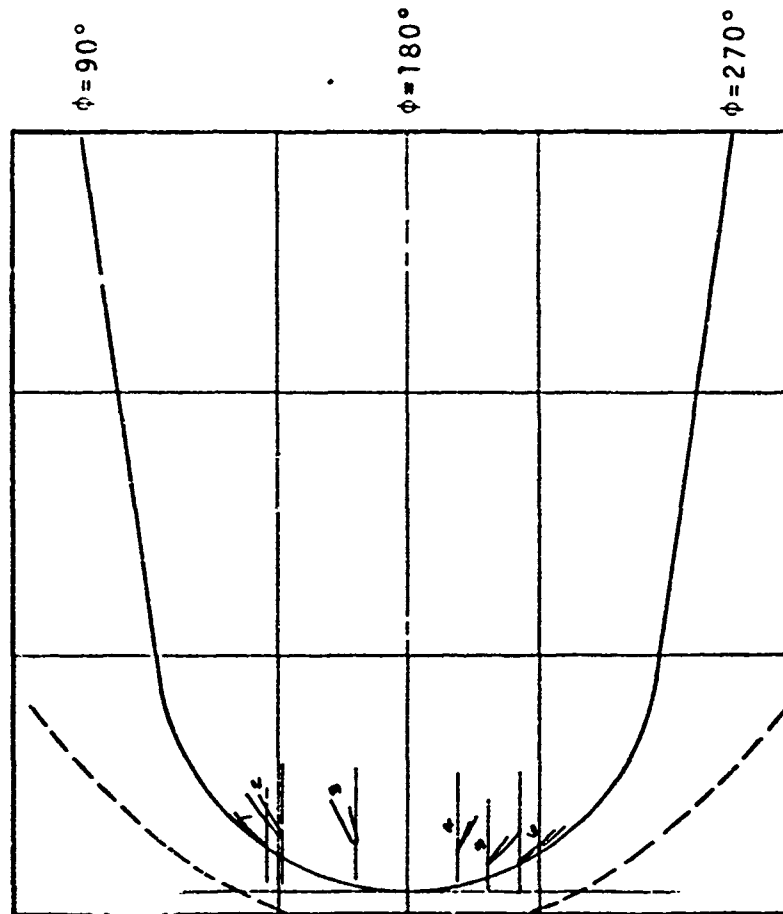


Lower Side
70mm Profile-view Camera

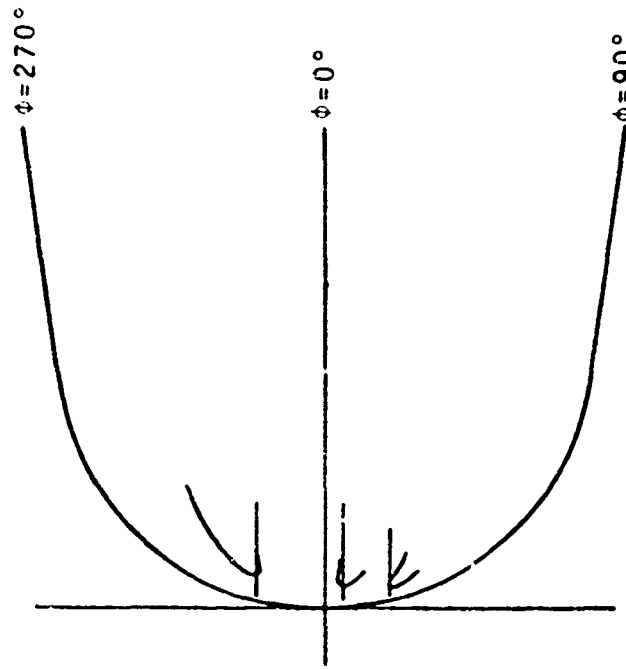


Upper Side
35mm Overhead Camera

Figure F-2. Initial Transition Location Tracings for Run 803 (1.5-Inch R_N Sphere-Cone;
 $Re_\infty = 6.54 \times 10^6/\text{ft}$; $T_0 = 927^\circ\text{F}$)

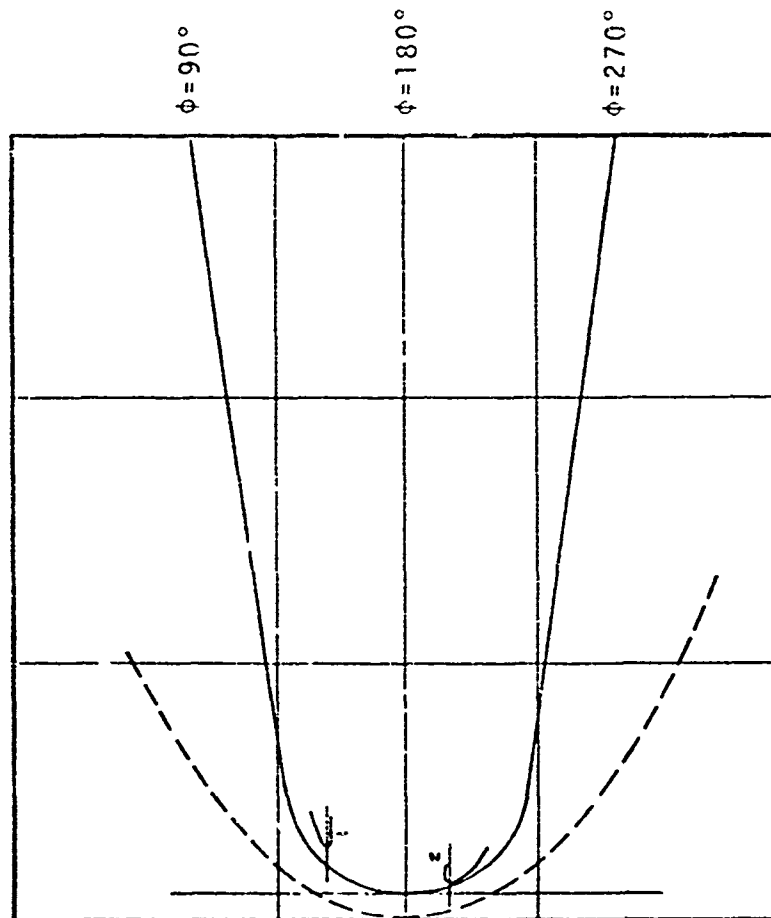


Lower Side
70mm Profile-view Camera

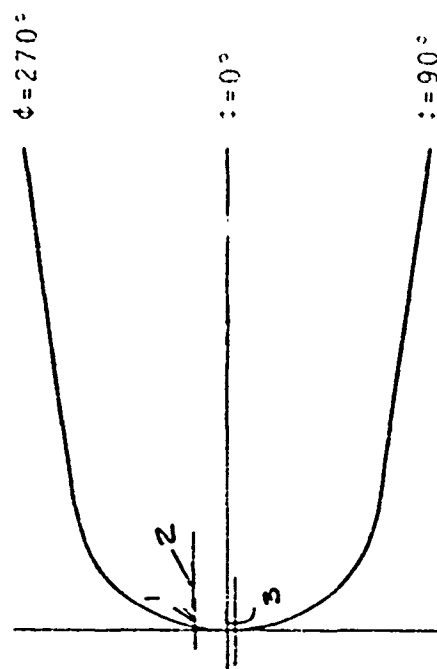


Upper Side
35mm Cverhead Camera

Figure F-3. Initial Transition Location Tracings for Run 805 (1.5-Inch R_N Sphere-Cone;
 $Re_\infty = 6.56 \times 10^6/\text{ft}$; $T_o = 987^\circ\text{F}$)



Lower Side
70mm Profile-view Camera



Upper Side
35mm Overhead Camera

Figure F-4. Initial Transition Location Tracings for Run 806 (0.75-Inch R_N Sphere-Cone;
 $Re_\infty = 7.36 \times 10^6/\text{ft}$; $T_o = 921^\circ\text{F}$)

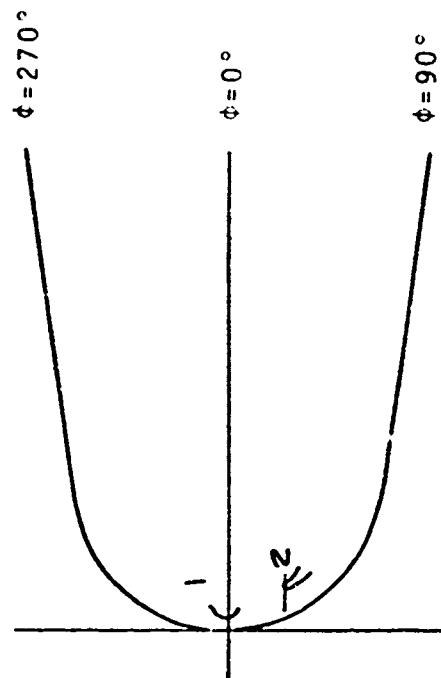
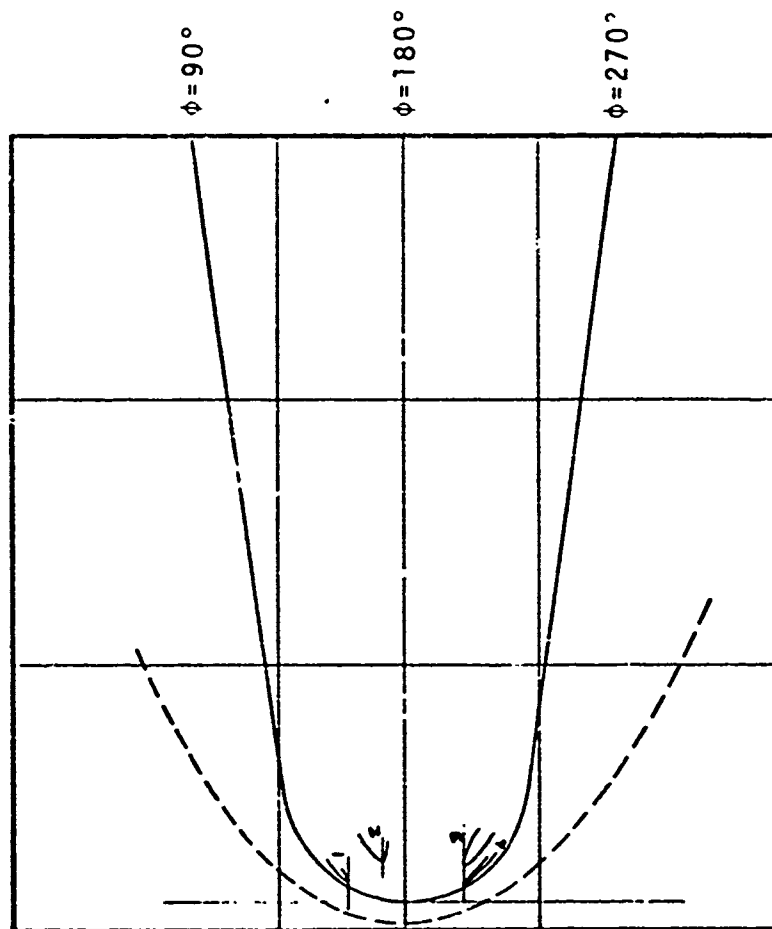
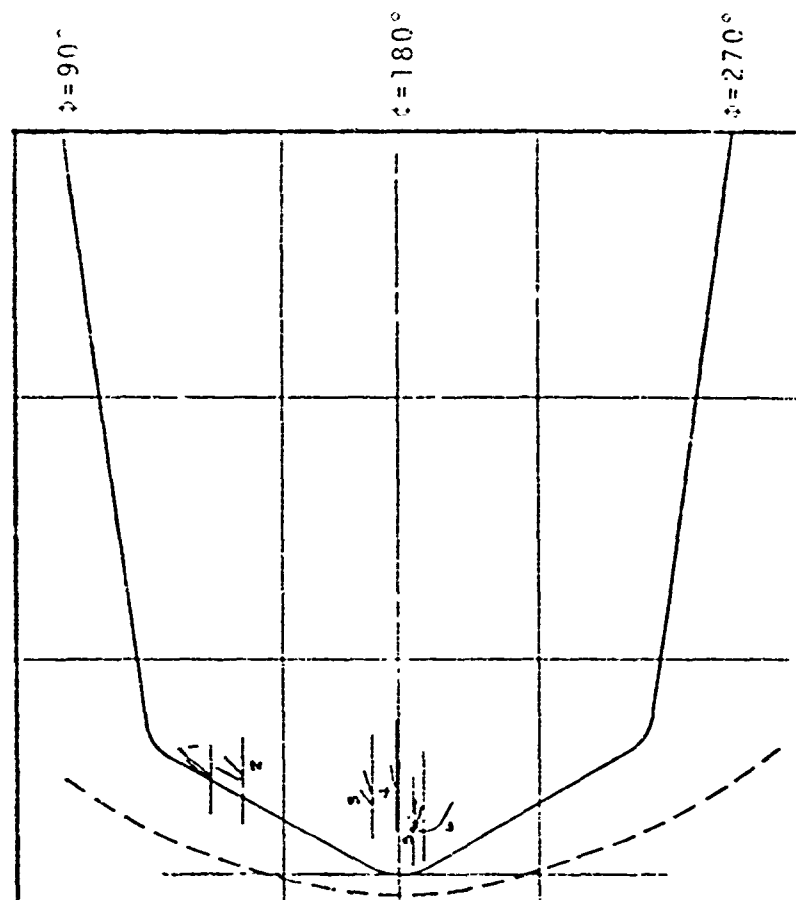


Figure F-5. Initial Transition Location Tracings for Run 809 (0.75-Inch R_N Sphere-Cone;
 $Re_\infty = 9.38 \times 10^6/\text{ft}$; $T_0 = 971^\circ\text{F}$)



Lower Side
70mm Profile-view Camera

Figure F-6. Initial Transition Location Tracings for Run 810 (1.5-Inch $R_S/60^\circ/8^\circ$ Biconic;
 $Re_\infty = 6.73 \times 10^6/\text{ft}$; $T_0 = 964^\circ\text{F}$)

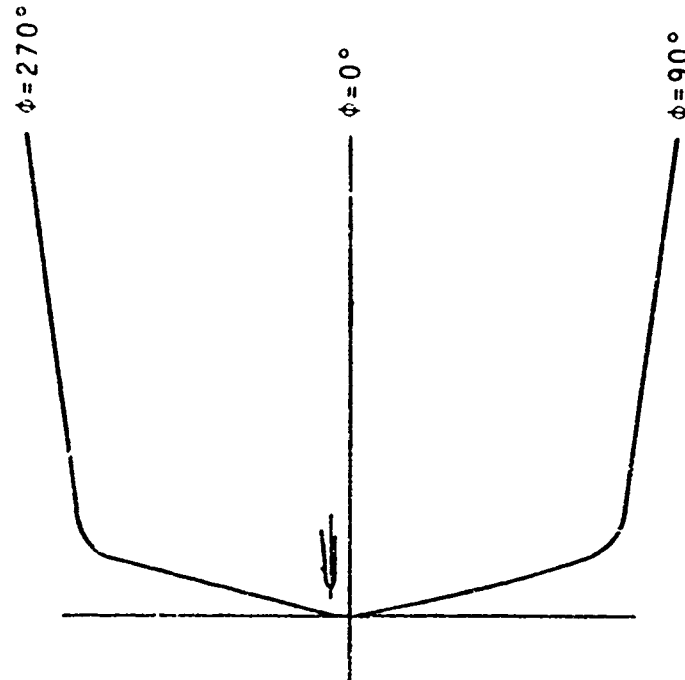
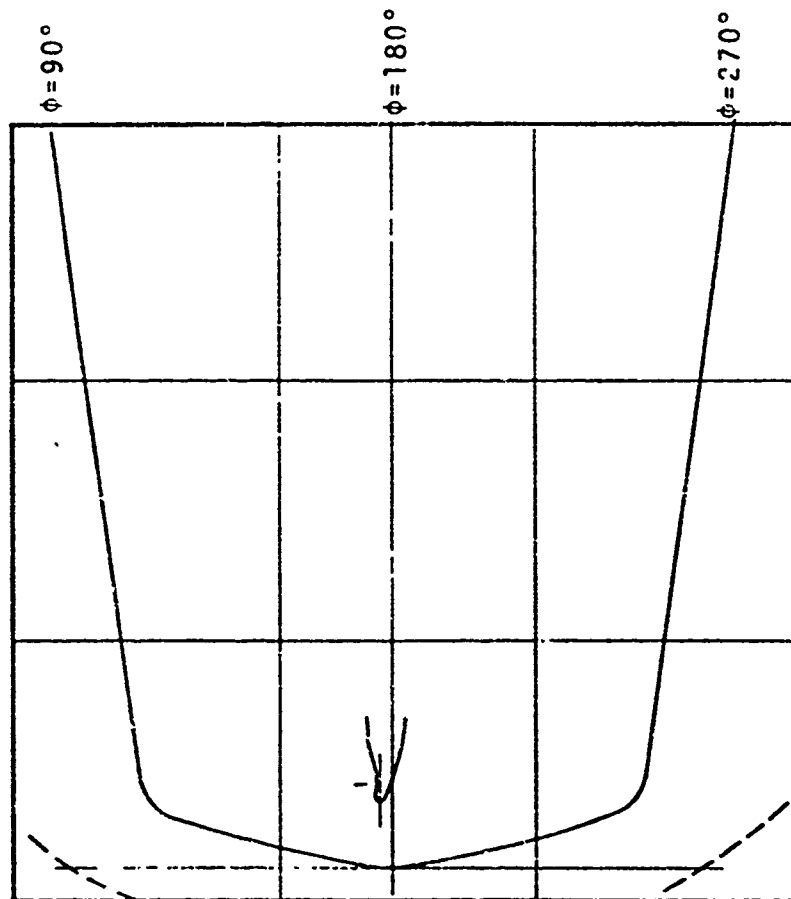


Figure F-7. Initial Transition Location Tracings for Run 813 (1.5-Inch $R_S/75^\circ/8^\circ$ Biconic;
 $Re_\infty = 6.70 \times 10^6/\text{ft}$; $T_0 = 970^\circ\text{F}$)

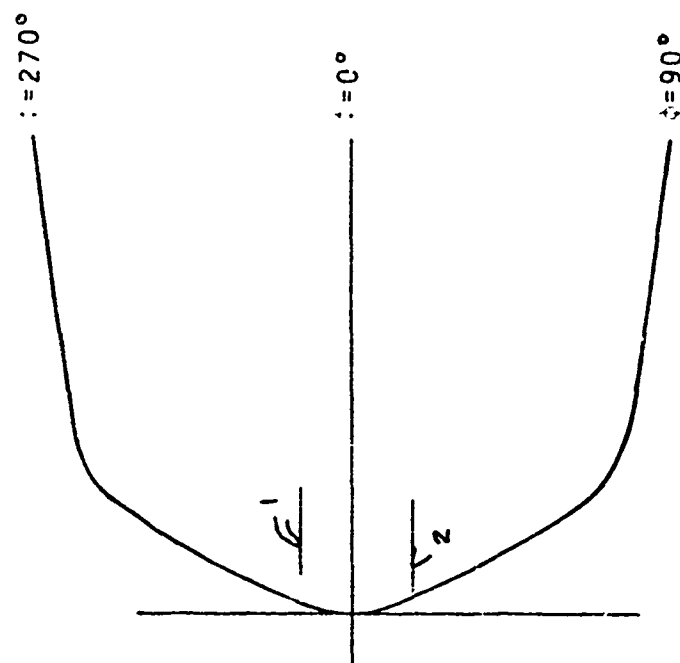
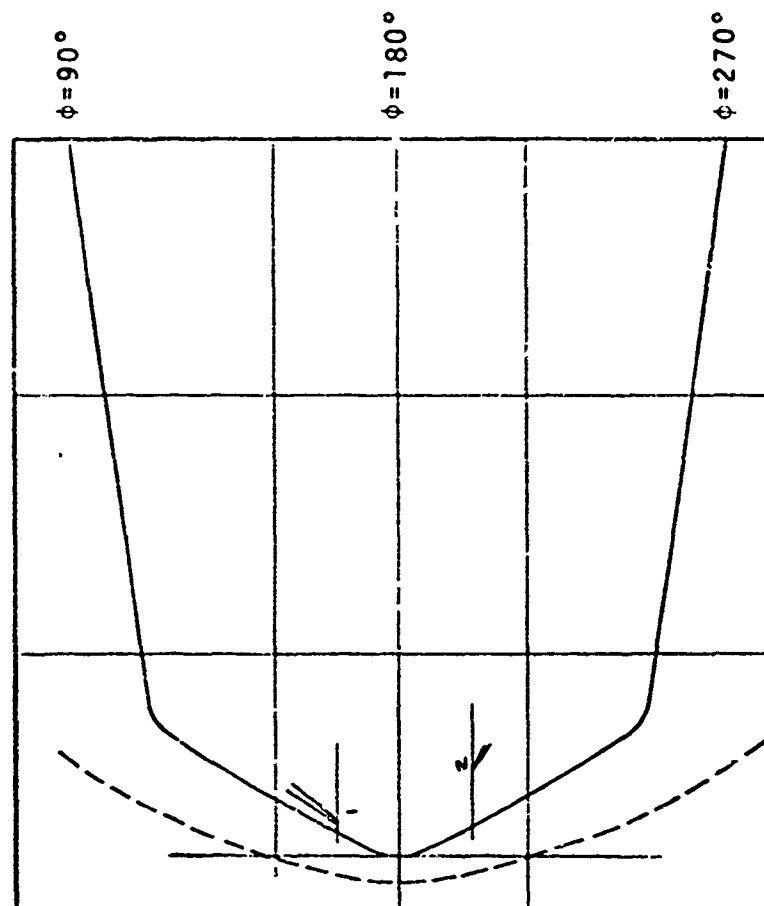
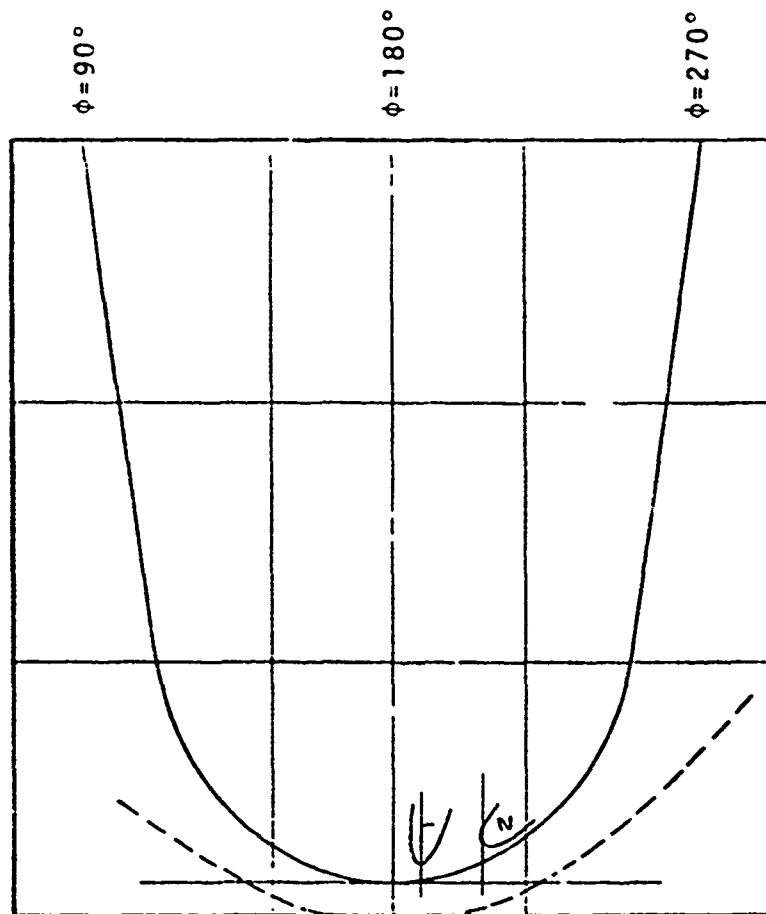
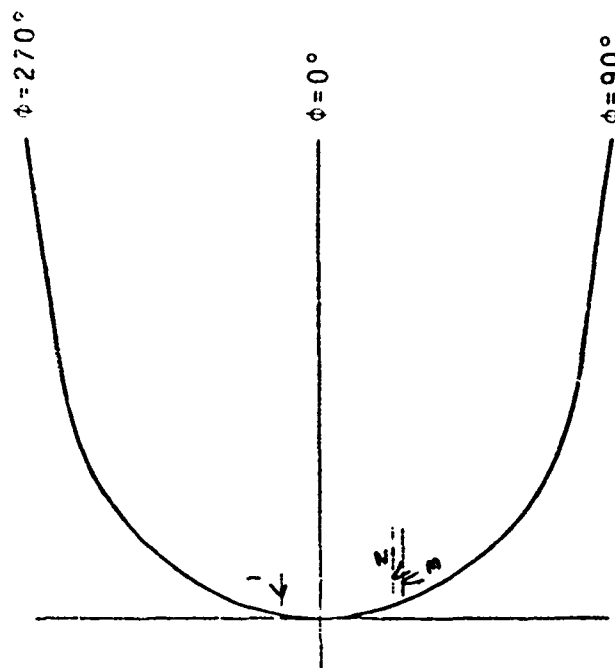


Figure F-8. Initial Transition Location Tracings for Run 816 (1.5-Inch $R_S/60^\circ/8^\circ$ Biconic;
 $Re_\infty = 5.20 \times 10^6/\text{ft}$; $T_o = 954^\circ\text{F}$)

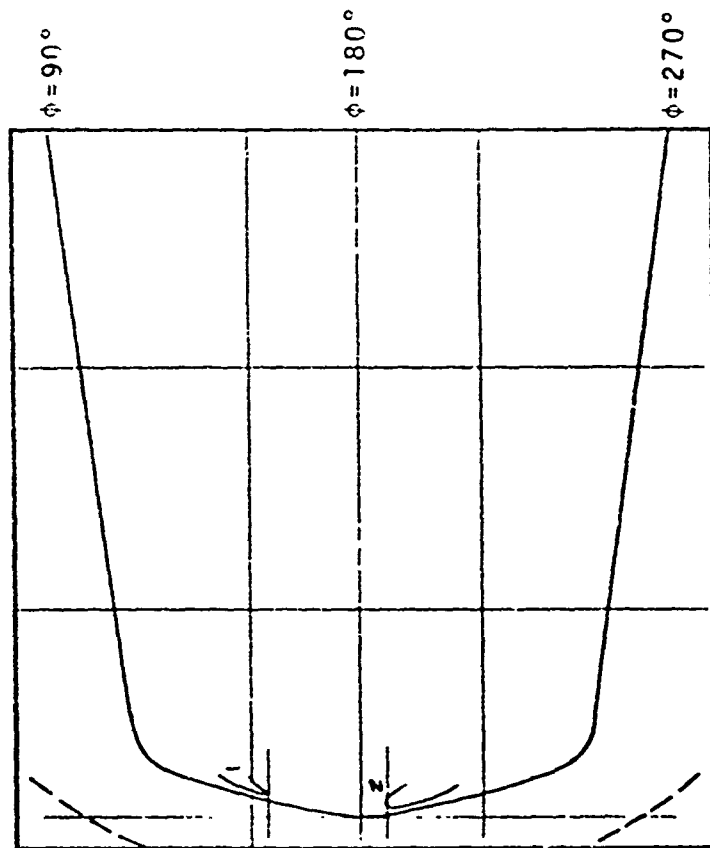


Lower Side
70mm Profile-view Camera

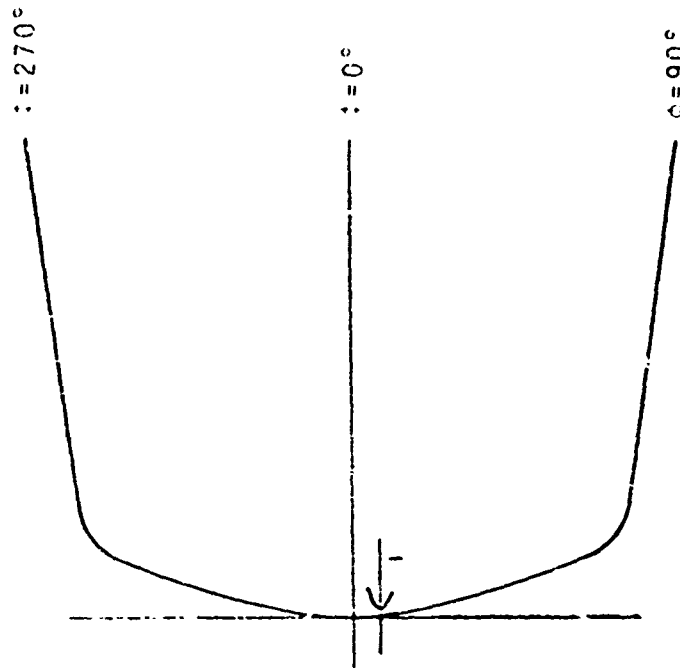


Upper Side
35mm Overhead Camera

Figure F-9. Initial Transition Location Tracings for Run 818 (1.5-Inch R_N Sphere-Cone;
 $Re_\infty = 9.56 \times 10^6/\text{ft}$; $T_0 = 508^\circ\text{F}$)

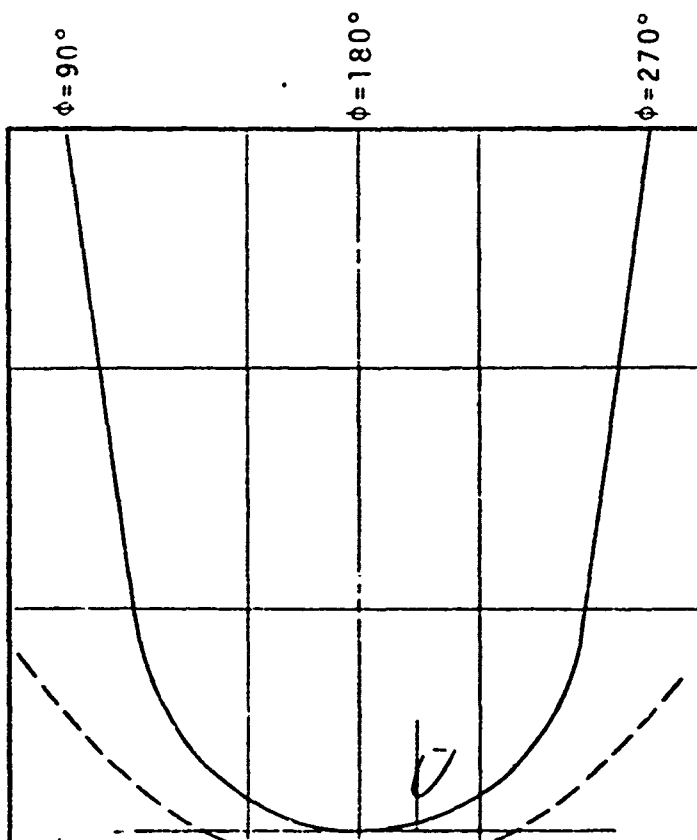


Lower Side
70mm Profile-view Camera

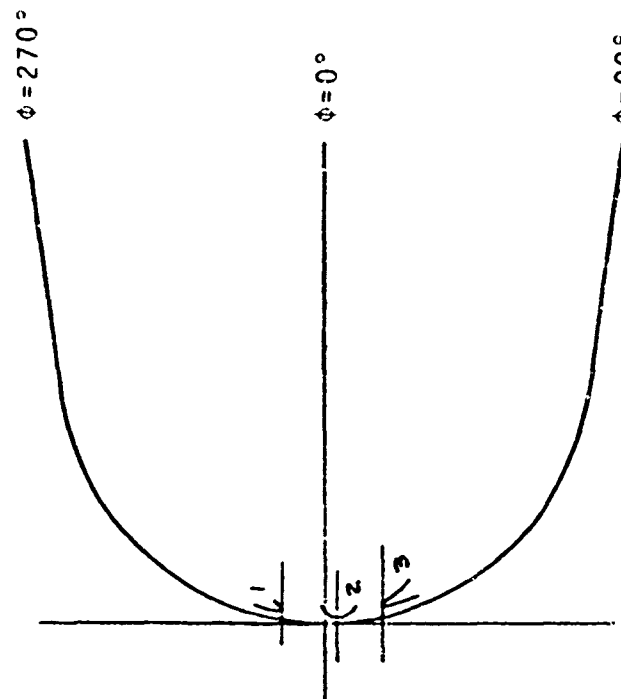


Upper Side
35mm Overhead Camera

Figure F-10. Initial Transition Location Tracings for Run 823 (1.5-Inch $R_S/75^\circ/8^\circ$ Biconic;
 $Re_\infty = 5.18 \times 10^6/\text{ft}$; $T_o = 986^\circ\text{F}$)



Lower Side
70mm Profile-view Camera



Upper Side
35mm Overhead Camera

Figure F-11. Initial Transition Location Tracings for Run 824 (1.5-Inch R_N Sphere-Cone;
 $Re_\infty = 9.44 \times 10^6/\text{ft}$; $T_o = 535^\circ\text{F}$)

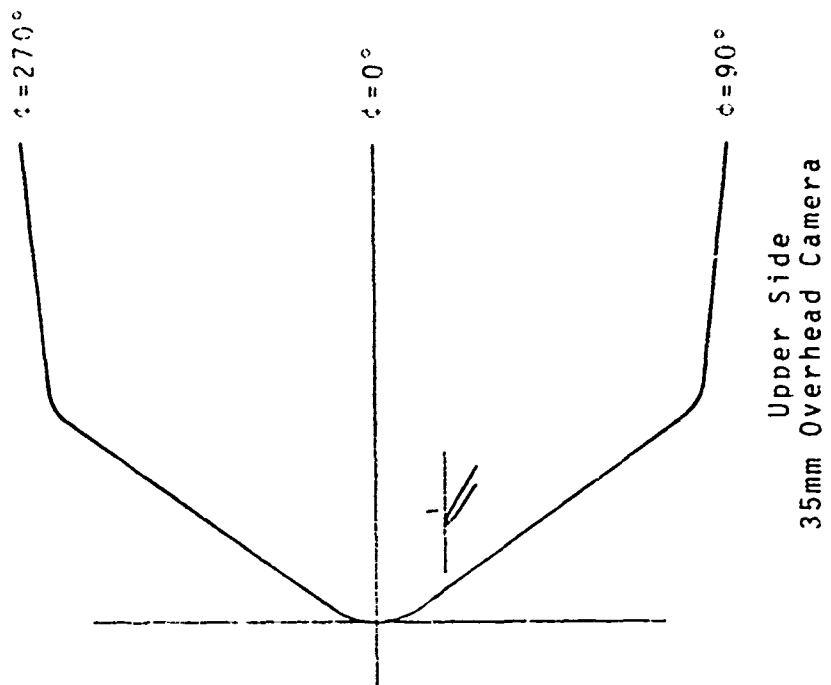
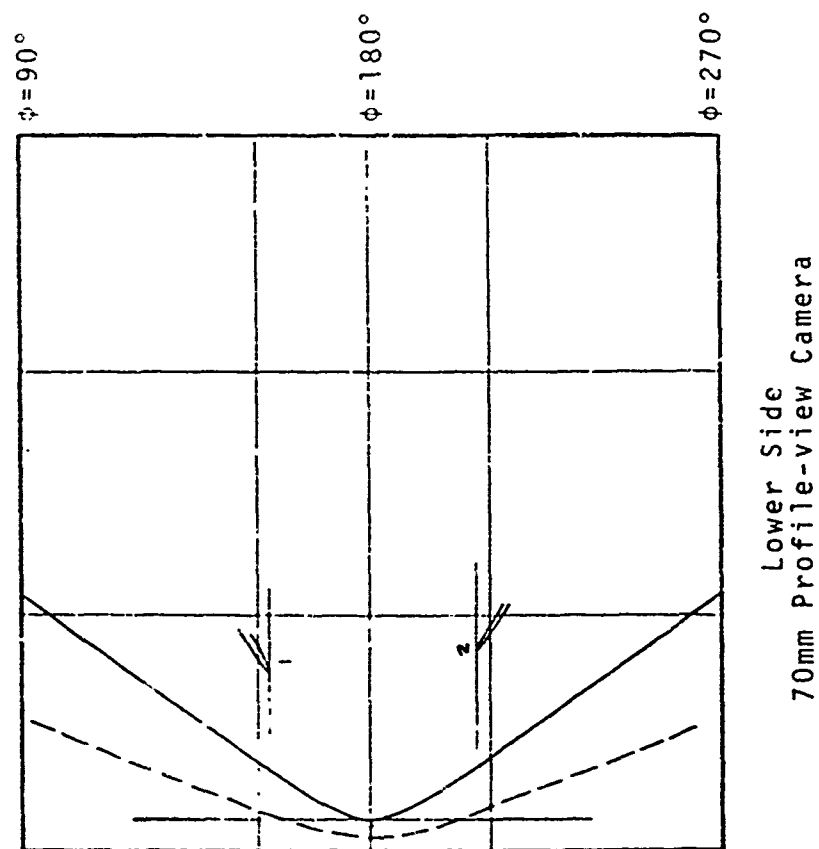
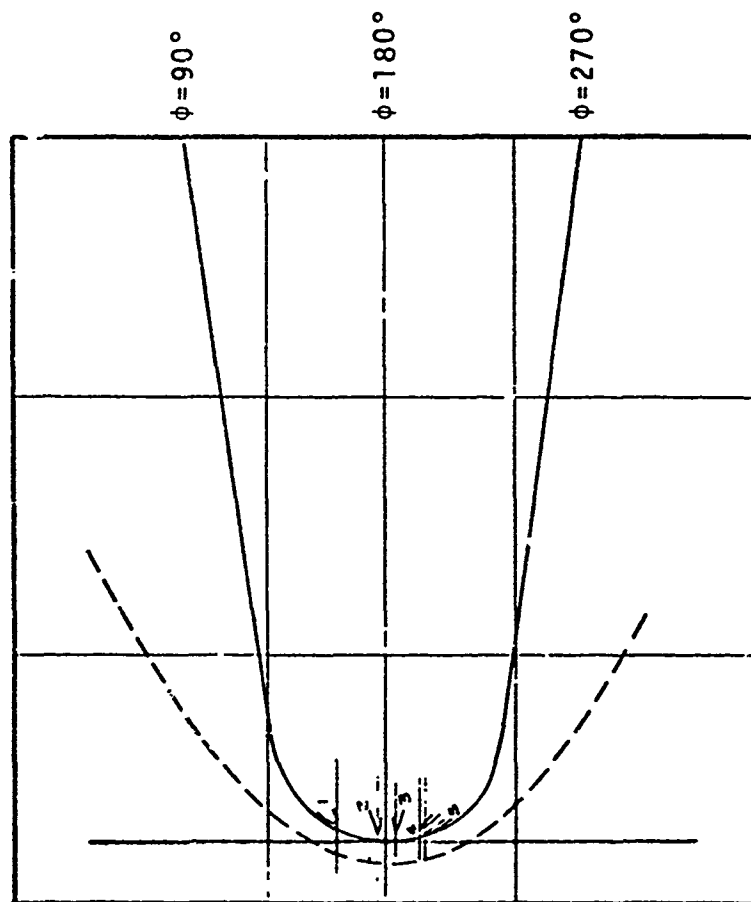
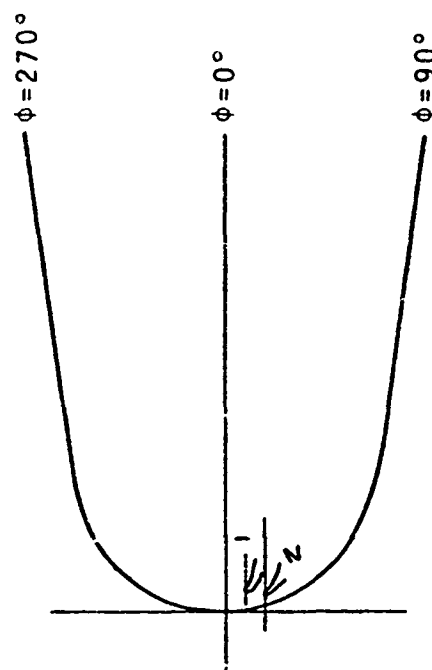


Figure F-12. Initial Transition Location Tracings for Run 825 (2.5-Inch $R_S/55^\circ/6^\circ$ Biconic;
 $Re_\infty = 4.76 \times 10^6/\text{ft}$; $T_o = 1008^\circ\text{F}$)

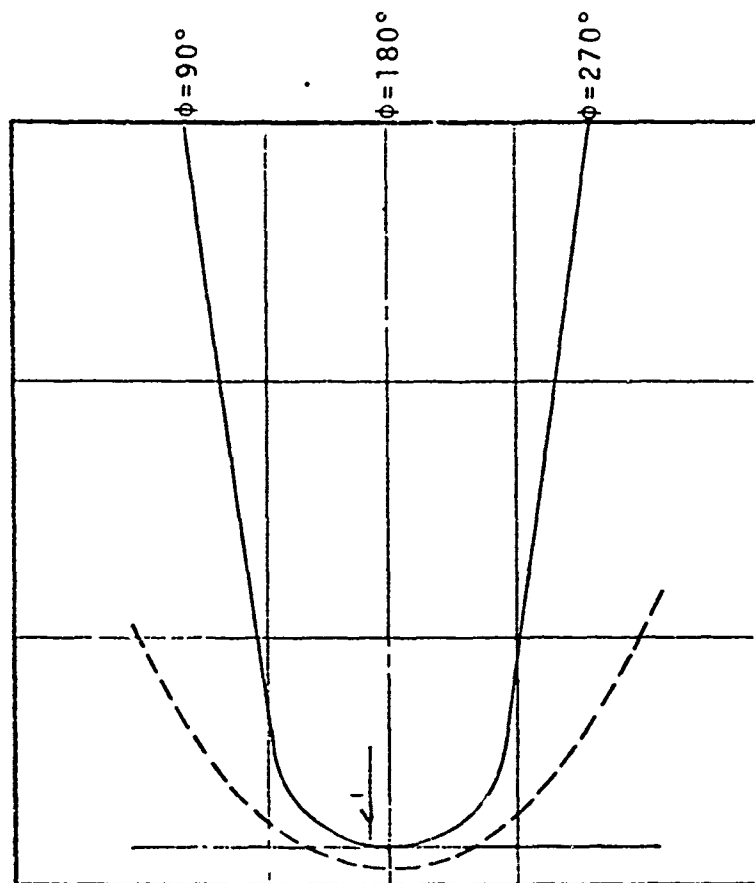


Lower Side
70mm Profile-view Camera

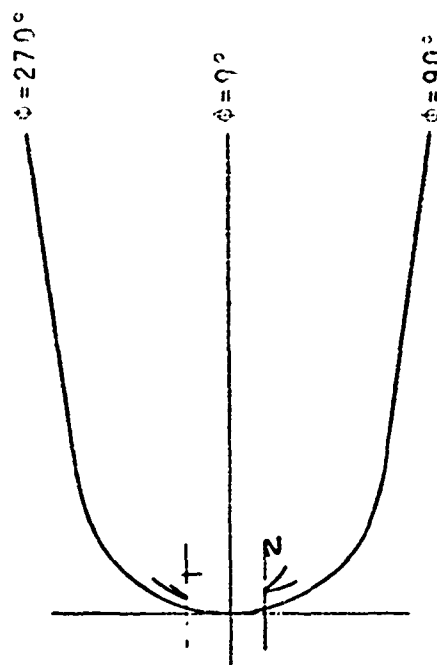


Upper Side
35mm Overhead Camera

Figure F-13. Initial Transition Location Tracings for Run 828 (0.75-Inch R_N Sphere-Cone;
Variable Re_∞)



Lower Side
70mm Profile-view Camera



Upper Side
35mm Overhead Camera

Figure F-14. Initial Transition Location Tracings for Run 829 (0.75-Inch R_N Sphere-Cone;
Variable Re_∞)

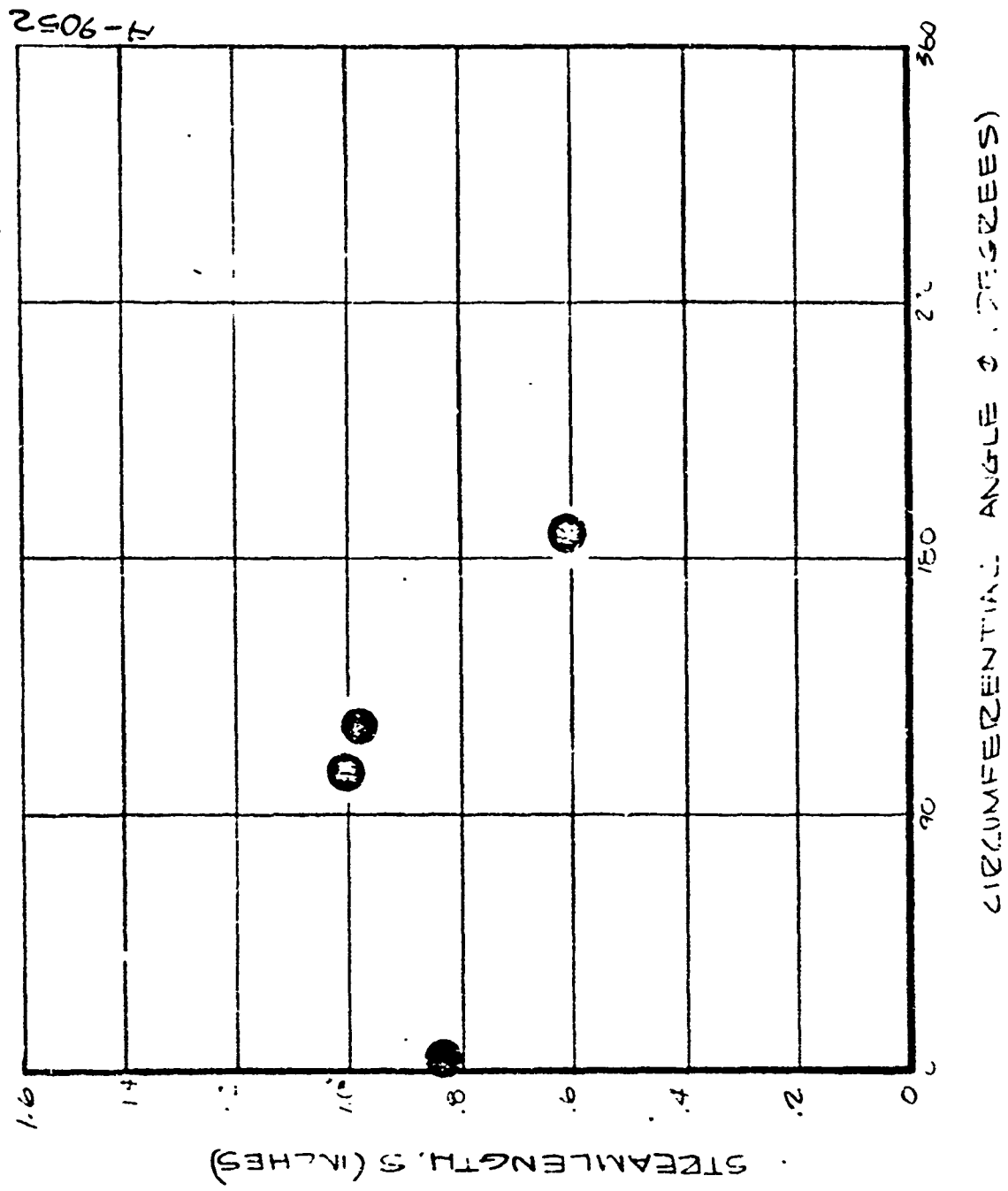


Figure F-15. Initial Transition Locations for Run 802 (1.5-Inch R_N Sphere-Cone;
 $Re_\infty = 4.09 \times 10^5/\text{ft}$; $T_0 = 970^\circ\text{F}$)

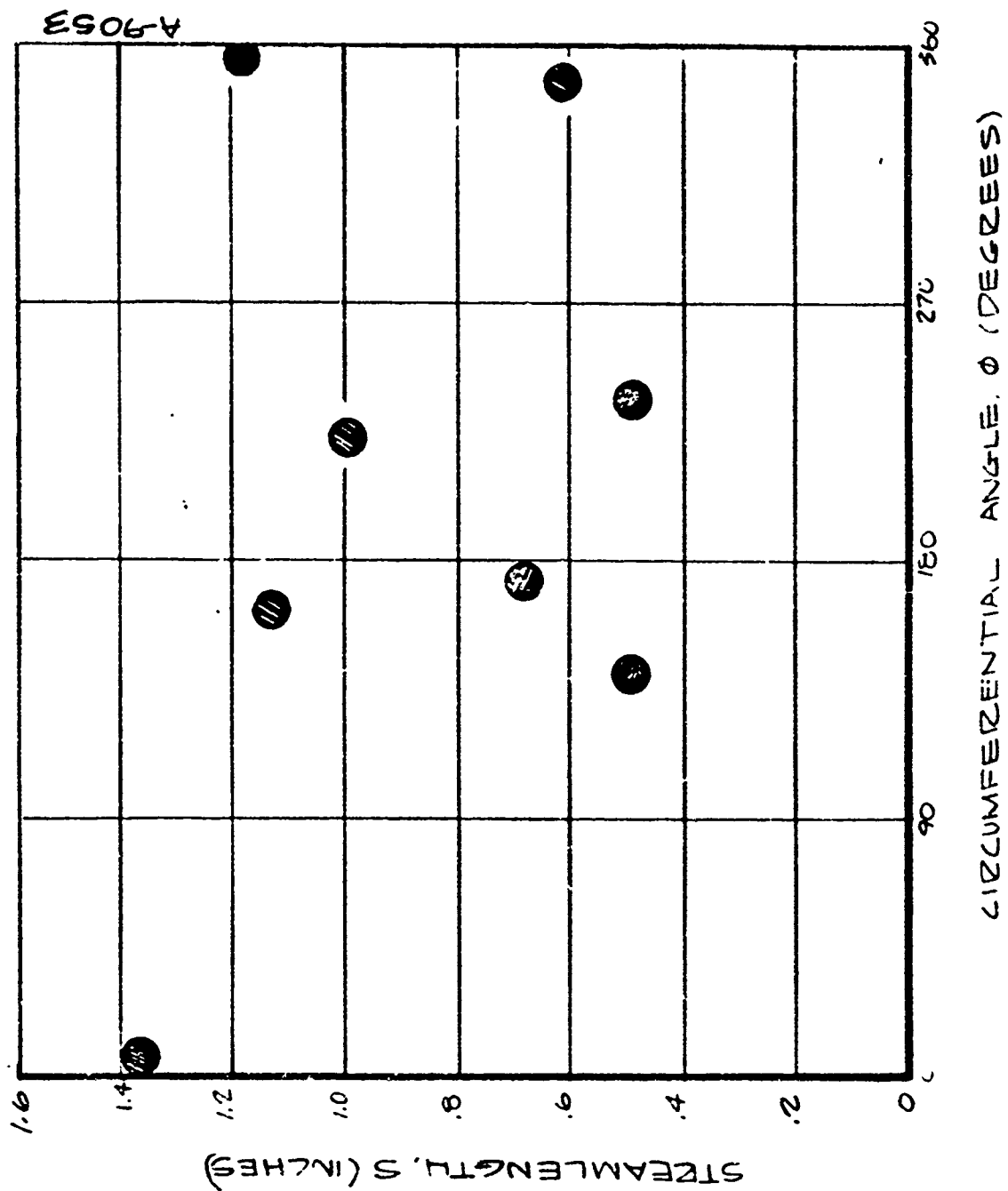


Figure F-16. Initial Transition Locations for Run 803 (1.5-Inch R_N Sphere-Cone;
 $Re_\infty = 6.54 \times 10^6/\text{ft}$; $T_0 = 927^\circ\text{F}$)

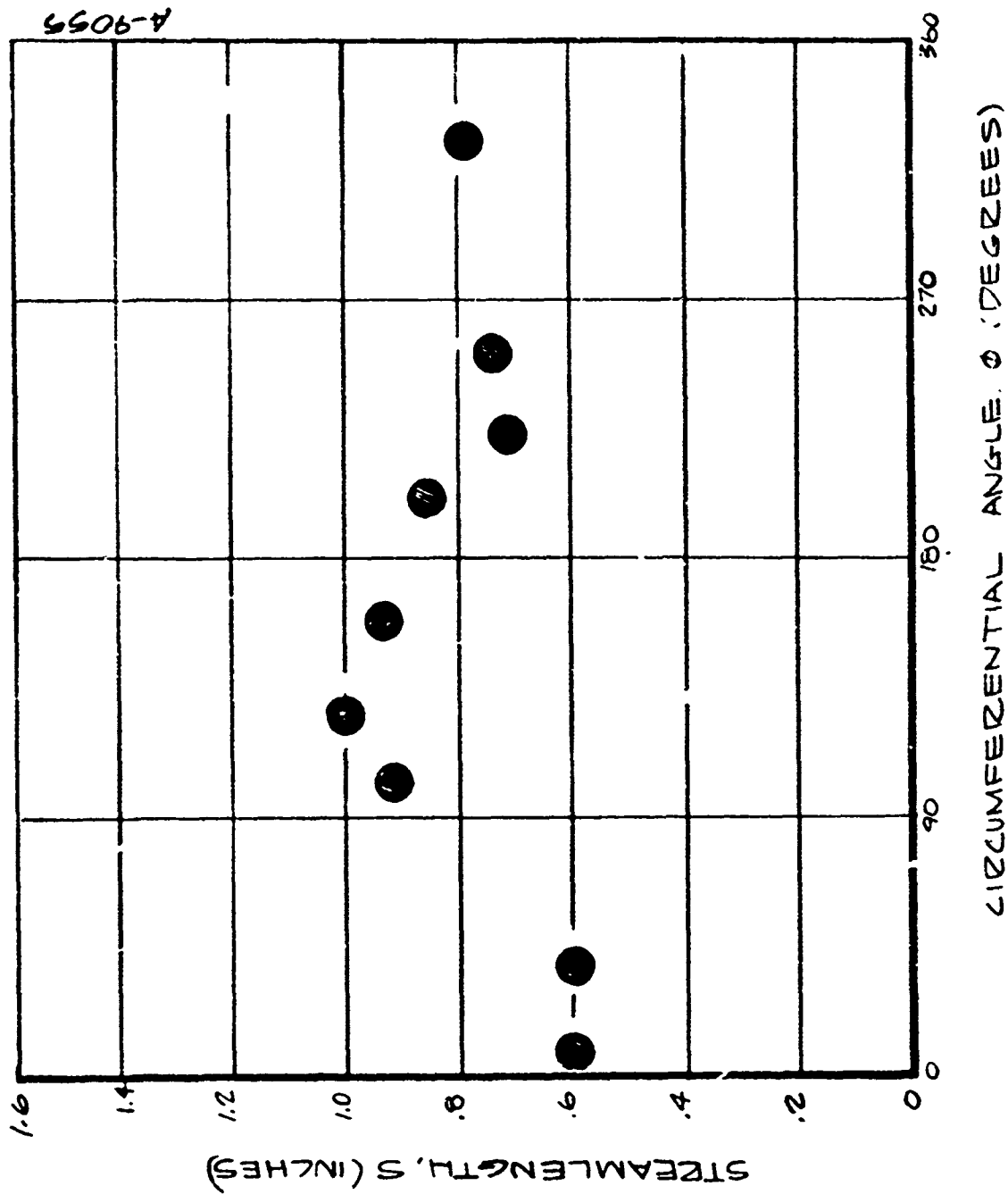


Figure F-17. Initial Transition Locations for Run 805 (1.5-Inch R_N Sphere-Cone;
 $Re_\infty = 6.56 \times 10^6/\text{ft}$; $T_o = 987^\circ\text{F}$)

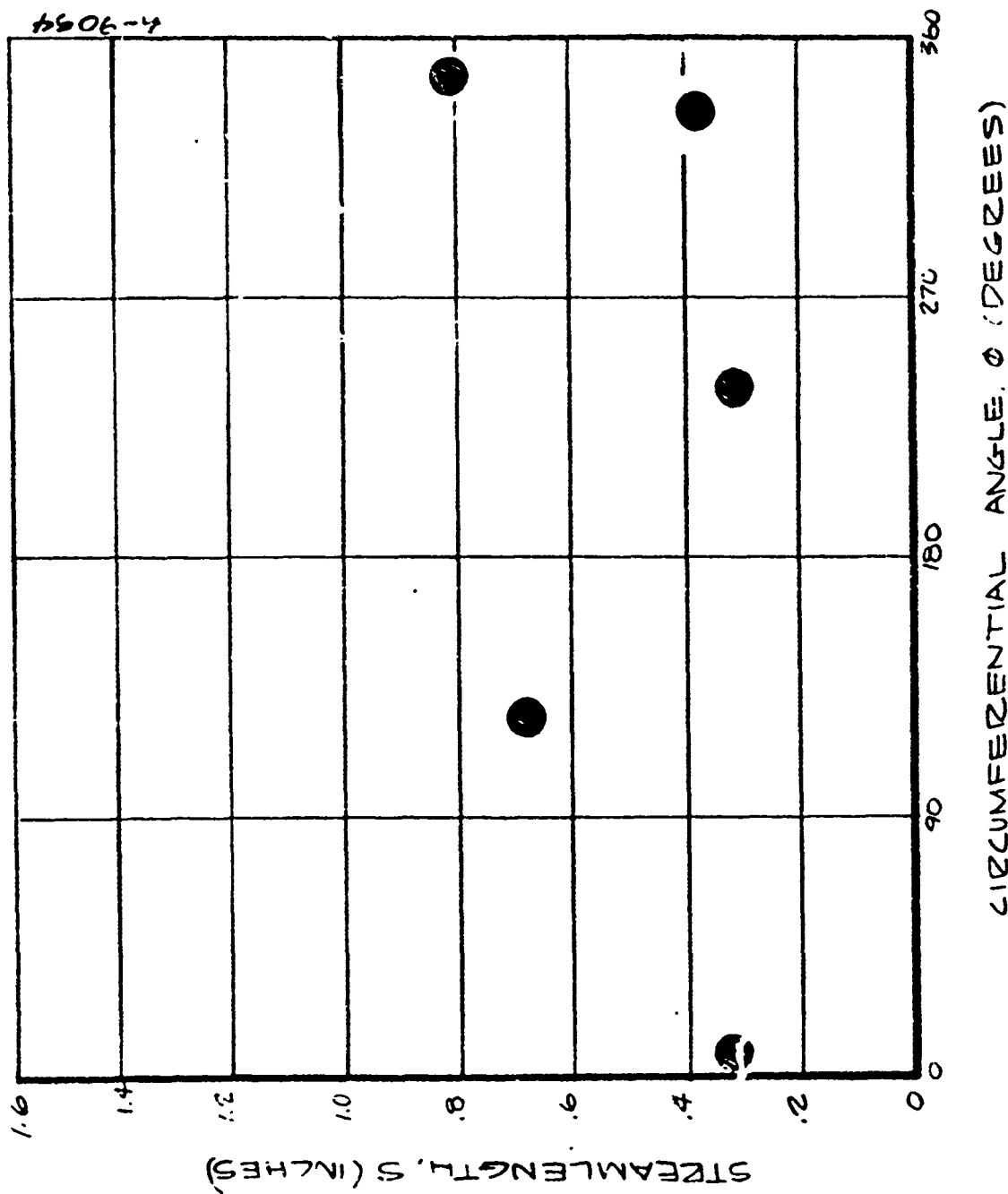


Figure F-18. Initial Transition Locations for Run 806 (0.75-Inch R_N Sphere-Cone;
 $Re_\infty = 7.36 \times 10^6/\text{ft}$; $T_0 = 921^\circ\text{F}$)

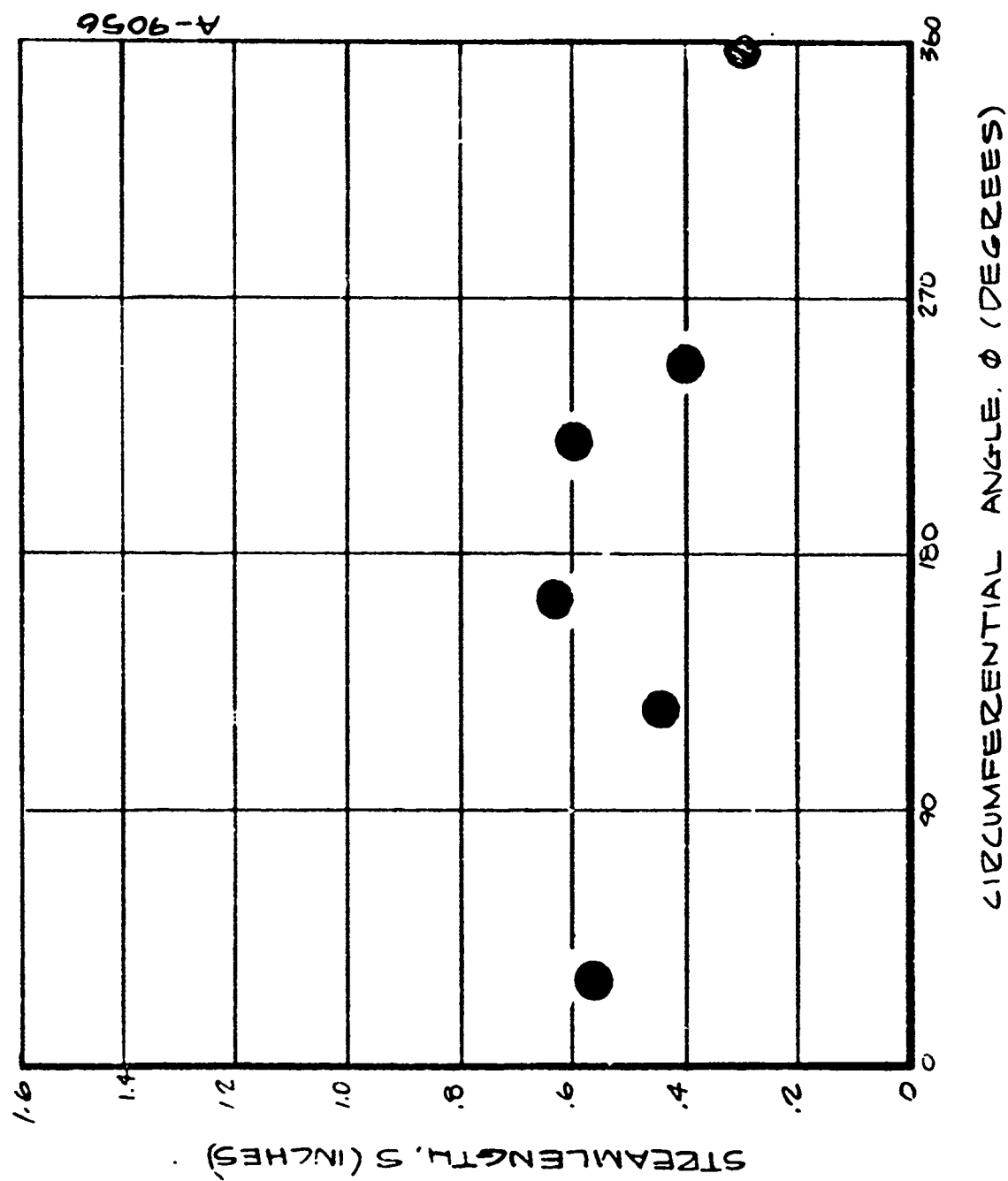


Figure F-19. Initial Transition Locations for Run 809 (0.75-Inch R_N Sphere-Cone;
 $Re_\infty = 9.38 \times 10^6/\text{ft}$; $T_0 = 971^\circ\text{F}$)

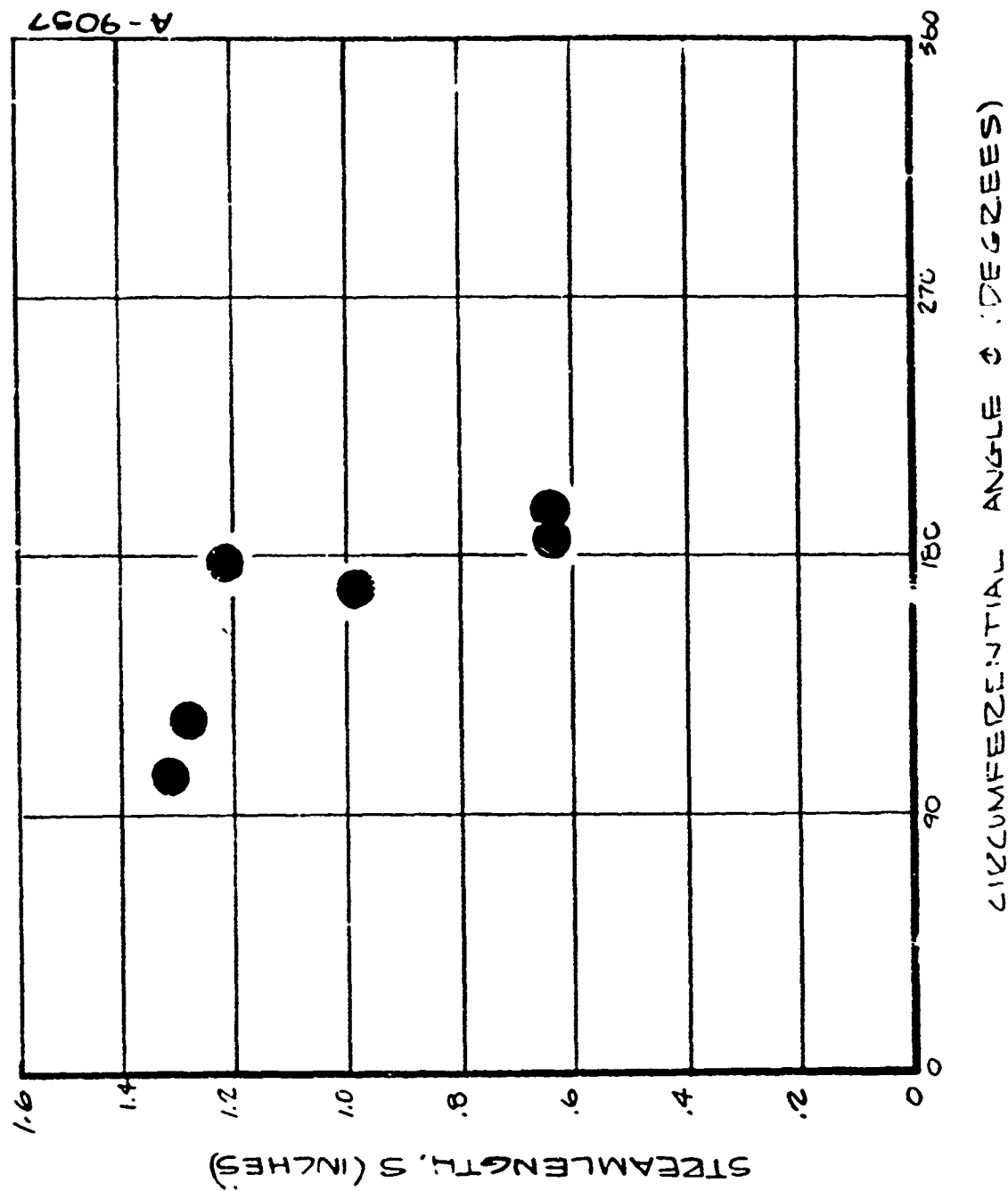


Figure F-20. Initial Transition Locations for Run 810 (1.5-Inch $R_S/60^\circ/8^\circ$ Biconic;
 $Re_\infty = 6.73 \times 10^6/f_u$; $T_0 = 964^\circ F$)

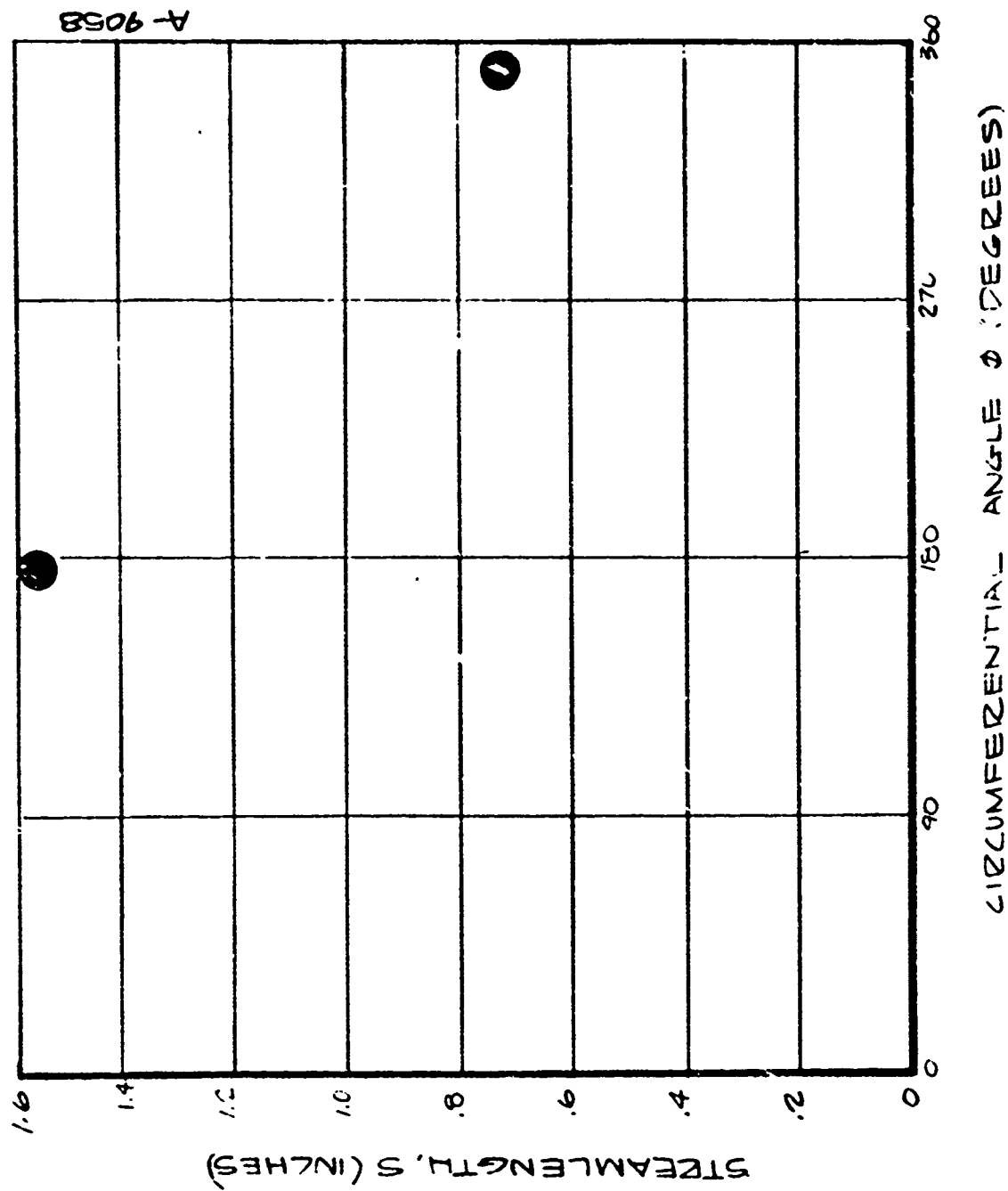


Figure F-21. Initial Transition Locations for Run 813 (1.5-Inch $R_S/75^\circ/8^\circ$ Biconic;
 $Re_\infty = 6.70 \times 10^6/\text{ft}$; $T_0 = 970^\circ\text{F}$)

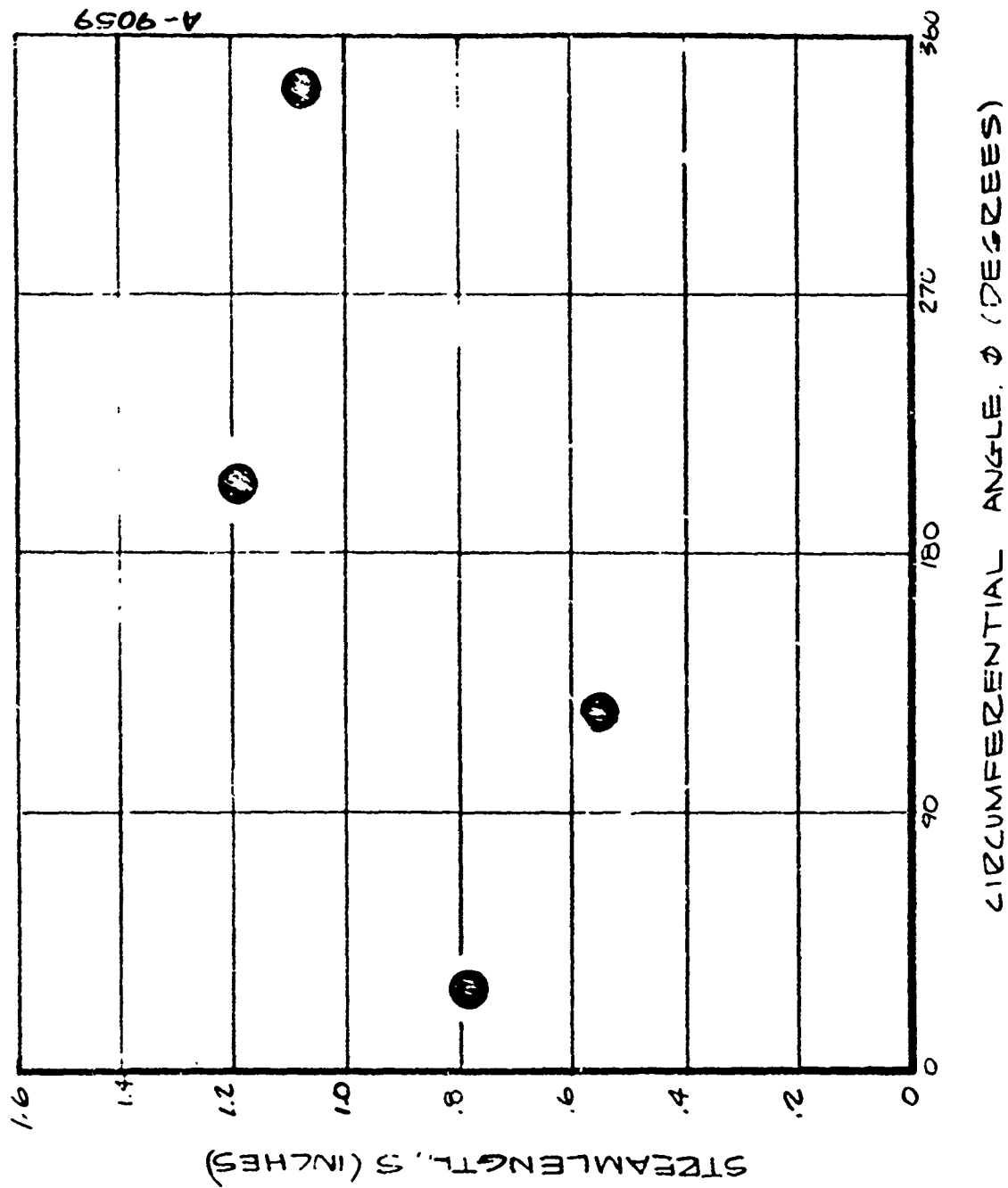


Figure F-22. Initial Transition Locations for Run 816 (1.5-Inch $R_S/60^\circ/8^\circ$ Biconic;
 $Re_\infty = 5.20 \times 10^6/\text{ft}$; $T_0 = 954^\circ\text{F}$)

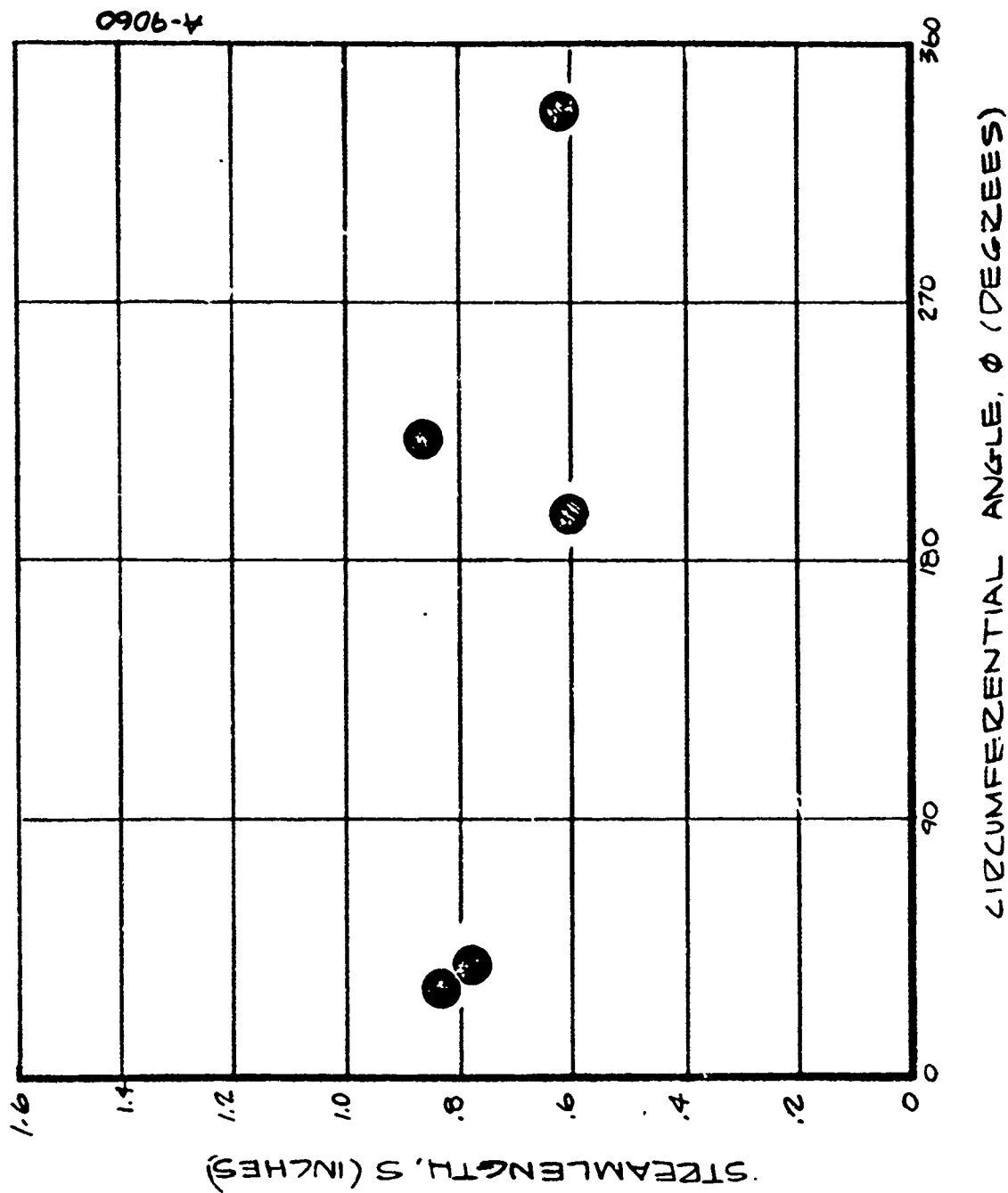


Figure F-23. Initial Transition Locations for Run 818 (1.5-Inch R_N Sphere-Cone;
 $Re_\infty = 9.56 \times 10^6/\text{ft}$; $T_0 = 508^\circ\text{F}$)

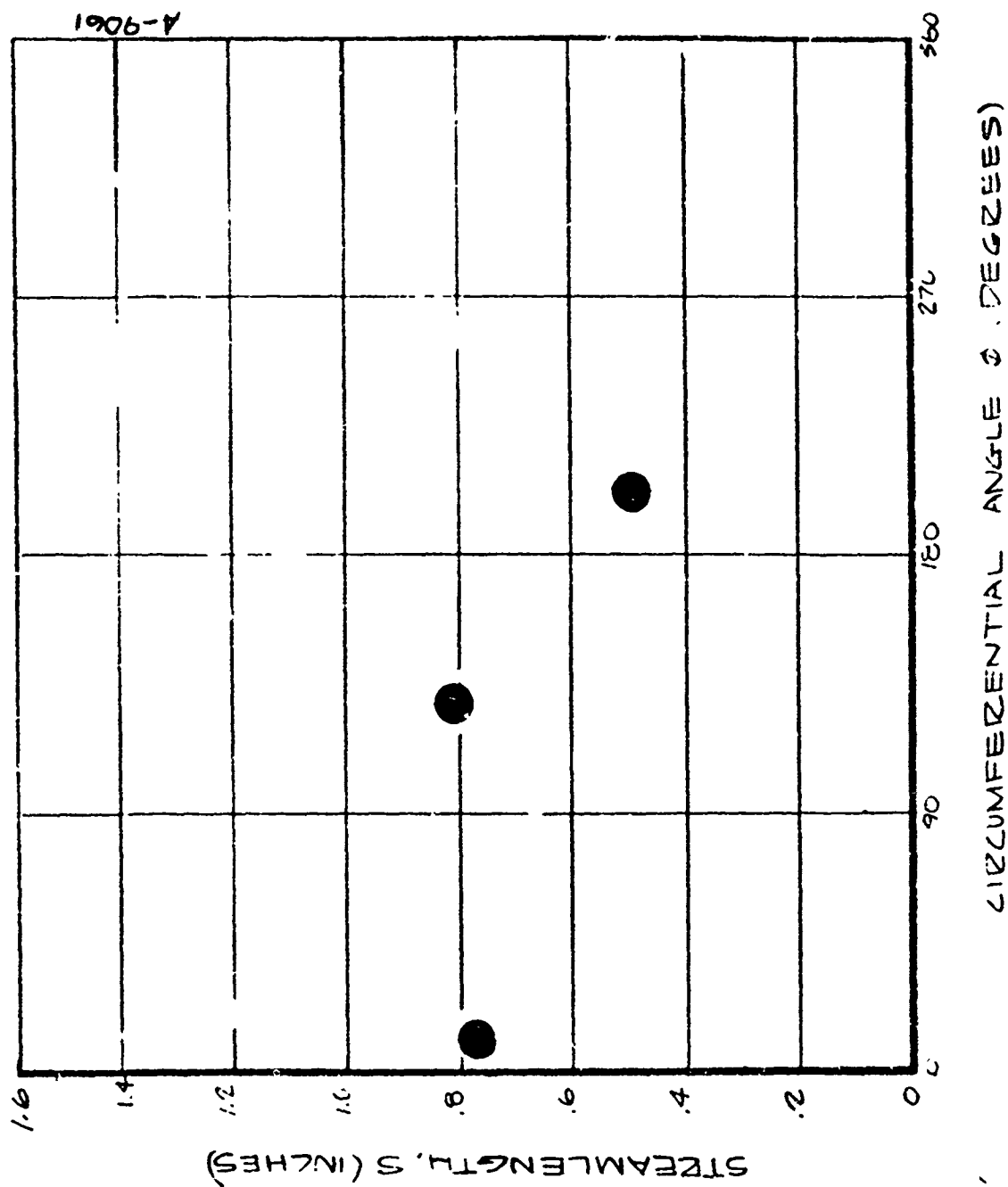


Figure F-24. Initial Transition Locations for Run 823 (1.5-Inch $R_5/75^\circ/8^\circ$ Biconic;
 $Re_\infty = 5.18 \times 10^6/\text{ft}$; $T_0 = 986^\circ\text{F}$)

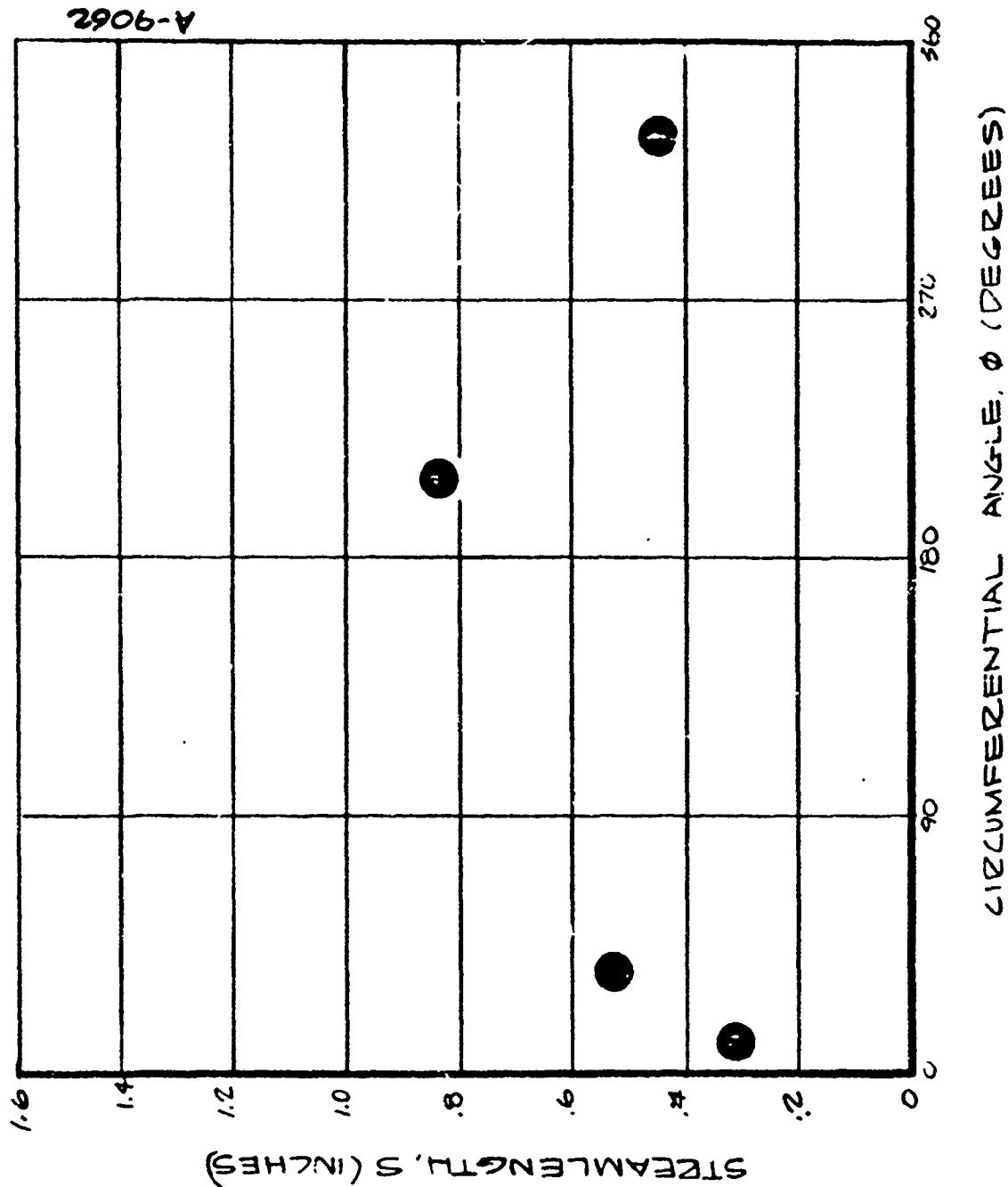


Figure F-25. Initial Transition Locations for Run 824 (1.5-Inch R_N Sphere-Cone;
 $Re_\infty = 9.44 \times 10^6/\text{ft}$; $T_0 = 535^\circ\text{F}$)

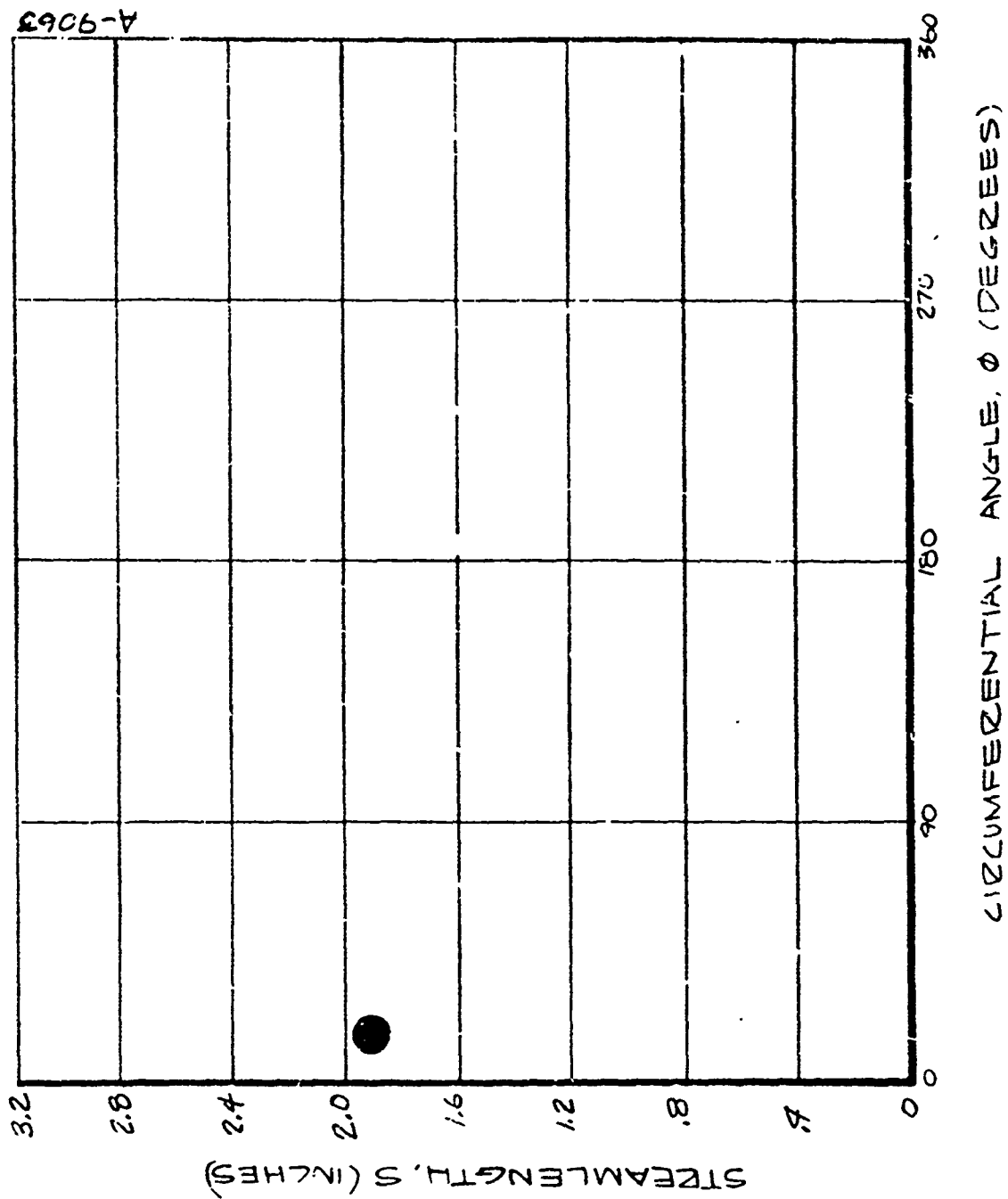


Figure F-26. Initial Transition Locations for Run 827 (2.5-Inch $R_S/55^\circ/6^\circ$ Biconic;
 $Re_\infty = 4.76 \times 10^6/\text{ft}$; $T_0 = 1008^\circ\text{F}$)

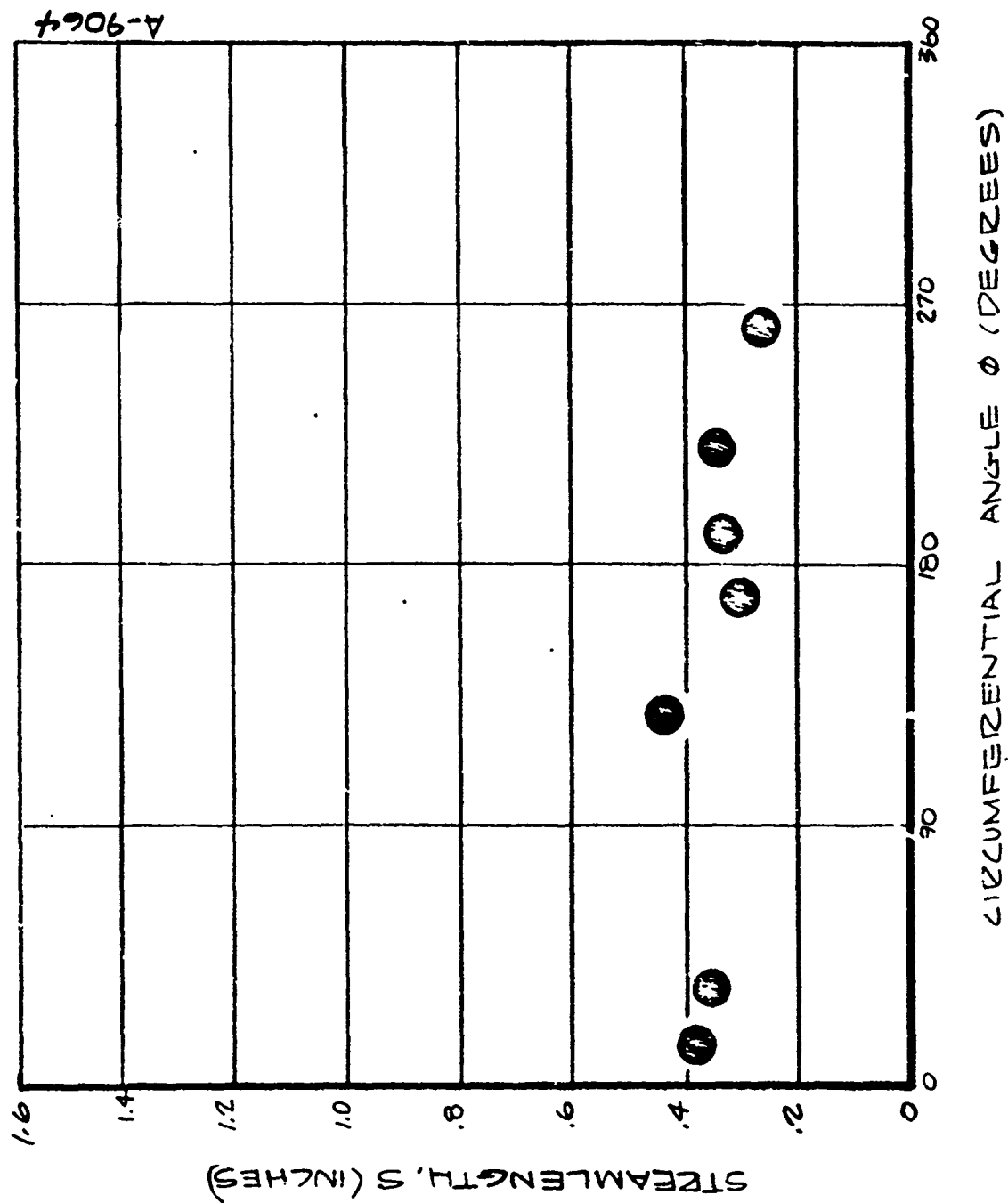


Figure F-27. Initial Transition Locations for Run 828 (0.75-Inch R_N Sphere-Cone; Variable Re_ϕ)

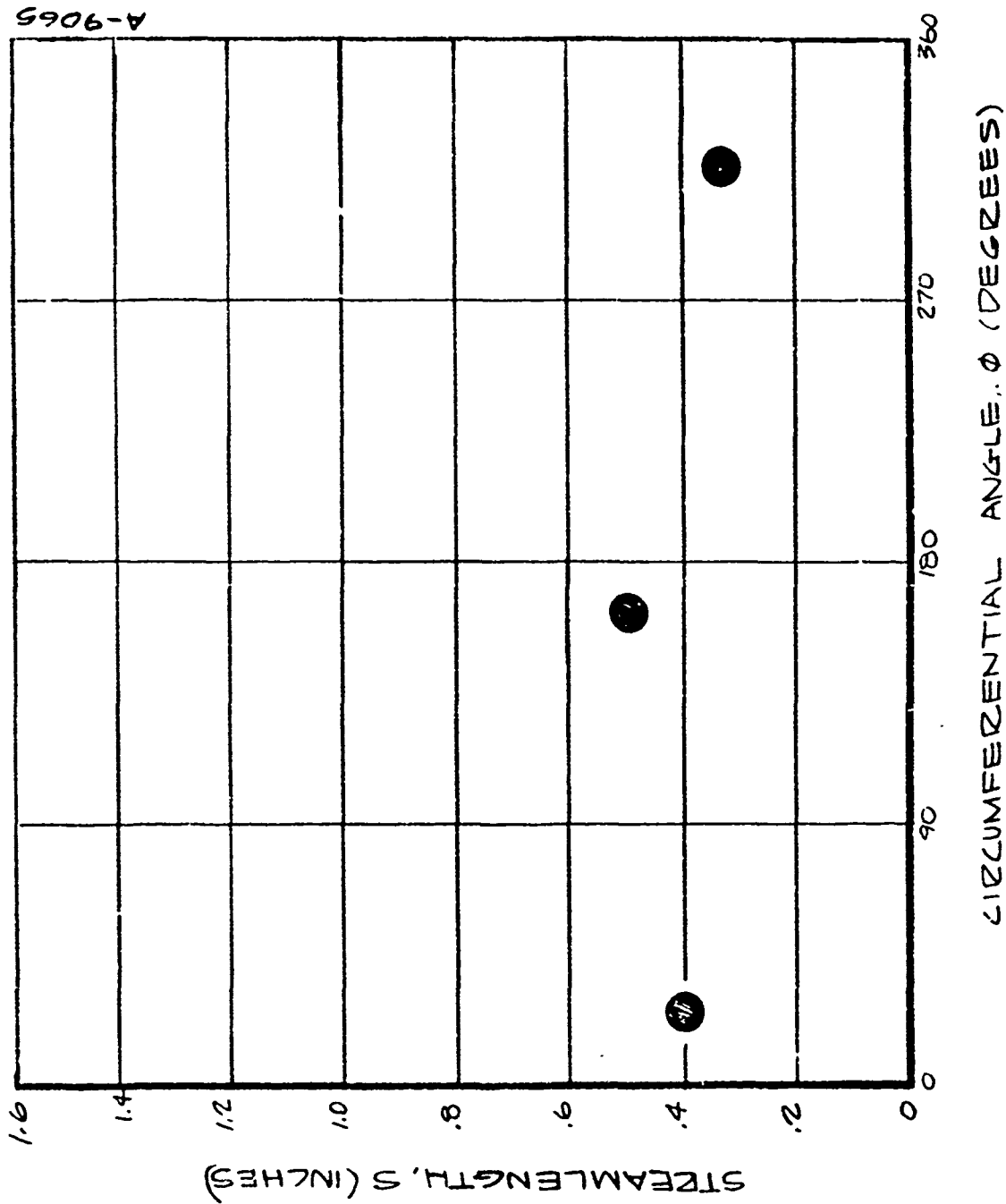


Figure F-28. Initial Transition Locations for Run 829 (0.75-Inch R_N Sphere-Cone; Variable Re_∞)